UNIVERSIDAD POLITÉCNICA DE MADRID
ESCUELA TÉCNICA SUPERIOR DE INGENIEROS DE TELECOMUNICACIÓN

CONTRIBUTION TO PHASED ARRAY AND RIS PROCESSING FOR SATELLITE, 5G AND 6G COMMUNICATION SYSTEMS

DOCTORAL THESIS

Submitted for the degree of Doctor by:

ARAL ERTUĞ ZORKUN
M. Sc. in Electrical and Electronic Engineering

Madrid, 2024

UNIVERSIDAD POLITÉCNICA DE MADRID
ESCUELA TÉCNICA SUPERIOR DE
INGENIEROS DE TELECOMUNICACIÓN

Doctoral Degree in Communication Technologies and Systems

CONTRIBUTION TO PHASED ARRAY AND RIS PROCESSING FOR SATELLITE, 5G AND 6G COMMUNICATION SYSTEMS

DOCTORAL THESIS

Submitted for the degree of Doctor by:

ARAL ERTUĞ ZORKUN
M. Sc. in Electrical and Electronic Engineering

Under the supervision of:
Dr. Miguel Alejandro Salas Natera
Associate Professor

Madrid, 2024

Title: Contribution to Phased Array and RIS Processing for Satellite, 5G and 6G Communication Systems

Author: Aral Ertuğ Zorkun

Doctoral Programme: Communication Technologies and Systems

Thesis Supervision: Dr. Miguel Alejandro Salas Natera, Associate Profesor, Universidad Politécnica de Madrid Escuela Técnica Superior de Ingenieros de Telecomunicación

External Reviewers:

Thesis Defense Committee:

Thesis Defense Date:

This thesis has been partially supported by the Spanish Government, the Ministry of Economy, and the National Program of Research, Development, and Innovation under the projects FUTURE-RADIO and INTERSPACE.

In Loving Memory of Ümit, Eren and Emin,

Acknowledgement

First and foremost, I would like to thank to my dearest mother Esin and my dearest father Ertuğrul, my family, Aysel, Sevgi and Nazlı, who are always by my side and for all their unconditioned giving and love. I would especially like to thank my closest friends Onur, Noyan, and Kaan, who have never refrained from supporting me throughout this long journey. I would also like to sincerely thank my dearest Aida for the support and her love she has given me throughout this journey. I would like to thank my dear friends Onur, Can, Üstün, Kutlu, Ekin and Yusuf for always giving me their support and attention. Even though we are far away I wish to thank to my friends all around the world, Sasan, Bürkan, Kaan, Ömer, Öykü, Müge, Mahmut, Coşkun, Tolga and Utku.

I would like to express my sincere gratitude to my advisors Assoc. Prof. Miguel Salas and Prof. Ramon Martinez for their support all over the thesis development time and their help in my difficult times. I would also like to thank Prof. Belen Galocha, Prof. Jose Manuel and Prof. Manuel Castañer. I would like to express my sincere gratitude to my thesis reviewers and jury members.

I would like to thank Chandru in particular, with whom I shared everything during my stay in Spain. I wish to thank you, Roberto and Fernando, who made me laugh during difficult times. I would like to thank Alfonso, one of my biggest supporters in Spain. To my best flatmate Lian, thank you for everything. I would also like to give a huge thank to Roberto, Juan, Flor, Celia, Fernando, and all the rest of my Lab friends and rest of the Grupo de Radiacióne.

I am grateful to all of those who gave me love and support for my entire life and during my thesis.

Abstract

The demand for high-speed data access or transmission is inevitably growing with the exponentially increasing number of communication ends, especially, in the satellite communication (SATCOM) which is one of the most active and challenging area among wireless communication systems. The new generation wireless communication standards have been introduced as fifth-generation (5G), beyond fifth-generation (B5G) and sixth-generation (6G) which work in millimeter-wave and/or sub millimeter-wave frequency spectrum. However, in millimeter-wave frequency bands there are fundamental technical challenges such as higher path losses, high blockage sensitivity, narrow beamwidth, directivity and scatter effects are more severe. Therefore, it is essential to model and develop novel technologies.

There are several wireless communication technologies that support effective deployments of the new emerging standards. Hybrid beamforming for massive multiple-input multiple-output systems (MIMO), which has been developed in recent years, is one of these technologies. Massive MIMO systems consist of large number of antennas to meet the demand of increased data rate, coverage and large amount of communication traffic as well as compensate the severe path losses. The communication relies on the line-of-sight paths of the signals, however, in the dense communication environments, the link between communication ends is most likely blocked. Therefore, reconfigurable intelligent surfaces (RIS) have been proposed to form a virtual LoS path to provide coverage between the blocked ends while improving the overall quality of service. The RIS are considered as cost-effective and energy-efficient auxiliary elements for massive MIMO systems.

The massive MIMO systems rely on advanced phased array and RIS processing. In this sense, this thesis presents contributions to several open issues in phased array and RIS processing. The contributions of thesis are discussed in four topics.

- An improved hybrid beamforming algorithm based on recursive least squares (RLS) algorithm and constant modulus algorithm for fast target tracking is proposed. The adaptive moment estimation method (ADAM) is adapted to update the forgetting factor using the gradient of the error signal. Moreover, sliding-window technique is adapted to reduce the steady-state noise and a variable regularization factor is adapted to reduce the ripples. It is overserved that the proposed algorithm has fast convergence rate and accurate target tracking performance.

- An improved inverse matrix approximation algorithm is proposed for array processing techniques where matrix inversion is required. The algorithm is based on a three-step approximation method using Homeier's approach and an iterative generalized inverse matrix approximation algorithm employing Karush-Kuhn-Tucker (KKT) conditions. To evaluate the performance of the proposed algorithm under realistic massive MIMO conditions, we propose a correlated channel model based on antenna array manifolds that includes mutual coupling, RF and radiating element impairments, and multipath channels with an angular spread. The correlated channel effects on the zero forcing precoding (ZF) algorithm were investigated. The bit error rate performance of the proposed method is close to benchmark (direct inverse ZF).
- A mutual coupling-based self-calibration method for uplink antenna arrays is proposed. The proposed method is suitable for off-line, on-site and online calibration schemes. The proposed method compensates the mutual coupling effects, gain/phase uncertainties and phase errors due to location errors with the reduced number of measurements. In addition, a novel calibration method is proposed for circularly polarized active antenna arrays based on axial ratio optimization for improvement of antenna array performance compensating errors and mutual coupling effects.
- An energy-efficient fast DoA estimation and tracking algorithm for RIS-aided massive MIMO system is proposed. The low power consumption was achieved by reducing the number of RF chains and including a switched antenna array in the receiver. The DoA estimation and tracking algorithm is based on ADAM adaptive forgetting factor RLS algorithm. The proposed algorithm accurately estimates multipath DoAs in both elevation and azimuth. Moreover, an efficient hybrid near-field and far-field channel estimation method for the RIS-aided massive MIMO systems was proposed. It has been showed that the proposed method has accurate channel estimation performance.

The common objective of all the contributions presented is to provide novel and robust solutions to specific open issues for future generation phased array and RIS processing in SATCOM. The research results obtained in this thesis are not limited to the case studies described but also to vast application areas.

Key Words:

Antenna arrays, massive MIMO, RIS, adaptive beamforming, adaptive forgetting factor, inverse matrix approximation, precoding, self-calibration, axial ratio, DoA estimation and tracking, iterative DoA estimation, hybrid-field channel estimation.

Resumen

La demanda de acceso o transmisión de datos a alta velocidad crece inevitablemente con el número exponencialmente creciente de extremos de comunicación, especialmente en la comunicación por satélite (SATCOM), que es una de las áreas más activas y desafiantes entre los sistemas de comunicación inalámbrica. Se han introducido los estándares de comunicación inalámbrica de nueva generación como quinta generación (5G), más allá de la quinta generación (B5G) y sexta generación (6G), que funcionan en el espectro de frecuencia de ondas milimétricas y/o submilimétricas. Sin embargo, en las bandas de frecuencia de ondas milimétricas existen desafíos técnicos fundamentales, como mayores pérdidas de trayectoria, alta sensibilidad al bloqueo, ancho de haz estrecho, directividad y los efectos de dispersión son más severos. Por lo tanto, es esencial modelar y desarrollar nuevas tecnologías.

Existen varias tecnologías de comunicación inalámbrica que respaldan implementaciones efectivas de los nuevos estándares emergentes. La formación de haces híbrida para sistemas masivos de múltiples entradas y múltiples salidas (MIMO), que se ha desarrollado en los últimos años, es una de estas tecnologías. Los sistemas MIMO masivos constan de una gran cantidad de antenas para satisfacer la demanda de mayor velocidad de datos, cobertura y gran cantidad de tráfico de comunicación, así como para compensar las graves pérdidas de trayectoria. La comunicación se basa en las trayectorias de línea de visión de las señales, sin embargo, en los entornos de comunicación densos, el enlace entre los extremos de la comunicación es más probable que esté bloqueado. Por lo tanto, se han propuesto superficies inteligentes reconfigurables (RIS) para formar una trayectoria virtual LoS para proporcionar cobertura entre los extremos bloqueados al tiempo que se mejora la calidad general del servicio. Las RIS se consideran elementos auxiliares rentables y energéticamente eficientes para sistemas MIMO masivos.

Los sistemas MIMO masivos se basan en un procesamiento avanzado de matriz en fase y RIS. En este sentido, esta tesis presenta contribuciones a varias cuestiones abiertas en el procesamiento de matriz en fase y RIS. Las contribuciones de la tesis se discuten en cuatro temas.

- Se propone un algoritmo de formación de haz híbrido mejorado basado en el algoritmo de mínimos cuadrados recursivos (RLS) y el algoritmo de módulo constante para el seguimiento rápido de objetivos. El método de estimación

de momento adaptativo (ADAM) se adapta para actualizar el factor de olvido utilizando el gradiente de la señal de error. Además, la técnica de ventana deslizante se adapta para reducir el ruido de estado estable y se adapta un factor de regularización variable para reducir las ondulaciones. Se destaca que el algoritmo propuesto tiene una tasa de convergencia rápida y un rendimiento de seguimiento de objetivos preciso.

- Se propone un algoritmo mejorado de aproximación de matriz inversa para técnicas de procesamiento de matrices donde se requiere inversión de matriz. El algoritmo se basa en un método de aproximación de tres pasos que utiliza el enfoque de Homeier y un algoritmo iterativo de aproximación de matriz inversa generalizada que emplea condiciones de Karush-Kuhn-Tucker (KKT). Para evaluar el rendimiento del algoritmo propuesto en condiciones MIMO masivas realistas, proponemos un modelo de canal correlacionado basado en colectores de matriz de antena que incluye acoplamiento mutuo, deterioros de RF y elementos radiantes, y canales de trayectos múltiples con una dispersión angular. Se investigaron los efectos del canal correlacionado en el algoritmo de precodificación de forzamiento a cero (ZF). El rendimiento de la tasa de error de bits del método propuesto está cerca del punto de referencia (ZF inversa directa).
- Se propone un método de autocalibración basado en acoplamiento mutuo para matrices de antenas de enlace ascendente. El método propuesto es adecuado para esquemas de calibración fuera de línea, en el sitio y en línea. El método propuesto compensa los efectos de acoplamiento mutuo, las incertidumbres de ganancia/fase y los errores de fase debidos a errores de ubicación con el número reducido de mediciones. Además, se propone un nuevo método de calibración para conjuntos de antenas activas polarizadas circularmente basado en la optimización de la relación axial para mejorar el rendimiento del conjunto de antenas compensando errores y efectos de acoplamiento mutuo.
- Se propone un algoritmo de estimación y seguimiento de DoA rápido y eficiente en energía para el sistema MIMO masivo asistido por RIS. El bajo consumo de energía se logró reduciendo el número de cadenas de RF e incluyendo un conjunto de antenas conmutadas en el receptor. El algoritmo de estimación y seguimiento de DoA se basa en el algoritmo RLS de factor de olvido adaptativo ADAM. El algoritmo propuesto estima con precisión los DoA de trayectos múltiples tanto en elevación como en acimut. Además, se

propuso un método eficiente de estimación de canal híbrido de campo cercano y campo lejano para los sistemas MIMO masivos asistidos por RIS. Se ha demostrado que el método propuesto tiene un rendimiento de estimación de canal preciso.

El objetivo común de todas las contribuciones presentadas es proporcionar soluciones nuevas y robustas a problemas abiertos específicos para el procesamiento de conjuntos en fase y RIS de próxima generación en SATCOM. Los resultados de investigación obtenidos en esta tesis no se limitan a los estudios de caso descritos sino también a amplias áreas de aplicación.

PALABRAS CLAVE:

Conjuntos de antenas, MIMO masivo, RIS, formación de haz adaptativo, factor de olvido adaptativo, aproximación de matriz inversa, precodificación, autocalibración, relación axial, estimación y seguimiento de DoA, estimación iterativa de DoA, estimación de canal de campo híbrido.

Table of Contents

Acknowledgement ..... *v*

Abstract ..... *vii*

Resumen ..... *x*

Table of Contents ..... *xiii*

List of Figures ..... *xvi*

List of Tables ..... *xx*

Abbreviations and Acronyms ..... *xxi*

1. Chapter 1: Introduction 1

1.1. Overview 1

1.2. Motivation 3

1.3. Outline of the Thesis 6

1.4. References Chapter 1 8

2. Chapter 2: Introduction to Phased Array Antennas and Reconfigurable Intelligent Surfaces 11

2.1. Array Fundamentals 11

2.2. Smart Antennas 16

2.2.1. Adaptive Beamforming Algorithms 16

2.2.2. DOA Estimation Algorithms 25

2.2.3. Antenna Array Calibration 29

2.3. Multiple-Input Multiple-Output Systems 32

2.4. Reconfigurable Intelligent Surfaces 40

2.5. References Chapter 2 44

3. Chapter 3: An Improved Hybrid Beamforming Algorithm for Fast Target Tracking Segment 51

3.1. Introduction 51

3.2. Main Contributions 52

3.3. Adaptive Beamforming Algorithm Application Tool 53

3.4. Use Cases and Trade-Offs 55

3.5. An Improved Hybrid Beamforming Algorithm for Fast Target Tracking 59

3.5.1. System Model 61

3.5.2. Constant Modulus Algorithm 63
3.5.3. Recursive Least Squares Algorithm 63
3.5.4. Sliding Window 64
3.6. Proposed Algorithm 64
3.7. Simulation Results 67
3.8. Conclusions 74
3.9. References Chapter 3 76
4. Chapter 4: An Improved Inverse Matrix Approximation Algorithm for Phased Antenna Array Applications 79
4.1. Introduction 79
4.2. Iterative Algorithms for Inverse Matrix Approximation 80
4.3. Main Contributions 83
4.4. Use Case: Zero-Forcing Precoding in Massive MIMO Systems 83
4.4.1. System Model 84
4.4.2. Linear Precoding Algorithms 86
4.4.3. The Proposed Improved Iterative Three-Step Generalized Inverse Matrix Approximation Algorithm 90
4.4.4. Computational Complexity 93
4.4.5. Simulation Results 95
4.5. Conclusions 101
4.6. References Chapter 4 102
5. Chapter 5: Novel Antenna Array Calibration Proposals 107
5.1. Introduction 107
5.2. A Mutual Coupling-Based Uplink Online Self-Calibration Method for Antenna Arrays 108
5.2.1. Evolution of Antenna Array Calibration 109
5.2.2. Main Contributions 111
5.2.3. Theoretical Formulation 111
5.2.4. Detailed Explanation of The Proposed Calibration Method 115
5.2.5. Simulation Results 121
5.2.6. Experimental Study 124
5.3. Calibration and Axial Ratio Improvement Method Based on Polarization Agile System Capability 130
5.3.1. Main Contributions 131
5.3.2. Theoretical Formulation 131
5.3.3. Calibration Procedure 137
5.3.4. Simulation Results 138
5.3.5. Experimental Study 144
5.4. Conclusions 151
5.5. References Chapter 5 153

6. Chapter VI: Direction of Arrival and Channel Estimation Proposals in RIS-Aided MIMO Systems 159

6.1. Introduction 159

6.2. Energy Efficient Low-Complexity RIS-Aided 3-D DoA Estimation and Target Tracking Algorithm via Matrix Completion 161

6.2.1. Main Contributions 161
6.2.2. System Model and Theoretical Formulation 162
6.2.3. Proposed Algorithm 164
6.2.4. Simulation Results 176
6.2.4.1. Single-Path Propagation 177
6.2.4.2. Multi-Path Propagation 179

6.3. Hybrid-Field Channel Estimation for RIS-Aided Millimeter-Wave Massive MIMO Systems 183

6.3.1. Main Contributions 184
6.3.2. System Model and Theoretical Formulation 184
6.3.3. Proposed Method 188
6.3.4. Simulation Results 193

6.4. Conclusions 197

6.5. References Chapter 6 198

7. Chapter 7: Conclusion and Future Work 205

7.1. Conclusion 205

7.2. Future Work 207

7.3. Publications 208

7.3.1. Journals 208
7.3.2. Conferences 209

List of Figures

Fig. 2.1. Antenna array with impinging planar wavefront. 12
Fig. 2.2. Weighting and sum array processing. 13
Fig. 2.3. Beamforming architectures [6]. 15
Fig. 2.4. Basic smart antenna model diagram for beamforming implementation. 17
Fig. 2.5. Calibration procedure flow-chart. 32
Fig. 2.6. Physical MIMO channel with L paths. 34
Fig. 2.7. Massive MIMO architecture [56]. 38
Fig. 2.8. Outdoor to indoor refractive RIS use case. 41
Fig. 2.9. Indoor user tracking via reflective type RIS. 41
Fig. 2.10. The uplink narrow-band RIS-aided millimeter-wave massive MIMO system. 43
Fig. 3.1. General structure of the tool. 53
Fig. 3.2. Main screen: 1) Target displacement, 2) Array geometry selection, 3) Array properties, 4) Signal type selection, defining source and interference, 5) Selection of DoA and adaptive beamforming algorithms, auxiliary user inputs, 6) Windowing selection, 7) Plot selection. 54
Fig. 3.3. Several use cases of adaptive beamforming algorithms [12]. 55
Fig. 3.4. GNSS reference (a) and monitoring station (b) [12]. 56
Fig. 3.5. Results of each case study of trade-offs, (a) SNR, (b) convergence rate, (c) interference cancelling (d) target tracking performance comparison of the selected beamforming algorithms. 59
Fig. 3.6. Communication links between maritime radar tower, satellite and marine vessels for docking traffic management in the port of Barcelona. 61
Fig. 3.7. Communication links between railroad controller, satellite and high-speed arriving trains for the control of arrival and departure traffic in the Madrid Atocha railway station. 61
Fig. 3.8. Smart antenna system. 62
Fig. 3.9. (a) NTN-LEO use case SINR versus number of snapshots comparison (b) V2X use case SINR versus number of snapshots comparison. 69
Fig. 3.10. (a) window size, Z, effect on convergence and convergence rate, (b) MSE comparison. 71
Fig. 3.11. Number of complex multiplications per iteration with respect to number of antennas. 72
Fig. 3.12. (a) SINR with respect to number of iterations, (b) forgetting factor variation of each user with respect to iteration number. 73

Fig. 3.13. Users and interference directions (a) at initial, (b) estimated after applying the proposed algorithm. 73
Fig. 4.1. Trade-off between implementation complexity and convergence of iterative algorithms 81
Fig. 4.2. Block diagram of massive MIMO system model with encoder and precoder. 84
Fig. 4.3. Computational complexity ($K = 16, i = 1$). 95
Fig. 4.4. Computational complexity ($M = 256, i = 1$) 95
Fig. 4.5. BER performance comparison, correlated channel model ($M = 256, K = 32, i = 1$). 97
Fig. 4.6. BER performance comparison, correlated channel model ($M = 256, K = 32, i = 3$). 97
Fig. 4.7. BER performance comparison, uncorrelated channel model ($M = 256, K = 32, i = 3$). 98
Fig. 4.8. BER performance perfect vs. imperfect channel estimation, correlated channel model ($M = 256, K = 32, i = 3$). 98
Fig. 4.9. The MSE comparison of approximate matrix inversion algorithms, correlated channel condition ($K = 8, i = 1$). 99
Fig. 4.10. The MSE comparison of approximate matrix inversion algorithms, correlated channel condition ($K = 8, i = 5$). 99
Fig. 4.11. The MSE comparison of approximate matrix inversion algorithms, correlated channel condition ($M = 256, K = 8$) 100
Fig. 4.12. Sum-rate vs SNR ($M = 256, K = 32, \ i = 1$) 100
Fig. 5.1. The flow chart of the proposed mutual coupling-based calibration method. 116
Fig. 5.2. The proposed online large-scale antenna array self-calibration system. 117
Fig. 5.3. The measurements of the Mm, m coefficients related to scan reflection 119
Fig. 5.4. The measurements of the Mm, k and Mk, m coefficients related to inter-element coupling. 119
Fig. 5.5. General uniform hexagonal antenna array with the true and the erroneous locations of the antenna elements. 122
Fig. 5.6. Element wise gain and phase deviations for broadside. 122
Fig. 5.7. Comparison of ideal array pattern, array pattern after calibration with tier-1 and tier-2 using IMA, array pattern after calibration with full array elements using IMA, array pattern after calibration with full array elements using DI, and not calibrated array pattern in pointing directions: (a) $\theta 0 = 0°$ and $\varphi 0 = 0°$, (b) $\theta 0 = 45°$ and $\varphi 0 = 0°$, (c) $\theta 0 = 30°$ and $\varphi 0 = 60°$. 124
Fig. 5.8. Processing system description for the FPGA unit for the measurements. 126

Fig. 5.9. Rack with RFSoC and experimental antenna elements for coupling coefficient measurements Cmk and Ckm..... 126
Fig. 5.10. Measurement setup including computer for measurement acquisition for coupling coefficient measurements Cmk and Ckm..... 126
Fig. 5.11. General uniform 4-element linear antenna array with the true and the erroneous locations of the antenna elements. 128
Fig. 5.12. Element wise gain/phase deviations and calibrated gain/phase values for broadside using IMA Tier-2. 129
Fig. 5.13. Comparison of ideal array pattern, array pattern after calibration with tier-1 and tier-2 using IMA, array pattern after calibration with full array elements using IMA, array pattern after calibration with full array elements using DI, and not calibrated array pattern in pointing direction: $\theta 0 = 0°$..... 130
Fig. 5.14. General definition of planar array geometry and circular polarization components. 132
Fig. 5.15. Procedure for the calibration and improvement of the AR for circular polarized active antenna arrays. 138
Fig. 5.16. Element wise phase and gain deviation for broadside. 139
Fig. 5.17. Pattern comparison of array, ideal, compensated with tier-1, tier-2, complete array elements and at: $\theta o = 0°$ and $\varphi o = 0°$. 141
Fig. 5.18. Pattern comparison of array, ideal, compensated with tier-1, tier-2, complete array elements and at: $\theta o = 20°$ and $\varphi o = 0°$. 142
Fig. 5.19. Pattern comparison of array, ideal, compensated with tier-1, tier-2, complete array elements and at: $\theta o = 45°$ and $\varphi o = 35°$..... 143
Fig. 5.20. Co-polar and cross-polar pattern of a planar uniform triangular array (UTA) formed by $M = 45$ active antenna element for (a) $\theta o = 0°$ and $\varphi o = 0°$, (b) $\theta o = 20°$ and $\varphi o = 0°$, (c) $\theta o = 45°$ and $\varphi o = 35°$..... 144
Fig. 5.21. Antenna array architecture used in the experimental example. 145
Fig. 5.22. General 45 elements planar antenna array sketch with 15 and 5 elements subarrays definition. 145
Fig. 5.23. (a) and (b): Pattern of the AUT based on the measured isolated element for $\theta o = 0°$ and $\varphi o = 0°$, (c) and (d): Pattern of the AUT before compensation for $\theta o = 0°$ and $\varphi o = 0°$, and (e) and (f): Pattern of the AUT after compensation for $\theta o = 0°$ and $\varphi o = 0°$. 147
Fig. 5.24. (a) and (b): Pattern of the AUT based on the measured isolated element for $\theta o = 45°$ and $\varphi o = 35°$, (c) and (d): Pattern of the AUT before compensation for $\theta o = 45°$ and $\varphi o = 35°$, and (e) and (f): Pattern of the AUT after compensation for $\theta o = 45°$ and $\varphi o = 35°$. 149

Fig. 5.25. Co-polar and Cross-polar pattern of a 9 elements sub-arrays of the AUT for (a) $\vartheta o = 0°$, (b) $\vartheta o = 20°$ and (c) $\vartheta o = 0°$. 150
Fig. 6.1. RIS-aided 3-D DoA estimation and target tracking system. 162
Fig. 6.2. Flow chart of the proposed 3-D DoA estimation and tracking algorithm. 164
Fig. 6.3. Illustration of the incomplete noisy signal data matrix, $\mathbf{Y}\boldsymbol{t}$, and the recovered signal data matrix, $\mathbf{Y}\boldsymbol{t}$. 165
Fig. 6.4. Low-rank case in signal data matrix, $\mathbf{Y}\boldsymbol{t}$. 166
Fig. 6.5. Computational complexity comparison of algorithms in terms of number of complex multiplications. 177
Fig. 6.6. Comparative representations of MUSIC, NLMS, VSS-NLMS, RLS and the proposed algorithm, (a) final theta spectrum, $\theta 6{,}1 = 51o$, (b) final phi spectrum, $\phi 6{,}1 = 51o$, (c) mean square errors at 10 dB SNR, (d) estimation RMSE of final theta angle under varying SNR, (e) estimation RMSEs of final phi angle under varying SNR, (f) performance of target tracking at 10 dB SNR, tracking average error. 179
Fig. 6.7. Comparisons of MUSIC, NLMS, VSS-NLMS, RLS and the proposed algorithm, (a) the spatial spectrum of the final DoAs of the user and its scatters: $\theta T, 2 = 21o$, $\theta T, 3 = 36o$ and $\theta T, 4 = 51o$, (b) and (c) RMSE of final elevation and azimuth angles of the user under varying SNR, (d) MSE at 10 dB SNR, (e) TE in each epoch at 10 dB SNR, (f) signal loss under varying $\%$ of switched-off antennas. 181
Fig. 6.8. Resolution probabilities of MUSIC, RLS and the proposed algorithm for $L = 3600$, (a) varying SNR with two signals with final DoAs, $\theta T, 1 = 36o$ and $\theta T, 2 = 41o$ under $\%25$ random switched-off antennas condition, (b) angle separation between two finals DoAs from $\theta T, 1 = 36o$ and $\theta T, 2 = 36o + \Delta\theta$, $\Delta\theta$ changes from $2o$ to $8o$, (c) varying $\%$ of switched-off antennas with final DoAs, $\theta T, 1 = 36o$ and $\theta T, 2 = 41o$. 183
Fig. 6.9. The uplink narrow-band RIS-aided mm-Wave massive MIMO system with mixed far-field and near-field scatters. 185
Fig. 6.10. Scatter plots for localization of the scatters: (a) between the RIS-BS channel (DoAs), (b) between the UE-RIS channel (DoDs). 195
Fig. 6.11. The RMSE comparison with respect to SNR of the 2D ANM, 2D SS-MUSIC and 2D LASSO: (a) DoAs, (b) DoDs. 195
Fig. 6.12. The NMSE comparison of LS, far-field OMP, near-field-OMP, LS, oracle and the proposed channel estimators. 196

List of Tables

Table 3-I. Inputs for the SNR and convergence rate comparison. 56
Table 3-II. Inputs for the interference cancelling comparison. 57
Table 3-III. Inputs for the target tracking comparison. 58
Table 3-IV. Simulation Parameters for SW-AFVF-CMARLS. 67
Table 3-V. Parameters for the NTN-LEO Simulation. 68
Table 3-VI. Parameters for the V2X Simulation. 68
Table 3-VII. Parameter for the multi-user case simulations. 70
Table 3-VIII. Complexity analysis. 71
Table 4-I. Comparison of Iterative Algorithms [13]. 81
Table 4-II. Computational complexity comparison. 94
Table 5-III. Comparison of discussed calibration methods from literature. 110
Table 5-IV. Standard uncertainties. 121
Table 5-V. Standard uncertainties. 139
Table 5-VI. S21 parameter measured of the radiating element 45 with respect to elements 43 and 44. 146
Table 5-VII. S21 parameter measured of the radiating element 30 with respect to elements 43, 41, 29 and 28. 146
Table 5-VIII. S21 parameter measured of the radiating element 42 with respect to elements 25, 29, 41, 40, 39 and 37. 146
Table 5-IX. Pattern parameters comparison for case study of $\theta o = 0°$ and $\varphi o = 0°$. 150
Table 5-X. Pattern parameters comparison for case study of $\theta o = 45°$ and $\varphi o = 35°$. 150
Table 5-XI. Compensated pattern parameters comparison for case study of $\theta o = 0°, 20°$ and $30°$, and $\varphi o = 0°$. 151
Table 6-I. Computational complexity comparisons of the algorithms: MUSIC, NLMS, VSS-NLMS, RLS and AF-RLS. 177
Table 6-II. Simulation parameters for the single-path propagation case. 177
Table 6-III. Simulation parameters for the multi-path propagation case. 179
Table 6-IV. Simulation parameters. 194

Abbreviations and Acronyms

AP	Access Point
ADAM	Adaptive Moment Estimation Method
ADC	Analog to Digital Converter
ADMM	Alternating Direction of Multipliers Method
AF	Array Factor
AMI	Approximate Matrix Inversion
ANM	Atomic Norm Minimization
AR	Axial Ratio
AUT	Antenna Under Test
BER	Bit Error Rate
BPSK	Binary Phase Shift Keying
BS	Base Station
B5G	Beyond Fifth Generation
CI	Chebyshev Iteration
CMA	Constant Modulus Algorithm
CP	Co-Polar
CRB	Cramer-Rao Bound
CR	Conjugate Residual
CSI	Channel State Information
dB	Decibel
DAC	Digital to Analog Converter
DDA	Direct Decision Algorithm
DOA	Direction of Arrival
DOD	Direction of Departure
DOF	Degree of Freedom
EM	Electro Magnetic
ESPIRIT	Estimation of Signal Parameters via Rotational Invariance Technique
EVD	Eigen Value Decomposition
FoV	Field of View
FPGA	Field Programmable Gate Array
GMRES	Generalized Minimal Residual
GSLC	Generalized Side Lobe Canceler
GUI	Graphical User Interface
IA	Internal Arithmetic
IASLE	Iterative Approaches for Solving Linear Equations
IMRN	Iterative Algorithms for Minimizing the Residual Norm
IoT	Internet of Things
KKT	Karush-Kuhn-Tucker
LASSO	Least Absolute Shrinkage Selection Operator
LEO	Low-Earth-Orbit
LMS	Least Mean Square
LOS	Line of Sight
LS	Least Squares
MC	Monte Carlo

MCO	Maximum Combined Output
MF	Matched Filter
ML	Maximum Likelihood
MIMO	Multiple Input Multiple Output
MMSE	Minimum Mean Square Error
MM-WAVE	Millimeter Wave
MNM	Minimum Norm
MSE	Mean Square Error
MUSIC	Multiple Signal Classification
MV	Minimum Variance
MVDR	Minimum Variance Distortion Response
NI	Newton Iteration
NLMS	Normalized Least Mean Square
NS	Neumann Series
NTN	Non-Terrestrial Network
OMP	Orthogonal Matching Pursuit
SAGE	Space Alternating Generalized Expectation-Maximization
SAS	Smart Antenna Systems
SATCOM	Satellite Communication
SINR	Signal to Interference Plus Noise Ratio
SDMA	Space Division Multiple Access
SMI	Sample Matrix Inversion
SNR	Signal to Noise Ratio
SOR	Successive Over Relaxation
SR	Spatial Reference
RF	Radio Frequency
RIS	Reconfigurable Intelligent Surfaces
RLS	Recursive Least Squares
RMSE	Root Mean Square Error
RZF	Regularized Zero Forcing
TR	Time Reference
TNNR	Truncated Nuclear Norm Regularization
UE	User Equipment
UHA	Uniform Hexagonal Arrays
ULA	Uniform Linear Arrays
URA	Uniform Rectangular Arrays
V2X	Vehicle-to-Thing
WSF	Weighted Subspace Fitting
XC	Cross Polar
XPD	Cross Polar Discrimination
ZF	Zero Forcing
5G	Fifth Generation
6G	Sixth Generation

1. Chapter 1: Introduction

1.1. Overview

Antennas and arrays are the key components that fulfill the developments and the evolving requirements of the wireless communication systems. In the design and implementation of fifth-generation (5G), beyond fifth-generation (B5G) and sixth-generation (6G) wireless communication systems, as well as satellite communication (SATCOM), new challenges are presented as the higher data transmission rates are in need for the increased number of end users.

In the 5G systems the operating frequencies are higher than the previous generation wireless communication systems, typically in the millimeter-wave (mm-Wave) frequency range. The mm-Wave frequencies provide higher data rates, more capacity and wider bandwidth. The frequency range is even more in B5G communication systems where potentially sub millimeter-wave frequency ranges are considered. On the other hand, the 6G communication systems are expected to provide higher data rates and lower latency than 5G and B5G systems. Those communication schemes can be implemented on SATCOM systems to transmit and receive signals between ground stations and orbiting satellites. Such systems are required to transmit and receive signals with low loss and high gain. Along with the high data transmission rate and low latency, noise and interference mitigation are also needed at the same time. However, in mm-Wave frequency meeting with those requirements are challenging tasks since signals are prone to attenuation due to atmospheric absorption and shorter wavelengths lead higher path losses in mm-Wave ranges and more scatters occur. Moreover, the electromagnetic spectrum is a scarce resource, therefore, higher capacities must be translated into a more efficient user of it.

In order to overcome the challenges that are introduced by the developments and enhancing of the future generation wireless communication systems, advanced signal processing and hardware architecture has been proposed over the years. One of the most effective technologies is the smart antennas. Smart antennas are intended to use to increase coverage, capacity, improve the quality of service (QoS), user localization, and decrease the delay dispersion. These achievements are enabled by advanced signal processing methods which are known as beamforming techniques in smart antennas.

The beamforming techniques are used to direct the transmitted or received signals in a desired direction or towards to a specific target. The beamforming techniques can improve the overall QoS by increasing the range and capacity of the communication system, mitigating the interreference and noise as well as enhancing signal strength. Beamforming is generally categorized as analog and digital beamforming. In analog

beamforming each antenna is fed by the same signal and analog phase shifters are used to steer or direct the signal transmitted by the antenna array. On the contrary, in digital beamforming different signals are generated and are assigned to each antenna in the digital domain. Therefore, there is more flexibility in digital beamforming compared to analog beamforming. Moreover, different amplitudes and phases, also different parts of the frequency bands can be assigned to different antennas. Since the superposition of signals are transmitted, each with a different direction, digital beamforming becomes very advantageous for spatial multiplexing. Additionally, a large bandwidth is advantageous as a signal with fixed phases would orient differently across the band. The beamforming techniques are for directional transmission or reception relying on the line-of-sight (LOS) condition and multi-path effects are not taken into account to improve the QoS. However, multi-path components can be used to increase the overall QoS.

The more advanced signal processing technique, the multiple-input and multiple-output (MIMO) has been developed which takes into account the multi-path effects, thus, MIMO supports the multi-stream transmission. The MIMO uses the antenna array to transmit and receive multiple data streams simultaneously which is known as full-duplex. The simultaneous data transmit and receive increase the capacity and spectral efficiency of the system significantly. However, the MIMO systems require more complex signal processing algorithms to distinguish the different data streams as well as mitigate the noise and interference. The MIMO systems support the space-division multiple access (SDMA), using directional or smart antennas to communicate on the same frequency with users in different locations within the range of the same base station which has significant advantage in multiple user case over beamforming. However, over the years, with enhancement in processing techniques and merges in applications, beamforming and MIMO have been evolved in same discussion.

The signal processing in beamforming was extended from analog phase shifters to multiple radio frequency (RF) chains which is, as mentioned before, digital beamforming. In the digital beamforming multi-beam transmission can be performed, moreover, the carrier signals can be transmitted and received from multi-path as in the MIMO transmission. Hence, the hardware set-up for digital beamforming can be equivalent to MIMO precoding and decoding, inducing similar systematic signal processing.

The massive MIMO systems, which are the direct extension of multi-user MIMO with more antenna elements in the receiver, are considered to play an important role not only in 5G mobile communications technology but also in B5G technology, 6G technology that will be used mainly for autonomous driving and industry 4.0, and will be used in the internet of things (IoT), respectively [1], [2], [3], [4]. The usage of massive MIMO systems at ultrahigh frequencies is to compensate for the high free path losses at millimeter wavelengths by using a large number of antenna elements [3], [5]. The densely numbered antenna structure of massive MIMO systems increases the transmission rate, spectral

efficiency and power spectral efficiency [6], [7], [8] as well. However, in highly dense environments the LOS channel between the transmitter and receiver is likely to be blocked [9], moreover, signal reflections, refractions, diffractions and scatterers highly effect the positioning signal [1]. In order to mitigate the effects of factors hindering accurate channel estimation and provide a virtual LOS channel where required, a new concept known as reconfigurable intelligent surface (RIS) has been proposed [10], [11].

The surfaces of RISs consist of a large number of small elements which are capable of reflect and manipulate the incident signals. The RISs are used for combining function of phase shift and radiation together on an electromagnetic surface. The RISs are cost-effective and easy to deploy since consist almost entirely of passive devices and low-power phase shifters [5], support full-duplex, and are compatible with existing standards and hardware [11]. Phase control of the antenna elements on the RIS can be simple enough to be done by PIN diodes. By controlling the phase and amplitude of the reflected waves, an IRS can be used to enhance signal strength, improve coverage, and reduce interference in the system. Therefore, RISs are cost-effective and energy-efficient auxiliary elements for massive MIMO systems [12]. It seems that RISs will be a research topic that will remain on the agenda for a long time for next generation wireless communication systems.

In the modern and future wireless communication systems, beamforming, massive MIMO and RIS are being developed to enhance QoS. However, there are vast open issues to overcome in those advanced technologies to be mentioned.

1.2. Motivation

The motivation of this thesis is based on the evaluation of new phased array and RIS processing techniques, and propose novel algorithms and methods to improve the overall performance of the smart antennas and massive MIMO systems. Therefore, solutions have been proposed to a wide range of open problems in the processing of general phased antenna arrays and RIS in this thesis.

The smart antenna systems and massive MIMO systems are considered to play an important role not only in 5G mobile communication technology but also in B5G technology, 6G technology that will be used mainly for autonomous driving and industry 4.0, and will be used in the internet of things (IoT), respectively [1], [2], [3], [4]. The demand for high-speed data access or transmission is inevitably growing with the exponentially increasing number of users. The smart antennas and massive MIMO systems can serve many users at the same time by increased number of antennas. The densely numbered antenna structure of smart antennas and massive MIMO systems provides high transmission rate, spectral efficiency, and power efficiency [3],[4],[5]. However, a large number of antennas have drawbacks that must be carefully considered along with the other challenging issues, thus, in order to maintain seamless

communication and carry the performances of the system any further advanced signal processing techniques are in need for the future generation communication systems. The performance of the system highly depends on the which algorithms or techniques are used [13].

In smart antenna system, adaptive beamforming algorithms generate weights for each antenna element in array to direct the array radiation pattern to desired directions [14], [15]. By applying beamforming, the output signals from an antenna array are summed and beam is directed to the target precisely, in the meantime, deep nulls are directed to undesired signal directions and thus interference suppression is performed. Moreover, the fast target tracking is a highly challenging task for SAS. Most likely, optimum results may not be achieved by only using one type of algorithm. Therefore, hybrid adaptive algorithms are proposed to achieve higher convergence rate, better interference suppression, low steady-state noise and fast target tracking. To cope with these issues, the Chapter 3 proposes an improved hybrid constant modulus RLS beamforming algorithm with adaptive forgetting factor and variable regularization factor. Forgetting factor is updated by low-complexity yet robust adaptive moment estimation method (ADAM). The sliding-window technique is applied to the proposed algorithm to mitigate the steady-state noise.

On the other hand, the large number of antennas leads significant computation burdens and inaccurate results in such cases the beamforming weight computation by Wiener optimum, pseudo inverse computation in maximum-likelihood (ML) based direction-of-arrival estimation, precoding in massive MIMO, etc. The Chapter 4 proposes an inverse matrix approximation algorithm to overcome this issue. Most of the inverse matrix approximation algorithms in the literature require initial conditions and pre-computations to converge to the optimal matrix inversion. The proposed improved iterative algorithm guarantees convergence under any circumstances without dependency on any optimized initial parameter or condition. Moreover, nonsymmetric diagonally dominant matrix inverses can be computed more accurately without pre-computation to optimize the initial values with the proposed algorithm.

The smart antenna systems and massive MIMO systems mostly require a calibration process for optimum performance. The overall objective is to make sure that each element's frequency-dependent amplitudes and phases are precisely adjusted to produce the desired beam pattern, while the techniques and details differ. However, large-scale antenna arrays require time-consuming measurements and trail-and-error methods with visual inspections, as the number of antennas increases the required time increases as well. Thus, low-complexity calibration algorithms are needed with automated measurement campaigns while the system is under operation. In Chapter 5, a novel mutual coupling-based uplink online self-calibration method is proposed to deal with this issue. The novel built-in self-calibration method for transmit made large-scale phased antenna arrays is compliant with all off-line, on-site and online calibration schemes with

the reduced number of measurements. Moreover, in many systems circularly polarized antenna arrays are used since circular polarization is much less prone to cross-pol interference. However, unequal co-polarized and cross-polarized wavefields due to the array impairments must not be ignored in such systems. Achieving accurate and reliable performance from the antenna arrays requires precise calibration of axial ratio. The axial ratio is a key parameter that characterizes the polarization purity of an antenna, and calibration is necessary to ensure optimal signal quality and minimize interference. Therefore, in Chapter 5, another calibration method is proposed to calibrate phase, gain, and location errors as well as mutual coupling to optimize and improve the axial ratio based on polarization agile system capability. The proposed method is suitable for off-line and on-site calibration processes with the reduced number of measurements.

Last but not least, in massive MIMO systems, the three-dimensional (3D) beamforming is considered to enable the link reliability enhancement [16]. The accurate estimation of the direction-of-arrival (DoA) is the preliminary stage of 3D beamforming [17], target localization [18] and channel estimation [19] in RIS-aided millimeter-wave massive MIMO systems, as in many communication applications. The subspace DoA estimation algorithms, such as, multiple signal classification (MUSIC) [20], estimation of signal parameters via rotational invariance technique (ESPIRIT) [21], weighted subspace fitting (WSF) [22] and maximum likelihood (ML) [23], are widely used in RIS-aided communication systems. The performance of subspace DoA algorithms depends on the correlation, which requires the signal information from each antenna in an array. However, the implementation of such algorithms becomes impractical in mMIMO systems since the power consumption of the radio frequency chain (RF) connected to each antenna in the access point (AP) will be high. Additionally, these algorithms include eigen value decomposition (EVD) or matrix inversion operations with high computational complexity. The high computation leads latency and disruptions in high-speed data flow, especially if targets are dynamic. To overcome these problems, in Chapter 6, we propose an energy-efficient fast DoA estimation and tracking algorithm for RIS-aided massive MIMO systems. The DoA estimation and tracking algorithm does not involve correlation matrix and EVD or inverse matrix operations and not require all elements in the antenna array for processing. Besides, the proposed algorithm is based on adaptive forgetting factor recursive least squares (AF-RLS) algorithm which exploits the computational effectiveness of adaptive moment estimation method (ADAM) to update the forgetting factor by using the first gradient of error signal as proposed in Chapter 3.

On the other hand, the channel estimation is another challenging task in RIS-aided massive MIMO systems since the total number of antennas is larger and there are multiple different channels (direct, cascaded, multiple cascaded, etc.). In practical communication systems mixed far-field and near-field signals exist resulting in hybrid-field communication scenario [24], [25]. The hybrid-field estimation is more complex than

the conventional channel estimation problem. In fact, most of the existing methods are limited with either near-field [26], [27], [28]or far-field channel estimation [29], [30], [31], thus, their channel estimation performances are limited in real cases. To tackle this problem, in Chapter 5, an efficient hybrid-field channel estimation method for RIS-aided millimeter-wave massive MIMO systems is proposed. A special fourth-order cumulant matrix and remove the near-field component for estimating the direction-of-departures (DoDs) and direction-of-arrivals (DoAs). In order to extract the angular information of DoDs and DoAs, the special fourth-order cumulant matrix is reconstructed by applying the atomic norm minimization (ANM). The ANM is used to increase the estimation resolution of DoDs and DoAs.

1.3. Outline of the Thesis

The content of this thesis has been organized in seven chapters:

- Chapter 1 discusses the general topics of the phased array and RIS processing for the SATCOM and the future generation communication systems, namely, 5G, B5G and 6G. A brief introduction to the open issues in phase array and RIS processing and their state-of-the-art solutions are given. The main objectives and motivations of this thesis are stated. Finally, an outline of the structure of this thesis given.
- Chapter 2 is dedicated to the detailed introduction to the theoretical receive and transmission models and mathematical formulations for the phased array and RIS processing. The fundamentals of antenna arrays are briefly discussed. The detailed explanations of smart antennas and multiple-input multiple output, which are the basics of the phase array and RIS processing, are given. The essential beamforming and direction of arrival estimation algorithms are briefly explained.
- Chapter 3 is dedicated to developed adaptive beamforming application tool to evaluate and compare the state-of-the-art beamforming and direction of arrival estimation algorithms. Trade-offs of the adaptive beamforming and direction of arrival algorithms are discussed. Additionally, the empirical analysis of the impact of mutual coupling, gain/phase uncertainties in the active antenna arrays, the array geometry and windowing on those algorithms are given which depend on the results of this developed tool. The derivation and analysis of the proposed hybrid constant modulus recursive least squares beamforming algorithm for fast target tracking and improved interference mitigation are given. The effectiveness of the proposed beamforming algorithm is discussed by comparing it with the state-of-the-art algorithms.
- Chapter 4 proposes a solution to the matrix inversion encountered in most signal processing schemes. The derivation of the proposed inverse matrix approximation algorithm is given. The analyses of the proposed algorithm are given. The proposed

algorithm is verified using a new correlated channel model that includes mutual coupling effects, gain/phase uncertainties and antenna element location in the receiver antenna array. The bit error rate performance of the proposed algorithm is compared with the prominent existing algorithms for the case of precoding massive multiple-input multiple-output communications systems.

- Chapter 5 deals with the calibration problem in large-scale phased antenna arrays. This chapter introduces two novel calibration methods for different applications. The formulation and derivation of a novel mutual coupling-based uplink online self-calibration method is discussed in details. On the other hand, another calibration technique for phase, gain, and location errors as well as mutual coupling is proposed to improve the axial ratio based on polarization agile system capability. The calibration performances are evaluated for both method as well as the real case results from the experimental studies are included.
- Chapter 6 deals with the two major problems in RIS-aided millimeter-wave massive multiple-input multiple-output systems, namely, low-complexity energy efficient direction of arrival estimation and mixed near-field and far-field channel estimation. In order to reduce the total power consumption in the receiver and at the same time increase the direction of arrival estimation and tracking capability in RIS-aided millimeter-wave massive multiple-input multiple-output systems, a novel algorithm is developed and detailed explanations are given. On the other hand, a hybrid-field channel estimation method for RIS-aided millimeter-wave massive multiple-input multiple-output system is proposed. Different performance metrics are determined for both the proposed algorithm and the proposed method, they are analyzed and compared with the state-of-the-art algorithms and methods.
- Chapter 7 summarises the contributions by giving brief conclusions of each chapter. The future frameworks, which are the continuations of the contributions of this thesis, are discussed and possible suggestions are made for the future studies. Finally, a list of academic publications used in and derived from this thesis is given.

1.4. References Chapter 1

[1] R. Chen, M. Liu, Y. Hui, N. Cheng, and J. Li, "Reconfigurable Intelligent Surfaces for 6G IoT Wireless Positioning: A Contemporary Survey," IEEE Internet of Things Journal, vol. 9, no. 23, pp. 23570–23582, Dec. 2022, doi: 10.1109/JIOT.2022.3203890.

[2] J. He, F. Jiang, K. Keykhosravi, J. Kokkoniemi, H. Wymeersch, and M. Juntti, Beyond 5G RIS mmWave Systems: Where Communication and Localization Meet. 2021.

[3] J. He, H. Wymeersch, and M. Juntti, "Channel Estimation for RIS-Aided mmWave MIMO Systems via Atomic Norm Minimization," IEEE Trans. Wireless Commun., vol. 20, no. 9, pp. 5786–5797, Sep. 2021, doi: 10.1109/TWC.2021.3070064.

[4] S. Dang, O. Amin, B. Shihada, and M.-S. Alouini, "What should 6G be?," Nat Electron, vol. 3, no. 1, pp. 20–29, Jan. 2020, doi: 10.1038/s41928-019-0355-6.

[5] R. Wang, H. Ren, C. Pan, J. Fang, M. Dong, and O. A. Dobre, "Channel Estimation for RIS-aided mmWave Massive MIMO System Using Few-bit ADCs." arXiv, Jan. 26, 2023. Accessed: Apr. 28, 2023. [Online]. Available: http://arxiv.org/abs/2301.11066

[6] E. Ali, M. Ismail, R. Nordin, and N. F. Abdulah, "Beamforming techniques for massive MIMO systems in 5G: overview, classification, and trends for future research," Frontiers Inf Technol Electronic Eng, vol. 18, no. 6, pp. 753–772, Jun. 2017, doi: 10.1631/FITEE.1601817.

[7] F. Rusek et al., "Scaling up MIMO: Opportunities and Challenges with Very Large Arrays," IEEE Signal Process. Mag., vol. 30, no. 1, pp. 40–60, Jan. 2013, doi: 10.1109/MSP.2011.2178495.

[8] A. E. Zorkun, M. A. Salas-Natera, and R. Martinez Rodriguez-Osorio, "Improved Iterative Inverse Matrix Approximation Algorithm for Zero Forcing Precoding in Large Antenna Arrays," IEEE Access, vol. 10, pp. 100964–100975, 2022, doi: 10.1109/ACCESS.2022.3208155.

[9] M. Xu, S. Zhang, C. Zhong, J. Ma, and O. A. Dobre, "Ordinary Differential Equation-Based CNN for Channel Extrapolation Over RIS-Assisted Communication," IEEE Commun. Lett., vol. 25, no. 6, pp. 1921–1925, Jun. 2021, doi: 10.1109/LCOMM.2021.3064596.

[10] M. Jian et al., "Reconfigurable intelligent surfaces for wireless communications: Overview of hardware designs, channel models, and estimation techniques," Intell. and Converged Netw., vol. 3, no. 1, pp. 1–32, Mar. 2022, doi: 10.23919/ICN.2022.0005.

[11] Y. Liu et al., "Reconfigurable Intelligent Surfaces: Principles and Opportunities," IEEE Communications Surveys Tutorials, vol. 23, no. 3, pp. 1546–1577, 2021, doi: 10.1109/COMST.2021.3077737.

[12] M. Dajer et al., "Reconfigurable intelligent surface: Design the channel – A new opportunity for future wireless networks," Digital Communications and Networks, Nov. 2021, doi: 10.1016/j.dcan.2021.11.002.

[13] M. Salas-Natera, R. Martínez, L. De Haro, and M. Sierra Perez, "Novel Reception and Transmission Calibration Technique for Active Antenna Array Based on Phase Center Estimation," IEEE Transactions on Antennas and Propagation, vol. PP, pp. 1–1, Aug. 2017, doi: 10.1109/TAP.2017.2738067.

[14] S. Kaur, N. Kumar, and S. Dubey, "Investigation of Adaptive Beam-forming Algorithms for Smart Antennas System," IOP Conf. Ser.: Mater. Sci. Eng., vol. 1033, no. 1, p. 012015, Jan. 2021, doi: 10.1088/1757-899X/1033/1/012015.

[15] P. Raj, A. Kumar, R. Mudavath, and B. Naik, "A NOVEL ALGORITHM DESIGN FOR ADAPTIVE BEAMFORMING IN UNIFORM LINEAR ARRAY ANTENNA," vol. 15, pp. 102–113, Mar. 2020, doi: 10.26782/jmcms.2020.03.00008.

[16] T. Wang, B. Ai, R. He, and Z. Zhong, "Two-Dimension Direction-of-Arrival Estimation for Massive MIMO Systems," IEEE Access, vol. 3, pp. 2122–2128, 2015, doi: 10.1109/ACCESS.2015.2496944.

[17] H. Halbauer, S. Saur, J. Koppenborg, and C. Hoek, "3D beamforming: Performance improvement for cellular networks," Bell Labs Tech. J., vol. 18, no. 2, pp. 37–56, Sep. 2013, doi: 10.1002/bltj.21604.

[18] A. Fascista, A. Coluccia, H. Wymeersch, and G. Seco-Granados, "RIS-Aided Joint Localization and Synchronization with a Single-Antenna Mmwave Receiver," in ICASSP 2021 - 2021 IEEE International Conference on Acoustics, Speech and Signal Processing (ICASSP), Toronto, ON, Canada: IEEE, Jun. 2021, pp. 4455–4459. doi: 10.1109/ICASSP39728.2021.9413515.

[19] N. Ruan, H. Wang, F. Wen, and J. Shi, "DOA Estimation in B5G/6G: Trends and Challenges," Sensors, vol. 22, no. 14, p. 5125, Jul. 2022, doi: 10.3390/s22145125.

[20] L. Yashvanth and C. R. Murthy, "Cascaded Channel Estimation for Distributed IRS Aided mmWave Massive MIMO Systems," in GLOBECOM 2022 - 2022 IEEE Global Communications Conference, Rio de Janeiro, Brazil: IEEE, Dec. 2022, pp. 717–723. doi: 10.1109/GLOBECOM48099.2022.10001263.

[21] Y. Lin, S. Jin, M. Matthaiou, and X. You, "Channel Estimation and User Localization for IRS-Assisted MIMO-OFDM Systems," IEEE Trans. Wireless Commun., vol. 21, no. 4, pp. 2320–2335, Apr. 2022, doi: 10.1109/TWC.2021.3111176.

[22] H. Krim and M. Viberg, "Two decades of array signal processing research: the parametric approach," IEEE Signal Processing Magazine, vol. 13, no. 4, pp. 67–94, Jul. 1996, doi: 10.1109/79.526899.

[23] W. Zhang, Z. Wang, and W. P. Tay, "Approximate Maximum-Likelihood RIS-Aided Positioning," IEEE Trans. Wireless Commun., pp. 1–1, 2023, doi: 10.1109/TWC.2023.3266457.

[24] J. Xiao, J. Wang, Z. Chen, and G. Huang, "U-MLP-Based Hybrid-Field Channel Estimation for XL-RIS Assisted Millimeter-Wave MIMO Systems," IEEE Wireless Commun. Lett., vol. 12, no. 6, pp. 1042–1046, Jun. 2023, doi: 10.1109/LWC.2023.3259465.

[25] M. Cui, Z. Wu, Y. Lu, X. Wei, and L. Dai, "Near-Field MIMO Communications for 6G: Fundamentals, Challenges, Potentials, and Future Directions," IEEE Commun. Mag., vol. 61, no. 1, pp. 40–46, Jan. 2023, doi: 10.1109/MCOM.004.2200136.

[26] J. Wu, S. Kim, and B. Shim, "Near-Field Channel Estimation for RIS-Assisted Wideband Terahertz Systems," in GLOBECOM 2022 - 2022 IEEE Global Communications Conference, Dec. 2022, pp. 3893–3898. doi: 10.1109/GLOBECOM48099.2022.10000979.

[27] Y. Pan, C. Pan, S. Jin, and J. Wang, "RIS-Aided Near-Field Localization and Channel Estimation for the Sub-Terahertz System." arXiv, Dec. 09, 2022. Accessed: May 17, 2023. [Online]. Available: http://arxiv.org/abs/2208.11343

[28] S. Yang, C. Xie, W. Lyu, B. Ning, Z. Zhang, and C. Yuen, "Near-Field Channel Estimation for Extremely Large-Scale Reconfigurable Intelligent Surface (XL-RIS)-Aided Wideband mmWave Systems." arXiv, Apr. 01, 2023. Accessed: May 17, 2023. [Online]. Available: http://arxiv.org/abs/2304.00440

[29] Z.-Q. He and X. Yuan, "Cascaded Channel Estimation for Large Intelligent Metasurface Assisted Massive MIMO," IEEE Wireless Communications Letters, vol. 9, no. 2, pp. 210–214, Feb. 2020, doi: 10.1109/LWC.2019.2948632.

[30] G. T. de Araújo, A. L. F. de Almeida, and R. Boyer, "Channel Estimation for Intelligent Reflecting Surface Assisted MIMO Systems: A Tensor Modeling Approach," IEEE Journal of Selected Topics in Signal Processing, vol. 15, no. 3, pp. 789–802, Apr. 2021, doi: 10.1109/JSTSP.2021.3061274.

[31] A. Taha, M. Alrabeiah, and A. Alkhateeb, "Enabling Large Intelligent Surfaces With Compressive Sensing and Deep Learning," IEEE Access, vol. 9, pp. 44304–44321, 2021, doi: 10.1109/ACCESS.2021.3064073.

2. Chapter 2: Introduction to Phased Array Antennas and Reconfigurable Intelligent Surfaces

2.1. Array Fundamentals

The general definition of antenna arrays in antenna theory and design is the assembly of a group of radiating elements [1]. The radiation pattern of a single radiating element is broad, so its directivity and gain in a particular pointing direction are low. Therefore, to increase both directivity and radiated power gain, the antenna array concept has been introduced in which the excitation of each radiating element can be arranged in different amplitudes and phases, thus, making steering possible. In antenna arrays, the radiating elements are often the identically selected for simpler and more practical designs, however, the characteristic of the elements need not be the same.

In antenna arrays various parameters effect its characteristic and overall performance. The geometrical configuration of the array, inter-element spacing, excitation (amplitude and phase) and pattern of individual elements can be listed as most crucial factors. The general form of an antenna array with M radiating elements can be defined and can be modelled in Cartesian coordinate system. An origin is selected and each radiating element is positioned in a certain location. The location vector of the m-th element, $\vec{\mathbf{r}}_m$, can be given as:

$$\vec{\mathbf{r}}_m = \begin{pmatrix} x_m \\ y_m \\ z_m \end{pmatrix} \tag{2-1}$$

Then, the unitary vector, $\hat{\mathbf{r}}$, associated with the far-field signals is defined as:

$$\hat{\boldsymbol{r}} = [sin\,\theta\,cos\,\varphi \quad sin\,\theta\,sin\,\varphi \quad cos\,\theta] \tag{2-2}$$

The individual elements receive the same signal with different time delays. The time delay of the m-th element, τ_m, with respect to the antenna array can be expressed as:

$$\tau_m = -\frac{\hat{\mathbf{r}}\vec{\mathbf{r}}_m}{c} \tag{2-3}$$

where c is the free space speed of light. The simple illustration of an antenna array and impinging wavefront is given in Fig. 2.1.

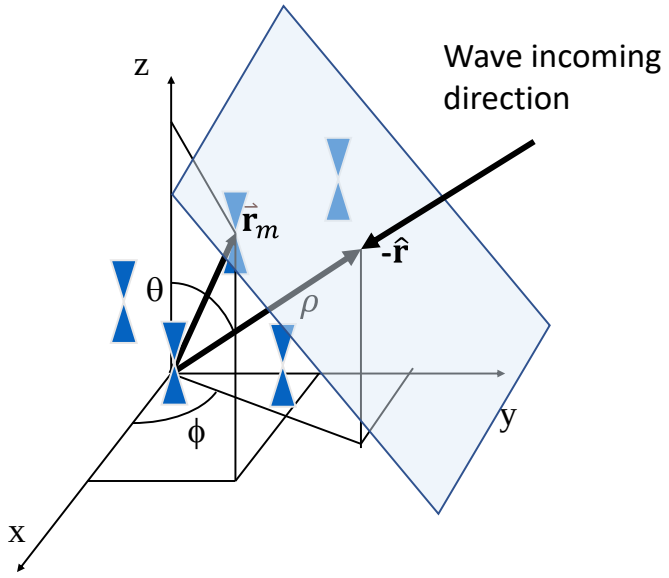

Fig. 2.1. Antenna array with impinging planar wavefront.

The signals received at time, t, from antenna array with M elements are then expressed in vector form as follows:

$$\mathbf{x}(t) = \begin{pmatrix} x(t-\tau_0) \\ x(t-\tau_1) \\ \vdots \\ x(t-\tau_{M-1}) \end{pmatrix} \tag{2-4}$$

The vector $\mathbf{x}(t)$ can be rewritten to expressed the phase offsets associated with the time delays of each element with respect to the antenna array origin as:

$$\mathbf{x}(t) = x(t) \begin{pmatrix} e^{-j\frac{2\pi}{\lambda_c}[x_0 \sin\theta \cos\varphi + y_0 \sin\theta \sin\varphi + y_0 \cos\theta]} \\ e^{-j\frac{2\pi}{\lambda_c}[x_1 \sin\theta \cos\varphi + y_1 \sin\theta \sin\varphi + z_1 \cos\theta]} \\ \vdots \\ e^{-j\frac{2\pi}{\lambda_c}[x_{M-1} \sin\theta \cos\varphi + y_{M-1} \sin\theta \sin\varphi + z_{M-1} \cos\theta]} \end{pmatrix} \tag{2-5}$$

where λ_c is the wavelength of the free space speed of light and the vector in (2-4) determines the geometrical characteristic of the antenna array and known as steering vector or array manifold vector, $\boldsymbol{a}$, and can be expressed as [2]:

$$\boldsymbol{a} = \begin{pmatrix} e^{-j\frac{2\pi}{\lambda_c}[x_0 \sin\theta \cos\varphi + y_0 \sin\theta \sin\varphi + z_0 \cos\theta]} \\ e^{-j\frac{2\pi}{\lambda_c}[x_1 \sin\theta \cos\varphi + y_1 \sin\theta \sin\varphi + z_1 \cos\theta]} \\ \vdots \\ e^{-j\frac{2\pi}{\lambda_c}[x_{M-1} \sin\theta \cos\varphi + y_{M-1} \sin\theta \sin\varphi + z_{M-1} \cos\theta]} \end{pmatrix} \tag{2-6}$$

For narrow-band signals which are defined for only a particular frequency, only the central frequency and its orientation with respect to the array are required to form the steering vector[2]. The signal, $\mathbf{x}(t)$, is considered as narrow band when the propagation time along the antenna is lower than inverse of the frequency bandwidth. The below expression holds for the narrow band signals:

$$t = \frac{D}{c} < \frac{1}{B} \tag{2-7}$$

where D is the maximum aperture size of the antenna and B is the bandwidth.

The antenna array output varies based on the angle of arrival of impinging wavefronts in this manner the antenna array can be considered as a spatial filter. The output of the antenna array at time, t, is the function of the arrival angle of a wavefront and the applied phase shifts and amplitudes applied to each antenna element for further array processing (Fig. 2.2). The antenna array output can be defined as:

$$\mathbf{y}(t) = \mathbf{w}^H \mathbf{x}(t) \tag{2-8}$$

where $\mathbf{w}$ is the weight vector being as $\mathbf{w} = [w_0, \dots, w_m, \dots, w_{M-1},]^T$ (w_m is the applied phase shift and amplitude to the m-th element).

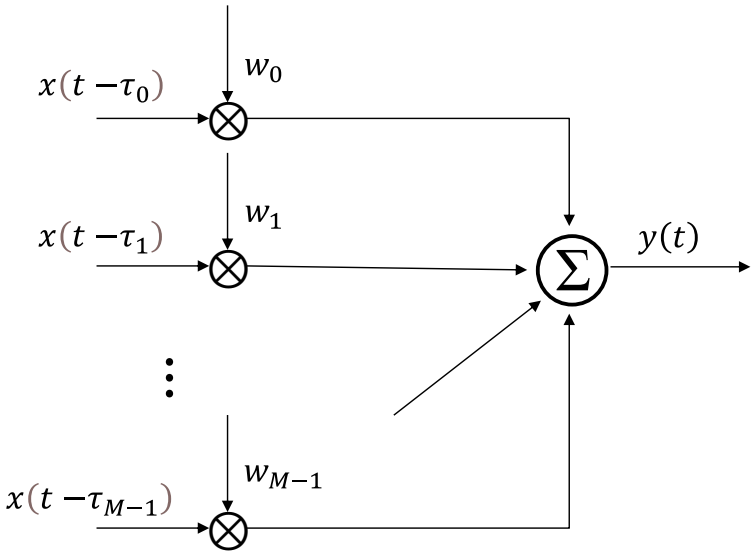

Fig. 2.2. Weighting and sum array processing.

In case of applying complex phase shifts and amplitudes to each element in the array, the overall radiation pattern will change. The characterization of the antenna array in terms complex phase shifts and amplitudes is known as array factor (AF). The array factor can be expressed as:

$$AF(\theta,\varphi) = \sum_{m=1}^{M-1} w_m e^{-j\frac{2\pi}{\lambda_c}\hat{\mathbf{r}}\vec{\mathbf{r}}_m} \tag{2-9}$$

A more compact form of the AF can be written as:

$$AF(\theta,\varphi) = \mathbf{w}^T\boldsymbol{a} \tag{2-10}$$

The array factor response depends on the applied weights, antenna array geometry and the angle of arrival of the wavefront. In the AF the replicas of the maxima are observed, known as grating lobes [2]. Since the array is considered as a spatial sampling, in order to mitigate or eliminate the grating lobes the inter-element spacings, d, must be comply with the Nyquist criterion as $d \leq \lambda_c/2$. Therewithal, it is possible to direct the maximum of the AF towards the direction of the desired signal by applying the optimized weights for each antenna element and this process is known as array beamforming. In beamforming, the output signals from each antenna element are added up and directed to precise transmit or receive angle. On the other hand, this system is also known as phased array antennas since the shifts in the maximum of the AF are obtained with only the changes in phases [2]. By definition, beamforming is the ability of an antenna array to adapt its radiation pattern to a desired direction by controlling phases and amplitudes of each antenna element [3]. Therefore, there is a close relationship between the antenna array pattern and the AF. If an antenna array consists of elements with approximately the same radiation pattern, then, the radiation pattern of the array is the multiplication of the AF and the radiation pattern of a single antenna element and this procedure is known as the pattern multiplication [1]. The antenna array radiation pattern, $E_a(\theta,\varphi)$, then, can be expressed as:

$$E_a(\theta,\varphi) = E_e(\theta,\varphi)AF(\theta,\varphi) \tag{2-11}$$

where $E_e(\theta,\varphi)$ is the radiation pattern of the single element.

In phased array antennas from past to present, three concepts have been adopted to direct the antenna array radiation pattern to the desired direction and they can be listed as follows [4]:

- Switched beam antennas
- Dynamically-phased arrays
- Adaptive antenna arrays

Switched beam antennas: Such antennas are also known as switched lobe antennas, which are directional antennas and have only basic switching functions between distinct directional antennas or predefined beams of an array. Samples of each element's output are taken continuously to determine which component has the best reception beam. Whichever direction the highest power is obtained, the radiation pattern of the antenna

array is directed in that direction. Such antenna array structures are practical and can be easily implemented into systems. However, their performances are limited.

Dynamically-phased arrays: Such phased arrays, the beams are predetermined and fixed in case of switched beam system. Generally, a direction of arrival (DoA) algorithm is used to track the position of the signal source as it moves within the beam range, thus ensuring that the source signal power is received with optimum gain. In this case, the received power is maximized, making it a generalization of the switched beam notion [4].

Adaptive antenna arrays: In this concept, adaptive beamforming algorithms are used to generate weights of each antenna element to direct the array radiation pattern in desired directions [5]. By applying beamforming, the output signals from an antenna array are summed and the beam is directed precisely to the target. In the meantime, deep nulls are directed to undesired signal directions, and thus, interference suppression is performed [5]. Since these antenna arrays can be considered the smartest among the defined antenna arrays, they are also referred to as smart antennas in the literature. In general, the smart antennas are classified under three topologies as analogue beamforming, digital beamforming and hybrid beamforming. The architectural differences between the beamforming methods are given in Fig. 2.3.

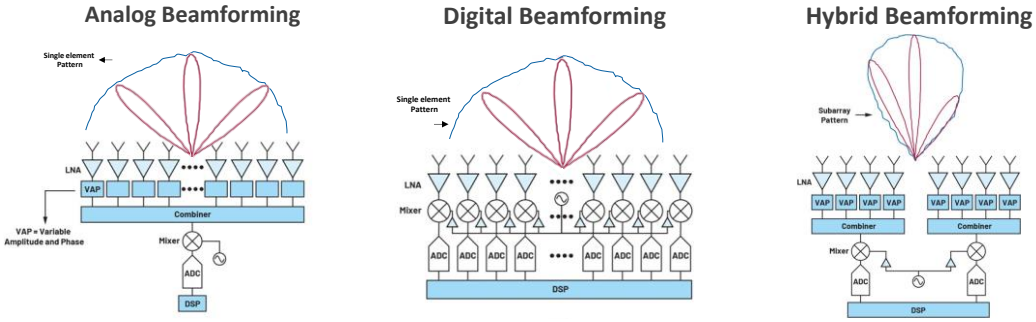

Fig. 2.3. Beamforming architectures [6].

In analogue beamforming the phase shifts and amplitudes of antenna elements are adjusted in RF domain. Phase and amplitude adjustment in the RF field has an impact on the overall antenna array radiation pattern that gives the opportunity to increase coverage and gain. On the other hand, in digital beamforming, the phases and amplitudes of the transmitted signals are first pre-coded in the baseband processing, and then are upconverted to radio frequencies. In digital beamforming each antenna is connected to analog-to-digital converter (ADC) to convert the radio frequency signals in to digital signals to process in baseband. Thus, they are considered as digital antenna arrays. The digital antenna arrays have extreme capabilities to control over phase and amplitude of the signals. Multiple beams can be formed and directed towards to each desired direction at the same time by using frequency and time resources. Frequency and time resource usage improves the capacity of the antenna array as well as increase the spectral efficiency

by increasing the degree of freedoms (DoF) to manipulate the transmitted and received signals [7]. Lastly, the hybrid beamforming is used to exploit the advantages of both digital beamforming and analogue beamforming, thus, increased energy efficiency is achieved [8], [9].

2.2. Smart Antennas

In modern wireless communication systems, there are severe challenges to overcome to increase the overall quality-of-service (QoS). The limited capacity due to scarce spectrum allocation, signal fading, scatters in time, space and frequency due to multipath propagation, tracking of the signal source and energy efficiency due to power constraints in devices can be given as some of the prominent concerns of modern communication systems. The smart antennas are considered as the key enabler not only in current but also in future generation wireless communication systems. Under harsh environmental conditions, smart antennas can maintain high beam resolution, provide effective interference suppression and reduce multipath fading, provide signal source tracking with improved DoA and direction estimation, allowing for a wide permissible frequency bandwidth and hence higher data rate. Adaptive beamforming algorithms are the backbone of the smart antennas.

2.2.1. Adaptive Beamforming Algorithms

Adaptive beamforming algorithms are used in smart antennas to calculate the antenna weights iteratively based on the statistics of the received signal/s. Adaptive beamforming algorithms are capable of to improve signal-to-noise ratio by directing nulls to interference directions and mitigate the received noise. The simple block diagram of the adaptive beamforming algorithm in smart antennas is given in Fig. 2.4 with two beamforming applications. Pattern in green color has the main beam pointing to the desired signal and nulls pointing to interferences while the pattern in orange color has a beam per signal.

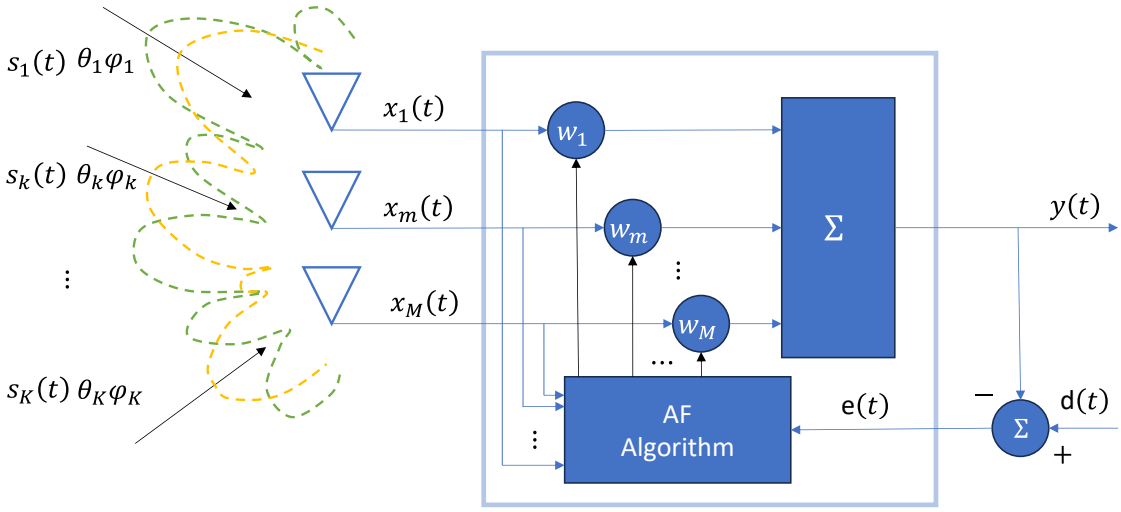

Fig. 2.4. Basic smart antenna model diagram for beamforming implementation.

In general, adaptive beamforming algorithms compare literately adapt the antenna weights according to error signal, $e(t)$, which is the difference between the received data from the antenna elements $\left(x_1(t), \dots x_m(t), \dots x_M(t)\right)$ and the reference signal, $d(t)$. In each time slot, t, each antenna element m receives data from different signal sources, $s_k(t)$, which are located in different spherical coordinates as θ_k and φ_k. Considering a uniform rectangular antenna array (URA), the received multi-path signals from the m-th antenna element as depicted in Fig. 2.4 can be expressed as:

$$x_m(t) = \sum_{k=1}^{K} s_k(t)\, e^{-j\frac{2\pi}{\lambda}\hat{\mathbf{r}}_k\vec{\mathbf{r}}_m} + n_m(t) \tag{2-12}$$

where $n_m(t)$ is the received noise signal at the m-th element.

Then, the output signal $y(t)$ can be written as:

$$y(t) = \sum_{m=1}^{M} w_m^H(t)\, x_m(t) \tag{2-13}$$

2.2.1.1. Optimization Criteria

Adaptive beamforming algorithms are the sub-optimal solutions to optimum weights and are derived from the several different optimization criteria. According to the type of the optimization criteria, the adaptive beamforming algorithms are generally classified under three categories: time reference adaptive beamforming algorithms, spatial reference adaptive beamforming algorithms and blind adaptive beamforming algorithms. The time slot, t, is sampled into N discrete signal samples and adaptive beamforming is applied to each n signal sample.

Minimum mean square error (MMSE):

The objective of the MMSE criterion is to minimize the square error of the received signal with respect to the reference signal. This criterion is known as time reference. The error signal can be estimated as:

$$e(n) = d(n) - \mathbf{w}^H \mathbf{x}(n) \tag{2-14}$$

where $e(n)$ is the error and $d(n)$ is the reference signal. Then, mean square error is denoted as:

$$\begin{aligned} E(|e(n)|^2) = E(|d(n)|^2) - \mathbf{w}^H E\big(d^*(n)\,\mathbf{x}(n)\big) - E\big(d(n)\,\mathbf{x}^H(n)\big)\,\mathbf{w} \\ + \mathbf{w}^H E\big(\mathbf{x}(n)\,\mathbf{x}^H(n)\big)\,\mathbf{w} \end{aligned} \tag{2-15}$$

The Wiener-Hopf solution for the optimum weights can be calculated as [2]:

$$\nabla_{\mathbf{w}^H}\{E(|e(n)|^2)\} = -\mathbf{r}_{xd} + \mathbf{R}_{xx}\mathbf{w} = 0 \tag{2-16}$$

where $\nabla_{\mathbf{w}^H}$ is the complex gradient of $\mathbf{w}^H$, $\mathbf{r}_{xd}$ is the cross-correlation vector of the received signal and the desired signal being as $\mathbf{r}_{xd} = E\big(d^*(n)\,\mathbf{x}(n)\big)$, $\mathbf{R}_{xx}$ is the array correlation matrix being as $\mathbf{R}_{xx} = E\big(\mathbf{x}(n)\mathbf{x}^H(n)\big)$.

Minimum variance (MV):

The objective of the MV criterion is to minimize the variance of the output noise, while maintaining a given AF response in the direction of the desired signal, this criterion is known as spatial reference and can be formulate as [2]:

$$\begin{aligned} min \quad & (\mathbf{w}^H \mathbf{R}_n \mathbf{w}) \\ \text{s.t} \quad & \mathbf{w}^T \boldsymbol{a} = \alpha \end{aligned} \tag{2-17}$$

where $\boldsymbol{a}$ is the steering vector, $\mathbf{R}_n = \sigma^2 \mathbf{I}_m$ and σ^2 is the noise variance. The The minimization problem can be solved by using Lagrange multipliers as:

$$\mathbf{w}^H \mathbf{R}_n \mathbf{w} + \lambda(\mathbf{w}^T \boldsymbol{a} - \alpha) + \lambda^*(\boldsymbol{a}^T \mathbf{w} - \alpha^*) \tag{2-18}$$

where λ is the Lagrange multiplier being as $\lambda = -\alpha(\boldsymbol{a}^T \mathbf{R}_n^{-1} \boldsymbol{a})^{-1}$. Then, the weights for the minimum variance can be expressed as:

$$\mathbf{w}_{mv} = \frac{\alpha \mathbf{R}_n^{-1} \boldsymbol{a}}{\boldsymbol{a}^T \mathbf{R}_n^{-1} \boldsymbol{a}} \tag{2-19}$$

when $\alpha = 1$, it is known as minimum variance distortion response (MVDR) or Capon's solution.

Maximum combined output (MCO):

The objective of maximum combined output SNR (MCOSNR) and maximum combined output signal to interference and noise ratio (MCOSINR) criteria is to maximize the output SNR and SINR, respectively [2]. The mathematical expressions can be given as:

$$SNR = \frac{\mathbf{w}^H \mathbf{R}_s \mathbf{w}}{\mathbf{w}^H \mathbf{R}_n \mathbf{w}} \tag{2-20}$$

$$SINR = \frac{\mathbf{w}^H \mathbf{R}_s \mathbf{w}}{\mathbf{w}^H \mathbf{R}_{n+i} \mathbf{w}} \tag{2-21}$$

where $\mathbf{R}_{n+i} = \mathbf{R}_n + \mathbf{R}_i$ and $\mathbf{R}_i$ is the interference correlation matrix.

The complex gradient according to the MCOSNR with respect to $\mathbf{w}^H$ can be calculated as:

$$\frac{\mathbf{R}_s \mathbf{w}\mathbf{w}^H \mathbf{R}_n \mathbf{w} - \mathbf{R}_n \mathbf{w}\mathbf{w}^H \mathbf{R}_s \mathbf{w}}{(\mathbf{w}^H \mathbf{R}_n \mathbf{w})^2} = 0 \tag{2-22}$$

$$\leftrightarrow \mathbf{R}_s \mathbf{w} = SNR \times \mathbf{R}_n \mathbf{w} = \lambda \mathbf{R}_n \mathbf{w} \tag{2-23}$$

$$\leftrightarrow [\mathbf{R}_n^{-1} \mathbf{R}_s] = \lambda \mathbf{w} \tag{2-24}$$

The eigen vector of the matrix $\mathbf{R}_n^{-1}\mathbf{R}_s$ maximizes the weight vector. The similar approach is valid for MCOSINR where the weight vector is obtained from the matrix $\mathbf{R}_{n+i}^{-1}\mathbf{R}_s$. It is evident that the optimal weight does not depend on a reference signal or a known steering matrix but only to output signal.

2.2.1.2. Time Reference Adaptive Beamforming Algorithms

The time reference (TR) adaptive beamforming algorithms require a pre-determined training signal as a reference signal. In order to converge to a solution, in every iteration cycle, n, an error signal $e(i)$ estimation is calculated between the reference signal $d(n)$ and the received signal/s $x(n)$. The error between the reference signal and the received signal/s is then iteratively minimized to increase the SNR by minimizing the noise and eliminating the interferences. The TR adaptive algorithms use minimum mean square error (MMSE) criteria to obtain optimal weight/s [2]. Beamforming is performed by minimizing the mean square error (MSE) between the array output $y(n)$ and the reference signal. The correlation matrix $R_{xx}(n)$ of the signal received by the antenna array and the cross-correlation vector $r_{xd}(n)$ between the desired and received signal are the key parameters for determining the optimal weights. The most prominent TR adaptive beamforming algorithms are explained in the following paragraphs.

Least mean square (LMS) Algorithm:

The least mean square algorithm (LMS) and variants of the LMS algorithms are the simplest adaptive algorithms. Step size μ, it the key parameter which determines the performance of the LMS algorithm. If the step size is small, then algorithm needs a large number of signal samples to converge to the optimal weight values. On the other hand, if the step size is too large then output signal becomes noisier. In order to mitigate these drawbacks, NLMS algorithm was derived. In NLMS the step size is divided by the norm of the input signal at each iteration. The formulation of the NLMS algorithm is given in the below equations [10]:

$$e(n) = d(n) - \mathbf{w}^H(n-1)\mathbf{x}(n) \tag{2-25}$$

$$\mathbf{w}(n) = \mathbf{w}(n-1) + \frac{\mu}{\|\mathbf{x}(n)\|^2}\mathbf{x}(n)e^*(n) \tag{2-26}$$

where $\mathbf{w}(n-1)$ previous weight vector, $\mathbf{w}(n)$ is the updated weight vector, $e(n)$ is the error and $d(n)$ is the reference signal.

Recursive least squares (RLS) Algorithm:

The RLS algorithm updates the weight vectors by considering the sum of the past least square errors. The RLS algorithm has extremely fast convergence rate and high output signal-to-noise ratio level. The forgetting factor, λ, and the regularization factor, Δ, are the key parameters for the RLS algorithm. The forgetting factor controls the memory of the algorithm and its value leads to a compromise between low mis adjustment and fast convergence [11], [12]. On the other hand, regularization factor is critical for the steady-state noise [12]. The RLS algorithm is given at below equations [13]:

$$initial, \mathbf{P}(0) = \Delta^{-1}\begin{bmatrix} 1 & \cdots & 0 \\ 0 & \ddots & 0 \\ 0 & 0 & 1 \end{bmatrix}_{M\times M}, \mathbf{w}(0) = 0 \tag{2-27}$$

$$e(i) = d(i) - \mathbf{w}^H(i)\mathbf{x}(i) \tag{2-28}$$

$$\mathbf{r}(n) = \frac{\lambda^{-1}\mathbf{P}(n-1)\mathbf{x}(n)}{1 + \lambda^{-1}\mathbf{x}^H(n)P(n-1)\mathbf{x}(n)} \tag{2-29}$$

$$\mathbf{w}(n) = \mathbf{w}(n-1) + \mathbf{r}(n)e^*(n) \tag{2-30}$$

$$\mathbf{P}(n) = \lambda^{-1}\big(\mathbf{P}(n-1) - \mathbf{r}(n)\mathbf{x}^H(n)\mathbf{P}(n-1)\big) \tag{2-31}$$

where $\mathbf{P}(n)$ is the autocorrelation matrix, $\mathbf{r}(n)$ is the Kalman gain vector.

Sample matrix inversion (SMI) Algorithm:

The SMI algorithm employs block adaptive approach. The SMI algorithm takes an average time to estimate the sequence correlation matrix using I time samples which allows discontinues transmission and SMI algorithm employs direct inversion of correlation matrix [14], [15]. The block approach ensures SMI to have high convergence rate and convergence to the near optimal weights. The only parameter that related with the performance of SMI is the averaging window length, N. The SMI algorithm is defined at below equations [14]:

$$\mathbf{R}_{xx} \approx \frac{1}{N}\sum_{n=1}^{N}\mathbf{x}(n)\mathbf{x}^{H}(n) \tag{2-32}$$

$$\mathbf{r} = \frac{1}{N}\sum_{n=1}^{N}d^{*}(n)\mathbf{x}^{H}(n) \tag{2-33}$$

where $\mathbf{R}_{xx}$ is the correlation matrix of the received signal samples and $\mathbf{r}$ correlation vector of the received signal samples and the reference signal. Then, the weight update for of the SMI algorithm can be calculated as:

$$\mathbf{w}_{SMI} = \mathbf{R}_{xx}^{-1}\mathbf{r} \tag{2-34}$$

2.2.1.3. Spatial Reference Adaptive Beamforming Algorithms

In spatial reference (SR) adaptive beamforming algorithms, spatial characteristics of the desired signal/s and interferences are first identified. Subsequently, nulls are directed towards interferences and the main beam/s are steered to desired directions simultaneously. The spatial reference adaptive beamforming algorithms employ two different algorithms, such the first algorithm estimates the direction of arrivals of the received signals and then a power thresholding is applied, the second algorithm uses the DoA information of the signals to calculate the optimal weight values for the desired signal/s and to eliminate the interference [2]. In general, generalized side-lobe cancellation algorithms [16] are applied once the DoA of the signal/s are estimated. The generalized side-lobe cancellation algorithms have superior capabilities to direct the nulls in undesired signal locations, thus, most of the applications adopt those algorithms.

Generalized sidelobe cancellation (GSLC) algorithm:

In GSLC algorithm, the optimum vector is split into two orthogonal components. At one of the branches of the algorithms a blocking matrix is formed according to the provided angular information of the impinging signals from DOA algorithm and the other branch the data simply passes with a delay. Thus, nulls are directed to the interference/s and desired signal remains with the same amplitude. The initialization of the GSLC is given as [17]:

$$\mathbf{w}_a = \begin{bmatrix} 1 \\ \vdots \\ 1 \end{bmatrix}_{(M-Q)\times 1} \tag{2-35}$$

$$\mathbf{B} = \begin{bmatrix} 1\,0 \cdots 0 \\ b_1 1 \cdots 0 \\ 0\; b_m \cdots 0 \\ \cdots\cdots\cdots \\ 0\,0 \;\cdots 1 \\ 0\,0 \;\cdots\; b_{M-Q} \end{bmatrix}, b_m = -\left(\frac{\boldsymbol{a}_m}{\boldsymbol{a}_{m+1}}\right)^* \tag{2-36}$$

$$\mathbf{w}(0) = \mathbf{w}_q - \mathbf{B}\mathbf{w}_a \tag{2-37}$$

where M is the number of antennas, $\mathbf{B}$ is the blocking matrix, Q is the number of desired signals, $\mathbf{w}_q = \boldsymbol{a}_d$ where $\boldsymbol{a}_d$ is the steering vector of the main pointing direction and $\boldsymbol{a}_m$ denotes the steering vector of the blocked (interference) directions.

The GSLC-NLMS algorithm is given below:

$$e(n) = \mathbf{w}(n-1)^H \mathbf{x}(n) \tag{2-38}$$

$$\mathbf{w}_a(n) = \mathbf{w}_a(n-1) + \frac{\mu}{\|\mathbf{x}(n)\|^2}\mathbf{x}(n)e^*(n) \tag{2-39}$$

$$\mathbf{w}(n) = \mathbf{w}_q - \mathbf{B}\mathbf{w}_a(n) \tag{2-40}$$

Subsequently, the GSLC-RLS algorithm is given below:

$$initial, \mathbf{P}(0) = \Delta^{-1}\begin{bmatrix} 1 & \cdots & 0 \\ 0 & \ddots & 0 \\ 0 & 0 & 1 \end{bmatrix}_{(M-Q)\times(M-Q)} \tag{2-41}$$

$$\mathbf{r}(n) = \frac{\lambda^{-1}\mathbf{B}^H\mathbf{P}(n-1)\mathbf{x}(n)}{1+\lambda^{-1}\mathbf{B}^H\mathbf{x}^H(n)\mathbf{P}(n-1)\mathbf{B}^H\mathbf{x}(n)}) \tag{2-42}$$

$$e(n) = \mathbf{w}(n-1)^H\mathbf{x}(n) \tag{2-43}$$

$$\mathbf{w}_a(n) = \mathbf{w}_a(n-1) + \mathbf{r}(n)e^*(n) \tag{2-44}$$

$$\mathbf{w}(n) = \mathbf{w}_q - \mathbf{B}\mathbf{w}_a(n) \tag{2-45}$$

$$\mathbf{P}(n) = \lambda^{-1}\left(\mathbf{P}(n-1) - \mathbf{r}(n)\left(\mathbf{B}^H\mathbf{x}^H(n)\right)^H\mathbf{P}(n-1)\right) \tag{2-46}$$

In this section the adaptation of GLSC to NLMS and RLS are discussed. The only difference between the GLSC-NLMS and GLSC-RLS is the weight adaptation. A detailed explanation of DoA algorithms is given in the section 2.2.2. DoA Estimation Algorithms.

2.2.1.4. Blind Adaptive Beamforming Algorithms

Blind adaptive beamforming algorithms do not require any reference signal or DOA algorithm. Blind adaptive beamforming algorithms perform beamforming only using the characteristics of the received signal/s, hence the name 'blind' [2]. Blind adaptive beamforming algorithms are relatively more convenient to implement than TR adaptive beamforming algorithms and SR adaptive beamforming algorithms, since matrix computations are not involved. With the relief of prior information of array manifold [18], training sequence or non-dependency on array calibration, pointing errors [19], blind adaptive beamforming algorithms are favorable for the low-complexity and low-cost applications. The most prominent blind adaptive beamforming algorithms are described in the following paragraphs.

Constant modulus algorithm (CMA):

The CMA use exploit the constant modulus (CM) characteristic of the received signal/s. The modulated signals lose their CM properties by interference/s or noise, hence, those degradations or effects can be detected and restored by using CMA. The structure of the algorithm is similar to NLMS. However, error signal does not depend on any reference signal. The CMA is given at below equations [20]:

$$y(n) = \mathbf{w}^H(n-1)\mathbf{x}(n) \tag{2-47}$$

$$e(n) = \frac{y(n)}{\|y(n)\|} - y(n) \tag{2-48}$$

$$\mathbf{w}(n) = \mathbf{w}(n-1) + \frac{\mu}{\|\mathbf{x}(n)\|^2}\mathbf{x}(n)e^*(n) \tag{2-49}$$

where μ is the step size as in NLMS algorithm.

Direct decision algorithm (DDA):

The idea and structure of both CMA and DDA algorithms are the same. The only difference is in the error update part. The DDA is given at below equations [20]:

$$y(i) = \mathbf{w}^H(n-1)\mathbf{x}(n) \tag{2-50}$$

$$e(n) = \frac{y(n)}{\|y(n)\|} - sgn(real(y(n))) \tag{2-51}$$

$$\mathbf{w}(n) = \mathbf{w}(n-1) + \frac{\mu}{\|\mathbf{x}(n)\|^2}\mathbf{x}(n)e^*(n) \tag{2-52}$$

where $sgn(.)$ is the signum function and $real(.)$ is the real part selector.

SIMPLE and SUMPLE algorithms:

Both algorithms are good examples to matrix free blind beamforming algorithms. The SIMPLE [21] algorithm selects an antenna in the antenna array as a reference and accepts the signal received from this antenna as the reference signal and correlates it pair-wise fashion with the signals from other antennas. On the other hand, SUMPLE [21] algorithm correlates each antenna signal with the sum of the other antenna signals. This is the main difference between these algorithms to calculating the weights iteratively. Normalized weights, SNR and further calculations for both algorithms are briefly described at [21]. Calculation of the SIMPLE and SUMPLE weights are given below:

Let $\mathbf{w}_{m0}^{K}$ is the weight derived from the correlation of the reference antenna and the m-th antenna, and T is the number of time intervals, then, the weight update of the SIMPLE can be expressed as [21]:

$$\mathbf{w}_{m0}^{t+1} = R_{t+1}\mathbf{w}_{m0}^{t}\left\{\frac{1}{ncorr}\sum_{t=T\,ncorr}^{(T+1)ncorr-1}[((\mathbf{w}_{m0}^{t})^{*}\mathbf{x}_{m}^{t})(\mathbf{x}_{0}^{t})^{*}]\right\} \tag{2-53}$$

where the sum of $ncorr$ time points correspond to the correlation averaging interval and $\mathbf{x}_0^t$ is the received signal from the reference antenna. The factor R_{t+1} provides normalization to guarantee the sum of the weights-squared over the antennas is equal to the number of antennas and prevents successive calculations of the weight amplitude from becoming unstable [21] and normalization can be given as:

$$\sum_{m=0}^{M-1}\mathbf{w}_{m0}^{t+1}(\mathbf{w}_{m0}^{t})^{*} = M \tag{2-54}$$

Let $\mathbf{w}_{m}^{K}$ is the weight derived from the m-th antenna that correlated against the sum of the others and T is the number of time intervals, then, the weight update of the SUMPLE can be expressed as [21]:

$$\mathbf{w}_{j}^{t+1} = R_{t+1}\mathbf{w}_{m}^{t}\left\{\frac{1}{ncorr}\sum_{t=T\,ncorr}^{(T+1)ncorr-1}\left[\left(\mathbf{x}_{j}^{t}\left(\mathbf{w}_{j}^{t}\right)^{*}\right)\sum_{m=0,m\neq j}^{M-1}((\mathbf{x}_{m}^{t})^{*}\mathbf{w}_{m}^{t})\right]\right\} \tag{2-55}$$

2.2.1.5. Hybrid Adaptive Beamforming Algorithms

Adaptive algorithms by themselves may have some inadequacies under certain circumstances. The hybrid adaptive algorithm is a concept of combining two or more different types of algorithms to achieve better convergence speed, improved noise mitigation and superior interference cancelling at once, which would not be possible using only one type of algorithm. Hybrid adaptive beamforming algorithms have sequential structure meaning that each algorithms output is fed to the input of the subsequent

algorithm. As an simple example of hybrid adaptive beamforming algorithms, the least square constant modulus algorithm (LS-CMA) has been proposed in both [22] and [23], which is the combination of NLMS and CMA adaptive beamforming algorithms. In [24], it can be seen that the tracking gradient of the cost function resulting in a negative offset vector, therefore, in weight updated the negative sign is used. In this algorithm, the interference suppression is achieved by using a reference signal and at the same time a better SNR level is acquired by exploiting the constant modulus property of the signal. In the first stage, CMA is applied to array output and then the weight calculation is carried on with the NLMS step. The hybrid LS-CMA algorithm is given below:

$$y(n) = \mathbf{w}_{CMA}^{H}(n-1)\mathbf{x}(n) \tag{2-56}$$

$$e_{CMA}(n) = \frac{y(i)}{\|y(n)\|} - y(n) \tag{2-57}$$

$$\mathbf{w}_{CMA}(n) = \mathbf{w}_{CMA}(n-1) - \frac{\mu}{\|\mathbf{x}(n)\|^2}\mathbf{x}(n)e_{CMA}^{*}(n) \tag{2-58}$$

$$e_{NLMS}(n) = d(n) - \mathbf{w}_{CMA}^{H}(n)\mathbf{x}(n) \tag{2-59}$$

$$\mathbf{w}_{NLMS}(n) = \mathbf{w}_{NLMS}(n-1) - \frac{\mu}{\|\mathbf{x}(i)\|^2}\mathbf{x}(n)e_{NLMS}^{*}(n) \tag{2-60}$$

where, $\mathbf{w}_{CMA}$ is the weights of the CMA step and $\mathbf{w}_{NLMS}$ is the final weights of the algorithm.

2.2.2. DOA Estimation Algorithms

The DoA estimation is the preliminary stage of beamforming [25], target localization [26] and channel estimation [27] in many communication applications. In general, DoA estimation algorithms are generally classified under three subcategories: subspace methods and parametric methods. In the subspace methods DoA estimation depends on the self-correlation of the received signal from all of the antenna elements and the angular information of the signals rely on the eigen values of the correlation matrix, thus, eigen decomposition of the correlation matrix is needed. On the contrary, parametric methods directly extract the angular information from the data model by adopting the straightforward maximum-likelihood approach, hence, there is no need of eigen decomposition. Lastly, the iterative DoA estimation methods which do not require any high computational matrix decomposition method nor self-correlation matrix. The iterative DoA estimation methods rely on the adaptive beamforming algorithm's structure and power inversion method.

2.2.2.1. Subspace Methods

In subspace methods eigen decomposition is used to extract orthogonal subspaces of received and interference signals from the correlation matrix $\mathbf{R}_{xx}$, where:

$$\mathbf{R}_{xx} \approx \frac{1}{N}\sum_{n=1}^{N} \mathbf{x}(n)\mathbf{x}^H(n) \tag{2-61}$$

Eigen values which are obtained from correlation matrix of received signal represents the desired signal/s and interference signal/s. Most of the algorithms which employ subspace methods are spectral based.

The most prominent spectral based algorithms which use different subspaces are multiple signal classification (MUSIC) and minimum norm method (MNM).

MUSIC and MNM:

MUSIC algorithm uses the noise subspace and MNM uses the signal subspace to form the angular spectrum. The angular spectrum for the maximum amplitude/s of array response $\boldsymbol{a}$ (steering vector) can be expressed as [28]:

$$\mathbf{S}_{MUSIC} = \frac{1}{\boldsymbol{a}^H \boldsymbol{E}_n \boldsymbol{E}_n^H \boldsymbol{a}} \; and \; \mathbf{S}_{MNM} = \frac{1}{\boldsymbol{a}^H \boldsymbol{E}_s \boldsymbol{E}_s^H \boldsymbol{a}} \tag{2-62}$$

where $\mathbf{E}_n$ is the eigen values of the noise subspace, $\mathbf{E}_s$ is the eigen values of signal subspace, $\mathbf{S}_{MUSIC}$ and $\mathbf{S}_{MNM}$ are the angular spectrums of MUSIC and MNM, respectively.

The spectral based algorithms are effective and have high angular resolution, however, eigen decomposition has high computational complexity. There are more existing spectral based algorithms such as maximum-likelihood (ML) algorithm [29] and weighted subspace fitting (WSF) algorithm [28], however for brevity these algorithms are excluded. In addition, the DoA estimation performance of spectral based algorithms highly depend on the antenna array geometry and they are susceptible to phase/gain deviations in antenna array and mutual coupling, thus, the array calibration is mandatory [2].

Another subspace method known as estimation of signal parameters via rotational invariance technique (ESPRIT) was developed to alleviate the array geometry and the need for array calibration.

ESPRIT:

The ESPRIT employs the property of shift invariance of the antenna array and imposes some constraints on array structure [30]. In ESPRIT, the separation between the sub-array elements is assumed to be equal, thus, array represents a translational invariance. Then, rotational invariance of the signal subspace allows to estimate direction of arrival of the incoming signal/s [30]. At first, signal subspace $\mathbf{U}_s$ is formed by eigen decomposition

as mentioned before, then invariance equations are solved, finally, DoA estimation is performed. The ESPRIT algorithm is simply defined as [31]:

$$\begin{aligned}\mathbf{K}_{U1}\mathbf{U}_s\mathbf{Y}_U &= \mathbf{K}_{U2}\mathbf{U}_s \\ \mathbf{K}_{V1}\mathbf{U}_s\mathbf{Y}_V &= \mathbf{K}_{V2}\mathbf{U}_s\end{aligned} \tag{2-63}$$

where $\mathbf{K}_{U1}$, $\mathbf{K}_{U2}$, $\mathbf{K}_{V1}$ and $\mathbf{K}_{V2}$ represent the two pairs represent of transformed selection matrices, while $\mathbf{Y}_U$ and $\mathbf{Y}_V$ are the real-valued matrices. If we assume the eigen values of $\mathbf{Y}_U + j\mathbf{Y}_V$ as $\{\lambda_1, \dots \lambda_k, \dots, \lambda_K\}$, then the DoAs can be extracted as:

$$u_k = 2\tan(Re\{\lambda_k\}) \tag{2-64}$$

$$v_k = 2\tan(Im\{\lambda_k\}) \tag{2-65}$$

$$\varphi_k = arg(u_k - jv_k) \tag{2-66}$$

$$\theta_k = \sin^{-1}(\|u_k - jv_k\|) \tag{2-67}$$

where φ_k and θ_k are the phi and theta angles of the incoming signal/s.

The subspace methods are highly efficient to estimate the DOA of the signal/s. However, in case of multiple signals are correlated, which is the case in multi-path propagation, the DoA estimation performance of the subspace methods degrades, since the rank of the correlation matrix is must be equal to the number of signals. The performance of the subspace methods degrades because when the correlation matrix becomes rank deficient, it diverges the signal eigenvectors into the noise subspace. To avoid this problem, two techniques are applied, one is forward-backward averaging and the other one is spatial smoothing [32].

2.2.2.2. Parametric Methods

In parametric methods, which are in the second subcategory for DoA estimation algorithms, eigen decomposition of the correlation matrix is not needed. Parametric methods directly extract the angular information from the data model by adopting the straightforward maximum-likelihood approach. Besides parametric methods are robust in case of correlated signal sources, low SNR and inadequate number of signal samples (snapshots) at the cost of increased computational complexity [33]. The space alternating generalized expectation-maximization (SAGE) algorithm is one of the most prominent algorithms among the parametric methods.

In classical approach of expectation-maximization, which is the predecessor of the SAGE, the parameters are estimated at once. Instead of computing all parameters in one stage, SAGE algorithm forms sequential conditioning on subsets of the parameters, then EM stage is applied [34]. Therefore, SAGE has several cycles for each iteration. The SAGE

consists of two cycles, the first one is expectation step and the second one is maximization step [35]. The SAGE algorithm is briefly explained below [34]:

Let **A** be the steering matrix and $\boldsymbol{s}$ is the signal vector as:

$$\begin{gathered}\mathbf{A}(\boldsymbol{\theta},\boldsymbol{\varphi}) = [\boldsymbol{a}(\theta_1,\varphi_1),\dots\boldsymbol{a}(\theta_k,\varphi_k),\dots\boldsymbol{a}(\theta_K,\varphi_K)] \\ \boldsymbol{s} = [s_1(t),\dots s_k(t),\dots s_K(t)]\end{gathered} \tag{2-68}$$

where θ_k and φ_k are the angle of arrivals of the k-th signal source.

Given the initial angles θ_0 and φ_0 for the algorithm as zero, then in the expectation step of the i-th iteration cycle, only k-th signal is accepted and the update stage can be expressed as:

$$\boldsymbol{y}_k^{(n)}(t) = \boldsymbol{a}\left(\theta_k^{(n-1)},\varphi_k^{(n-1)}\right)s_k^{(n-1)}(t) + \frac{1}{M}\left\{\mathbf{x}(t) - \boldsymbol{a}\left(\theta_k^{(n)},\varphi_k^{(n)}\right)s_k^{(n)}(t)\right\} \tag{2-69}$$

$$\boldsymbol{\theta}^{(n)} = \left[\theta_1^{(n)}\dots\theta_{k-1}^{(n)}\,\theta_1^{(n-1)}\dots\theta_K^{(n-1)}\right] \tag{2-70}$$

$$\boldsymbol{\varphi}^{(n)} = \left[\varphi_1^{(n)}\dots\varphi_{k-1}^{(n)}\,\varphi_1^{(n-1)}\dots\varphi_K^{(n-1)}\right] \tag{2-71}$$

$$\boldsymbol{s}^{(n)} = \left[s_1^{(n)}(t)\dots s_{k-1}^{(n)}(t)\,s_1^{(n-1)}(t)\dots s_K^{(n-1)}(t)\right] \tag{2-72}$$

In the expectation step of the n-th iteration cycle, DoAs are estimated for the k-th signal source using the subtracted signal $\boldsymbol{y}_k^{(n)}$ as:

$$\boldsymbol{R}_{yy}^{(n)} = \frac{1}{T}\sum_{t=0}^{T-1}\boldsymbol{y}_k^{(n)}(t)\boldsymbol{y}_k^{(n)H}(t) \tag{2-73}$$

$$\varphi_k^{(n)} = \underset{\varphi}{argmax}\,\frac{\boldsymbol{a}^H\left(\varphi,\theta_k^{(n-1)}\right)\boldsymbol{R}_{yy}^{(n)}\boldsymbol{a}\left(\varphi,\theta_k^{(n-1)}\right)}{\left\|\boldsymbol{a}\left(\varphi,\theta_k^{(n-1)}\right)\right\|^2} \tag{2-74}$$

$$\theta_k^{(n)} = \underset{\theta}{argmax}\,\frac{\boldsymbol{a}^H\left(\theta,\varphi_k^{(n)}\right)\boldsymbol{R}_{yy}^{(n)}\boldsymbol{a}\left(\theta,\varphi_k^{(n)}\right)}{\left\|\boldsymbol{a}\left(\theta,\varphi_k^{(n)}\right)\right\|^2} \tag{2-75}$$

$$s_k^{(n)}(t) = \frac{\boldsymbol{a}^H\left(\theta_k^{(n)},\varphi_k^{(n)}\right)\boldsymbol{y}_k^{(n)}(t)}{\left\|\boldsymbol{a}\left(\theta_k^{(n)},\varphi_k^{(n)}\right)\right\|^2} \tag{2-76}$$

where T denotes the number of snapshots, $\theta_k^{(n)}$ and $\varphi_k^{(n)}$ are the estimated phis and thetas respectively.

2.2.2.3. Iterative Methods

The iterative DoA estimation methods are simple and have less computational complexities compared to other methods yet robust and accurate. The basic idea is selecting a reference antenna in the array and sample the signal from that antenna as reference signal. Then obtain the weights of the remaining antennas adopting an adaptive beamforming algorithm such as NLMS. After obtaining the optimal weight vector, the array pattern is calculated. Finally, the spatial spectrum is obtained by the reciprocal of the array pattern. The NLMS based DoA estimation algorithm is given as:

$$e(n) = x_0(n) - \mathbf{w}^H(n)\mathbf{x}(n) \tag{2-77}$$

$$\mathbf{w}(n) = \mathbf{w}(n-1) + \frac{\mu}{\|\mathbf{x}(n)\|^2}\mathbf{x}(n)e^*(n) \tag{2-78}$$

It is seen that the weight calculation is similar for the beamforming however the length of the weight vector is $M-1$. The final weight vector is denoted as $\widetilde{\mathbf{w}} = [1; -\mathbf{w}]$. Then output spatial spectrum can be obtained by:

$$\mathbf{D}(\theta, \phi) = \frac{1}{|\widetilde{\mathbf{w}}^H \mathbf{a}(\theta, \phi)|} \tag{2-79}$$

where $\mathbf{a}(\theta, \phi) \epsilon\, \mathbb{C}^{M \times \Theta}$ is the steering vector and Θ is the total number of elevation and azimuth pairs, (θ, ϕ), to be scanned in output spatial spectrum and $|\widetilde{\mathbf{w}}^H \mathbf{a}(\theta, \phi)|$ is the calculated array pattern.

Once the DoAs are estimated correctly by using one of the explained DoA estimation algorithms so far, an adaptive beamforming algorithm, such as GSLC-RLS, can be applied according to DoA information.

2.2.3. Antenna Array Calibration

The adaptive beamforming algorithms and DoA estimation algorithms are derived on the assumption that the antenna array is theoretically error free [36]. However, in reality, antenna arrays contain errors that might severely affect the performance of beamforming algorithms and data DoA estimation algorithms. These errors are especially prominent in subspace DoA estimation methods, which are highly dependent on antenna array geometry and characteristics.

The precise excitation of each antenna element is crucial for antenna arrays to agile estimation of direction of arrivals and to steer the beam. Moreover, by amplitude tapering and phase control of the elements, obtaining desired array pattern features, high directivity, low side lobe levels and null controlling is possible [37], [38], [39]. However, in practice the excitation of the each antenna element differs due to the mechanical manufacturing imperfections as well as different RF chain, which are associated with each

antenna element, phase/gain variations, component aging and temperature variations [39], [40]. Therefore, in reality these errors might cause undesired array pattern, gain degradation, higher side lobe levels, null drifts and as well as inaccurate DoA estimation [41], [42]. Proper calibration by accurately modelling and defining the errors in the antenna array is important for real applications of antenna arrays. Among the defined errors for antenna arrays mutual coupling effects, element location errors, phase/gain errors and loss of coherence can be given as examples.

The mutual coupling is known as interactions among antenna array elements. When a signal is transmitted or received by an antenna element, its impact affects the neighbouring antenna elements. The magnitude of the mutual coupling highly depends on inter-element spacing and the isolation among antenna elements [43]. The mutual coupling has a significant effect on overall performance of adaptive beamforming since it distorts the radiation patterns of antennas hence significantly decreases the total efficiency of the antenna array. Besides mutual coupling, phase and gain uncertainties also have inadmissible effects on antenna arrays [44]. On the other hand, the mutual coupling effect has and impact on array response in the receiving mode which results in inaccurate DoA estimation, especially for the subspace-based algorithms.

Consensus in theory is that each antenna element has almost identical radiation patterns and are known priorly. However, in reality, radiation patterns and the positions of the antenna elements are not fully known due to the manufacturing errors. Manufacturing errors might lead each individual element has different radiation pattern and also significant phase shifts which do not correspond to the actual theoretical locations of the antennas. On the other hand, RF front-end components which are connected to antenna elements could introduce phase shifts and gain uncertainties to antenna elements. Such an example can be considered as, amplifiers and mixers have gain or loss ripples in wide frequency ranges that might cause a change when exciting an antenna element at different frequencies. Non-linearity is another problem which is introduced by the power amplifiers [45]. Most of the systems are highly sensitive to non-linearity but it could be mitigated by using pre- or post-distortion techniques. Besides, at the receiver front-end part, depending on the type of the receiver, there might be DC offsets (due to direct conversion) or I/Q imbalances (superheterodyne due to the image frequencies) [46]. However, these could be mitigated by using low rank-model of the covariance matrix with a sufficient number of quantization bits. Finally, cross-polarization effects have an impact on the beamforming algorithms. The characterization of the antenna array according to cross-polarization discrimination (XPD) [47], which denotes the gain ratio between co-polarized and cross-polarized wavefields received by the antenna, must be close to 1 in order to perform beamforming properly. It should be mentioned that, all aforementioned effects, not only the mutual coupling, must be taken into account to construct an array manifold that is used to compensate the errors, thus, calibration of the antenna array is performed.

As previously mentioned, the effects of excitation errors on the performance of the antenna array must be accurately assessed before the calibration procedure. In general, the analysis methods are classified under two topics, probabilistic methods and interval arithmetic (IA) based methods. The common concept of the probabilistic methods is that the excitation errors follow a probability distribution function (PDF) and the calibration problem is considered in statistic derivations [48], [49]. By taking use of the central limit theorem, they may offer straightforward closed-form representations of the array pattern's properties, however, even with well-established statistical techniques, confidence boundaries are not always guaranteed, and extreme situations may still fall beyond the bounds [39]. On the other hand, IA-based methods are more reliable since the determined bounds of antenna radiation patterns are finite thanks to possibility of representation of probable values of the element excitations are limited in upper and lower bounds [39]. Another advantage of the IA-based methods is that these methods exclude the time-consuming Monte Carlo (MC) trials and instead of MC trials, they analyse the excitation effect in the means of analytic expression fashion.

In line with these analyses, the antenna array must be accurately calibrated to compensate for excitations and maintain the performance of the antenna array in both transmitting and receiving mode. In the calibration procedure, signal samples are collected from each antenna element or subarrays and then these signal samples are used to determine the compensation weights [39]. The calibration process of phased antenna arrays, whether transmitting or receiving, are similar to each other except for minor differences [39]. In receive mode, a test signal is injected as the input of each element, a special reference or self-correlation process with a beamformer is required to combine all inputs [50]. On the contrary, in the transmit mode, each element must be excited by a source signal and a combined signal monitoring at the output is required [51], therefore only RF chain information can be obtained or an external sensor is used to receive and monitor the signal from each element. Flow chart of the calibration procedure is given in Fig. 2.5. Although calibration methods vary according to applications and systems, they are generally classified under four different categories. Calibration methods are defined under below topics:

- The near-field or far-field probing methods
- The peripheral-fixed probe method
- The mutual (MC) coupling methods
- The built-in network methods

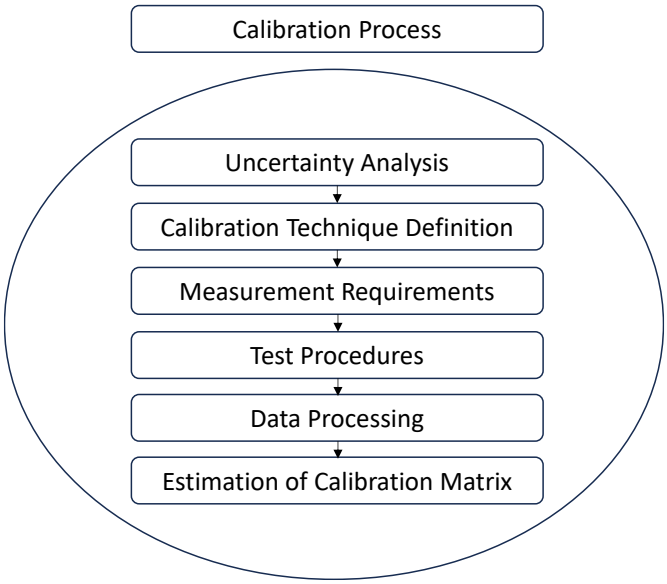

Fig. 2.5. Calibration procedure flow-chart.

These methods were developed to eliminate the time-consuming trial-and-error methods with visual inspection. Detailed information about these methods and the calibration methods developed for this thesis are given in Chapter 5.

2.3. Multiple-Input Multiple-Output Systems

The multiple-input multiple-output (MIMO), an advanced multi-antenna processing approach different from beamforming but using the same time and frequency sources, is used to communicate with signal sources that are spatially separated from each other. In MIMO, reflections/scatters (channel fading), attenuations (path-loss), direction-of-departures (DoD) and direction-of-arrivals (DoA) are taken into account and different than the beamforming, in MIMO multi-paths are used for establishing the channel between communication ends. According to those parameters, the channel between communication ends is characterized, and this is usually known as channel state information (CSI). Once the CSI is known, it is used to increase signal-to-noise ratio (SNR) of a transmitted signal and the channel capacity for the mm-Wave communication systems.

The channel path-loss and fading are the main reasons that lead physical transmissions channels have uncertain and unknown characteristics. The channel path-loss is generally defined as the power density loss of an electromagnetic wave (EM) as it propagates through the transmission environment and can be determined by the propagation environment, the propagation medium and the distance between the transmitter and the receiver [52]. Based on the Frii's transmission for free space propagation [53], the equation for the received power can be given as:

$$P_r = P_t G_t G_r \left(\frac{\lambda}{4\pi d}\right)^2 \tag{2-80}$$

where P_t is the transmitted signal power, G_t is the transmitter antenna gain, G_r is the receiver antenna gain, λ is the wavelength of the carrier signal frequency and d is the distance between transmitter and receiver antennas which is large enough to satisfy the far-field condition. Then the free space loss can be defined as:

$$\alpha = \frac{P_t}{P_r} = \left(\frac{4\pi d}{\lambda}\right)^2 \tag{2-81}$$

It can be seen that the path-loss is directly proportional to the square of the distance and is inversely proportional to the square of wavelength [52]. In terms of decibels (dB), the path-loss can be expressed as:

$$\alpha = 20\log_{10}(d) + 20\log_{10}(f) + 20\log_{10}\left(\frac{4\pi}{c}\right) \tag{2-82}$$

where f is the operating frequency and the term $20\log_{10}\left(\frac{4\pi}{c}\right) = -147.55$.

On the other hand, the EM waves are reflected or scattered randomly in the transmission environment and receiver sense might sense the same signal from multiple paths which is called muti-path effect. The reflected or scattered EM signals from different paths have different phases and superposition sum of the received signals from different paths either have constructive or destructive effect in the receiver [53] where this phenomena is known as channel fading. The unknown and uncertain environment conditions introduce a class of random variation on the losses of reflected or scattered signals, thus, the channel fading modelled as a random variable [52]. The path-loss with fading can be expressed in dB as [52]:

$$\alpha = 20\log_{10}(d) + 20\log_{10}(f) + \mathrm{V}_\sigma - 147.55 \tag{2-83}$$

where V_σ is the random variable that having a standard distribution because of the channel fading.

The physical channel between of the transmitter and receiver relies on the estimation of DoDs and DoAs of the multi-path signals. The simple illustration of a MIMO system with L propagation paths is given in Fig. 2.6.

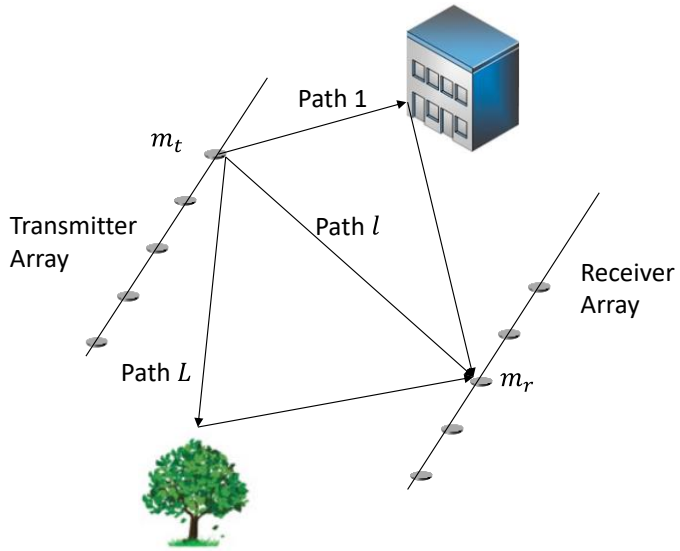

Fig. 2.6. Physical MIMO channel with L paths.

Similar to the beamforming model, the transmission model of the MIMO system can be expressed as:

$$\mathbf{x}(t) = \sum_{l=1}^{L} \alpha_l \boldsymbol{a}_r(\theta_{rl}, \varphi_{rl}) \boldsymbol{a}_t(\theta_{tl}, \varphi_{tl})^H \boldsymbol{s}(t) + \mathbf{n}(t) \tag{2-84}$$

where α_l is the path-loss of the l-th path, θ_{tl} and φ_{tl} are the direction of departures in elevation and azimuth of the l-th path and θ_{rl} and φ_{rl} are the direction of direction of arrival in elevation and azimuth of the l-th path, $\boldsymbol{s}(t) = \left[s_1(t), \dots s_{m_t}(t), \dots s_{M_t}(t)\right]$ is the signal vector from the transmitting array, $\mathbf{n}(t)$ is the additive noise in the receiver array, and the steering vectors for receiving and transmitting arrays can be expressed as:

$$\boldsymbol{a}_r(\theta_{rl}, \varphi_{rl}) = \begin{pmatrix} e^{-j\frac{2\pi}{\lambda_c}[x_0 \sin\theta_{rl}\cos\varphi_{rl} + y_0 \sin\theta_{rl}\sin\varphi_{rl} + z_0\cos\theta_{rl}]} \\ e^{-j\frac{2\pi}{\lambda_c}[x_1 \sin\theta_{rl}\cos\varphi_{rl} + y_1 \sin\theta_{rl}\sin\varphi_{rl} + z_1\cos\theta_{rl}]} \\ \vdots \\ e^{-j\frac{2\pi}{\lambda_c}[x_{M_r-1} \sin\theta_{rl}\cos\varphi_{rl} + y_{M_r-1} \sin\theta_{rl}\sin\varphi_{rl} + z_{M_r-1}\cos\theta_{rl}]} \end{pmatrix} \tag{2-85}$$

$$\boldsymbol{a}_t(\theta_{tl}, \varphi_{tl}) = \begin{pmatrix} e^{-j\frac{2\pi}{\lambda_c}[x_0 \sin\theta_{tl}\cos\varphi_{tl} + y_0 \sin\theta_{tl}\sin\varphi_{tl} + z_0\cos\theta_{tl}]} \\ e^{-j\frac{2\pi}{\lambda_c}[x_1 \sin\theta_{tl}\cos\varphi_{tl} + y_1 \sin\theta_{tl}\sin\varphi_{tl} + z_1\cos\theta_{tl}]} \\ \vdots \\ e^{-j\frac{2\pi}{\lambda_c}[x_{M_t-1} \sin\theta_{tl}\cos\varphi_{tl} + y_{M_t-1} \sin\theta_{tl}\sin\varphi_{tl} + z_{M_t-1}\cos\theta_{tl}]} \end{pmatrix} \tag{2-86}$$

The basic idea of the MIMO systems is exploiting the multi-path effect of the wireless channel to scale or allocate the channel capacity; thus, multiple signal streams can be transmitted. As in beamforming, in MIMO systems, the weights of the elements in the antenna array are optimized and thus the signal is transmitted to the desired location. However, unlike beamforming, in MIMO systems, the weights of the elements are calculated according to the estimation of the physical channel between the transmitter and receiver, and multi-paths are also used. The processing matrices for the weights in the transmitters and receivers are generally called precoding and decoding matrices, respectively. The output signal vector $\boldsymbol{y} \in \mathbb{C}^{D\times 1}$ for the uplink in MIMO system can be expressed as:

$$\boldsymbol{y} = \mathbf{DHPs} + \mathbf{Dn} \tag{2-87}$$

where $\mathbf{D} \in \mathbb{C}^{D\times M_r}$ is the decoding matrix where D is the number of RF chains in the receiver and M_r is the number of antennas in the receiver, $\mathbf{P} \in \mathbb{C}^{M_t\times P}$ is the precoding matrix where P is the number of RF chains in the transmitter and M_t is the number of antennas in the receiver, $\mathbf{s} \in \mathbb{C}^{P\times 1}$ is the received signal and $\mathbf{n} \in \mathbb{C}^{M_r\times 1}$ is the additive noise. It should be noted the number of RF chains in the receiver and transmitter may be lower than the number of antennas (Hybrid precoding or decoding). Lastly, $\mathbf{H} \in \mathbb{C}^{M_r\times M_t}$ is the combined channel matrix between the receiver and transmitter and can be expressed as:

$$\mathbf{H} = \mathbf{A}_r \mathbf{\Phi} \mathbf{A}_t^H \tag{2-88}$$

where $\mathbf{A}_r \in \mathbb{C}^{M_r\times L}$ is the steering matrix of the received signals whose l-th column represents $\boldsymbol{a}(\theta_{rl}, \varphi_{rl})$, $\mathbf{A}_t \in \mathbb{C}^{M_t\times L}$ is the steering matrix of transmitted signals whose l-th column represents $\boldsymbol{a}(\theta_{tl}, \varphi_{tl})$, and $\mathbf{\Phi} \in \mathbb{C}^{L\times L}$ is the diagonal matrix whose l, l-th entry denotes the l-th path-loss as α_l. Once the combined physical channel $\mathbf{H}$ is estimated the channel capacity of MIMO system can be based on the Shannon's capacity. The Shannon's capacity [54] can be expressed as:

$$C = W \log_2\left(1 + \frac{P_r}{WN_0}\right) \tag{2-89}$$

where C is the channel capacity, W is the frequency bandwidth, P_r is the received signal power and N_0 is the spectral density of the received noise power.

The first step for estimating channel capacity is applying singular value composition (SVD) to the channel matrix $\mathbf{H}$ as:

$$\mathbf{H} = \mathbf{U\Sigma V}^H \tag{2-90}$$

where $\mathbf{U} \in \mathbb{C}^{M_r\times M_r}$ and $\mathbf{V} \in \mathbb{C}^{M_t\times M_t}$ are the unitary matrices, whose columns are the singular vectors and $\mathbf{\Sigma} \in \mathbb{C}^{M_r\times M_t}$ is a rectangular diagonal matrix, whose diagonal elements represents the singular values. The diagonal elements are the singular elements of the

matrix **H** and are ordered as $\lambda_1 \geq \lambda_2 \ldots \geq \lambda_q$ where q is the number of non-zero singular values ($q = L$). The rank of the **H** is exactly the number of paths L if the $L < M_r \leq M_t$ is satisfied. Then, the channel matrix **H** can be rewritten as:

$$\mathbf{H} = \sum_{l=1}^{L} \alpha_l \boldsymbol{a}_r(\theta_{rl}, \varphi_{rl}) \boldsymbol{a}_t(\theta_{tl}, \varphi_{tl})^H = \sum_{l=1}^{L} \lambda_l \mathbf{u}_l \mathbf{v}_l^H \tag{2-91}$$

where $\mathbf{u}_l$ is the l-th column of the matrix **U**, $\mathbf{v}_l$ is the l-th column of the matrix **V**, and λ_l is the l-th diagonal element of the matrix **Σ**. If L is smaller than both D and P, the following expressions hold:

$$\mathbf{D} = \mathbf{U}^H, \mathbf{P} = \mathbf{V}^H, \tilde{\mathbf{n}} = \mathbf{U}^H \mathbf{n} \tag{2-92}$$

Then, the output signal vector, $\boldsymbol{y}$, can be rewritten as:

$$\boldsymbol{y} = \boldsymbol{\Sigma}\mathbf{s} + \tilde{\mathbf{n}} \tag{2-93}$$

It should be noted the $\tilde{\mathbf{n}}$ and **n** have the same distribution. In line with the above equations, it can be seen that L streams are transmitted in parallel. Then, the capacity of MIMO system can be expressed as:

$$C = \sum_{l=1}^{L} \log_2 \left(1 + \frac{P_l \lambda_l^2}{N_0}\right) \text{ bits/s/Hz} \tag{2-94}$$

where P_l is the power allocations at l-th path satisfying the total power constraint $\sum_l^L P_l = P$ where P is the total power. It can be seen that there is a direct relation between number of paths and the channel capacity, thus, we conclude MIMO systems leverage to improve the transmission rate by take into account more reflecting and scattering paths [52].

The power allocation in MIMO system is usually performed by the technique known as water filling or water pouring. The water filling is based on the following optimization problem [55]:

$$\begin{aligned} &\max_{\{P_l\}} \sum_{l=1}^{L} \log_2 \left(1 + \frac{P_l \lambda_l^2}{N_0}\right) \\ &\text{s.t.} \sum_{l=1}^{L} \lambda_l \leq P \\ &P_l \geq 0, \qquad 1 \leq l \leq L \end{aligned} \tag{2-95}$$

given by

$$P_l = \left(\mu - \lambda_l^{-1}\right)^+ \tag{2-96}$$

where $(P_l)^+ \triangleq \max(0, P_l)$ and μ is the water level which satisfies the power constraint $\sum_l^L P_l = P$.

The overall performance of the MIMO systems majorly depends on channel estimation and precoding. In practice, to use all the advantages of MIMO systems, it is of great importance to make accurate channel estimation at the receiver side [56]. There is a need to switch CSI between transmitters on a fast timescale and low latency basis [56]. In general, for the narrow band signals, the channel estimation means to estimate the DoDs, DoAs and the path gain/loss. The DoDs and DoAs can be estimated using advanced techniques, as well as they can be estimated with the standard previously described algorithms such as MUSIC, ESPRIT, ML, etc. Once the angles are estimated the path gain/loss coefficients can be extract using the least squares approach (detailed explanation is given in Chapter VI). On the other hand, precoding is an important signal processing technique to maximize the link performance depending on the CSI at the transmitter side and the precoding is used in the down-link to concentrate each signal at its intended receiver along with interference mitigation [56]. In this respect, precoding is similar to beamforming. There are two types of precoding algorithms, linear and non-linear precoding algorithms. In terms of capacity, nonlinear precoding algorithms are superior to linear ones, however, their complexities are considerably higher and their hardware implementation is costly, thus, MIMO systems general employ linear precoding algorithms [57]. The most prominent precoding algorithms are the matched filter (MF), zero-forcing (ZF), regularized zero-forcing (RZF) and minimum mean square error (MMSE) precoders when $M_t \geq M_r$. The formulations of those precoding algorithms are given as [58]:

$$\mathbf{W}_{\mathrm{MF}} = \beta \mathbf{H}^H \tag{2-97}$$

$$\mathbf{W}_{\mathrm{ZF}} = \beta \mathbf{H}^H (\mathbf{H}\mathbf{H}^H)^{-1} \tag{2-98}$$

$$\mathbf{W}_{\mathrm{RZF}} = \beta \mathbf{H}^H (\mathbf{H}\mathbf{H}^H + \alpha \mathbf{I})^{-1} \tag{2-99}$$

$$\mathbf{W}_{\mathrm{MMSE}} = \beta \mathbf{H}^H \left(\mathbf{H}\mathbf{H}^H + \frac{\sigma^2}{P} \mathbf{I} \right)^{-1} \tag{2-100}$$

where $\mathbf{W}_{\mathrm{MF}} \in \mathbb{C}^{M_t \times M_r}$, $\mathbf{W}_{\mathrm{ZF}} \in \mathbb{C}^{M_t \times M_r}$, $\mathbf{W}_{\mathrm{RZF}} \in \mathbb{C}^{M_t \times M_r}$ and $\mathbf{W}_{\mathrm{MMSE}} \in \mathbb{C}^{M_t \times M_r}$ are the precoding matrices (assuming number of RF chains are equal to number of antennas in both receiver and transmitter), α regularization factor, $\mathbf{I}$ is the $M_r \times M_r$ identity matrix, σ is the noise variance, P is the total power and the scalar β is chosen to satisfy $\|\mathbf{W}\|_F^2 = tr(\mathbf{W}\mathbf{W}^H) = P$.

The massive MIMO is the extension of MIMO systems. The massive MIMO takes this concept to a larger scale with a significantly higher number of antennas, enabling even greater spatial multiplexing and improved system performance [59]. The most significant

difference between MIMO and massive MIMO is that massive MIMO provides service to multiple users at the same time. The massive architecture is given in Fig. 2.7.

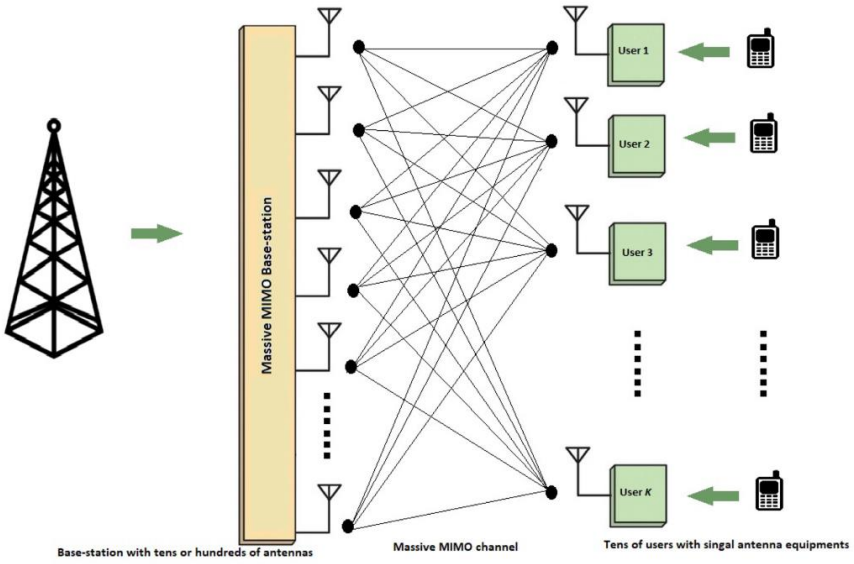

Fig. 2.7. Massive MIMO architecture [56].

Assuming K users each has L propagation paths the channel for the downlink massive MIMO can be written as:

$$\mathbf{H}_k = \sum_{l=1}^{L} \alpha_{k,l} \boldsymbol{a}_{BS}\left(\theta_{k,l}^{BS}, \varphi_{k,l}^{BS}\right) \boldsymbol{a}_{UE}\left(\theta_{k,l}^{UE}, \varphi_{k,l}^{UE}\right)^T \tag{2-101}$$

where $\boldsymbol{a}_{BS}\left(\theta_{k,l}^{BS}, \varphi_{k,l}^{BS}\right)$ and $\boldsymbol{a}_{UE}\left(\theta_{k,l}^{UE}, \varphi_{k,l}^{UE}\right)$ are the steering vectors and can be expressed as:

$$\boldsymbol{a}_{BS}\left(\theta_{k,l}^{BS}, \varphi_{k,l}^{BS}\right) = \begin{pmatrix} e^{-j\frac{2\pi}{\lambda_c}\left[x_0 \sin\theta_{k,l}^{BS} \cos\varphi_{k,l}^{UE} + y_0 \sin\theta_{k,l}^{BS} \sin\varphi_{k,l}^{UE} + z_0 \cos\theta_{k,l}^{BS}\right]} \\ e^{-j\frac{2\pi}{\lambda_c}\left[x_1 \sin\theta_{k,l}^{BS} \cos\varphi_{k,l}^{UE} + y_1 \sin\theta_{k,l}^{BS} \sin\varphi_{k,l}^{UE} + z_1 \cos\theta_{k,l}^{BS}\right]} \\ \vdots \\ e^{-j\frac{2\pi}{\lambda_c}\left[x_{M_{BS}-1} \sin\theta_{k,l}^{BS} \cos\varphi_{k,l}^{UE} + y_{M_{BS}-1} \sin\theta_{k,l}^{BS} \sin\varphi_{k,l}^{UE} + z_{M_{BS}-1} \cos\theta_{k,l}^{BS}\right]} \end{pmatrix} \tag{2-102}$$

$$\boldsymbol{a}_{UE}\left(\theta_{k,l}^{UE}, \varphi_{k,l}^{UE}\right) = \begin{pmatrix} e^{-j\frac{2\pi}{\lambda_c}\left[x_0 \sin\theta_{k,l}^{UE} \cos\varphi_{k,l}^{UE} + y_0 \sin\theta_{k,l}^{UE} \sin\varphi_{k,l}^{UE} + z_0 \cos\theta_{k,l}^{UE}\right]} \\ e^{-j\frac{2\pi}{\lambda_c}\left[x_1 \sin\theta_{k,l}^{UE} \cos\varphi_{k,l}^{UE} + y_1 \sin\theta_{k,l}^{UE} \sin\varphi_{k,l}^{UE} + z_1 \cos\theta_{k,l}^{UE}\right]} \\ \vdots \\ e^{-j\frac{2\pi}{\lambda_c}\left[x_{M_{UE}-1} \sin\theta_{k,l}^{UE} \cos\varphi_{k,l}^{UE} + y_{M_{UE}-1} \sin\theta_{k,l}^{UE} \sin\varphi_{k,l}^{UE} + z_{M_{UE}-1} \cos\theta_{k,l}^{UE}\right]} \end{pmatrix} \tag{2-103}$$

Then, the received signal, $\boldsymbol{y}_r \epsilon\, \mathbb{C}^{M_r \times 1}$ can be given as:

$$\boldsymbol{y}_r = \sum_{k=1}^{K} \mathbf{H}_k \boldsymbol{s}_k + \mathbf{n} \tag{2-104}$$

The more advanced feature of massive MIMO, which is different than MIMO, the massive MIMO is a multicarrier cellular network with multiple cells that operate according to a

synchronous time-division duplexing (TDD) protocol [60]. The massive number of antennas allows channel hardening and the base station (BS) communicates with single-antenna users simultaneously on each time/frequency sample [60]. Therefore, massive MIMO systems use orthogonal frequency-division multiplexing for the 5G communications systems. Different base stations operate separately and process their signals using linear decoding in the uplink transmission and linear precoding in the downlink transmission.

The received signal (uplink), $\boldsymbol{y}_{l_c} \in \mathbb{C}^{M_r \times 1}$, at the l_c-th BS in a multi-cell massive MIMO system with K single antenna users can be expressed as [60]:

$$\boldsymbol{y}_{l_c} = \sum_{i=1}^{L_c} \mathbf{H}_i^{l_c} \boldsymbol{s}_i + \mathbf{n}_{l_c} \tag{2-105}$$

where $\mathbf{H}_i^{l_c} \in \mathbb{C}^{M_r \times K}$ is a matrix, whose columns represent the channel between k-th user and l_c-th BS being as $\mathbf{H}_i^{l_c} = \left[\mathbf{h}_{i,1}^{l_c} \dots \mathbf{h}_{i,K}^{l_c}\right]$, $\boldsymbol{s}_i \in \mathbb{C}^{K \times 1}$ is the received signal vector being as $\boldsymbol{s}_i = \left[s_{i,1} \dots s_{i,K}\right]^T$ and $\mathbf{n}_{l_c}$ is zero mean Gaussian noise distributed with variance σ_{UL}^2. The l_c-th BS discriminates the signal transmitted by its k-th user from the interference by multiplying $\boldsymbol{y}_{l_c}$ with a linear detection vector $\mathbf{v}_{l_c,k} \in \mathbb{C}^{M_r \times 1}$ as [60]:

$$\begin{aligned} \mathbf{v}_{l_c,k}^H \boldsymbol{y}_{l_c} &= \sum_{i=1}^{L_c} \sum_{t=1}^{K} \mathbf{v}_{l_c,k}^H \mathbf{h}_{i,t}^{l_c} \boldsymbol{s}_{i,t} + \mathbf{v}_{l_c,k}^H \mathbf{n}_{l_c} \\ &= \underbrace{\mathbf{v}_{l_c,k}^H \mathbf{h}_{l_c,k}^{l_c} s_{l_c,k}}_{\text{Desired signal}} + \underbrace{\sum_{\substack{t=1 \\ t \neq k}}^{K} \mathbf{v}_{l_c,k}^H \mathbf{h}_{l_c,t}^{l_c} s_{l_c,t}}_{\text{Intra-cell interference}} + \underbrace{\sum_{\substack{i=1 \\ i \neq l_c}}^{L_c} \sum_{t=1}^{K} \mathbf{v}_{l_c,k}^H \mathbf{h}_{i,t}^{l_c} s_{i,t}}_{\text{Inter-cell interference}} + \underbrace{\mathbf{v}_{l_c,k}^H \mathbf{n}_{l_c}}_{\text{Residual noise}} \end{aligned} \tag{2-106}$$

where $\boldsymbol{s}_{i,t}$ is the transmitted signal form user t in cell i.

Considering the downlink in multi-cell massive MIMO, where $\mathbf{x}_{l_c} \in \mathbb{C}^{M_t \times 1}$ is the transmitted signal vector for selected K users with the linear precoding vector, $\mathbf{w}_{l_c,k} \in \mathbb{C}^{M_t \times 1}$ can be expressed as [60]:

$$\mathbf{x}_{l_c} = \sum_{k=1}^{K} \mathbf{w}_{l_c,k} \, s_{l_c,k} \tag{2-107}$$

Then, the received signal, $y_{l_c,k} \in \mathbb{C}$, at user k in cell l_c can be expressed as [60]:

$$y_{l_c,k} = \sum_{i=1}^{L_c} \left(\mathbf{h}_{l_c,k}^{i}\right)^H \mathbf{x}_i + n_{l_c,k} = \underbrace{\left(\mathbf{h}_{l_c,k}^{l_c}\right)^H \mathbf{w}_{l_c,k} s_{l_c,k}}_{\text{Desired signal}} + \tag{2-108}$$

$$\underbrace{\sum_{\substack{t=1 \\ t\neq k}}^{K}\left(\mathbf{h}_{l_c,k}^{l_c}\right)^H \mathbf{w}_{l_c,t}s_{l_c,t}}_{\text{Intra-cell interference}} + \underbrace{\sum_{\substack{i=1 \\ i\neq l_c}}^{L_c}\sum_{t=1}^{K}\left(\mathbf{h}_{l_c,k}^{i}\right)^H \mathbf{w}_{i,t}s_{i,t}}_{\text{Inter-cell interference}} + \underbrace{n_{l_c,k}}_{\text{Residual noise}}$$

where $n_{l_c,k}$ is zero mean additive white noise with variance σ_{DL}^2 and $\mathbf{h}_{l_c,k}^{i}$ is the same channel response as in the uplink.

Cell-free massive MIMO systems concept has been developed to comprise a large number of distributed, low cost, and low power access point antennas, connected to a network controller [61]. Therefore, in this Thesis we consider only single cell massive MIMO systems and also for the brevity in the formulations; thus, we discard inter-cell interference.

2.4. Reconfigurable Intelligent Surfaces

In highly dense environments the LoS channel between the transmitter and receiver is likely to be blocked [62], moreover, signal reflections, refractions, diffractions and scatterers highly effect the positioning signal [63]. In order to mitigate the effects of factors hindering accurate channel estimation and provide a virtual LoS channel where required, a new concept known as reconfigurable intelligent surface (RIS) has been proposed [64], [65]. Thus, as an emerging technology, the reconfigurable intelligent surfaces (RIS) are promising auxiliary elements for millimeter-wave, even sub millimeter-wave massive MIMO systems for 5G, B5G and 6G wireless communication systems for enhancing spectral efficiency, energy efficiency and providing auxiliary LOS path for the receiver [66]. The RISs might improve the both the spectral and energy efficiencies of wireless communication systems. Since a RIS almost entirely consists of passive RF components it is considered as an energy-efficient technology [63], [65]. There is no need of power amplifiers and ADCs/DACs as in traditional massive MIMO base stations or like any other transceiver. Additionally, RISs support full-duplex, and are compatible with existing standards and hardware [65]. In order to enhance received power at the end users, it accomplishes this by appropriately adjusting the phase shifts imposed by each reflecting element to constructively combine the incoming signals. The RISs can be in either fixed architecture or dynamic architecture. Since just the related phase shifter is required for passive reflection in fixed design, the versatility of beamforming is not fully utilized due to the fixed structure, however, dynamic RIS structure capable of adapting phase shifts according to channel state information [67]. The RISs are capable of controlling polarization and can be in the form of scattering, focusing, reflective or refractive mode. The refractive mode outdoor to indoor RIS use case is given in Fig. 2.8.

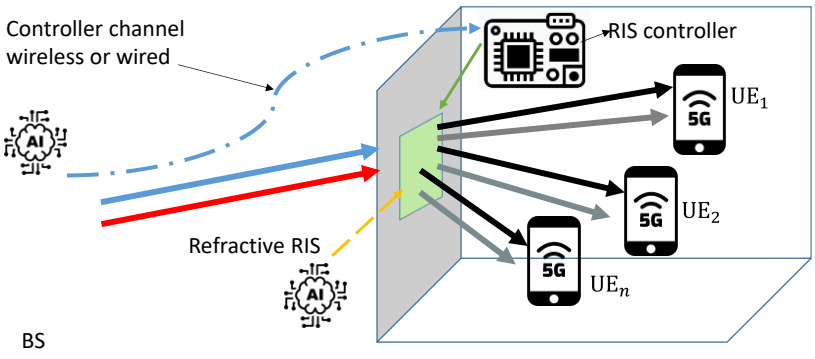

Link	Frequency (GHz)	Conv.	Frequency (GHz)
→	24.25-29.5	Up	57-71
→	3.4-3.8	Up	24.25-29.5 and 57-71
→	24.25-29.5	Down	3.4-3.8
→	57-71	Down	24.25-29.5 and 3.4-3.8

Fig. 2.8. Outdoor to indoor refractive RIS use case.

The RISs are resilient, thus, with deployment of them, the wireless channels the wireless channels within the natural environment become controllable with such surface posting on the basic building block [52]. Since RISs are resilient, they can be used in many scenarios for wireless communication systems. The beam focusing by the e beam focusing by the reflection of IRS can be used to increase SNR for obtaining better QoS, moreover, devices of internet of things (IoT) can also benefit from beam focusing for wireless power transfer [63]. On the other hand, the sent signal can avoid any potential eavesdropping devices in the physical transmission line by utilizing numerous RIS components by corporation of such signals that propagate via multiple times of reflect beam focusing and steering [26], [52], [64]. Also, RIS can be programmable to block any unauthorized users from transmitting/receiving any signals to/from the access point (AP) [69]. To achieve this property RIS can implement beam scattering to minimize malicious user power or nullifies the them with zero forcing algorithm [52]. Last but not the least, RIS can be used to transmit modulated signals passively. The reflective type RIS use case is given in Fig. 2.9.

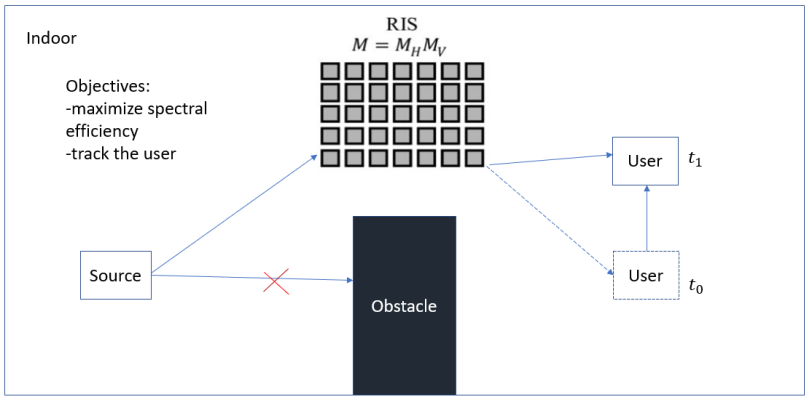

Fig. 2.9. Indoor user tracking via reflective type RIS.

The RISs can be controlled in real-time by some software programming and with aid of a controller as depicted in Fig. 2.9. The control signal to RIS can be either wired or wireless. Since RIS has been suggested to serve a wide range of wireless transmission applications, prior research on RIS has concentrated on a number of areas, including beamforming, hardware implementation, channel estimation, resource allocation [52], [64]. Numerous objective and subjective factors are also taken into consideration in the literature. In general, RIS are classified under four transmission schemes as [52]:

- Single RIS assisted single user transmission
- Single RIS assisted multi-user transmission
- Multiple RIS assisted single user transmission
- Multiple RIS assisted multiple-user transmission

The main open issue for the RIS-aided MIMO systems is the channel estimation. Although, RISs are additional auxiliary elements for massive MIMO systems which enhance the overall communication quality, channel estimation becomes more challenging task in RIS-aided massive MIMO systems than the conventional MIMO systems since the total number of antennas is larger and there are multiple different channels (direct, cascaded, multiple cascaded, etc.). In the literature, many existing studies propose different solutions to the RIS-enabled massive MIMO channel estimation problem. Such as, Alternative direction multiplier method (ADMM) was used to iteratively optimize the multi-objective optimization problem. In [3] and [18], nuclear norm minimization was used for estimating the off-grid angular information. On the other hand, the channel estimation was performed by solving the block-sparse recovery problem using the polar-domain frequency-dependent block orthogonal least squares (PF-BOLS) algorithm. However, more effective novel channel estimation algorithms and methods are needed to be developed for RIS-aided MIMO systems. This thesis focused on the single RIS assisted single user transmission model. The uplink narrow-band RIS-aided millimeter-wave massive MIMO system is presented in Fig. 2.10.

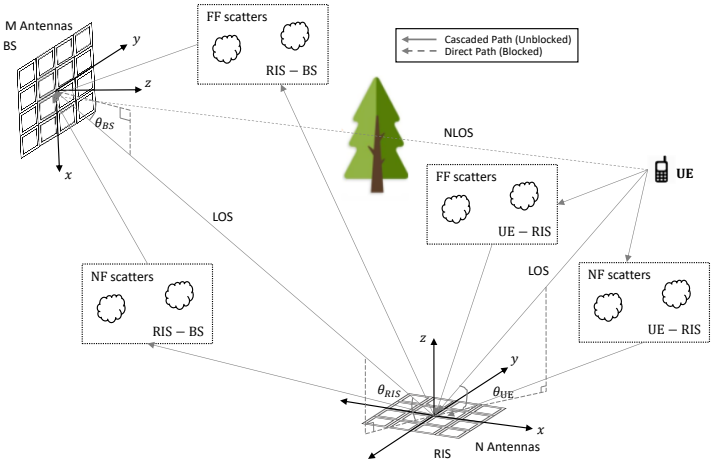

Fig. 2.10. The uplink narrow-band RIS-aided millimeter-wave massive MIMO system.

The cascaded channel model for the Fig. 2.10 can be modelled in two components as, the channel between UE and RIS, $\mathbf{H}_1$, and the channel between RIS and BS, $\mathbf{H}_2$. The cascaded channel components can be modelled as:

$$\mathbf{H}_1 = \sum_{k=1}^{K} \alpha_k \, \boldsymbol{a}_{RIS}\left(\theta_k^{RIS-DoA}, \varphi_k^{RIS-DoA}\right)\boldsymbol{a}_{UE}\left(\theta_k^{UE-DoD}, \varphi_k^{UE-DoD}\right)^T \tag{2-109}$$

$$\mathbf{H}_2 = \sum_{p=1}^{P} \beta_p \, \boldsymbol{a}_{BS}\left(\theta_p^{BS-DoA}, \varphi_p^{BS-DoA}\right)\boldsymbol{a}_{RIS}\left(\theta_p^{RIS-DoD}, \varphi_p^{RIS-DoD}\right)^T \tag{2-110}$$

where α_k and β_p are the path losses between channel UE-RIS and RIS-BS, respectively, DoA and DoD, denote the direction of arrival and direction of departure, respectively. Given the related number of antennas and angles the steering vectors $\boldsymbol{a}_{RIS}\left(\theta_k^{RIS-DoA}, \varphi_k^{RIS-DoA}\right)$, $\boldsymbol{a}_{UE}\left(\theta_k^{UE-DoD}, \varphi_k^{UE-DoD}\right)$, $\boldsymbol{a}_{BS}\left(\theta_p^{BS-DoA}, \varphi_p^{BS-DoA}\right)$ and $\boldsymbol{a}_{RIS}\left(\theta_p^{RIS-DoD}, \varphi_p^{RIS-DoD}\right)$ can be expressed as in (2-102) and (2-103).

The effective cascaded uplink channel, $\mathbf{H}$, can be expressed as:

$$\mathbf{H} = \mathbf{H}_1 \boldsymbol{\Theta} \mathbf{H}_2 \tag{2-111}$$

where $\boldsymbol{\Theta} \in \mathbb{C}^{N \times N}$ is a diagonal matrix, whose complex elements denotes the gain and phase coefficients of the RIS elements as $\vartheta_n e^{j\Phi_n}$.

Then, the received uplink pilot signal at the BS, $\boldsymbol{y}_{BS} \in \mathbb{C}^{M_{BS} \times 1}$, is given by:

$$\boldsymbol{y}_{BS} = \mathbf{H}\mathbf{s} + \mathbf{n} \tag{2-112}$$

where $\mathbf{s} \in \mathbb{C}^{K \times 1}$ is the received signal vector being as $\mathbf{s} = \left[s_1 \ldots s_{M_{BS}}\right]^T$ and $\mathbf{n}$ is zero mean Gaussian noise distributed with variance σ^2.

2.5. References Chapter 2

[1] C. A. Balanis, Antenna theory: analysis and design, Fourth edition. Hoboken, New Jersey: Wiley, 2016.

[2] A. Antón Sánchez, "Statistical techniques and algorithms applied in satellite communications antenna arrays for direction of arrival estimation and calibration," PhD Thesis, Universidad Politécnica de Madrid, 2016. doi: 10.20868/UPM.thesis.42959.

[3] "Principles of Adaptive Array Processing." Accessed: Jan. 25, 2024. [Online]. Available: https://apps.dtic.mil/sti/citations/ADA470687

[4] I. Stevanovic, A. Skrivervik, and J. R. Mosig, "Smart Antenna Systems for Mobile Communications," Ecole Polytechnique Federale De Lausanne, vol. Lausanne, Switzerland, Jan. 2003, Tech. Rep.

[5] A. E. Zorkun, M. A. Salas-Natera, and R. M. Rodríguez-Osorio, "An Improved Hybrid Beamforming Algorithm for Fast Target Tracking in Satellite and V2X Communication," Remote Sensing, vol. 16, no. 1, Art. no. 1, Jan. 2024, doi: 10.3390/rs16010013.

[6] "A Quantitative Analysis of the Power Advantage of Hybrid Beamforming for Multibeam Phased Array Receivers | Analog Devices." Accessed: Mar. 08, 2024. [Online]. Available: https://www.analog.com/en/resources/technical-articles/power-advantage-of-hybrid-beamforming.html

[7] N. Al-Falahy and O. Y. K. Alani, "Millimetre wave frequency band as a candidate spectrum for 5G network architecture: A survey," Physical Communication, vol. 32, pp. 120–144, Feb. 2019, doi: 10.1016/j.phycom.2018.11.003.

[8] I. A. Hemadeh, K. Satyanarayana, M. El-Hajjar, and L. Hanzo, "Millimeter-Wave Communications: Physical Channel Models, Design Considerations, Antenna Constructions, and Link-Budget," IEEE Commun. Surv. Tutorials, vol. 20, no. 2, pp. 870–913, 2018, doi: 10.1109/COMST.2017.2783541.

[9] E. Ali, M. Ismail, R. Nordin, and N. F. Abdulah, "Beamforming techniques for massive MIMO systems in 5G: overview, classification, and trends for future research," Frontiers Inf Technol Electronic Eng, vol. 18, no. 6, pp. 753–772, Jun. 2017, doi: 10.1631/FITEE.1601817.

[10] C. Paleologu, S. Ciochină, J. Benesty, and S. L. Grant, "An overview on optimized NLMS algorithms for acoustic echo cancellation," EURASIP Journal on Advances in Signal Processing, vol. 2015, no. 1, p. 97, Nov. 2015, doi: 10.1186/s13634-015-0283-1.

[11] S. Ciochina, C. Paleologu, J. Benesty, and A. A. Enescu, "On the influence of the forgetting factor of the RLS adaptive filter in system identification," in 2009 International Symposium on Signals, Circuits and Systems, Jul. 2009, pp. 1–4. doi: 10.1109/ISSCS.2009.5206117.

[12] C. Elisei-Iliescu, C. Paleologu, and R. Tamaş, "On the performance of the variable-regularized recursive least-squares algorithms," vol. 10977, p. 109771W, Dec. 2018, doi: 10.1117/12.2323462.

[13] B. Jalal, O. Elnahas, and Z. Quan, "Efficient DOA Estimation Under Partially Impaired Antenna Array Elements," IEEE Trans. Veh. Technol., vol. 71, no. 7, pp. 7991–7996, Jul. 2022, doi: 10.1109/TVT.2022.3169404.

[14] A. A. M. Khalaf, A.-R. B. M. El-Daly, and H. F. A. Hamed, "Different adaptive beamforming algorithms for performance investigation of smart antenna system," in 2016 24th International Conference on Software, Telecommunications and Computer Networks (SoftCOM), Split, Croatia: IEEE, Sep. 2016, pp. 1–6. doi: 10.1109/SOFTCOM.2016.7772134.

[15] R. L. Dilsavor and R. L. Moses, "Analysis of Modified SMI Method For Adaptive Array Weight Control," IFAC Proceedings Volumes, vol. 25, no. 15, pp. 417–422, Jul. 1992, doi: 10.1016/S1474-6670(17)50668-0.

[16] N. Jablon, "Adaptive beamforming with the generalized sidelobe canceller in the presence of array imperfections," IEEE Trans. Antennas Propagat., vol. 34, no. 8, pp. 996–1012, Aug. 1986, doi: 10.1109/TAP.1986.1143936.

[17] Samer Emad Eldin and Military Technical College (MTC), "A Performance Evaluation of Signal Filtering with different Adaptive Algorithms on Doppler-Angular Adaptive Generalized Sidelobe Canceler (GSC)," IJERT, vol. V8, no. 11, p. IJERTV8IS110098, Nov. 2019, doi: 10.17577/IJERTV8IS110098.

[18] C. W. Reed and K. Yao, "Performance of blind beamforming algorithms," in Ninth IEEE Signal Processing Workshop on Statistical Signal and Array Processing (Cat. No.98TH8381), Sep. 1998, pp. 256–259. doi: 10.1109/SSAP.1998.739383.

[19] J. F. CARDOSO and A. SOULOUMIAC, "Blind beamforming for non-Gaussian signals," IEE proc. F, Radar signal process, vol. 140, no. 6, pp. 362–370, 1993.

[20] R. Thakur and K. S. Mourya, "Performance Comparison of Blind and Non Blind Adaptive Beamforming Algorithms in Mobile Communication," IOSR J. Electron. Commun. Eng, vol. 12, no. 6, pp. 51–57, 2017.

[21] D. H. Rogstad, "The SUMPLE Algorithm for Aligning Arrays of Receiving Radio Antennas: Coherence Achieved with Less Hardware and Lower Combining Loss," IPN Progress Report, vol. 42, no. 162, pp. 1–29, 2005.

[22] Z. Ahmad, S. Yaoliang, and Q. Du, "A robust adaptive beamforming algorithm based on LSCMA," in 2017 2nd Workshop on Recent Trends in Telecommunications Research (RTTR), Feb. 2017, pp. 1–6. doi: 10.1109/RTTR.2017.7887861.

[23] B. Sharma and I. Sarkar, "Performance Analysis of Smart Antenna Beam forming Techniques," IOSR Journal of Electronics and Communication Engineering (IOSR-JECE), vol. 10, 2015.

[24] S. Ganguly, J. Ghosh, and P. K. Kumar, "Performance Analysis of Array Signal Processing Algorithms for Adaptive Beamforming," in 2019 URSI Asia-Pacific Radio

Science Conference (AP-RASC), Mar. 2019, pp. 1–6. doi: 10.23919/URSIAP-RASC.2019.8738291.

[25] H. Halbauer, S. Saur, J. Koppenborg, and C. Hoek, "3D beamforming: Performance improvement for cellular networks," Bell Labs Tech. J., vol. 18, no. 2, pp. 37–56, Sep. 2013, doi: 10.1002/bltj.21604.

[26] A. Fascista, A. Coluccia, H. Wymeersch, and G. Seco-Granados, "RIS-Aided Joint Localization and Synchronization with a Single-Antenna Mmwave Receiver," in ICASSP 2021 - 2021 IEEE International Conference on Acoustics, Speech and Signal Processing (ICASSP), Toronto, ON, Canada: IEEE, Jun. 2021, pp. 4455–4459. doi: 10.1109/ICASSP39728.2021.9413515.

[27] N. Ruan, H. Wang, F. Wen, and J. Shi, "DOA Estimation in B5G/6G: Trends and Challenges," Sensors, vol. 22, no. 14, p. 5125, Jul. 2022, doi: 10.3390/s22145125.

[28] H. Krim and M. Viberg, "Two decades of array signal processing research: the parametric approach," IEEE Signal Processing Magazine, vol. 13, no. 4, pp. 67–94, Jul. 1996, doi: 10.1109/79.526899.

[29] M. Pesavento and A. B. Gershman, "Maximum-likelihood direction-of-arrival estimation in the presence of unknown nonuniform noise," IEEE Trans. Signal Process., vol. 49, no. 7, pp. 1310–1324, Jul. 2001, doi: 10.1109/78.928686.

[30] T. Wang, B. Ai, R. He, and Z. Zhong, "Two-Dimension Direction-of-Arrival Estimation for Massive MIMO Systems," IEEE Access, vol. 3, pp. 2122–2128, 2015, doi: 10.1109/ACCESS.2015.2496944.

[31] N. Anwar Baig and M. Bilal Malik, "Comparison of Direction of Arrival (DOA) Estimation Techniques for Closely Spaced Targets," IJFCC, pp. 654–659, 2013, doi: 10.7763/IJFCC.2013.V2.246.

[32] A. A. Hussain, N. Tayem, and A.-H. Soliman, "Computationally Efficient Forward/backward Averaged DOA Estimation of Coherent Sources in Pairs," in 2021 IEEE 94th Vehicular Technology Conference (VTC2021-Fall), Norman, OK, USA: IEEE, Sep. 2021, pp. 1–7. doi: 10.1109/VTC2021-Fall52928.2021.9625061.

[33] N. D. Sidiropoulos, F. Gini, R. Chellappa, and S. Theodoridis, Eds., Communications and radar signal processing. in Academic Press library in signal processing, no. volume 2. Amsterdam: Academic Press, 2014.

[34] M. Takanashi, T. Nishimura, Y. Ogawa, and T. Ohgane, "Precise DOA Estimation Using SAGE Algorithm with a Cylindrical Array," IEICE Transactions on Communications, vol. E91B, Nov. 2008, doi: 10.1093/ietcom/e91-b.11.3784.

[35] K. Xiong, Z. Liu, and W. Jiang, "SAGE-Based Algorithm for Direction-of-Arrival Estimation and Array Calibration," International Journal of Antennas and Propagation, vol. 2014, p. e217482, Jun. 2014, doi: 10.1155/2014/217482.

[36] M. H. Haroun, "8×1 Antenna Array System for Uplink Beamforming in LTE-A and 5G NR," Tesis doctoral, Universitat Politècnica de València, 2019. doi: 10.4995/Thesis/10251/129852.

[37] J. S. Herd and M. D. Conway, "The Evolution to Modern Phased Array Architectures," Proc. IEEE, vol. 104, no. 3, pp. 519–529, Mar. 2016, doi: 10.1109/JPROC.2015.2494879.

[38] C. Fulton, M. Yeary, D. Thompson, J. Lake, and A. Mitchell, "Digital Phased Arrays: Challenges and Opportunities," Proc. IEEE, vol. 104, no. 3, pp. 487–503, Mar. 2016, doi: 10.1109/JPROC.2015.2501804.

[39] G. He, X. Gao, and R. Zhang, "Impact Analysis and Calibration Methods of Excitation Errors for Phased Array Antennas," IEEE Access, vol. 9, pp. 59010–59026, 2021, doi: 10.1109/ACCESS.2021.3073222.

[40] M. A. Salas-Natera, R. M. Rodriguez-Osorio, L. de Haro Ariet, and M. Sierra-Perez, "Novel Reception and Transmission Calibration Technique for Active Antenna Array Based on Phase Center Estimation," IEEE Trans. Antennas Propagat., vol. 65, no. 10, pp. 5511–5522, Oct. 2017, doi: 10.1109/TAP.2017.2738067.

[41] R. Lebron, J. D. Dıaz, and J. L. Salazar-Cerreno, "A Procedure to Characterize and Predict Active Phased Array Antenna Radiation Patterns from Planar Near-Field Measurements," In 2018 AMTA Proceedings, pp. 1–4, 2018.

[42] M. Yeary, D. Conway, J. Herd, M. Fosberry, M. Harger, and K. Hondl, "A least mean squares approach of iterative array calibration for scalable digital phased array radar panels," in 2013 IEEE International Symposium on Phased Array Systems and Technology, Waltham, MA, USA: IEEE, Oct. 2013, pp. 276–278. doi: 10.1109/ARRAY.2013.6731841.

[43] H. Singh, H. L. Sneha, and R. M. Jha, "Mutual Coupling in Phased Arrays: A Review," International Journal of Antennas and Propagation, vol. 2013, pp. 1–23, 2013, doi: 10.1155/2013/348123.

[44] M. A. Salas Natera, R. Martinez Rodriguez-Osorio, L. De Haro Ariet, and M. Sierra Perez, "Calibration Proposal for New Antenna Array Architectures and Technologies for Space Communications," Antennas Wirel. Propag. Lett., vol. 11, pp. 1129–1132, 2012, doi: 10.1109/LAWP.2012.2215952.

[45] M. A. Salas-Natera, R. M. Rodriguez-Osorio, and L. De Haro, "Procedure for Measurement, Characterization, and Calibration of Active Antenna Arrays," IEEE Trans. Instrum. Meas., vol. 62, no. 2, pp. 377–391, Feb. 2013, doi: 10.1109/TIM.2012.2217662.

[46] J. Meng et al., "I/Q Linear Phase Imbalance Estimation Technique of the Wideband Zero-IF Receiver," Electronics, vol. 9, no. 11, Art. no. 11, Nov. 2020, doi: 10.3390/electronics9111787.

[47] Y.-G. Lim, Y. J. Cho, T. Oh, Y. Lee, and C.-B. Chae, "Relationship Between Cross-Polarization Discrimination (XPD) and Spatial Correlation in Indoor Small-Cell MIMO Systems," IEEE Wireless Commun. Lett., vol. 7, no. 4, pp. 654–657, Aug. 2018, doi: 10.1109/LWC.2018.2808346.

[48] A. J. Van Den Biggelaar, U. Johannsen, P. Mattheijssen, and A. B. Smolders, "Improved Statistical Model on the Effect of Random Errors in the Phase and Amplitude of Element Excitations on the Array Radiation Pattern," IEEE Trans. Antennas Propagat., vol. 66, no. 5, pp. 2309–2317, May 2018, doi: 10.1109/TAP.2018.2800519.

[49] Jeongheum Lee, Yongbeum Lee, and Hyeongdong Kim, "Decision of error tolerance in array element by the Monte Carlo method," IEEE Trans. Antennas Propagat., vol. 53, no. 4, pp. 1325–1331, Apr. 2005, doi: 10.1109/TAP.2005.844444.

[50] K. Kim, H. Yang, J. Jang, T. Sun, S. Choi, and J. Jung, "Online Calibration for LTE-Based Antenna Array System," International Journal of Antennas and Propagation, vol. 2016, p. e2645870, Nov. 2016, doi: 10.1155/2016/2645870.

[51] A. Nafe, K. Kibaroglu, M. Sayginer, and G. M. Rebeiz, "An In-Situ Self-Test and Self-Calibration Technique Utilizing Antenna Mutual Coupling for 5G Multi-Beam TRX Phased Arrays," in 2019 IEEE MTT-S International Microwave Symposium (IMS), Boston, MA, USA: IEEE, Jun. 2019, pp. 1229–1232. doi: 10.1109/MWSYM.2019.8701072.

[52] Y. Liu, "Multi-user Beamforming on Intelligent Reflecting Surface and Networks," Doctoral dissertation, University of Glasgow, 2022.

[53] S. Kutty and D. Sen, "Beamforming for Millimeter Wave Communications: An Inclusive Survey," IEEE Commun. Surv. Tutorials, vol. 18, no. 2, pp. 949–973, 2016, doi: 10.1109/COMST.2015.2504600.

[54] L. Ding, A. R. Vilenskiy, R. Devassy, M. Coldrey, T. Eriksson, and E. G. Strom, "Shannon Capacity of LOS MIMO Channels with Uniform Circular Arrays," in 2022 IEEE 33rd Annual International Symposium on Personal, Indoor and Mobile Radio Communications (PIMRC), Kyoto, Japan: IEEE, Sep. 2022, pp. 1–7. doi: 10.1109/PIMRC54779.2022.9977586.

[55] D. P. Palomar and J. R. Fonollosa, "Practical algorithms for a family of waterfilling solutions," IEEE Trans. Signal Process., vol. 53, no. 2, pp. 686–695, Feb. 2005, doi: 10.1109/TSP.2004.840816.

[56] M. A. Albreem, M. Juntti, and S. Shahabuddin, "Massive MIMO Detection Techniques: A Survey," IEEE Commun. Surv. Tutorials, vol. 21, no. 4, pp. 3109–3132, 2019, doi: 10.1109/COMST.2019.2935810.

[57] A. E. Zorkun, M. A. Salas-Natera, and R. Martínez Rodriguez-Osorio, "Improved Iterative Inverse Matrix Approximation Algorithm for Zero Forcing Precoding in Large Antenna Arrays," IEEE Access, vol. 10, pp. 100964–100975, 2022, doi: 10.1109/ACCESS.2022.3208155.

[58] D. H. Nguyen and T. Le-Ngoc, "MMSE precoding for multiuser MISO downlink transmission with non-homogeneous user SNR conditions," EURASIP Journal on Advances in Signal Processing, vol. 2014, no. 1, p. 85, Jun. 2014, doi: 10.1186/1687-6180-2014-85.

[59] "Difference between mimo and massive mimo," Telecom Trainer. Accessed: Mar. 11, 2024. [Online]. Available: https://www.telecomtrainer.com/difference-between-mimo-and-massive-mimo/

[60] T. Van Chien and E. Björnson, "Massive MIMO Communications," in 5G Mobile Communications, W. Xiang, K. Zheng, and X. Shen, Eds., Cham: Springer International Publishing, 2017, pp. 77–116. doi: 10.1007/978-3-319-34208-5_4.

[61] E. Nayebi, A. Ashikhmin, T. L. Marzetta, and H. Yang, "Cell-Free Massive MIMO systems," in 2015 49th Asilomar Conference on Signals, Systems and Computers, Nov. 2015, pp. 695–699. doi: 10.1109/ACSSC.2015.7421222.

[62] M. Xu, S. Zhang, C. Zhong, J. Ma, and O. A. Dobre, "Ordinary Differential Equation-Based CNN for Channel Extrapolation Over RIS-Assisted Communication," IEEE Commun. Lett., vol. 25, no. 6, pp. 1921–1925, Jun. 2021, doi: 10.1109/LCOMM.2021.3064596.

[63] R. Chen, M. Liu, Y. Hui, N. Cheng, and J. Li, "Reconfigurable Intelligent Surfaces for 6G IoT Wireless Positioning: A Contemporary Survey," IEEE Internet of Things Journal, vol. 9, no. 23, pp. 23570–23582, Dec. 2022, doi: 10.1109/JIOT.2022.3203890.

[64] M. Jian et al., "Reconfigurable intelligent surfaces for wireless communications: Overview of hardware designs, channel models, and estimation techniques," Intell. and Converged Netw., vol. 3, no. 1, pp. 1–32, Mar. 2022, doi: 10.23919/ICN.2022.0005.

[65] Y. Liu et al., "Reconfigurable Intelligent Surfaces: Principles and Opportunities," IEEE Communications Surveys Tutorials, vol. 23, no. 3, pp. 1546–1577, 2021, doi: 10.1109/COMST.2021.3077737.

[66] R. Alghamdi et al., "Intelligent Surfaces for 6G Wireless Networks: A Survey of Optimization and Performance Analysis Techniques," IEEE Access, vol. 8, pp. 202795–202818, 2020, doi: 10.1109/ACCESS.2020.3031959.

[67] N. T. Nguyen et al., Hybrid Relay-Reflecting Intelligent Surface-Aided Wireless Communications: Opportunities, Challenges, and Future Perspectives. 2021.

[68] H. U. Rehman, "Reconfigurable Intelligent Surface-Assisted Multi-User Wireless Communications Systems," Master Thesis, University of Manitoba, 2021.

[69] J. He, H. Wymeersch, and M. Juntti, "Channel Estimation for RIS-Aided mmWave MIMO Systems via Atomic Norm Minimization," IEEE Trans. Wireless Commun., vol. 20, no. 9, pp. 5786–5797, Sep. 2021, doi: 10.1109/TWC.2021.3070064.

[70] R. Schroeder, J. He, and M. Juntti, "Passive RIS vs. Hybrid RIS: A Comparative Study on Channel Estimation," in 2021 IEEE 93rd Vehicular Technology Conference (VTC2021-Spring), Apr. 2021, pp. 1–7. doi: 10.1109/VTC2021-Spring51267.2021.9448802.

3. Chapter 3: An Improved Hybrid Beamforming Algorithm for Fast Target Tracking Segment

3.1. Introduction

The smart antenna systems are still considered one of the main technologies, not only for modern wireless systems but also for next-generation communication systems such as SATCOM and 5G, B5G and 6G, especially in cases like non-terrestrial networks, accurate mapping with unmanned aerial vehicles or vehicle-to-thing tracking systems where it is necessary to direct the antenna beam to a specific target with high interference suppression [1]. In highly dense communication environments, where there are many communication ends, estimating the directions of each source with high accuracy is important and challenging since there exits extremely large number of RF interference signals. Therefore, it is hard to distinguish and track the desired signal sources or targets and to ensure seamless communication by transmitting signals at high speed. For these reasons, in cases where communication depends on the line-of-sight (LoS) component, smart antenna systems (SAS) using adaptive beamforming algorithms come into play [1].

The SAS consists of digital phased arrays to perform beamforming in order to accomplish interference suppression and fast tracking [2], [3], [4]. A large number of antenna elements and low-complexity adaptive beamforming algorithms fulfill these tasks [2]. In a SAS, adaptive beamforming algorithms generate weights for each antenna element in the arrays to direct the array radiation pattern to desired directions [2], [5]. By applying beamforming, the output signals from an antenna array are summed and the beam is directed precisely to the target. In the meantime, deep nulls are directed to undesired signal directions, and thus, interference suppression is performed. The adaptive beamforming algorithms work efficient, and the characteristic performances of different algorithms are almost identical under ideal conditions. However, non-ideal cases due to the highly dense complex communication environments, bring trade-offs in accordance with implementation costs and complexities [6], [7]. The performance characteristics of the systems are highly dependent on which adaptive beamforming is used in a particular scenario. Moreover, fast target tracking is a highly challenging task for SASs. Most likely, optimum results may not be achieved by using only one type of algorithm. Therefore, hybrid adaptive algorithms are proposed to achieve a higher convergence rate, better interference suppression, low steady-state noise, and fast target tracking. However, the performance metrics of algorithms depend not only on the adaptability of the algorithm but also on the adaptive parameters in the algorithm. In order to develop and improve an application specific hybrid beamforming algorithm, first, the performance metrics and trade-offs between the existing adaptive beamforming algorithms must be evaluated.

Therefore, this chapter first introduces a tool with user friendly graphical user interface (GUI) which was developed in MATLAB® environment. This tool provides a set of real-time interactive experiments for adaptive beamforming algorithms in antenna array processing subject. The developed tool is useful to understand the impact of using different mathematical algorithms including time reference, spatial reference and blind beamforming algorithms, as well as the implication of the processing required for the detection of the direction of arrival (DoA). In addition, with use of the developed tool it is possible to analyze the impact of mutual coupling, gain/phase uncertainties in the active antenna arrays, the array geometry and windowing on both beamforming and DoA algorithms.

As a result of the analysis made in this prepared tool, many algorithms were compared and thus the trade-offs between the algorithms were obtained in a shorter time. An improved hybrid constant modulus (CM) recursive least squares (RLS) beamforming algorithm with adaptive forgetting factor and variable regularization factor for fast target tracking was developed in line with the information obtained from the analysis. The sliding-window technique is applied to the proposed algorithm to mitigate the steady-state noise. The proposed algorithm is compared with existing RLS based algorithms in terms of convergence, convergence rate, and computational complexity. The proposed algorithm was compared with its counterparts in satellite and vehicle-to-thing (V2X) communication scenarios. Moreover, the multi-user case was also evaluated for the proposed algorithm.

3.2. Main Contributions

The main contributions of this chapter are summarized as follows:

- An adaptive beamforming algorithm application tool was prepared to evaluate the trade-offs between different adaptive beamforming and DoA algorithms as well as to analyze the impact of mutual coupling, gain/phase uncertainties in the active antenna arrays, the array geometry and windowing on those algorithms. It should be noted that the tool has been implemented with use-cases into laboratory and gamification sessions in the contents of the subject From Array Processing to MIMO systems (APMC) which is a Master level course with 6 ECTS. This course covers the two main multiple antenna fields that are antenna array processing and MIMO systems including radiofrequency technologies.
- An improved hybrid constant modulus RLS beamforming algorithm with adaptive forgetting factor and variable regularization factor is proposed based on low-complexity robust adaptive moment estimation method (ADAM) update for forgetting factor with sliding-window technique. The proposed algorithm has superior target tracking, convergence rate, interference and steady-state noise suppression than the state-of-the art beamforming algorithms.

3.3. Adaptive Beamforming Algorithm Application Tool

The main purpose of the prepared tool is to help to improve the perceptions on adaptive beamforming algorithms by quickly visualizing the expected performance of the different algorithms under varying conditions. It is considered that a tool is useful way to comprehend the adaptive beamforming algorithm for any level of knowledge on adaptive beamforming and DoA algorithms. The designed application structure is given in Fig. 3.1.

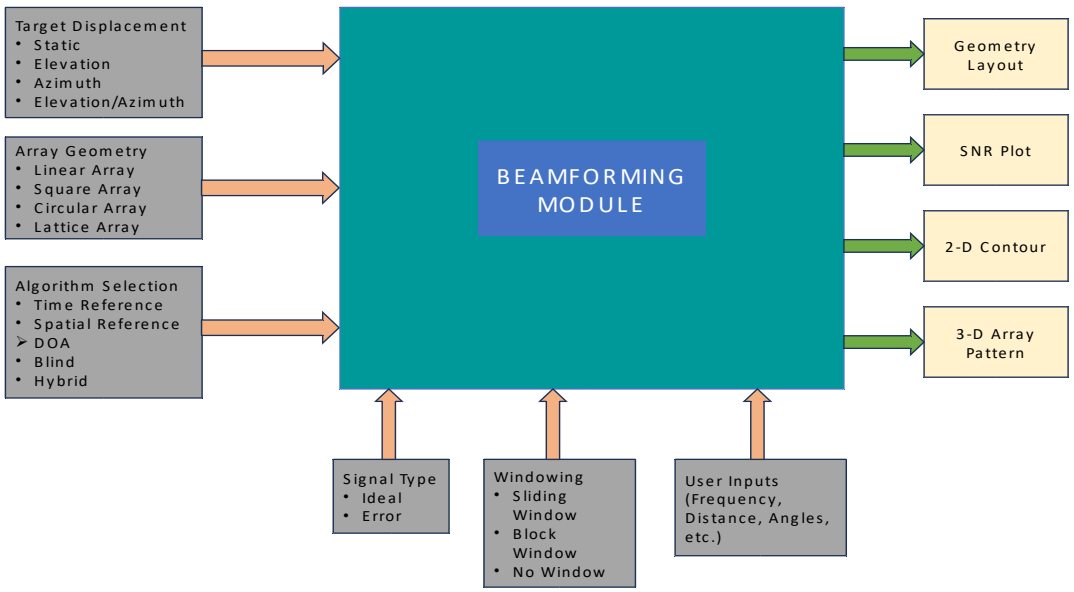

Fig. 3.1. General structure of the tool.

The prepared tool is initialized with default parameters and with default selections. However, the application allows users to change the parameters and the selections upon their requests. The main screen of the prepared tool with initialized default values, is given in Fig. 3.2. In the first part, the movement of the source can be selected as either static or dynamic. Multiple options for dynamic source are available as displacement only in elevation, displacement only in azimuth or displacement in both elevation and azimuth. In addition, users can define the angular speed and track time. In the next part, the geometry of the array can be selected. There are four common types of available as linear array, square planar array, circular planar array and triangular lattice array. Then, array properties can be defined as number of elements in the antenna array, operating frequency, spacing between the antenna elements in terms of wavelength. In the signal type part, Users can define elevation and azimuth angles of the source and the interferences with their power levels in terms of dB with respect to the source. Ideal and error signals are available for the simulations. If the error signal is selected the adaptive beamforming algorithms consider the mutual coupling effects and the array manifolds according to the model in [8], [9], [10], [11] otherwise, the random generated signal is

employed. Moreover, users can introduce extracted s-parameters files which can be generated in CST or other antenna simulation software to get more realistic results.

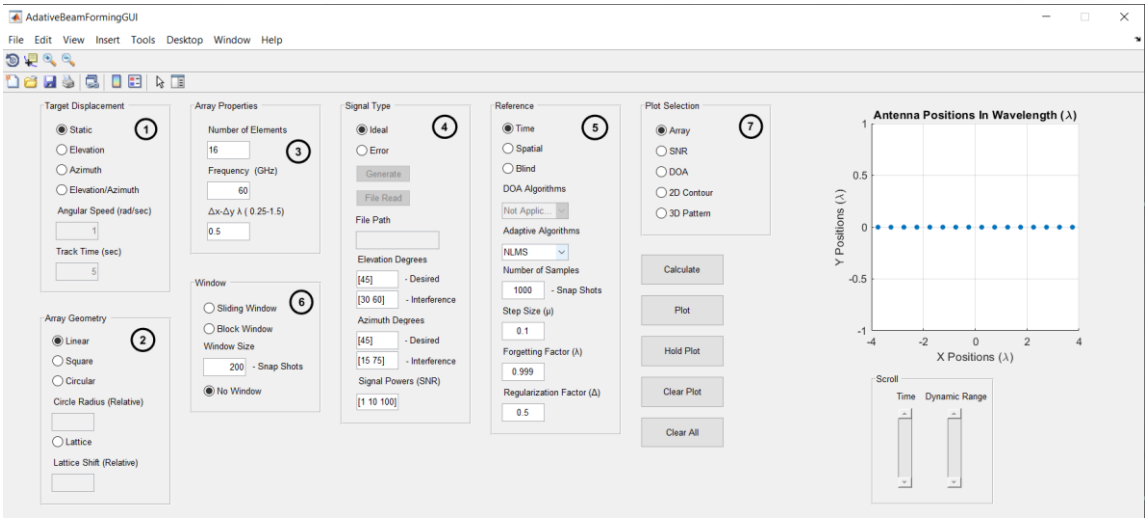

Fig. 3.2. Main screen: 1) Target displacement, 2) Array geometry selection, 3) Array properties, 4) Signal type selection, defining source and interference, 5) Selection of DoA and adaptive beamforming algorithms, auxiliary user inputs, 6) Windowing selection, 7) Plot selection.

In the reference part, users can choose adaptive beamforming algorithms from among three different algorithm type. In addition, auxiliary inputs such as step size for iterative algorithms least mean squares (LMS), forgetting factor and regularization factor for RLS and number of signal samples can be defined by users. Finally, in the window part, users can choose between a sliding window or a block window to implement windowing on the adaptive beamforming algorithm of their choice. Once all the inputs are provided properly, users should click the “calculate” button to get the optimum weights.

In order to observe the performances of the adaptive beamforming algorithms virtually, a plot selection is reserved for the user. In section, selected array configuration can be plotted. Signal-to-noise ratio (SNR) performances of the adaptive beamforming algorithms can be plotted or by clicking the “Hold Plot” button several SNR performances of the algorithms can be plotted. On the other hand, spatial resolutions of the DOA algorithms can also be plotted. By using the 2-D contour option users can easily examine where interference and source fall into the plot. The 3-D pattern plotting option is provided, thus, users can observe whether the main beam is directed to desired direction after the beamforming algorithm applied. Finally, there is a time scroll which allow users to observe changes in beam direction over time and the other scroll is for dynamic range.

The tool is simple to use even for those lack of smart antenna theory. Including the usage of the tool, some experimental studies have been prepared to improve perception of adaptive beamforming algorithms and the theory of smart antennas. Moreover, remote

access to the tool via local network access is possible and users can also provide data from real signals measured then used emulating the system response.

3.4. Use Cases and Trade-Offs

The adaptive beamforming algorithms can be used in various cases and scenarios such as in low-earth-orbit (LEO) and V2X communication systems. Moreover, the connection between several systems is possible via adaptive beamforming algorithms. The suitability of the adaptive algorithm can be evaluated by the prepared GUI by entering the parameters which are defined by the prerequisites of the system. Fig. 3.3 shows the general use cases of adaptive beamforming algorithms.

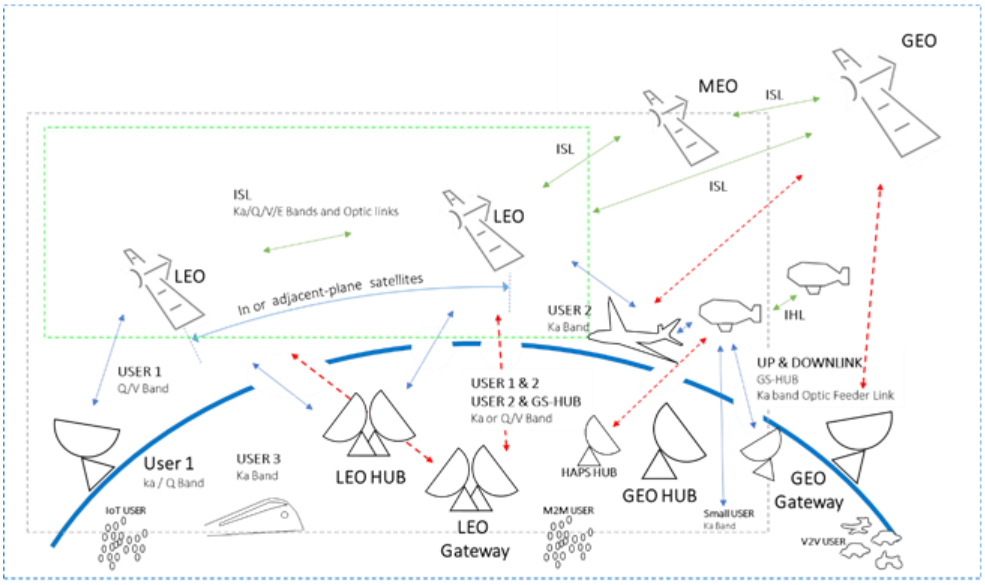

Fig. 3.3. Several use cases of adaptive beamforming algorithms [12].

The adaptive beamforming algorithms work highly efficient under ideal conditions. Absence of any interferences and with the sufficient number of signal samples, the performances of different algorithms are almost the same. In non-ideal cases there are trade-offs in accordance with convergence, convergence speed, interference cancelling and target tracking.

Signal-to-noise ratio (SNR): The SNR is a crucial performance metric for the adaptive beamforming algorithms. Adaptive algorithms tend to converge to an optimal value of SNR. The SNR level indicates how close an algorithm is to form the beam in the desired direction. The SNR comparison over the number of signal samples between different types of adaptive algorithms and unit output beamforming, can be done without any presence of interference.

The SNR comparison over the number of signal samples between different types of adaptive algorithms and unit output beamforming, can be done without any presence of interference. The parameters for the results in Fig. 3.5 (a) are given in Table 3-I. .

Convergence Rate: The convergence rate has a crucial role if the intended processing time is low. Simply, it indicates the number of signal samples required for the adaptive beamforming algorithm to reach the steady-state.

The parameters for the results in Fig. 3.5 (b) are given in Table 3-II.

Table 3-II. Inputs for the SNR and convergence rate comparison.

Algorithms	Units	NLMS, RLS, GSLC-RLS, CMA
Displacement	-	Static
Array	-	Square
# of Elements	-	16
Frequency	GHz	60
Spacing	λ	0.5
Signal Type	-	Ideal
Source Elevation	degree	45
Source Azimuth	degree	45
Signal Power	dBm	0
# of Samples	-	2000
Step Size	-	0.005
Forgeting Factor	-	0.999
Regularization Factor	-	0.5
Plot Option	-	SNR

Interference Cancelling: In reality, the presence of interference signals is unavoidable in most cases. The impinging interference signals must be suppressed to properly direct the beam in the desired direction. In order to provide seamless communication and distinguish the users from the undesired signal sources, interference suppression is an important feature for the adaptive beamforming algorithms. Especially, in global navigation satellite systems (GNSS) and monitoring systems interference cancelling plays major role as depicted in Fig. 3.4.

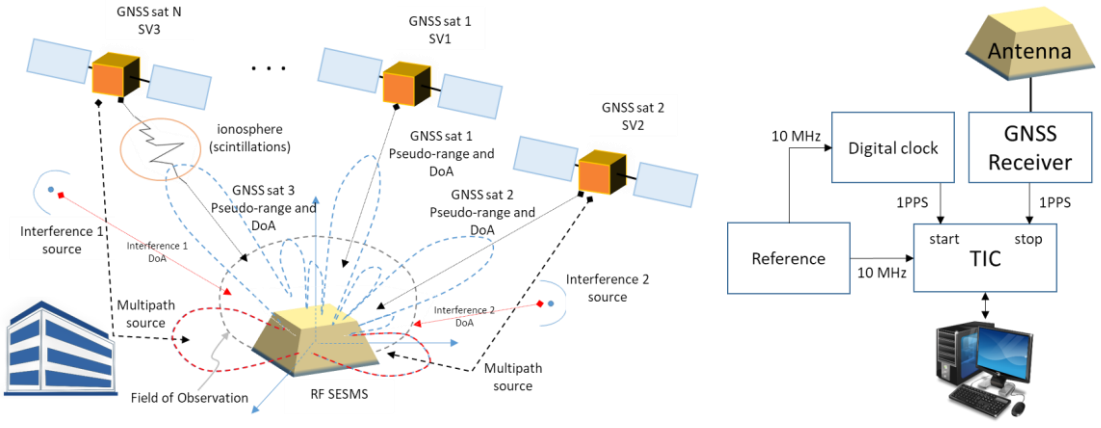

(a) **(b)**

Fig. 3.4. GNSS reference (a) and monitoring station (b) [12].

The interference suppression performance of the any kind of adaptive beamforming algorithms is different and might be considered as the main feature to make a trade-off. The RLS algorithm, the generalized side-lobe canceller RLS (GSLC-RLS) algorithm, the constant modulus algorithm (CMA), and the least squares-CMA (LS-CMA) can be compared to observe interference cancelling performances of different types of adaptive beamforming algorithms. The parameters for the results in Fig. 3.5 (c) are given in Table 3-III. Inputs for the interference cancelling comparison.

Table 3-III. Inputs for the interference cancelling comparison.

Algorithms	**Units**	**RLS, GSLC-RLS, CMA, LS-CMA**
Displacement	-	Static
Array	-	Square
# of Elements	-	16
Frequency	GHz	60
Spacing	λ	0.5
Signal Type	-	Ideal
Source Elevation	degree	45
Source Azimuth	degree	45
Inter. Elevation	degree	30, 60
Inter. Azimuth	degree	15, 75
Signal Power	dBm	0, -10, -20
# of Samples	-	2000
Step Size	-	0.005
Forgeting Factor	-	0.999

Target Tracking: The target tracking is another crucial key point for the adaptive beamforming algorithms since the users are not stationary in real scenarios. In order to maintain the quality and more importantly, continuity of the signal transmission, the adaptive beamforming algorithms must be able to dynamically direct beams to users.

In order to observe the target tracking capabilities of the adaptive beamforming algorithms in Fig. 3.5 (d) the RLS algorithm, the GSLC-RLS algorithm and the LS-CMA can be compared by using the input parameters in Table 3-IV.

Table 3-IV. Inputs for the target tracking comparison.

Algorithms	Units	RLS, GSLC-RLS, LS-CMA
Displacement	-	Elevation
Angular Speed	deg./sec.	5
Track Time	sec.	5
Array	GHz	Square
# of Elements	λ	16
Frequency	-	60 GHz
Spacing	λ	0.5
Signal Type	-	Ideal
Source Elevation	degree	45
Source Azimuth	degree	45
Inter. Elevation	degree	30, 60
Inter. Azimuth	degree	15, 75
Signal Power	dBm	0, -10, -20
# of Samples	-	2000
Step Size	-	0.005
Forgeting Factor	-	0.999
Regularization Fac.	-	0.5
Plot Option	-	SNR

Sample results from the trade-offs case for comparing SNR, convergence rate, interference cancelling, and target tracking are given in Fig. 3.5. According to Fig. 3.5 (a) and (b), it can be seen that the SNR performances of RLS and CMA algorithms are similar, followed by GLSC-RLS, and NLMS has the lowest SNR level in steady-state. On the other hand, CMA has the fastest convergence rate. Convergence rates of RLS and GSLC-RLS are almost similar since they share almost the same algorithm structure and NLMS has poor convergence rate which makes it impractical for fast tracking scenarios such as V2X communication.

According to Fig. 3.5 (c), the convergence performances of RLS, GSLC-RLS and LS-CMA show that the interference are mitigated, however, the CMA fails to converge. The CMA only depends on the output signal where there is no information for desired signal to distinguish the desired signal from interference. Hence, the CMA is impractical for scenarios such as non-terrestrial-networks LEO (NTN-LEO) where the multiple users and interference exist. On the other hand, the hybrid algorithm LS-CMA has the fast convergence property of CMA and interference cancelling property of LMS, hence, its performance is in-between.

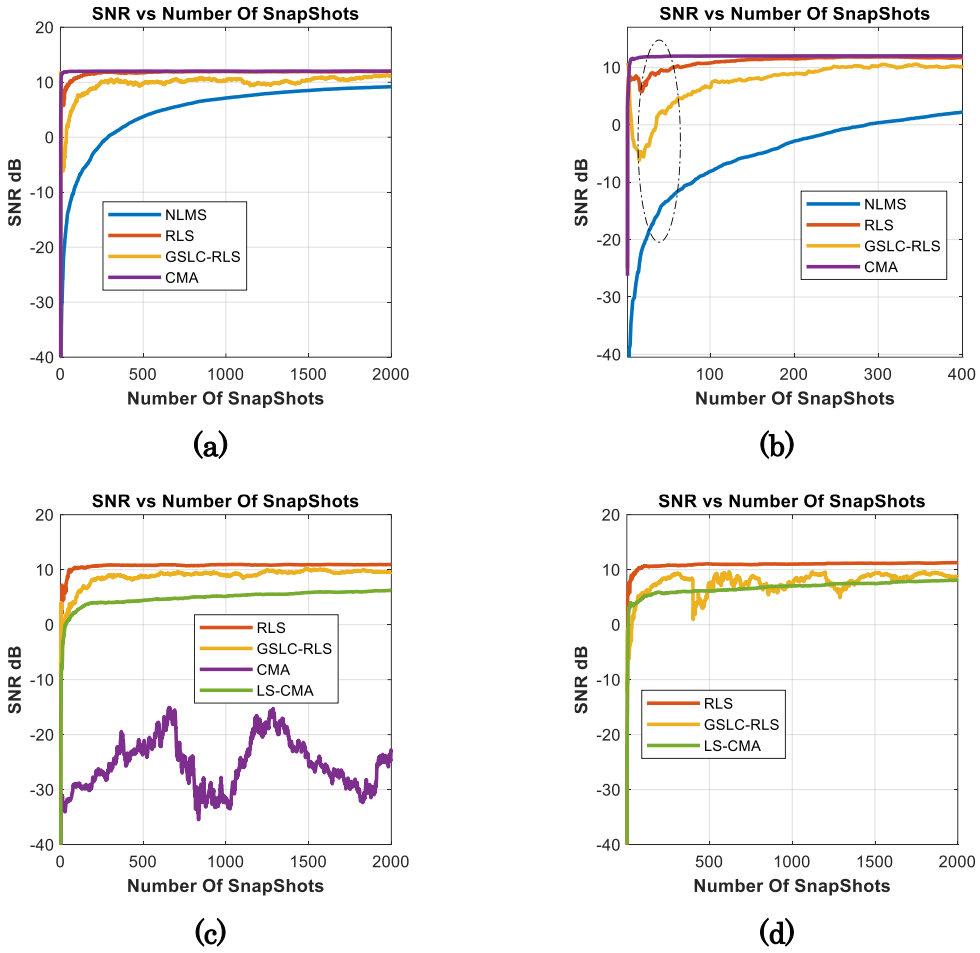

Fig. 3.5. Results of each case study of trade-offs, (a) SNR, (b) convergence rate, (c) interference cancelling (d) target tracking performance comparison of the selected beamforming algorithms.

Regarding GSLC-RLS algorithm, according to Fig. 3.5 (d), it has fast convergence rate and fair SNR level, the noise and ripples are high in the steady-state. High ripples and noise might cause losing the track of moving target and might lead algorithm to converge false angle direction. Finally, RLS and LS-CMA algorithms are compatible for fast tracking under prone to interference scenarios such as NTN-LEO and V2X communication.

3.5. An Improved Hybrid Beamforming Algorithm for Fast Target Tracking

In highly dense communication environments, adaptive algorithms by themselves may have some inadequacies, where, the hybrid adaptive algorithm is a concept of combining two or more different type of algorithms to achieve better convergence speed, noise reduction, and interference canceling at once, which would not be possible using only one type of algorithm [13]. In order to achieve fast convergence rate and target tracking as well as higher interference suppression, an improved hybrid adaptive beamforming

algorithm based on constant modulus algorithm (CMA) and recursive least squares (RLS) algorithm is proposed.

The CMA has ability to track without any training sequence, simple and has robust convergence [2]. However, it has slower convergence rate and its steady state error is large. In addition, blind algorithms including CMA are not capable of suppressing interference. On the other hand, RLS algorithm has faster convergence rate, more robust at steady state [14]. Unlike other algorithms, RLS has superior convergence performance as past examples are taken into account in calculating the weights [3]. The performance of RLS algorithm is depends on two parameters, the forgetting factor and the regularization factor. In the case of fast target tracking, the fixed and high value of forgetting factor makes the past samples more effective in calculating the weights and this causes the convergence rate degradation [7], [14]. Conversely, convergence also degrades if the forgetting factor is fixed and has a low value since the error contribution will be more. Besides, the regularization factor reduces the variance without causing the important data loss. However, if regularization parameter is fixed, after a certain number of samples, important data loss exists and convergence degradation occurs [7]. For the proposed algorithm, low-complexity adaptive moment estimation method (ADAM) based adaptive forgetting factor, and non-closed form variable regularization factors are adopted in RLS algorithm in order to achieve faster tracking ability and better convergence. The sliding window technique is also implemented to reduce the steady state noise [15].

The proposed algorithm is compared with revised state-of-the-art algorithms under various performance metrics in two different use cases: a) NTN-LEO and b) V2X. Both scenarios can be adapted to provide position data of ships and vessels in the port of Barcelona for docking traffic management, and can be adapted to provide location data of high-speed trains at Madrid Atocha railway station for the control of arrival and departure traffic. Fig. 3.6 and Fig. 3.7 illustrate the brief vehicle traffic in the port of Barcelona and at Madrid Atocha railway station, respectively. First, the performance characteristics of the proposed methods were investigated in single user scenarios and then, the performance of the proposed algorithm was analyzed in the multi-user case since in highly dense environments there might be tens of users.

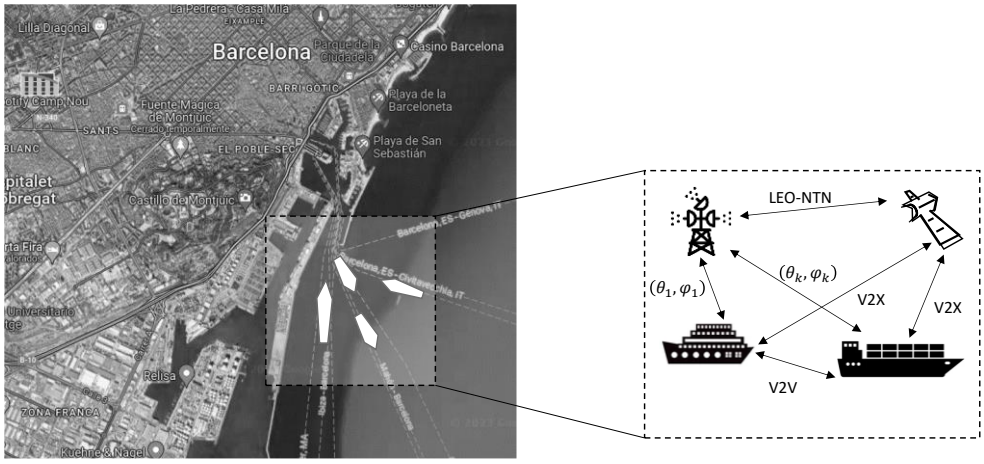

Fig. 3.6. Communication links between maritime radar tower, satellite and marine vessels for docking traffic management in the port of Barcelona.

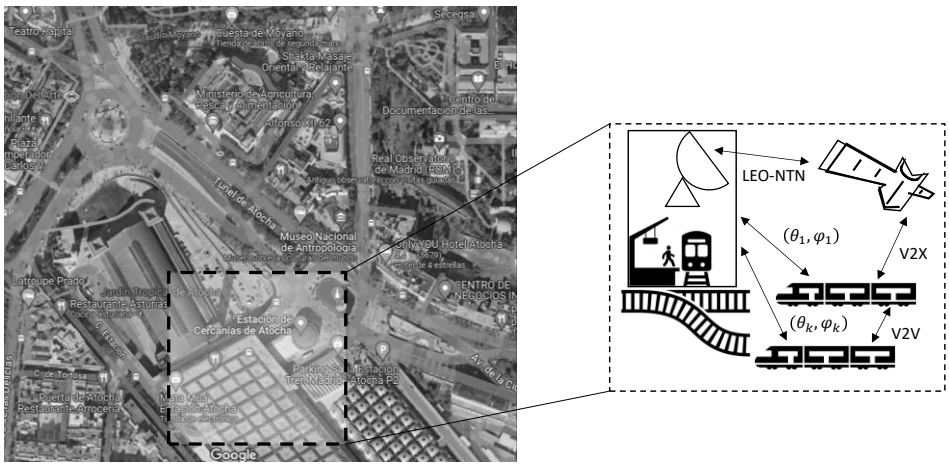

Fig. 3.7. Communication links between railroad controller, satellite and high-speed arriving trains for the control of arrival and departure traffic in the Madrid Atocha railway station.

3.5.1. System Model

This section explains the smart antenna system model that used in this study. We consider a receiver structure consist of M number of antennas serving K different signals. In our model, each antenna element receives k different user signals as $[s_1, s_2, \dots, s_k]$ and $K - k$ different interference signals as $[s_{k+1}, s_{k+2}, \dots, s_K]$, at the same time. The beamforming is applied in the receiver part. The user signals are digitally modulated, and multiplied by a same radio frequency (RF) carrier. In Fig. 3.8, a simple illustration of a smart antenna system is given.

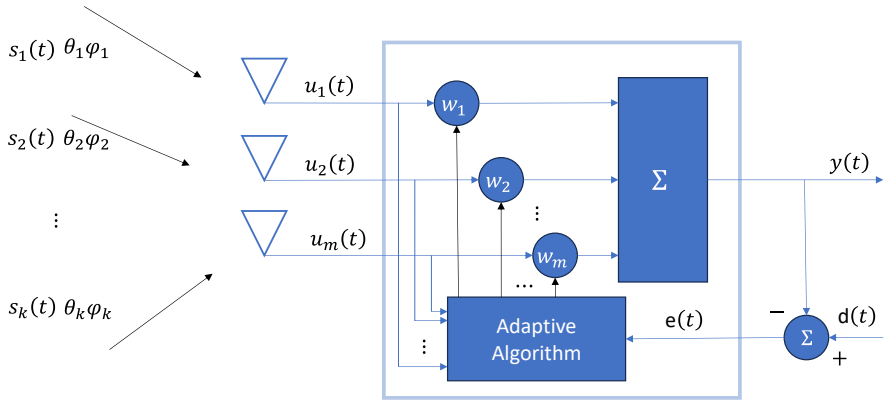

Fig. 3.8. Smart antenna system.

In this study, users are considered as moving signal sources and interference are considered as static signal sources. Displacement of a moving source in both elevation and azimuth with different angular speeds can be written as [16]:

$$\theta_k(t) = \theta_{0,\mathrm{k}} + c_k(t) \tag{3-1}$$

$$\varphi_k(t) = \varphi_{0,\mathrm{k}} + r_k(t) \tag{3-2}$$

where $\theta_k(t)\epsilon[0,\frac{\pi}{2})$ is the elevation angle of the source at time t, $\varphi_k(t)\epsilon[0,2\pi)$ is the azimuth angle of the source at time t, $\theta_{0,\mathrm{k}}$ (rad) is the initial elevation angle of the source and $\varphi_{0,\mathrm{k}}$ (rad) is the initial azimuth angle of the k-th source. Assuming the source has a linear motion model, then $c_k(t) = \omega_{1,\mathrm{k}}t$ and $r_k(t) = \omega_{2,\mathrm{k}}t$, where $\omega_{1,\mathrm{k}}$(rad/sec) and $\omega_{2,\mathrm{k}}$ (rad/sec) are angular velocities in elevation and azimuth angles of the k-th source, respectively. Considering a uniform rectangular array (URA) of M elements receiving K signals in total from both users and interference. We assume that desired and interference are multipath signals with L propagation paths. For brevity, L is the same for all signals. The received signal at the n-th element with Cartesian coordinates (x_m, y_m) at a time t can be formulated as:

$$u_m(t) = \sum_{k=1}^{K}\sum_{l=1}^{L} \alpha_{k,l}(t)s_k(t)\, e^{-j\frac{2\pi f}{c}\hat{r}_{k,l}\vec{r}_m} + n_m(t) \tag{3-3}$$

where $\alpha_{k,l}(t)\epsilon\mathbb{C}$ is the complex coefficient (amplitude) of the l-th path of the signal. The complex coefficients follow i.i.d. normal distribution $\mathcal{CN}(0,1)$, the phase of the n-th element is $\hat{r}_{k,l}\vec{r}_m = \left(x_n \sin\theta_{k,l}\cos\varphi_{k,l} + y_n \sin\theta_{k,l}\sin\varphi_{k,l}\right)$, c is the speed of light, f is the operating frequency, $n_m(t)$ is the additive white Gaussian noise and interelement spacing between two adjacent antenna element is $\lambda/2$ in both axis.

The impinging signal s_k in time t can be formulated as follows:

$$s_k(t) = a_k(t)b_k(t)\cos(2\pi f t) \tag{3-4}$$

where $b_k(t)\epsilon\{-1,+1\}$ is the BPSK modulated signal and $a_k(t)\epsilon\mathbb{C}$ is the complex amplitude of the carrier signal.

Then, the output signal $y(t)$ can be expressed as:

$$y(t) = \sum_{n=1}^{N} w_m^H(t)\, u_m(t) \tag{3-5}$$

where $w_m(t)\epsilon\mathbb{C}$ is the beamformer weighting coefficients in time t.

3.5.2. Constant Modulus Algorithm

The CMA exploits the constant modulus (CM) characteristic of the signal. The CMA seeks for a signal with constant magnitude and only detects signal with the greatest power. The CMA is given at below equations [17]:

$$y(n) = \boldsymbol{w}^H(n-1)\boldsymbol{u}(n) \tag{3-6}$$

$$e(n) = \frac{y(n)}{|y(n)|} - y(n) \tag{3-7}$$

$$\boldsymbol{w}(n) = \boldsymbol{w}(n-1) + \frac{\mu}{\|\boldsymbol{u}(n)\|^2}\boldsymbol{u}(n)e^*(n) \tag{3-8}$$

where n denotes the iteration, μ is the step-size and $e(n)$ is the error at n-th iteration.

3.5.3. Recursive Least Squares Algorithm

The RLS algorithm updates the weight vectors by taking into account the sum of the past least square errors. The RLS algorithm has high convergence rate since past samples effects are stored. The forgetting factor λ and the regularization factor Δ are the key parameters for the RLS algorithm. The RLS algorithm is given at below equations [17]:

$$\mathbf{P}(0) = \Delta^{-1}\begin{bmatrix} 1 & \cdots & 0 \\ 0 & \ddots & 0 \\ 0 & 0 & 1 \end{bmatrix}_{(M)\times(M)}, \qquad \mathbf{w}(0) = 0, \tag{3-9}$$

$$\boldsymbol{g}(n) = \frac{\lambda^{-1}\mathbf{P}(n-1)\boldsymbol{u}(n)}{1+\lambda^{-1}\boldsymbol{u}^H(n)\mathbf{P}(n-1)\boldsymbol{u}(n)} \tag{3-10}$$

$$e(n) = d(n) - \boldsymbol{w}^H(n-1)\boldsymbol{u}(n) \tag{3-11}$$

$$\boldsymbol{w}(n) = \boldsymbol{w}(n-1) + \boldsymbol{g}(n)e^*(n) \tag{3-12}$$

$$\mathbf{P}(n) = \lambda^{-1}\big(\mathbf{P}(n-1) - \boldsymbol{g}(n)\boldsymbol{u}^H(n)\boldsymbol{P}(n-1)\big) \tag{3-13}$$

where, N is the number of receiving antennas, $\mathbf{P}(n)$ is autocorrelation matrix of received signal samples and $\boldsymbol{g}(n)$ is the Kalman gain at i-th iteration.

3.5.4. Sliding Window

The sliding window technique is applied to adaptive beamforming algorithms in two steps. The first step is the update part and second step is the downdate part. In the update step, a new input sample $\boldsymbol{u}(n+1)$ is added, using $Z+1$ samples from $\boldsymbol{u}(n-Z+1)$ to $\boldsymbol{u}(n+1)$, where Z is the window size, and in the downdate step $\boldsymbol{u}(n-Z+1)$ is discarded to conserve the Z subsequent samples from $\boldsymbol{u}(n-Z+2)$ to $\boldsymbol{u}(n+1)$ [7]. As a simple example, the sliding window technique CMA is given as at below equations:

$$y_{ud}(n) = \boldsymbol{w}_{dd}^{H}(n-1)\boldsymbol{u}(n) \tag{3-14}$$

$$e_{ud}(n) = \frac{y_{ud}(n)}{|y_{ud}(n)|} - y_{ud}(n) \tag{3-15}$$

$$\boldsymbol{w}_{ud}(n) = \boldsymbol{w}_{dd}(n-1) - \frac{\mu}{\|\boldsymbol{u}(n)\|^2}\boldsymbol{u}(n)e_{ud}(n)^{*} \tag{3-16}$$

$$y_{dd}(n) = \boldsymbol{w}_{ud}^{H}(n)\boldsymbol{u}(n-\mathrm{Z}) \tag{3-17}$$

$$e_{dd}(n) = \frac{y_{dd}(n)}{\|y_{dd}(n)\|} - y_{dd}(n) \tag{3-18}$$

$$\boldsymbol{w}_{dd}(n) = \boldsymbol{w}_{ud}(n) + \frac{\mu}{\|\boldsymbol{u}(n)\|^2}\boldsymbol{u}(n-Z)e_{dd}^{*}(n) \tag{3-19}$$

where $y_{ud}(n)$ is update step output $e_{ud}(n)$ is update step error, $y_{dd}(n)$ is downdate step output and $e_{dd}(n)$ is downdate step at n-th iteration.

3.6. Proposed Algorithm

The proposed adaptive beamforming is the combination of CMA and RLS algorithm with adaptive forgetting factor and variable regularization factor implemented with sliding window technique.

In RLS, forgetting factor takes into account previous data and new data. The error may be increased and passed to the next iterations when the forgetting factor is constant and results in performance degradation, especially in fast target tracking. This problem is solved here by adapting the forgetting factor gradually. In this sense, we adapted adaptive moment estimation method (ADAM) [18] to update the forgetting factor at each iteration by running averages of both gradient and the second moment of the gradient of the according to the cost function $j(n) = \sum_{l=0}^{n} \lambda^{n-l}|e(n)|^2$. Adaptive forgetting factor based on ADAM can be expressed as following equations:

$$p(n) = \beta_1 p(n-1) + (n-\beta_1)\nabla_\lambda(n) \tag{3-20}$$

$$v(n) = \beta_2 v(n-1) + (1-\beta_2)\nabla_\lambda(n)^2 \tag{3-21}$$

$$\lambda(n) = \lambda(n-1) - \left[\mathrm{Re}\left\{\eta \frac{p(n)}{\sqrt{v(n)}+\xi}\right\}\right]_{\lambda_{min}}^{\lambda_{max}} \tag{3-22}$$

where β_1, β_2 $\epsilon(0,1]$, ξ is a small scalar to prevent division by 0, η is the step size and $\nabla_\lambda(n)$ is the gradient of the forgetting factor in each iteration calculated by taking the partial derivative of the $j(n)$ with respect to λ. The decay rate for the gradient, β_1, is typically selected as 0.9 to give high weighting to recent gradients. On the other hand, decay rate for the squared gradient, β_2, is typically selected as 0.999 to stabilize the estimate of variance by keeping the gradients for long-term [18], [19]. The gradient of the forgetting factor, $\nabla_\lambda(n)$, can be expressed as [20], [21]:

$$\nabla_\lambda(n) = \frac{dj(n)}{d\lambda} = -\frac{1}{2}\mathrm{E}[\boldsymbol{\psi}^H(n-1)\boldsymbol{u}(n)e^*(n) + \boldsymbol{u}^H(n)\boldsymbol{\psi}(n-1)e(n)] \tag{3-23}$$

where $\boldsymbol{\psi}(n) = \frac{d\boldsymbol{w}(n)}{d\lambda}$ and can be expressed as:

$$\boldsymbol{\psi}(n) = [\mathbf{I}_M - \boldsymbol{g}(n)\boldsymbol{u}^H(n)]\boldsymbol{\psi}(n-1) + \mathbf{S}(n)\,\boldsymbol{u}(n)e^*(n) \tag{3-24}$$

where $\mathbf{S}(n) = \frac{d\mathbf{P}(n)}{d\lambda}$ and can be expressed as:

$$\begin{aligned}\mathbf{S}(n) = \lambda(n-1)^{-1}[\mathbf{I}_M - \boldsymbol{g}(n)\boldsymbol{u}^H(n)]\mathbf{S}(n-1) + [\mathbf{I}_M - \boldsymbol{u}(n)\boldsymbol{g}^H(n)] + \\ \lambda(n-1)^{-1}\boldsymbol{g}(n)\boldsymbol{g}^H(n) - \lambda(n-1)^{-1}\mathbf{P}(n)\end{aligned} \tag{3-25}$$

The regularization parameter is important since noise variations can be very high when the fast target tracking is required. Practically, optimum regularization factor has no closed-form solution. However, optimal regularization factor can be approximated as follows [16]:

$$\Delta_{opt} \approx \frac{M\sigma_n^2}{\mathrm{tr}[\mathbf{R}_{\mathrm{uu}}]} \tag{3-26}$$

where σ_n^2 is noise variance, M is number of antennas and $\mathbf{R}_{\mathrm{uu}} \triangleq \boldsymbol{u}\boldsymbol{u}^H$.

Finally, the sliding windowing technique is adapted in our proposed method which contains downdating and updating procedures. Our proposed sliding window adaptive forgetting variable regularization factor CMARLS adaptive beamforming algorithm is, hereinafter, referred to as SW-AFVF-CMARLS to improve traceability. The proposed algorithm is given in Algorithm 1 as follows:

Algorithm 1 Proposed Algorithm (SW-AFVF-CMARLS)

Initialize: $\Delta^{-1}(0) = 0.5,\ \lambda(0) = 0.97, p(0) = v(0) = 0, \mu = \eta = 0.001, \xi = 10^{-6}, \beta_1 = 0.9, \beta_2 = 0.99,\ \mathbf{P}(0) = \Delta^{-1}(0)\mathbf{I}_N, \boldsymbol{w}_{RLS-dd}(0) = \boldsymbol{w}_{CMA-dd}(0) = \mathbf{0},\ \lambda_{min} = 0.96,\ \lambda_{max} = 0.999$

Input: **u**, **d,** N, M, Z.

Output: **w.**

for $n = 1$ *to* N **do**

//updating weights

$y_{ud}(n) = \boldsymbol{w}_{CMA-dd}^{H}(n-1)\boldsymbol{u}(n)$

$e_{CMA-ud}(n) = \dfrac{y_{ud}(n)}{|y_{ud}(n)|} - y_{ud}(n)$

$\boldsymbol{w}_{CMA-ud}(n) = \boldsymbol{w}_{CMA-dd}(n-1) - \dfrac{\mu}{\|\boldsymbol{u}(n)\|^2}\boldsymbol{u}(n)e_{CMA-ud}^{*}(n)$

$\boldsymbol{g}_{ud}(n) = \dfrac{\mathbf{P}_{dd}(n-1)\boldsymbol{u}(n)}{1 + \lambda^{-1}\boldsymbol{u}(n)^{H}\mathbf{P}_{dd}(n-1)\boldsymbol{u}(n)}$

$e_{RLS-ud}(n) = d(n) - \boldsymbol{w}_{CMA-ud}^{H}(n)\boldsymbol{u}(n)$

$\boldsymbol{w}_{RLS-ud}(n) = \boldsymbol{w}_{RLS-dd}(n-1) - \boldsymbol{g}_{ud}(n)e_{RLS-ud}^{*}(n)$

$\mathbf{P}_{ud}(n) = \lambda(n-1)^{-1}\left(\mathbf{P}_{dd}(n-1) - \boldsymbol{g}_{ud}(n)\boldsymbol{u}(n)^{H}\mathbf{P}_{dd}(n-1)\right)$

//updating forgetting factor

$\mathbf{S}(n) = \lambda(n-1)^{-1}[\mathbf{I}_M - \boldsymbol{g}_{ud}(n)\boldsymbol{u}^{H}(n)]\mathbf{S}(n-1) + [\mathbf{I}_M - \boldsymbol{u}(n)\boldsymbol{g}_{ud}^{H}(n)] + \lambda(n-1)^{-1}\boldsymbol{g}_{ud}(n)\boldsymbol{g}_{ud}^{H}(n) - \lambda(n-1)^{-1}\mathbf{P}_{ud}(n)$

$\boldsymbol{\psi}(n) = [\mathbf{I}_M - \boldsymbol{g}_{ud}(n)\boldsymbol{u}^{H}(n)]\boldsymbol{\psi}(n-1) + \mathbf{S}(n)\ \boldsymbol{u}(n)e_{RLS-ud}^{*}(n),$

$\nabla_{\lambda}(n) = -\dfrac{1}{2}\mathrm{E}[\boldsymbol{\psi}^{H}(n-1)\boldsymbol{u}(n)e_{RLS-ud}^{*}(n) + \boldsymbol{u}^{H}(n)\boldsymbol{\psi}(n-1)e_{RLS-ud}(n)]$

//apply ADAM algorithm

$p(n) = \beta_1 p(n-1) + (n - \beta_1)\nabla_{\lambda}(n)$

$v(n) = \beta_2 v(n-1) + (1-\beta_2)\nabla_{\lambda}(n)^2$

$\lambda(n) = \lambda(n-1) - \left[\mathrm{Re}\left\{\eta\dfrac{p(n)}{\sqrt{v(n)} + \xi}\right\}\right]_{\lambda_{min}}^{\lambda_{max}}$

//downdating weights

$y_{dd}(n) = \boldsymbol{w}_{CMA-ud}^{H}(n)\boldsymbol{u}(n - \mathrm{Z})$

$e_{CMA-dd}(n) = \dfrac{y_{dd}(n)}{\|y_{dd}(n)\|} - y_{dd}(n)$

$\boldsymbol{w}_{CMA-dd}(n) = \boldsymbol{w}_{CMA-ud}(n) + \dfrac{\mu}{\|\boldsymbol{u}(n)\|^2}\boldsymbol{u}(n-Z)e_{CMA-dd}^{*}(n)$

$\boldsymbol{g}_{dd}(n) = \dfrac{\mathbf{P}_{ud}(n)\boldsymbol{u}(n-Z)}{1 - \lambda(n-1)^{-1}\boldsymbol{u}(n-Z)^{H}\mathbf{P}_{ud}(n)\boldsymbol{u}(n-Z)}$

$e_{RLS-dd}(n) = d(n-Z) - \boldsymbol{w}_{CMA-ud}^{H}(n)\boldsymbol{u}(n-Z)$

$\boldsymbol{w}_{RLS-dd}(n) = \boldsymbol{w}_{RLS-ud}(n) + \boldsymbol{g}_{dd}(n)e_{RLS-dd}^{*}(n)$

$\mathbf{P}_{dd}(n) = \lambda(n-1)^{-1}\left(\mathbf{P}_{ud}(n) + \boldsymbol{g}_{dd}(n)\boldsymbol{u}(n-Z)^{H}\mathbf{P}_{ud}(n)\right)$

//update regularization factor

$\Delta(n) = \dfrac{M\sigma_n^2(n)}{\mathrm{tr}[(\boldsymbol{u}(n)\boldsymbol{u}(n)^{H})]} - \Delta(n-1)$

$\mathbf{P}_{dd}(n) = \mathbf{P}_{dd}(n-1) - \Delta(n)\mathbf{P}_{dd}(n)$

//final weights

$\boldsymbol{w} = \boldsymbol{w}_{RLS-ud}(n)$

end for

3.7. Simulation Results

The signal-to-noise plus interference ratio (SINR) is considered for one of the performance metrics, which can be calculated as follows [22]:

$$\mathrm{SINR}_n = \frac{\sigma_k^2(n)\left|\boldsymbol{w}_k^H(n)\mathbf{a}_k(n)\right|^2}{\boldsymbol{w}_k^H(n)\mathbf{R}_{int+n}(n)\boldsymbol{w}_k(n)} \tag{3-27}$$

where $\sigma_k^2(n)$ is the source signal power in iteration n, $\mathbf{a}_k(n) = [\hat{r}_k\vec{r}_1, \dots, \hat{r}_k\vec{r}_m, \dots, \hat{r}_k\vec{r}_M]^T$ is the actual steering vector of the desired signal in iteration n, $\boldsymbol{w}_n$ is the estimated weights in iteration n and $\boldsymbol{R}_{int+n}[t]$ is the interference-plus-noise covariance matrix in iteration n.

The SINR performance of the proposed algorithm SW-AFVF-CMARLS is compared with three different RLS algorithm under single user case. The SW-RLS is the conventional sliding window RLS algorithm with a fixed forgetting factor, SW-CMARLS is sliding window hybrid CMA and RLS algorithm with a fixed forgetting factor and sliding window variable regularization factor (SW-VRF-CMARLS) is the proposed sliding window variable regularization factor with a fixed forgetting factor in [16] extended with CMA. All algorithms are compared in two use cases: a) NTN connecting a ground station of LEO, and b) V2X. In both use cases, there are two static interference signals located at $\theta_{int1} = 40^o$, $\theta_{int2} = 60^o$ and $\varphi_{int1} = 30^o$, $\varphi_{int2} = 75^o$ in spherical coordinates and $L = 3$. The interference-to-noise ratios (INR) of interference signals are 10 dB. The step sizes in all related algorithms are, $\mu = \eta = 0.001$. Moreover, the forgetting factor, λ, for the SW-RLS, SW-CMARLS, SW-VRF-RLS is fixed and equals to 0.99 and regularization parameter, Δ, equals to 0.5. Additional parameters used in the simulations for the presented algorithm SW-AFVF-CMARLS (in both use cases) are given in Table 3-V.

Table 3-V. Simulation Parameters for SW-AFVF-CMARLS.

Parameters	Value
β_1, β_2	0.9, 0.99
Initial λ, Δ	0.97, 0.5
Initial p, v	0, 0
ξ	10^{-6}

In the case of NTN-LEO, the realistic parameters in [23] are used. In addition, the samples are considered to be collected per minute and the window length, Z, is set to 20 samples. In this case target (satellite) moves in elevation. The scenario lasts for 15 minutes and scanning of 44 degrees in elevation is done. Fig. 3.9 (a) shows the simulation results according to the parameters in Table 3-VI. for the NTN-LEO use case. First of all, SW-CMARLS has the worst performance and cannot converge. It can be seen that conventional SW-RLS algorithm worse convergence rate, almost 3 dB lower steady state gain than the proposed SW-AFVF-CMARLS and SW-VRF-CMARLS. In addition, the SW-RLS algorithm has the highest steady state noise since the regularization parameter is fixed. On the other

hand, according to Fig. 3.9 (a), our proposed SW-AFVF-CMARLS algorithm outperforms SW-RLS algorithm in terms of convergence rate, steady state gain and noise. In the case of V2X, the realistic parameters in [24] are used. In addition, the samples are considered to be collected per second and the window length, Z, is set to 20 samples. In this case target (vehicle) moves in elevation. The scenario lasts for 12 seconds and scanning of 60 degrees in elevation is done. Fig. 3.9 (b) shows the simulation results according to the parameters in Table 3-VII for the V2X use case. Similar results with the previous example are observed. The Fig. 3.9 (b) shows that the SW-AFVF-RLSCMA algorithm outperforms compared algorithms in terms of convergence rate, steady-state noise and SINR gain.

Table 3-VI. Parameters for the NTN-LEO Simulation.

Parameters	Units	Value
Satellite height	km	600
Minimum elevation angle	degree	40
Field of view	degree	44
Num. of Rx antennas, x-dim.	-	4
Num. of Rx antennas, y-dim.	-	4
Simulation time	min.	15
Displacement of satellite	deg./min.	≈2.9
Samples per minute	-	400

Table 3-VII. Parameters for the V2X Simulation.

Parameters	Units	Value
V2I Euclidean distance (initial)	m.	100 m.
Infrastructure to road distance	m.	≈70.71 m.
Vehicle velocity	km/h (m/sec.)	60 (≈16.6)
Minimum elevation angle	degree	30 deg.
Field of view	degree	60 deg.
Num. of Rx antennas, x-dim.	-	4
Num. of Rx antennas, y-dim.	-	4
Simulation time	sec.	12
Displacement of vehicle	deg./sec.	5
Samples per second	-	500

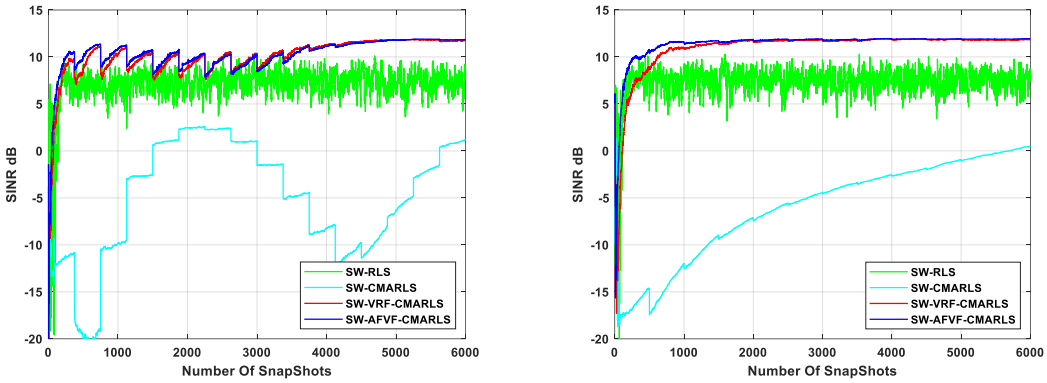

Fig. 3.9. (a) NTN-LEO use case SINR versus number of snapshots comparison (b) V2X use case SINR versus number of snapshots comparison.

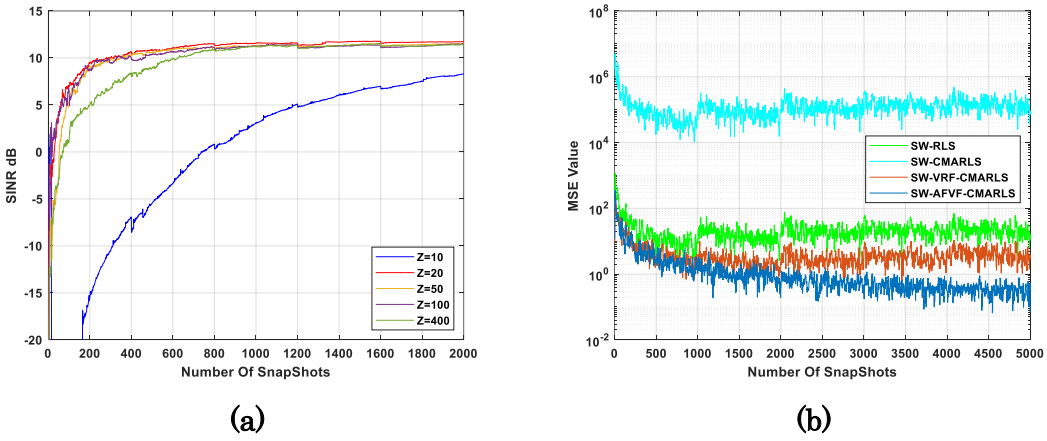

Fig. 3.10 (a) demonstrates the effect of window size on the convergence performance and convergence rate of the proposed algorithm. Iterations up to 2000 are given because it is sufficient for demonstration of the desired effect. It can be seen that $Z = 20$ is sufficient for a proper application. The optimal size of Z was found with trial-and-error method since there is no closed expression for the optimal window size.

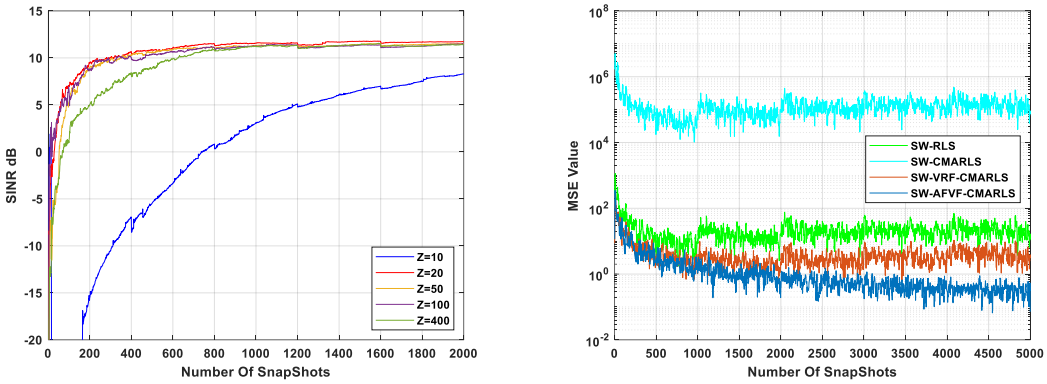

(a) (b)

Fig. 3.10 (b) shows the mean-square-error comparison of the proposed and state-of-the art algorithms revised. In MSE analyze, we consider the squared mean error between the ideal output signal whose weights are calculated using the Wiener optimal weight calculation and the estimated output signal whose weights are calculated using the proposed algorithm. The MSE between the ideal output signal and the estimated output signal is$\text{MSE} = \frac{1}{n}\sum_{i=1}^{n}(\hat{y}_n - y_n)^2$. It is clear that the proposed algorithms outperform all compared algorithms in terms of MSE at steady state by at least 10 times. The initial parameters of the ADAM algorithm are given in Table 3-V. The initial forgetting factor, λ, and the initial regularization factor, Δ, are 0.96 and 0.5, respectively. The related parameters for the

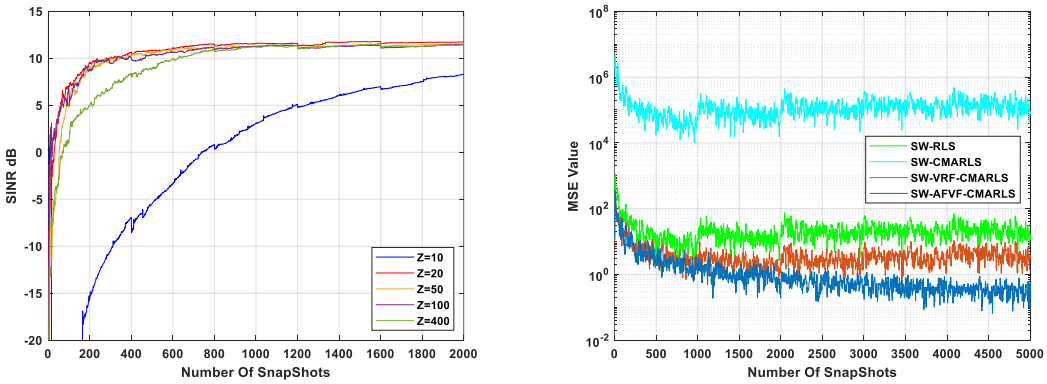

(a) (b)

Fig. 3.10 are given in Table 3-VIII.

Table 3-VIII. Parameter for the multi-user case simulations.

Parameters	Units	Value
Num. of Rx antennas, x-dim.	-	4
Num. of Rx antennas, y-dim.	-	4
Simulation time	sec.	5
Displacement of target	deg./sec.	1 (θ), 2(φ)
Samples per second	-	1000

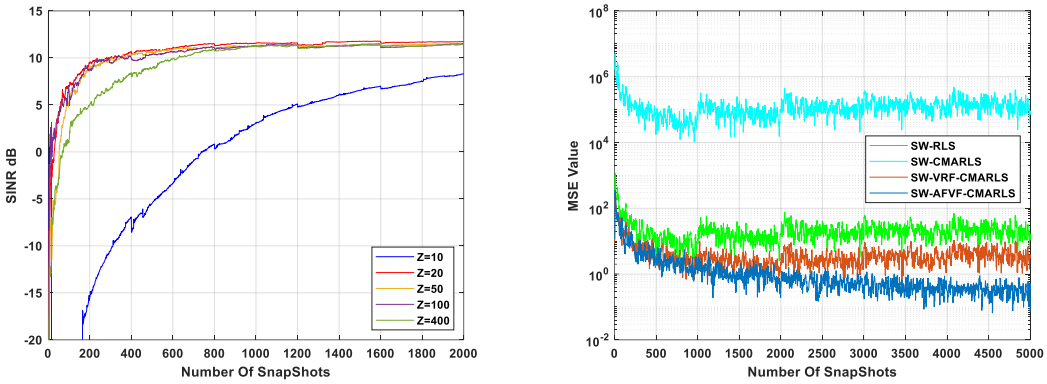

(a) (b)

Fig. 3.10. (a) window size, Z, effect on convergence and convergence rate, (b) MSE comparison.

The computational complexity analysis of the algorithms is given in Table 3-IX. In Table 3-IX, the complexity comparison of the algorithms is given with respect to the number of antennas in the antenna array. The computational complexity is calculated according to complex multiplications involved per iteration in the algorithms. The MUSIC [25] and Wiener optimal weights [26] are given for a better perception. The MUSIC algorithm involves high computational cost covariance matrix and eigen value decomposition and Wiener optimal involves high computational cost inverse matrix (computation is often inaccurate in hardware). The window size $Z = 20$ for MUSIC and Wiener optimal. The proposed algorithm has more complexity than the revised adaptive algorithms since more computations are involved to calculate the adaptive forgetting factor and variable regularization factor but the cost of better performance metrics. The related parameters for the Fig. 3.11 are given in Table 3-VIII.

Table 3-IX. Complexity analysis.

Algorithm	Complex Multiplications
SW-RLS	$5M^2 + 8M$
SW-CMARLS	$5M^2 + 14M$
SW-VRF-CMARLS	$8M^2 + 16M$
SW-AFF-CMARLS	$13M^2 + 18M$
MUSIC	$M^3 + MZ^3(N - Z) + M^2Z$
Wiener-Optimal	$M^3 + M^2Z + M^2$

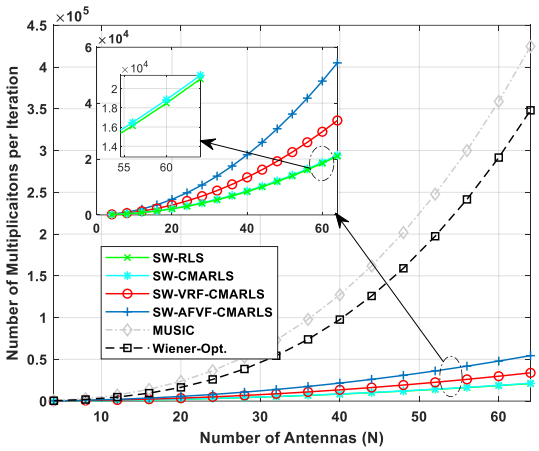

Fig. 3.11. Number of complex multiplications per iteration with respect to number of antennas.

In the second part of the analysis, after concluding that the proposed algorithm has better performance than its counterparts, the proposed SW-AFVF-CMARLS algorithm was tested in the multi-user case. In order to evaluate our proposed algorithms' robustness, we tested the proposed algorithm in more detail in the multi-user case.

In multi-user case analysis we considered four spatially uncorrelated different users. The users are, also, considered as moving sources as the previous examples, but with different angular speeds and there are two static interference signals. In order to get a better perception later in transmitted signal analyze, users are initially located at $\varphi_1 = 45^o$, $\varphi_2 = 135^o$, $\varphi_3 = 225^o$, $\varphi_4 = 315^o$ and $\theta_1 = \theta_2 = \theta_3 = \theta_4 = 45^o$, and $L = 3$. The static interference signals are located at $\varphi_5 = 30^o$, $\varphi_6 = 60^o$ and $\theta_5 = 90^o$, $\theta_6 = 180^o$ in spherical coordinates and $L = 3$. The interference-to-noise ratios (INR) of interference signals are 10 dB. For multiuser case analysis the step sizes are $\mu = \eta = 0.01$. Lastly, the window length, Z, is set to 75 samples. The initial parameters of the ADAM algorithm are given in Table 3-V. The initial forgetting factor, λ, and the initial regularization factor, Δ, are 0.96 and 0.5, respectively. Each user has same angular speed and moves in azimuth coordinate only. Fig. 3.12 shows the SINR performance of the proposed algorithm with four users. The related parameters for the multi-user case are given in Table 3-VIII. Fig. 3.12 (a) shows that there is 6 dB loss at the steady state gain, according to the previous SINR analysis, however, it is expected since the same number of antennas are used for more users. Apart from the loss, the performance degradation related with the convergence rate can be observed. The reason is the algorithm needs to extract four different users' information from the same signal. Despite slight performance degradation the proposed SW-AFVF-CMARLS algorithm still has expectable convergence and convergence rate. We can conclude that the proposed algorithm can be used in multi-user case. Fig. 3.12 (b) shows the variations of the forgetting factor according to the number of iterations for each user. It should be noted that the forgetting factor value is given in Fig. 3.12 (b) for every 100

iterations. This is because, given the forgetting factor value for all iterations, the graph becomes very complex and hard to comprehend.

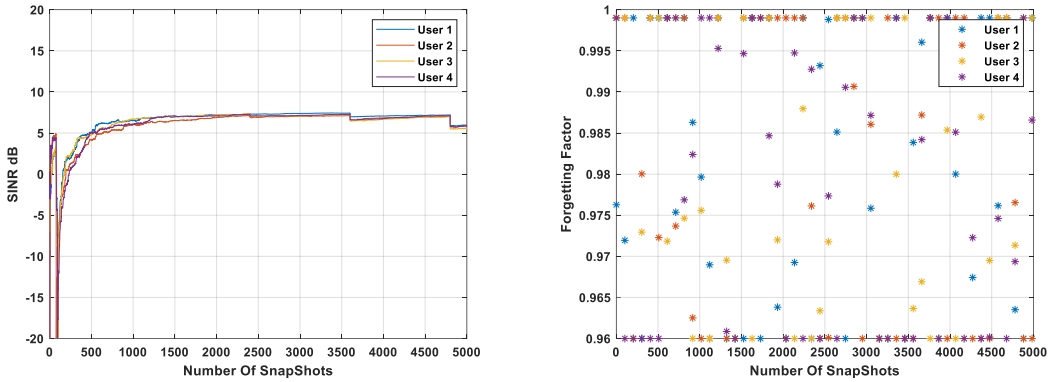

(a) (b)

Fig. 3.12. (a) SINR with respect to number of iterations, (b) forgetting factor variation of each user with respect to iteration number.

In Fig. 3.13, the normalized radiation pattern of the estimated transmitter signals is given. The purpose here is to demonstrate if the antenna array beams are correctly directed to each desired user direction, as well as with canceled interference signals, after 5 seconds (as specified as simulation time) with using our proposed SW-AFVF-CMARLS algorithm. In Fig. 3.13 (a), users and interference signals are located at their initial directions. Fig. 3.13 (b), after the proposed algorithm was applied, the directions of the users are given with suppressed interference. The interference free displacements of the users are clearly seen.

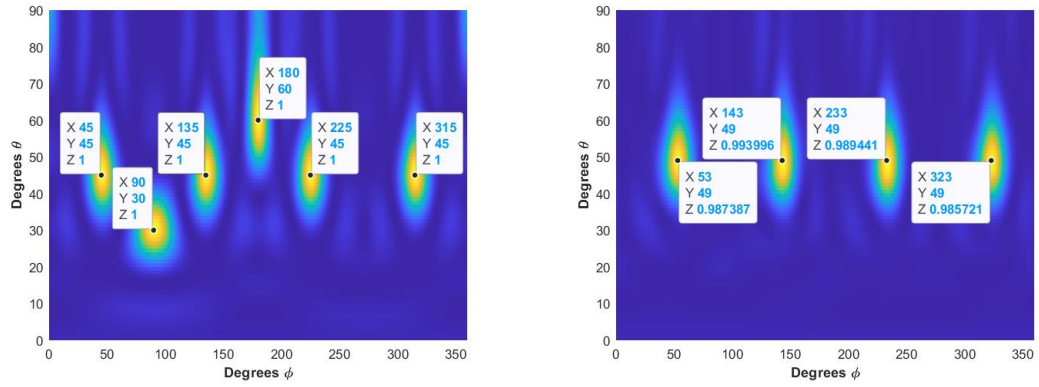

(a) (b)

Fig. 3.13. Users and interference directions (a) at initial, (b) estimated after applying the proposed algorithm.

As a remark, assuming that we have a satellite communication on the move (SOTM) terminal in the in the transmitting time of movement area with 30 GHz carrier and 30 MHz sampling frequency with a modulation coding (exp. DVB-S2) the proposed algorithm is able to obtain the relative position and angular velocity in ≅ 0.083 milliseconds of the trains in the same service area. Regarding Fig. 3.6 and Fig. 3.7, it is worth to mention that by using the proposed algorithm θ_k and φ_k can be obtained by NTN-LEO or V2X system. In addition, the proposed algorithm also reduces the estimation error of the relative position and angular velocity of trains in the service area by ≅ 10^5 times.

3.8. Conclusions

In order to increase perception on adaptive beamforming and DoA algorithms, a computer-aided application was prepared and the adaptive beamforming application tool is useful to enhance the knowledge on fundamentals of array processing and smart antenna theory. The prepared tool is an open-source for the course under Matlab® educational license and so many more algorithms can be added and can be simulated with different signal models or array features. This is also important to highlight that with the different scenarios are analyzed where system requirements can be verified with respect to the adaptive antenna system performance. As the students gain more experience and knowledge about adaptive beamforming algorithms, they can perform their own models and system analyses. The analyses were made on the trade-off of the adaptive beamforming algorithms in order to determine pros and cons time reference, spatial reference and blind adaptive algorithms. In line with the outcomes of the analyses an improved hybrid beamforming algorithm was developed.

The proposed algorithm exploits the fast convergence rate of RLS and high convergence of CMA. The finite memory is also taken into account to reduce the steady state noise by sliding-window technique. Besides, ADAM method was introduced to adaptively update the forgetting factor. The proposed algorithm was evaluated under two use cases, NTN-LEO and V2X respectively, and compared with the conventional RLS and other two different RLS-based algorithms. Results demonstrate that our proposed algorithm outperforms its counterparts in terms of convergence rate, steady state gain and noise when the variable forgetting factor is used. In addition, the performance of the proposed algorithm was analyzed in multi-user tracking scenario. It can be concluded that the proposed algorithm can be used to track both fast moving single and multiple targets in interference environments. Based on the results, the proposed method has 3 dB SINR gain and far more less steady-state noise than the conventional sliding window RLS. The ripple is 5 dB for sliding window RLS and almost 0.1 dB for sliding window adaptive forgetting factor variable regularization factor CMA-RLS, however, has same performance with sliding window variable regularization factor CMA-RLS. On the other hand, the proposed algorithm has at least 2 times faster convergence than revised algorithms and outperform

all compared algorithms in terms of MSE at steady state by at least 10 times with the cost of only $8M^2 + 10M$ more complex multiplication. The next step for the future line will be to implement the proposed algorithm on a real-time processor and compare the measured results with simulation results.

3.9. References Chapter 3

[1] A. E. Zorkun, M. A. Salas-Natera, and R. M. Rodríguez-Osorio, "An Improved Hybrid Beamforming Algorithm for Fast Target Tracking in Satellite and V2X Communication," Remote Sensing, vol. 16, no. 1, Art. no. 1, Jan. 2024, doi: 10.3390/rs16010013.

[2] S. Kaur, N. Kumar, and S. Dubey, "Investigation of Adaptive Beam-forming Algorithms for Smart Antennas System," IOP Conf. Ser.: Mater. Sci. Eng., vol. 1033, no. 1, p. 012015, Jan. 2021, doi: 10.1088/1757-899X/1033/1/012015.

[3] S. W. Varade and K. D. Kulat, "Robust Algorithms for DOA Estimation and Adaptive Beamforming for Smart Antenna Application," in 2009 Second International Conference on Emerging Trends in Engineering & Technology, Dec. 2009, pp. 1195–1200. doi: 10.1109/ICETET.2009.194.

[4] P. R. Jeripotula, B. R. Naik, and R. Mudavath, "A Novel Hybrid Weighted Method-Based Beamforming for Sidelobe Level Reduction in Radar Applications," Arab J Sci Eng, vol. 47, no. 11, pp. 14133–14145, Nov. 2022, doi: 10.1007/s13369-022-06656-1.

[5] P. R. Jeripotula, "A novel algorithm design for adaptive beamforming in uniform linear array antenna," JMCMS, vol. 15, no. 3, Mar. 2020, doi: 10.26782/jmcms.2020.03.00008.

[6] H. Zhao et al., "MIMO signal processing for mode division multiplexing with RLSCMA algorithm," in 2014 13th International Conference on Optical Communications and Networks (ICOCN), Nov. 2014, pp. 1–3. doi: 10.1109/ICOCN.2014.6987077.

[7] H. Liu and Z. He, "A sliding-exponential window RLS adaptive filtering algorithm: Properties and applications," Signal Processing, vol. 45, no. 3, pp. 357–368, Sep. 1995, doi: 10.1016/0165-1684(95)00063-J.

[8] A. Antón Sánchez, "Statistical techniques and algorithms applied in satellite communications antenna arrays for direction of arrival estimation and calibration," PhD Thesis, Universidad Politécnica de Madrid, 2016. doi: 10.20868/UPM.thesis.42959.

[9] A. E. Zorkun, M. A. Salas-Natera, and R. Martinez Rodriguez-Osorio, "Improved Iterative Inverse Matrix Approximation Algorithm for Zero Forcing Precoding in Large Antenna Arrays," IEEE Access, vol. 10, pp. 100964–100975, 2022, doi: 10.1109/ACCESS.2022.3208155.

[10] M. A. Salas-Natera and Rodrez-Osorio, "Analytical Evaluation of Uncertainty on Active Antenna Arrays," IEEE Trans. Aerosp. Electron. Syst., vol. 48, no. 3, pp. 1903–1913, Jul. 2012, doi: 10.1109/TAES.2012.6237569.

[11] M. Salas-Natera, R. Martínez, L. De Haro, and M. Sierra Perez, "Novel Reception and Transmission Calibration Technique for Active Antenna Array Based on Phase

Center Estimation," IEEE Transactions on Antennas and Propagation, vol. PP, pp. 1–1, Aug. 2017, doi: 10.1109/TAP.2017.2738067.

[12] M. A. Salas Natera, "Chapter 2: Antenna Array Processing, section 2.4: hybrid algorithms and complexity, Subject: From Array Processing to MIMO Communications (APMC)," presented at the Academic course 2023/24. ETSIT-UPM, 2024.

[13] M. A. Salas-Natera, A. E. Zorkun, and R. M. Rodríguez-Osorio, "Computer-aided experimental studies for adaptive beamforming algorithms and array processing in engineering education," Computer Applications in Engineering Education, vol. n/a, no. n/a, p. e22741, doi: 10.1002/cae.22741.

[14] L. Shan, H. Chen, J. Luan, and J. Li, "Application of adaptive forgetting factor RLS algorithm in target tracking," in 2017 Chinese Automation Congress (CAC), Oct. 2017, pp. 1838–1843. doi: 10.1109/CAC.2017.8243067.

[15] M. Belge and E. L. Miller, "A sliding window RLS-like adaptive algorithm for filtering alpha-stable noise," IEEE Signal Processing Letters, vol. 7, no. 4, pp. 86–89, Apr. 2000, doi: 10.1109/97.833005.

[16] M. Mahadi, T. Ballal, M. Moinuddin, and U. Al-Saggaf, "A Recursive Least-Squares with a Time-Varying Regularization Parameter," Applied Sciences, vol. 12, p. 2077, Feb. 2022, doi: 10.3390/app12042077.

[17] Y. Xiao and J. Sun, "RLS CMA blind equalization with adaptive forgetting factor controlled by energy steady state," in 2016 9th International Congress on Image and Signal Processing, BioMedical Engineering and Informatics (CISP-BMEI), Oct. 2016, pp. 935–939. doi: 10.1109/CISP-BMEI.2016.7852845.

[18] Z. Fei, Z. Wu, Y. Xiao, J. Ma, and W. He, "A new short-arc fitting method with high precision using Adam optimization algorithm," Optik, vol. 212, p. 164788, Jun. 2020, doi: 10.1016/j.ijleo.2020.164788.

[19] D. P. Kingma and J. Ba, "Adam: A Method for Stochastic Optimization." arXiv, Jan. 29, 2017. Accessed: Apr. 23, 2024. [Online]. Available: http://arxiv.org/abs/1412.6980

[20] S. Lee, J. Lim, and K.-M. Sung, "A low-complexity AFF-RLS algorithm using a normalization technique," IEICE Electron. Express, vol. 6, no. 24, pp. 1774–1780, 2009, doi: 10.1587/elex.6.1774.

[21] S. Song, J.-S. Lim, S. Baek, and K.-M. Sung, "Gauss Newton variable forgetting factor recursive least squares for time varying parameter tracking," Electronics Letters, vol. 36, no. 11, pp. 1–2, 2000.

[22] Y. Chen, T. Le-Ngoc, B. Champagne, and X. Changjiang, "Recursive Least Squares Constant Modulus Algorithm for Blind Adaptive Array," Signal Processing, IEEE Transactions on, vol. 52, pp. 1452–1456, Jun. 2004, doi: 10.1109/TSP.2004.826167.

[23] M. Caus, A. Perez-Neira, and E. Mendez, "Smart Beamforming for Direct LEO Satellite Access of Future IoT," Sensors, vol. 21, no. 14, p. 4877, Jul. 2021, doi: 10.3390/s21144877.

[24] L. Montero, C. Ballesteros, C. de Marco, and L. Jofre, “Beam management for vehicle-to-vehicle (V2V) communications in millimeter wave 5G,” Vehicular Communications, vol. 34, p. 100424, Apr. 2022, doi: 10.1016/j.vehcom.2021.100424.

[25] H. Krim and M. Viberg, “Two decades of array signal processing research: the parametric approach,” IEEE Signal Processing Magazine, vol. 13, no. 4, pp. 67–94, Jul. 1996, doi: 10.1109/79.526899.

[26] B. Jalal, O. Elnahas, and Z. Quan, “Efficient DOA Estimation Under Partially Impaired Antenna Array Elements,” IEEE Trans. Veh. Technol., vol. 71, no. 7, pp. 7991–7996, Jul. 2022, doi: 10.1109/TVT.2022.3169404.

4. Chapter 4: An Improved Inverse Matrix Approximation Algorithm for Phased

4.1. Introduction

In many numerical and engineering applications such as image and signal processing [1], encryption [2] and control system analysis [3], it is common to solve the large sparse systems as [4], [5]:

$$\mathbf{Ax} = \mathbf{b}, \quad \mathbf{x}, \mathbf{b} \in \mathbb{C}^P \tag{4-1}$$

where $\mathbf{A} \in \mathbb{C}^{P \times P}$, is a large sparse complex valued matrix. A matrix which most of the elements are equal to zero is called sparse matrix. The computation of direct inversion for finding the solution for (4-1) is very difficult task with a high computational cost, especially if the dimensions of **A** is large [4], [5]. Moreover, large storage is required for the direct inversion [5]. On the other hand, in hardware the direct inversion usually leads inaccurate solutions since it involves division operator. For these reasons, the derivation of inverse matrix approximation algorithms has become inevitable. Iterative algorithms combining preconditioning techniques are considered the most effective way to approach the solution of (4-1) [5]. Lately, many iterative algorithms of different orders of convergence have been proposed to estimate the inverse of **A** or at least its generalized inverse such as Moore-Penrose inverse [4]. This type of iterative algorithms is usually reducing the calculation into matrix-matrix and matrix-vector multiplications and sums. In addition, some iterative algorithms use matrix decompositions, such as, LDU and QR to relief the computational load and increase the accuracy. The inverse matrix approximation algorithms which only consist of multiplications and sums have been derived based on the limit to the infinity of the formula below:

$$(\mathbf{I} - \mathbf{A})^{-1} = (\mathbf{I} + \mathbf{A} + \mathbf{A}^2 + \mathbf{A}^3 + \mathbf{A}^4 + \cdots + \mathbf{A}^p) \tag{4-2}$$

where **I** is the $n \times n$ identity matrix and p is the order.

Along with the iterative inverse matrix approximation algorithms, there are also truncated number series approximation algorithms based on the polynomial expansions. The most widely used truncated number series algorithm is the Neumann [6] series, since it has a very simple hardware implementation. Although the Neuman series is favourable in terms of complexity, its convergence and accuracy are insufficient. On the other hand, the Taylor [7] and Kapteyn series [8] have better convergence and accuracy but at the cost of higher computational complexity. In addition, rapid matrix inversion updates are required in many applications such as on-line calibration of antenna arrays or instantaneous precoding in massive MIMO systems. However, the inverse matrix update

slows down as the polynomial terms of the truncated number series increase. Moreover, the computation of the optimal coefficients of the matrix polynomial with the smallest possible number of terms places a higher burden on hardware [9]. Thus, many practical applications adopt the iterative algorithms which have implementation facility, faster convergence rate, and have fair accuracy. In terms of approaches to the problem, iterative algorithms can generally be classified into three categories: approximate matrix inversion algorithms (AMIA), iterative approaches for solving linear equations (IASLE), and iterative algorithms for minimizing the residual norm (IMRN) [10].

4.2. Iterative Algorithms for Inverse Matrix Approximation

AMIA is derived from a truncated number series, such as Newton-Schulz iteration (NI) and Chebyshev iteration (CI) [11], [12]. The IASLE algorithm approaches the matrix inversion problem by solving the system equation, and the optimal transmitted signal vector is calculated by applying iterative processes to decomposed matrix elements, such as the Gauss-Seidel (GS) algorithm and its derivative successive over-relaxation (SOR) algorithm [13]. Finally, IMRN algorithms focus on the minimization of the residual norm application order to bypass the approximate matrix inversion operations and directly find the transmitted signal vector, such as the conjugate residual (CR) algorithm (further improvement of the conjugate gradient algorithm) [14] and generalized minimal residual (GMRES) algorithm [15]. Moreover, iterative algorithms can be obtained by combining two or more algorithms, such as the joint CI and Neumann series (CI-NS) algorithms and the SOR-based approximate matrix inversion (SOR-AMI) algorithm [11]. Among the three types of iterative algorithms, the AMIA is the most inefficient. As the dimensions of the channel matrix increase, the number of polynomial terms or iterations increases to maintain the accuracy. Hence, the computational complexity of the algorithm increases significantly. It should be noted that the implementation complexity and computational complexity are different. Iterative algorithms have a trade-off between implementation complexity and convergence, as shown in Fig. 4.1. However, under inappropriate initial conditions, such as when the channel matrix is nonsymmetric, positive, definitive, and strictly diagonally dominant, many IASLE and IMRN algorithms fail to converge to a proper solution [10].

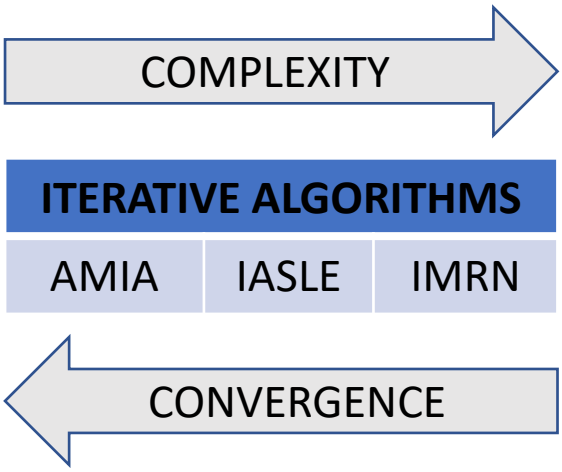

Fig. 4.1. Trade-off between implementation complexity and convergence of iterative algorithms.

The simple comparison of the various inverse matrix approximation algorithms is given in Table 4-I.

Table 4-I. Comparison of Iterative Algorithms [13].

Classification	Algorithm	Pros	Cons
AMIAZ	NI and CI	-If the optimal initial values adapted convergence is fast and accurate	-Optimal initial values are cumbersome to calculate
IASLE	GS	-If the number of transmitter and receiver antennas are equal it gives near-optimal solution	-Unable to implement on parallel computing structure -Includes matrix decomposition
	SOR	-If the ratio of BS antennas and user antennas, is large, it gives near optimal solution	-Unable to implement on parallel computing structure -Includes matrix decomposition -Relaxation parameter is uncertain
IMRN	CR	-If the ratio of BS antennas and user antennas, is large, it gives near optimal solution	-It requires a large number of iterations and initial vector is crucial for convergence
	GMRES	-Suitable for non-symmetric matrices and very robust	-Hard to implement and complexity rises linearly as the number of iterations increase

The three aforementioned types of algorithms require pre-computations for the optimal initial parameters to guarantee convergence. In general, one algorithm alone is not

sufficient to satisfy the convergence, fast convergence rate, and accuracy requirements. However, most algorithms proposed in the literature require initial conditions and an appropriate initial matrix, known as the precondition matrix to guarantee convergence. Hence, this section proposes a novel improved algorithm based on the combination of Homeier's cubically iterative algorithm [16] and the Karush-Kuhn–Tucker (KKT) constraint, [14] resulting in an approach different from Xia's iterative algorithm [17]. Thus, the proposed algorithm converges globally. The proposed algorithm is globally convergent, without the need for any preconditions, can use any square matrix without symmetry, and the initial matrix can be diagonally dominant. Hence, there is no need for any preconditions, and pre-computation is discarded. This has the advantage of processing nonsymmetric matrices and since there is no need to perform pre-computation, convergence rate in flexible condition is higher. The proposed algorithm was divided into two parts. The first part computes the initial approximation, whereas the second part processes the iterative generalized inverse matrix approach. The two parts are described as follows:

- *Initial approximation:* The first part of the algorithm was a three-step iterative algorithm based on Homeier's algorithm. However, in the third step, a secant approach was adopted to keep the polynomial order low to avoid a higher computational complexity [5]. After one iteration, the output of the three-step iterative algorithm was passed as an input to the second iterative algorithm. The second algorithm is based on iteratively approximating the generalized inverse using the KKT conditions [17]. If the KKT conditions hold for a problem, optimality is guaranteed [18]. The advantage of this algorithm is that no initial condition is needed for convergence because the Moore-Penrose rules hold for KKT [19]. Thus, nonsymmetric diagonally dominant matrix inverses can be computed more accurately without pre-computation to optimize the initial values. (see section 4.4.3)
- *Iterative generalize inverse matrix approach:* In the second part, there is typically a need for direct inversion of the acceleration scheme, as proposed in [17]. Otherwise, the convergence rate degrades as the dimensions of the input matrix increase. Hence, we replaced the direct inversion with a highly accurate iterative estimation algorithm. The need for a proper precondition matrix to guarantee the convergence of the iterative algorithm based on Homeier's algorithm in the literature is discarded here by applying KKT conditions, as in [17]. Thus, the proposed algorithm can be categorized as AMIA-type. (see section 4.4.2.1)

The proposed algorithm was evaluated for the zero-force precoding receiver in massive MIMO systems.

4.3. Main Contributions

In the ZF precoding algorithm, interference is forced to zero. The ZF precoding was selected because interference, rather than additive noise, is the dominant factor when the number of antennas at the BS increases [20]. The bit error rate (BER) and sum rate of the proposed algorithm were evaluated using both the correlated and uncorrelated channel models. One of the main focuses of this section was to evaluate and analyze the proposed algorithm under realistic conditions; thus, a new correlated channel model is considered. Referring to the channel model, a mutual coupling channel model [21] is used, including array manifolds, which are modelled as in, [22] and extended to massive MIMO. Array manifolds include manufacturing tolerances, active radio frequency (RF) element gain, phase variations, and mutual coupling, which are modelled using the k-nearest neighbor approach, as explained in detail in [22]. By contrast, the Rayleigh fading channel model was used for a simpler evaluation of the performance of the proposed algorithm. The main contributions of this chapter are summarized as follows:

- First, we propose a channel model that produces correlated channels, including mutual coupling, gain, and phase variances, caused by RF component errors and manufacturing tolerances. A model was developed to evaluate the performance of the proposed algorithm under realistic conditions.
- Second, we propose an improved approximate matrix inversion algorithm for the ZF precoding. The proposed algorithm always converges without depending on any initial conditions, and is suitable for correlated channel conditions.
- Finally, the performance of the proposed algorithm was evaluated with respect to different criteria, and its performance was compared with that of various iterative algorithms in the literature, as summarized in Based on these results, the effectiveness of the proposed algorithm was discussed.

4.4. Use Case: Zero-Forcing Precoding in Massive MIMO Systems

The densely numbered antenna structure of massive MIMO systems provides high transmission rate, spectral efficiency, and power efficiency [21], [23], [24]. However, a large number of antennas have drawbacks that must be carefully considered, such as pilot-signal contamination and interference at the base station (BS) and user equipment (UE) [23], [25], [26]. In massive MIMO systems, precoding algorithms are used to provide seamless signal transmission and interference cancellation [13].

Massive MIMO systems track the instantaneous state of a channel by using pilot signals. In this sense, channel state information (CSI) is used to mitigate channel impairments to optimize signal transmission at the BS through precoding. Precoding algorithms are

classified as linear or nonlinear. In terms of capacity, nonlinear precoding algorithms are superior to linear ones [27]. However, their complexities are considerably higher and their hardware implementation is costly. Thus, massive MIMO systems generally employ linear precoding algorithms [24].

4.4.1. System Model

We consider a downlink massive MIMO system in which M transmit antennas at the BS are employed to serve K single UEs. In our model, an encoder digitally modulates the transmitted signal **s**, and a precoder weights the information stream **x**, at the BS. Fig. 4.2 shows the massive MIMO system employed in this study.

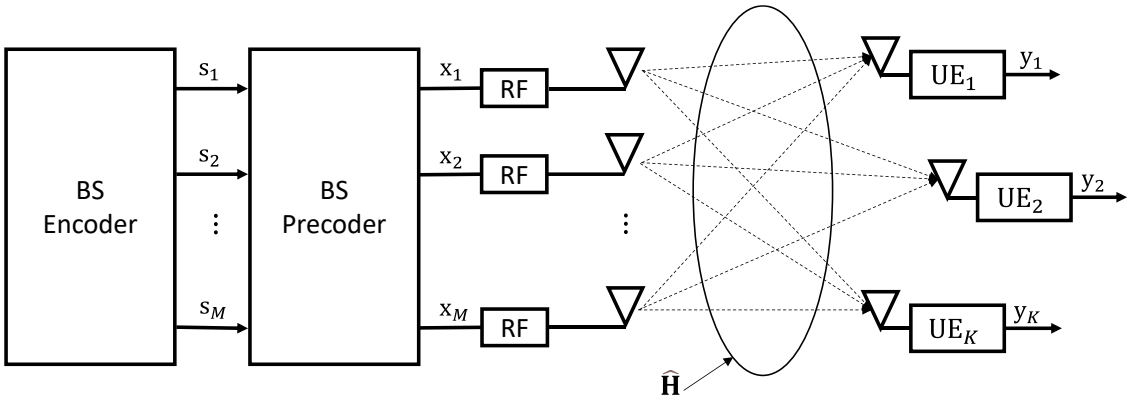

Fig. 4.2. Block diagram of massive MIMO system model with encoder and precoder.

We consider a mutual coupling channel model that includes an array manifold to create a more realistic channel model. The estimated imperfect channel between the antenna transmitter array and users is modelled as $\widehat{\mathbf{H}} \in \mathbb{C}^{K\times M}$ and can be expressed as:

$$\widehat{\mathbf{H}} = \sqrt{1-\tau^2}\widetilde{\mathbf{H}} + \tau\mathbf{v} \tag{4-3}$$

where $\tau \in [0,1]$ is a scalar parameter denoting the imperfection of channel estimation. When $\tau = 0$, perfect channel estimation is obtained. The estimated channel noise $\mathbf{v} \in \mathbb{C}^{1\times M}$ is independent and identically distributed over the real channel matrix $\widetilde{\mathbf{H}} = [\tilde{\mathbf{h}}_1, \tilde{\mathbf{h}}_2, \dots, \tilde{\mathbf{h}}_\mathrm{K}]$ which follows a Gaussian distribution with a zero mean and unit variance. The correlation coefficients of the real channel matrix $\widetilde{\mathbf{H}}$ are obtained according to the correlation channel model and can be expressed as:

$$\tilde{\mathbf{h}}_\mathrm{k} = \boldsymbol{\alpha_k}\mathbf{A}_k^H, \;\; k = 1,2,\dots,K \tag{4-4}$$

where $\boldsymbol{\alpha_k} = [\alpha_1, \alpha_2 \dots, \alpha_L]$ denotes the complex gains, which are independent and identically distributed i.i.d. complex Gaussian distributions with zero mean and unit variance, and L denotes the number of propagation paths of the incoming signals to the BS. $\mathbf{A}_k \in \mathbb{C}^{M\times L}$ is the array steering matrix of the BS antenna array and is given as follows:

$$\mathbf{A}_k = \left[\boldsymbol{a}\left(\theta_{\mathrm{M},1}, \varphi_{k,1}\right), \boldsymbol{a}\left(\theta_{\mathrm{M},2}, \varphi_{\mathrm{M},2}\right), \ldots, \boldsymbol{a}\left(\theta_{\mathrm{M,L}}, \varphi_{\mathrm{M,L}}\right)\right] \tag{4-5}$$

where $(\theta_{\mathrm{M}}, \varphi_{\mathrm{M}})$ are the L scattered i.i.d. uniformly distributed angles of arrival, with an angular spread of 5°, The BS steering vectors $\boldsymbol{a}(\theta, \varphi)$ can be calculated as follows:

$$\boldsymbol{a}(\theta, \varphi) = \frac{1}{\sqrt{M}} e^{-j\frac{2\pi}{\lambda}(x_m \sin\theta \cos\varphi + y_m \sin\theta \sin\varphi + z_m \cos\theta)}, \quad m = 1..M \tag{4-6}$$

where x_m and y_m are the m-th antenna coordinates in the x-y plane, $\lambda$is the wavelength of the carrier frequency, and M is the number of antennas in the antenna array.

To obtain a more realistic channel model, array errors including mutual coupling, antenna element gain/phase deviations, gain/phase deviations due the unequal RF chains and location errors are taken into account. The array manifold channel model $\mathbf{H} \in \mathbb{C}^{K \times M}$ is expressed as follows:

$$\mathbf{H} = \widetilde{\mathbf{H}} \Delta_{\mathrm{M}} \tag{4-7}$$

where $\Delta_{\mathrm{M}} \in \mathbb{C}^{M \times M}$ denotes the BS antenna array manifold, and, which considers the mutual coupling matrix. The array manifold matrix $\Delta(\theta, \varphi)$ is given [22] by:

$$\Delta(\theta, \varphi) = \mathbf{C}\left(\Delta \boldsymbol{G}_{RF} \Delta \boldsymbol{G}(\theta, \varphi) \Delta \boldsymbol{A}(\theta, \varphi)\right) \boldsymbol{G}_{RF}\left(g(\theta, \varphi) \odot \boldsymbol{a}(\theta, \varphi)\right) \tag{4-8}$$

where $\boldsymbol{G}_{RF}$, $\Delta \boldsymbol{G}_{RF}$, $\Delta \boldsymbol{A}(\theta, \varphi)$ and $\Delta \boldsymbol{G}(\theta, \varphi)$ are $M \times M$ diagonal matrices with complex elements represent each (θ, φ), is the gain of the RF circuit, and the effect of the gain and phase uncertainty sources due to the active antenna array components and antenna elements, respectively [22], [28]. In addition, $\boldsymbol{g}(\theta, \varphi) \in \mathbb{C}^{M \times 1}$ denotes the amplitude and phase of the m-th element, and $\boldsymbol{a}(\theta, \varphi) \in \mathbb{C}^{M \times 1}$ denotes the ideal steering vector of the array containing the information for each (θ, φ) [22]. The mutual coupling matrix $\mathbf{C} \in \mathbb{C}^{M \times M}$ consists of the amplitude and phase coupling coefficients $C_{m,k}$, k is the k-th neighbor of the antenna element m. The coefficient of mutual coupling $\mathbf{C}$ can be calculated as follows:

$$C_{m,k} = 1 + e^{-j\frac{2\pi}{\lambda}(x_m \sin\theta \cos\varphi + y_m \sin\theta \sin\varphi + z_m \cos\theta)}\left(\boldsymbol{a}_0^T \boldsymbol{s}_{(m)}\right) \tag{4-9}$$

where $\boldsymbol{a_0}$ is the steering vector that contains all the k-neighboring antenna elements of m-th antenna element, and $\boldsymbol{s}_{(m)} = [S_{1m}, \ldots, S_{mk}]$ is the $1 \times k$ vector of the scattering coefficients of the m-th antenna element.

The received complex baseband signal $\mathbf{y} \in \mathbb{C}^{K \times 1}$ is given as:

$$\mathbf{y} = \sqrt{\rho}\mathbf{H}\mathbf{x} + \mathbf{n} \tag{4-10}$$

where ρ is the normalized average transmit symbol energy by the number of transmit antennas, which denotes the signal-to-noise power ratio (SNR); $\mathbf{n} \in \mathbb{C}^{1 \times K}$ denotes the

additive white Gaussian vector; and $\mathbf{x} \in \mathbb{C}^{M\times 1}$ represents the transmitted signal vector after precoding and can be expressed as:

$$\mathbf{x} = \mathbf{G}\mathbf{s} \tag{4-11}$$

where $\mathbf{s} \in \mathbb{C}^{K\times 1}$ is the symbol vector of the constellation symbols to be transmitted and $\mathbf{G} \in \mathbb{C}^{M\times K}$ is the precoding matrix, which can be expressed as [12]:

$$\mathbf{G} = \beta\widehat{\mathbf{H}}^{H}\left(\widehat{\mathbf{H}}\widehat{\mathbf{H}}^{H}\right)^{-1} \tag{4-12}$$

where the scalar β is chosen to satisfy the equation $\|\mathbf{G}\|_F^2 = \mathrm{tr}(\mathbf{G}\mathbf{G}^H) = P$. The P is the total transmitted power. The BER and sum rate were considered as criteria for measuring the performance of the precoding algorithms.

After precoding, the sum-rate capacity [5] of the massive MIMO system can be calculated as:

$$\mathrm{C} = \sum_{k=1}^{K} \log_2(1+\gamma_k) \tag{4-13}$$

where $\gamma_k = \rho/K\,|g_{kk}|^2$, and g_{kk} is the k-th row and k-th column of matrix $\mathbf{G}$.

4.4.2. Linear Precoding Algorithms

Based on the diagonalisation of the entries in the Gramian matrix $\mathbf{W} = \widehat{\mathbf{H}}\widehat{\mathbf{H}}^{H}$, there are many proposed algorithms in the literature which find a solution for the inverse matrix, $\mathbf{W}^{-1}$ [13].

4.4.2.1. The Approximate Matrix Inversion Algorithms

Approximate matrix inversion algorithms are based on number series. These algorithms are derived from the higher-order recursions [29], which can be expressed as:

$$\mathbf{X}_{i+1} = \mathbf{X}_i(\mathbf{I}_\mathrm{K} + (\mathbf{I}_\mathrm{K} - \mathbf{W}\mathbf{X}_i) + \cdots + (\mathbf{I}_\mathrm{K} - \mathbf{W}\mathbf{X}_i)^{p-1}) \tag{4-14}$$

where i is the number of iterations, p is the order of the polynomial series, $\mathbf{X}_i \in \mathbb{C}^{K\times K}$ is the estimated inverse matrix when $i = 0$, $\mathbf{X}_0$ is defined as the preconditioning matrix when $i = 0$, and $\mathbf{I}_\mathrm{K}$ is an identity matrix of size K.

Neumann Series: The Neumann series (NS) are known as the simplest way for approximating the matrix inversion which also reduces complexity of the linear detector. The Gramian matrix is decomposed into $\mathbf{W} = \mathbf{D} + \mathbf{E}$, where $\mathbf{D}$ is the main diagonal matrix and $\mathbf{E}$ is the non-diagonal matrix, thus, NS expansion of $\mathbf{W}$ is expressed as [30]:

$$\mathbf{W}^{-1} = \sum_{i=0}^{\infty} (-\mathbf{D}^{-1}\mathbf{E})^{i}\mathbf{D}^{-1} \tag{4-15}$$

The polynomial expansion in (4-15) converges to the inverse of matrix, $\mathbf{W}^{-1}$ when

$$\lim_{i\to\infty} (-\mathbf{D}^{-1}\mathbf{E})^{i} = 0 \tag{4-16}$$

In practice, a finite number i is selected and as the number of iterations increases the accuracy of the solution increases at the cost of increased computational complexity. Although, the NS based algorithms reduces the computational complexity from $O(K^3)$ to $O(K^2)$ if the $i \leq 2$, their convergence rates are slow and mostly with the low number of iterations, results are inaccurate [13], [31].

Newton Iteration and Chebyshev Iteration Algorithms: The Newton algorithm converges to the inverse matrix when p = 2 [12] and if the inequality condition $\|\mathbf{I}_K - \mathbf{W}\mathbf{X}_0\| < 1$ is satisfied. The estimated inverse matrix at the i-th iteration can be expressed as:

$$\mathbf{X}_{i+1} = \mathbf{X}_i(2\mathbf{I}_K - \mathbf{W}\mathbf{X}_i) \tag{4-17}$$

Similarly, if $p = 3$ [29] and the same inequality condition for NI is satisfied, this algorithm is called the Chebyshev iteration, and can be expressed as:

$$\mathbf{X}_{i+1} = \mathbf{X}_i\big(3\mathbf{I}_K - \mathbf{W}\mathbf{X}_i(3\mathbf{I}_K - \mathbf{W}\mathbf{X}_i)\big) \tag{4-18}$$

The convergence of the approximate matrix inversion algorithms depends on the number of iterations i, the order p and as well as on the preconditioning matrix $\mathbf{X}_0$. A Better convergence can be achieved as the i and p increase with the cost of increased complexity. However, the initial values of the preconditioning matrix also affect the convergence and complexity. In [12] the optimized initial values of $\mathbf{X}_0$ were calculated for both the NI and CI algorithms, and it was shown that both algorithms had better convergence with the optimized values.

4.4.2.2. The Iterative Approaches for Solving Linear Equations

Iterative approaches for solving linear equations, solve $\mathbf{W}\mathbf{z} = \mathbf{s}$ to approximate a solution, where $\mathbf{z} \in \mathbb{C}^{K\times 1}$ is an unknown vector solution. First, the Gram matrix $\mathbf{W}$ is decomposed into its subcomponents, and then, an iterative process is applied to the decomposed parts of the $\mathbf{W}$.

Gauss-Seidel and Successive Over-Relaxation Algorithms: The GS and SOR algorithms are similar. The Gram matrix is decomposed into $\mathbf{W} = \mathbf{D} + \mathbf{L} + \mathbf{U}$, where $\mathbf{D} \in \mathbb{C}^{K\times K}$ is a diagonal matrix containing the diagonal elements of matrix $\mathbf{W}$, $\mathbf{L} \in \mathbb{C}^{K\times K}$contains the lower triangular components, and the $\mathbf{U} \in \mathbb{C}^{K\times K}$contains the upper triangular component matrix

W. Subsequently, the estimated transmitted signal vector **z** is computed iteratively using the decomposed components. The GS algorithm can be expressed as [13]:

$$\mathbf{z}_{i+1} = (\mathbf{D} + \mathbf{L})^{-1}(\mathbf{s} - \mathbf{U})\mathbf{z}_i \tag{4-19}$$

The SOR algorithm was derived from the GS algorithm with a slight difference. The iteratively calculated estimated transmitted signal vector **z** using the SOR algorithm is given as [11]:

$$\mathbf{z}_{i+1} = \left(\frac{1}{\omega}\mathbf{D} + \mathbf{L}\right)^{-1}\left(\mathbf{s} + \left(\left(\frac{1}{\omega} - 1\right)\mathbf{D} - \mathbf{U}\right)\mathbf{z}_i\right) \tag{4-20}$$

where ω denotes the relaxation parameter, which is crucial to the performance of the SOR algorithm. The relaxation parameter must be between $0 < \omega < 2$ to satisfy the convergence [13]. However, in [11], an optimized value for the relaxation parameter is given as:

$$\alpha_{opt} = 0.404e^{\left(-0.323\frac{M}{K}\right)} + 1.035 \tag{4-21}$$

In [11], the authors combined the SOR and approximate matrix inversion (AMI) algorithm proposed a joint SOR-AMI to increase the convergence of the SOR algorithm. Moreover, the authors combined the CI algorithm with the SOR-AMI and proposed a joint CI-SOR-AMI to increase the convergence rate. In the first step, one iteration is spared for the CI, and then the SOR-AMI is performed. The structure is similar to that of our proposed algorithm; however, the CI-SOR-AMI is highly dependent on the initial conditions and relaxation parameters.

4.4.2.3. The Iterative Algorithms for Minimizing Residual Norm

As mentioned previously, the IMRN algorithms focus on minimizing the residual norm rather than approximating a direct solution [13]. This type of algorithm directly estimates the transmitted signal vector without computing matrix inversion. In IMRN algorithms, the norm of the residual vector $\mathbf{r}_i$ is reduced until the desired tolerance is obtained or the direct solution of **z** is obtained.

Conjugate Residual Algorithm: The CR algorithm is derived from the well-known conjugate gradient (CG) algorithm to achieve better BER performance than the CG algorithm [13]. The CR algorithm can be expressed as [14]:

$$\alpha_i = \frac{\mathbf{r}_i^{\mathrm{T}}\mathbf{W}\mathbf{r}_i}{(\mathbf{W}\mathbf{p}_i)^{\mathrm{T}}\mathbf{W}\mathbf{p}_i} \tag{4-22}$$

$$\mathbf{z}_{i+1} = \mathbf{z}_i + \alpha_k \mathbf{p}_i \tag{4-23}$$

$$\mathbf{r}_{i+1} = \mathbf{r}_i + \alpha_i \mathbf{W}\mathbf{p}_i \tag{4-24}$$

$$\beta_i = \frac{\mathbf{r}_{i+1}^{\mathrm{T}}\mathbf{W}\mathbf{r}_{i+1}}{\mathbf{r}_i^{\mathrm{T}}\mathbf{W}\mathbf{r}_i} \tag{4-25}$$

$$\mathbf{p}_{i+1} = \mathbf{r}_{i+1} + \beta_i \mathbf{p}_i \tag{4-26}$$

$$\mathbf{W}\mathbf{p}_{i+1} = \mathbf{W}\mathbf{r}_{i+1} + \beta_i \mathbf{W}\mathbf{p}_i \tag{4-27}$$

where $\mathbf{z}_0$ denotes some arbitrary initial guess, $\mathbf{r}_0 = \mathbf{y} - \mathbf{W}\mathbf{z}_0$ and $\mathbf{p}_0 = \mathbf{r}_0$.

Generalized Minimal Residual Algorithm: In GMRES algorithm the residual vector r_i is defined as $r_i = Hz_i - y$ in GMRES algorithm. The solution vector $z_i \in \tau_i$, τ_i is a set that contains all linearly independent combinations of vectors, is given as [13]:

$$\boldsymbol{\tau_i} = \boldsymbol{span}\{\boldsymbol{y}, \boldsymbol{Hy}, \dots, \boldsymbol{H^{i-1}y}\} \tag{4-28}$$

In some cases, the vectors $\mathbf{y}, \mathbf{Hy}, \dots, \mathbf{H}^{i-1}\mathbf{y}$ are not fully linearly independent. Therefore, orthogonalization algorithms, such as Arnoldi and Householder algorithms, are applied to find orthonormal vectors to form an orthonormal basis [32]. The formulation of GMRES can be found in [15].

***Richardson Algorithm*:** The Richardson algorithm consists of vector operations and multiplication by the channel matrix **H**. The Richardson convergence rate of the Richardson algorithm slows down as the algorithm converges to the optimal solution. Similar to SOR algorithm a relaxation parameter, ω, has been introduced between $0 < \omega < \frac{2}{\lambda}$ for fast convergence rate, where$\lambda$is the largest eigenvalue of the symmetric positive definite matrix **H**. The Richarson algorithm is described as [33]:

$$\mathbf{x}_{i+1} = \mathbf{x}_i + \omega(\mathbf{y} - \boldsymbol{H}\mathbf{x}_i) \tag{4-29}$$

The initial solution vector $\mathbf{x}_0$ is the zero vector. The Richardson algorithm is simple, fast and hardware friendly. However, it requires the channel matrices to be symmetric matrices which is not the case in practical applications and degrades the convergence [13]. Moreover, Richardson algorithm requires large number of iterations to converge to the optimal solution.

***Lanczos Algorithm*:** This kind of algorithm uses Krylov subspace methods to large sparse linear equations. First, the orthogonal basis of the co-efficient matrix is constructed, then, the best solution with least residual which is orthogonal to Krylov subspace is found. As

the number of basis large Lanczos algorithm converges faster to the optimal solution. The iterative process of the Lanczos algorithm is given as [13]:

$$\mathbf{x}_{i+1} = \mathbf{Q}_{i+1}\mathbf{F}_i\mathbf{Q}_{i+1}^H\mathbf{W}\mathbf{x}_i + \mathbf{Q}_{i+1}\mathbf{F}_i\mathbf{Q}_{i+1}^H\mathbf{H}^H\mathbf{n} \tag{4-30}$$

where $\mathbf{Q}$ and $\mathbf{F}$ are the matrix formed by the orthogonal basis, and the tridiagonal matrix, respectively. The initial solution $\mathbf{x}_0$ is crucial as it is for all iterative algorithms, especially, GS and SOR algorithms. A possible initial solution can be introduced to Lanczos algorithm as [34]:

$$\mathbf{x}_0 = \mathbf{D}^{-1}\ddot{\mathbf{y}} \tag{4-31}$$

where $\mathbf{D}$ is the diagonal matrix where its non-zero entries are the diagonal entries of the $\mathbf{W}$ and $\ddot{\mathbf{y}} = \mathbf{H}^{-1}\mathbf{y}$.

The Lanczos algorithm is generally fast, converges well to the optimal solution, however, it either has low performance of requires high computational complexity under the time-varying channel. The detailed information about Lanczos algorithm can be found in [35].

Coordinate Descent Algorithm: The coordinate descent (CD) algorithm converges to the convex optimal solutions of the inverse of the large linear system at low complexity by coordinate-wise updates. The iterative process for the approximate solution can be given as [36]:

$$\mathbf{x}_k = (\|\mathbf{h}_k\|^2 + N_0)^{-1}\mathbf{h}_k^H\left(\mathbf{y} - \sum_{i\neq k}\mathbf{h}_i\,\mathbf{x}_i\right) \tag{4-32}$$

where N_0 is the noise variance and $\mathbf{h}_k$ is the k-th column of the channel matrix $\mathbf{H}$. The iterative process is performed sequentially for each user k where the new updated results are used immediately of the k-th user in subsequent steps. The iterative process is completed in K iterations, thus, depends on the number of users.

The coordinate descent algorithm has fast convergence, has superior performance in terms of hardware efficiency [37] and convergence, however, its drastically degrades in low SNR levels and susceptible to array uncertainties.

4.4.3. The Proposed Improved Iterative Three-Step Generalized Inverse Matrix Approximation Algorithm

A three-step generalized inverse matrix approximation (TSGIM) algorithm was proposed [38]. First, the system model determined the features required for the proposed algorithm. Unequal couplings and different gain/phase deviations in array manifold distort the conjugate symmetric matrix property of the gram matrix, $\mathbf{W}$. As mentioned previously, when algorithms deal with nonsymmetric positive definitive matrices, convergence cannot

be ensured. Among all algorithms, only GMRES offers a robust solution in this case. However, the implementation of the GMRES is extremely difficult and requires many restarts to ensure convergence. The computational complexity increases rapidly as the number of iterations increases. These drawbacks of GMRES make it reluctant to use it, and we propose an approximate matrix inversion algorithm; hence, matrix-vector operations are irrelevant to our case. Convergence, low complexity, and easy implementation are key requirements of approximation algorithms, which are commonly used to fulfill each other's inadequacies.

The AMIA has fast convergence, fair precision, and easy implementation but at the cost of increased computational complexity. Thus, in the first step, we selected a fifth-order ($p = 5$) three-step iterative algorithm based on (4-14). However, the computational complexity of the algorithm increased with the number of orders. In [5], a three-step iterative algorithm was proposed based on two-step cubically iterative Homeier and secant algorithms. The proposed three-step algorithm for solving any function that equals zero ($f(x) = 0$) is given as:

$$y_i = x_i - f'(x_i)^{-1} f(x_i) \tag{4-33}$$

$$z_i = x_i - \frac{1}{2} f(x_i)(f'(x_i)^{-1} + f'(y_i)^{-1}) \tag{4-34}$$

$$x_{i+1} = z_i - (f[z_i, x_i])^{-1} f(z_i) \tag{4-35}$$

where $f[z_i, x_i] = (z_i - x_i)^{-1}\big(f(z_i) - f(x_i)\big)$ is the two-point divided difference.

To iteratively approximate the matrix inversion, $f(x) = x^{-1} - \mathbf{W}$ was applied to the above equations. The iterative process can then be expressed as:

$$\mathbf{X}_{i+1} = \frac{1}{2}\mathbf{X}_i[9\mathbf{I}_K - \mathbf{W}\mathbf{X}_i(16\mathbf{I}_K - \mathbf{W}\mathbf{X}_i(14\mathbf{I}_K - \mathbf{W}\mathbf{X}_i(6\mathbf{I}_K - \mathbf{W}\mathbf{X}_i)))] \tag{4-36}$$

In the second part of the algorithm, we adopt a novel iterative algorithm to compute the generalized inverse matrix in [17]. It applies the KKT condition to minimize the Frobenius norm and iteratively solves the Moore-Penrose generalized inverse conditions [17] with vector-matrix multiplications. The KKT condition was used for the convex optimization of the Frobenius norm. In [17], an acceleration scheme that replaces vector-matrix multiplications with matrix-matrix multiplications was proposed. Unlike the algorithms in, the proposed solution does not require an initial precondition matrix, norm condition, or symmetric or conjugate symmetric matrix, as in the Newton and Chebyshev algorithms. It is important to highlight that their algorithm for the acceleration scheme uses a direct inversion matrix computation. Thus, the inverse matrix approximation problem has not been properly solved. The first part of the proposed algorithm replaces the direct inversion matrix using a robust iterative algorithm.

Computation of the initial values of the initial matrix allows for faster computation and easier implementation, as is the case with the proposed algorithm. However, the inverse matrix approximation algorithm must converge under any circumstances, such as uncertainties in the gain and phase as well as mutual coupling between adjacent antenna elements in a real implementation.

To adopt an iterative algorithm for computing the generalized inverse matrix, significant algorithms in the literature are based on the Moore-Penrose condition, [19] which denotes that for any matrix $\mathbf{A} \in \mathbb{C}^{a\times b}$, there exists only one matrix $\mathbf{P} \in \mathbb{C}^{b\times a}$ that satisfies the following equations:

$$\begin{cases} \mathbf{A} = \mathbf{APA} \\ \mathbf{P} = \mathbf{PAP} \\ (\mathbf{AP})^T = \mathbf{AP} \\ (\mathbf{XP})^T = \mathbf{XP} \end{cases} \tag{4-37}$$

where $\mathbf{P}$ is the generalized inverse of matrix $\mathbf{A}$. Subsequently, the generalized inverse problem can be solved by minimizing the Frobenius norm with equality constraints. The optimization problem for $a \geq b$ with solution $\mathbf{P}^*$ can be expressed as:

$$\begin{aligned} &minimize\ \frac{1}{2}\|\mathbf{P}\|_F^2 \\ &subject\ to\ \mathbf{A}^T\mathbf{AP} = \mathbf{A}^T \end{aligned} \tag{4-38}$$

Applying the KKT condition to (4-38), the optimum solution $\mathbf{P}^*$ exists if and only if $\mathbf{R}^* \in C^{b\times a}$ exists, and $(\mathbf{P}^*, \mathbf{R}^*)$ satisfies below equations:

$$\begin{aligned} \mathbf{P}^* &= \mathbf{A}^T\mathbf{AR}^* \\ \mathbf{A}^T &= (\mathbf{A}^T\mathbf{A})^2\mathbf{R}^* \end{aligned} \tag{4-39}$$

Subsequently, given matrix $\mathbf{R} \in C^{a\times a}$, as well as a positive scalar ϵ, the iterative algorithm is given as:

$$\mathbf{R}_{i+1} = \mathbf{R}_i + \mathbf{M}^{-1}(\mathbf{A}^T - \mathbf{B}_1\mathbf{R}_i) \tag{4-40}$$

where $\mathbf{B}_1 = (\mathbf{A}^T\mathbf{A})^2$ and $\mathbf{M} = (\mathbf{I}_K + (\mathbf{A}^T\mathbf{A})^2)$ and stopping criteria is $\|\mathbf{A}^T - \mathbf{B}_1\mathbf{R}_i\|_F^2 \leq \epsilon$ or when the set maximum number of iterations is reached. Inverse matrix $\mathbf{M}$ must be computed only once because it is not an iterative process. Proof of the global convergence of (4-40) can be found in [17].

From (4-40), we obtain the following algorithm. However, because $\mathbf{M}^{-1}$ is a direct inverse matrix, an iterative algorithm cannot be applied. Hence, we first approximated the $\mathbf{M}^{-1}$ as $\mathbf{M}^{-1} = (\mathbf{I}_K + (\mathbf{W}^T\mathbf{W})^2)$. Matrix $\mathbf{A}$ is replaced with a gram matrix because we are interested in approximating the inverse of the gram matrix $\mathbf{W}$. Subsequently, matrix $\mathbf{B}_1$ becomes $\mathbf{B}_1 = (\mathbf{W}^T\mathbf{W})^2$, and the proposed algorithm can be expressed as:

$$\mathbf{W}_{i+1}^{-1} = \mathbf{W}_i^{-1} + \mathbf{X}\left(\mathbf{W}^T - \mathbf{B}_1\mathbf{W}_i^{-1}\right) \tag{4-41}$$

where $\mathbf{X}$ is the estimated inverse matrix of $\mathbf{M}$.

The proposed improved iterative algorithm is described in detail below, where r is the number of iterations, and $\mathbf{W}^{-1}$ is the estimated inverse matrix as the output of the algorithm.

Algorithm TSGIM Algorithm

Input: $\mathbf{W}$, r.
Output: $\mathbf{W}^{-1}$

$\mathbf{X} = (\mathbf{I}_K + (\mathbf{W}^T\mathbf{W})^2)$
$\mathbf{T} = \mathbf{WX}$
$\mathbf{Z} = 14\mathbf{I} - (6\mathbf{I} - \mathbf{T})$ // intermediate step
$\mathbf{X} = \frac{1}{2}\mathbf{X}\,(9\mathbf{I} - \mathbf{T}\,(16\mathbf{I} - \mathbf{TZ}))$ // first step
// second step
$\mathbf{B} = \mathbf{W}^{\mathrm{T}}\mathbf{W}$
$\mathbf{W}^{-1} = \mathbf{D}^{-1}$
for $i = 1$ **to** r **do**
    $\mathbf{W}^{-1} = \mathbf{W}^{-1} + \mathrm{X}\,(\mathbf{W}^{\mathrm{T}} - \mathbf{B}^2\mathbf{W}^{-1})$
end for
Output: $\mathbf{W}^{-1}$

4.4.4. Computational Complexity

We evaluate the computational complexity of the proposed algorithm in terms of the number of complex matrix multiplications required.

The computational complexity of ZF precoding with the direct inverse matrix technique is based on the evaluation of matrix $\mathbf{G}$. According to (4-14), if the pseudo-inverse of the term $\widehat{\mathbf{H}}\widehat{\mathbf{H}}^H$ is calculated directly, then the complexity of the ZF precoding technique can be determined using the following steps: We assume that the constant β is known. First, the complexity of matrix multiplication $\widehat{\mathbf{H}}\widehat{\mathbf{H}}^H$ contains K^2Mcomplex multiplications. The computational complexity of the direct inversion of the resultant square matrix includes K^3 complex multiplications. The complexity of multiplying the resultant direct inverse matrix by $\widehat{\mathbf{H}}^H$ includes K^2M multiplications. Then, the number of complex multiplications required to calculate the $\mathbf{G_o s}$ is MK where $\mathrm{G}_o = G/\beta$ and it denotes $\widehat{\mathbf{H}}^H\left(\widehat{\mathbf{H}}\widehat{\mathbf{H}}^H\right)^{-1}$. In the final step, the resultant M-by-1 vector is multiplied by scalar β and M complex multiplications. To calculate the transmitted signal vector $\mathbf{x}$ with ZF precoding $K^3 + 2K^2M + KM + M$ complex multiplications are required.

In our algorithm, the computational complexity in terms of the required number of complex matrix multiplications is calculated as follows: We assume $\mathbf{A}^{\mathrm{T}}\mathbf{A}$, $6\mathbf{I}_K$, $9\mathbf{I}_K$, $14\mathbf{I}_K$, $16\mathbf{I}_K$ and the constant β are known. According to three-step iterative process, $5K^3 + K^2$ complex multiplications are required because the equation includes five matrix-matrix multiplications and one matrix-scalar multiplication. In the second part of the proposed

algorithm, because matrix B is assumed to be known, only $2K^3$ complex multiplications are required. In total $7K^3 + 2K^2M + K^2 + KM + M$ complex multiplication was required to calculate the transmitted signal vector **x**. According to the above analysis, the computational complexities for the first iteration ($i = 1$) of the NI and TSGIM algorithms and the computational complexity of the ZF precoding with DMI are listed in Table 4-II.

Table 4-II. Computational complexity comparison.

Precoding Algorithm	Computational Complexity
ZF-Direct Matrix Inversion (DMI)	$K^3 + 2K^2M + KM + M$
ZF-NI	$2K^3 + 2K^2M + KM + M$
ZF-TSGIM (Proposed)	$7K^3 + K^2(M + 1) + KM + M$

The ZF precoding with DMI was chosen as the reference and ZF with the NI algorithm was chosen because it is the simplest algorithm in terms of implementation among the algorithms. It is observed that ZF with direct matrix conversion precoding has the lowest computational complexity. However, as previously mentioned, direct inversion is unfavourable for hardware. Although the proposed algorithm has more computational complexity than the NI algorithm, it converges without depending on any initial preconditions. However, convergence is only possible with appropriate initial conditions in inverse-matrix approximation algorithms including the NI algorithm. Therefore, there is a trade-off between robustness and computational complexity for iterative inverse matrix approximation algorithms. Fig. 4.3 shows the computational complexity in terms of the number of complex multiplications versus the number of BS antennas M, comparing the ZF precoding with the different inverse-matrix approximation algorithms mentioned in this section. In the case of fixing the number of UE antennas to K = 16 and increasing only the number of BS antennas, the proposed algorithm has a lower computational complexity. This situation is favourable, because massive MIMO systems require hundreds of antenna elements. Fig. 4.4 depicts the computational complexity in terms of the number of complex multiplications versus the number of UE antennas K, comparing the ZF precoding with different inverse matrix approximation algorithms with the different algorithms mentioned in this section. In this case, our proposed algorithm has a slightly higher computational complexity than that of the NI algorithm. The number of BS antennas is fixed at M = 256, as shown in Fig. 4.4.

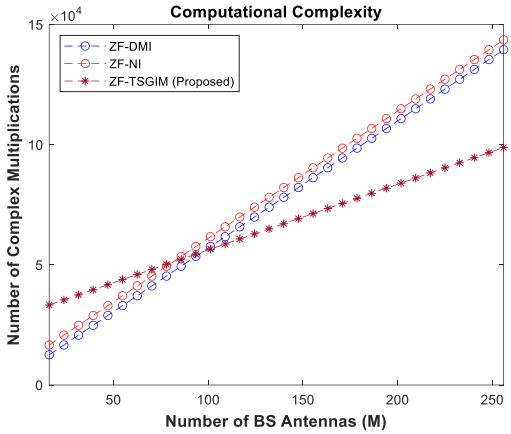

Fig. 4.3. Computational complexity ($K = 16$, $i = 1$).

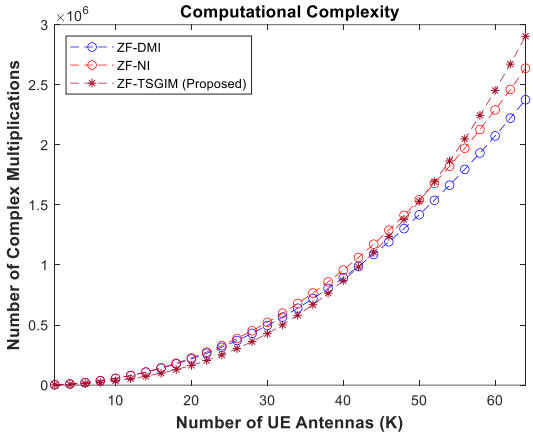

Fig. 4.4. Computational complexity ($M = 256$, $i = 1$).

4.4.5. Simulation Results

Simulations were conducted to verify the effectiveness of the proposed algorithm. The BER, sum rate, and convergence performance of the proposed TSGIM algorithm are evaluated. The correlated channel model proposed as below sections, was used in the simulations. Furthermore, the Rayleigh uncorrelated channel model was used to evaluate algorithms in the literature. The proposed TGSIM algorithm was compared to different types of algorithms (AMIA, IASLE, and IMRN). The optimized initial values in [12] were used for the CI algorithm, whereas the optimized relaxation parameter was used for the SOR and joint SOR-AMI algorithms. In addition, a noisy random $\mathbf{x}$ vector is used as the initial vector, a diagonal matrix that contains the inverse diagonal elements of the resultant matrix $\widehat{\mathbf{H}}\widehat{\mathbf{H}}^H$ is used for the CR and SOR algorithms, and a diagonal matrix that contains the inverse diagonal elements of the resultant matrix $\widehat{\mathbf{H}}\widehat{\mathbf{H}}^H$. ZF precoding, which contains direct matrix inversion, was included as a benchmark.

With respect to the use case, a typical downlink massive MIMO configuration with $M \times K = 256 \times 32$ [15], [16] is considered for the BER analysis. For all combinations and analyses, there were $L = 8$ propagation paths. In this study, QPSK was used as the

modulation scheme; however, any modulation technique can be used. The transmitted signal was normalized in the BER and sum-rate analyzes. The SNR, denoted as ρ in Section 4.4.1, is the ratio of transmitted signal power to received noise power for BER and sum-rate analysis, and can simply be expressed as:

$$\rho = \frac{\left\|\widehat{\mathbf{H}}\right\|_F^2}{\sigma_n^2} \tag{4-42}$$

where $\left\|\widehat{\mathbf{H}}\right\|_F^2$ Frobenius norm of the channel and σ_n^2 is the noise variance.

The parameters for the correlated channel model are as follows: the mutual coupling between adjacent antenna elements is uniformly distributed between -20 dB and -10 dB, as used in [28] for the first tier of neighboring elements; gain and phase variations are $\pm 5\%$ and manufacturing tolerance is $\pm 10\%$ which affects the inter-antenna element spacing, d.

The BER performances of the different algorithms are compared in Fig. 4.5. The algorithms are simulated using the proposed correlated channel model. The number of iterations for all algorithms was $i = 1$. ZF precoding with direct matrix inversion was used as the benchmark. According to the results, the BER performances of the CI, SOR, CR, and GMRES algorithms were insufficient. However, the joint CI-SOR-AMI and proposed TSGIM algorithms performed well. This is because the CI, SOR, and CR is highly dependent on the initial conditions. In this case, the Gram matrix is not a symmetric or conjugate symmetric matrix; hence, the BER performances of CI and SOR are poor. In addition, because we did not consider multiple restarts, the BER performance of GMRES was insufficient. However, it can be seen that the BER performance of the CR algorithm is fair because the random initial vector is appropriate.

As shown in Fig. 4.6, when the number of iterations was increased to $i = 3$, all algorithms performed better BER performance but the CR algorithm. Although the number of iterations was higher, the BER performance of the CR algorithm degraded without a suitable initial vector. The BER performances of the joint CI-SOR-AMI and the proposed TSGIM algorithms converged to the optimal ZF as the number of iterations increased.

Fig. 4.7 shows that when the channels are uncorrelated, the Gram matrix becomes conjugate-symmetric; hence, the BER performance of the CI algorithm is satisfactory. However, more iterations are required to achieve a better BER performance. In addition, CI-SOR-AMI has a near-optimal BER performance because the initial parameters and conditions are optimal in this case. The relaxation parameter was optimized according to, [12] and the optimum initial matrix was, as in [11] the CI-SOR-AMI. The initial matrix for the proposed algorithm was a random square matrix. There is no optimization of the initial values for our proposed algorithm; hence, CI-SOR-AMI performs better. Although all the initial parameters of CI-SOR-AMI are optimized, CI-SOR-AMI performs better

than the proposed algorithm under uncorrelated channel conditions. The proposed TSGIM algorithm also exhibits good BER performance under uncorrelated channels near the optimum. The SOR and CR algorithms require more iterations and more suitable initial vectors. Finally, the GMRES algorithm requires more restarts and iterations to improve BER performance.

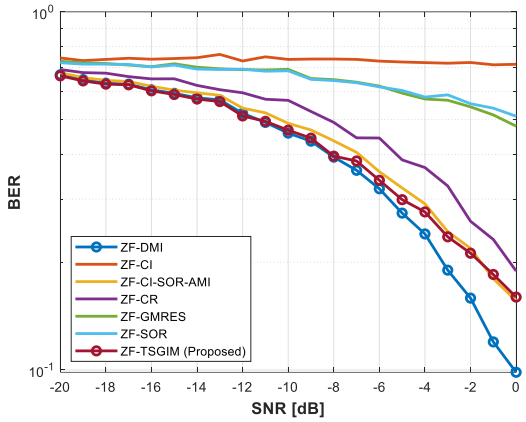

Fig. 4.5. BER performance comparison, correlated channel model ($M = 256$, $K = 32$, $i = 1$).

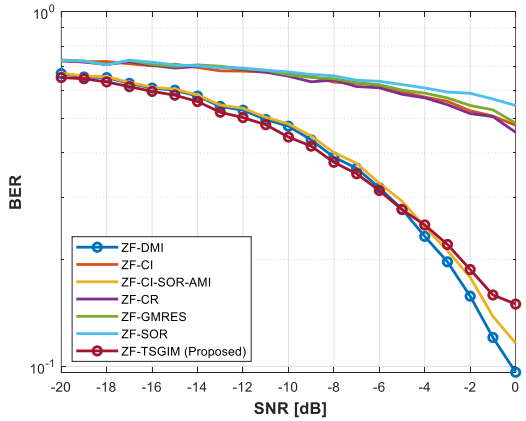

Fig. 4.6. BER performance comparison, correlated channel model ($M = 256$, $K = 32$, $i = 3$).

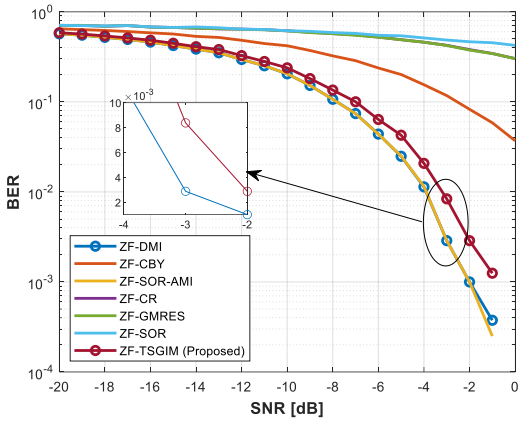

Fig. 4.7. BER performance comparison, uncorrelated channel model ($M = 256$, $K = 32$, $i = 3$).

Fig. 4.8 shows that if the channel estimation is not perfect, i.e., CSI is incomplete, then the performance of the proposed algorithm decreases. Performance degradation due to the imperfect channel estimation is valid for all algorithms even if they are not shown in Fig. 4.8. In reality, perfect channel estimation is impossible but near-perfect approximations can be made. Referring to (1), $\tau = 0$ states that perfect channel estimation and $\tau = 0.3$ states that $\approx 95\%$ of the channel is estimated correctly.

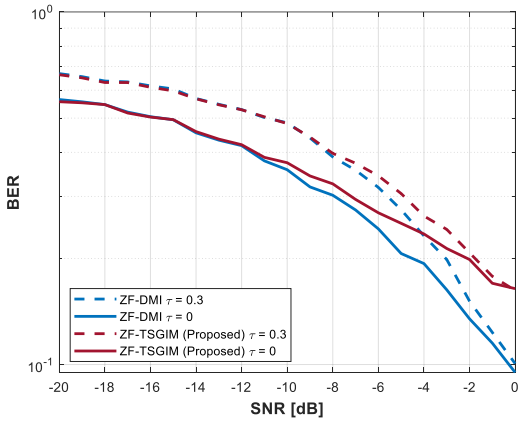

Fig. 4.8. BER performance perfect vs. imperfect channel estimation, correlated channel model ($M = 256$, $K = 32$, $i = 3$).

The Frobenius norm errors of the CI, SOR-AMI, and proposed TSGIM algorithms are compared in Fig. 4.9 and Fig. 4.10 according to the increasing number of BS antennas. In addition, in Fig. 4.11 the number of BS antennas is fixed and the Frobenius norm errors are compared according to the increasing number of iterations for the algorithms. A total of 1,000 Monte Carlo (MC) trials were conducted under correlated channel conditions. It is worth noting that the BER performances of the other algorithms were not considered in this analysis because they skipped the inverse matrix calculation. In the Frobenius norm error analysis, we consider the mean squared error (MSE) between the ideal inverse of the Gram matrix $\mathbf{W}^{-1}$, and the estimated inverse of the Gram matrix $\widehat{\mathbf{W}}^{-1}$. The Frobenius

norm error is $F_{error} = \left\|\mathbf{W}^{-1} - \widehat{\mathbf{W}}^{-1}\right\|_F$. In Fig. 4.9 and Fig. 4.10, for the sake of brevity, only the first iterations, $i = 1$, and fifth iteration, $i = 5$, of the algorithms were considered. As shown in Fig. 4.9, under the correlated channel condition, the MSE of the proposed CI-SOR-AMI algorithm outperformed those of the CI and TSGIM algorithms in the first iteration. In this analysis, the initial parameters for the CI, CI-SOR-AMI, and TSGIM algorithms were optimized. However, Fig. 4.10 shows that, after five iterations, TSGIM outperformed CI and CI-SOR-AMI. As shown in Fig. 4.11, the convergence rate of the proposed TSGIM algorithm outperformed those of CI and CI-SOR-AMI. After four iterations, the Frobenius norm errors of the proposed TSGIM algorithm, CI, and CI-SOR-AMI were 6.37×10^{-4}, 4.09×10^{-2} and 2.67×10^{-2} respectively. Moreover, after ten iterations proposed TSGIM and CI converge to the exact matrix inversion, while CI-SOR-AMI still has the same convergence magnitude.

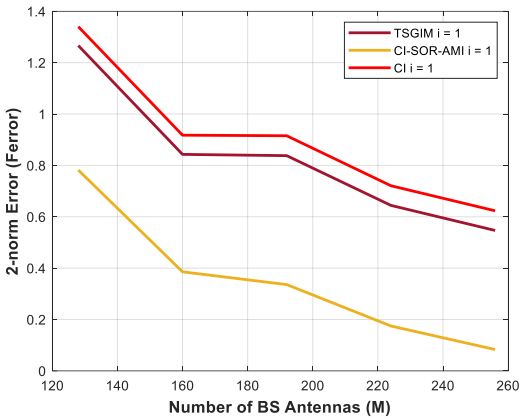

Fig. 4.9. The MSE comparison of approximate matrix inversion algorithms, correlated channel condition ($K = 8$, $i = 1$).

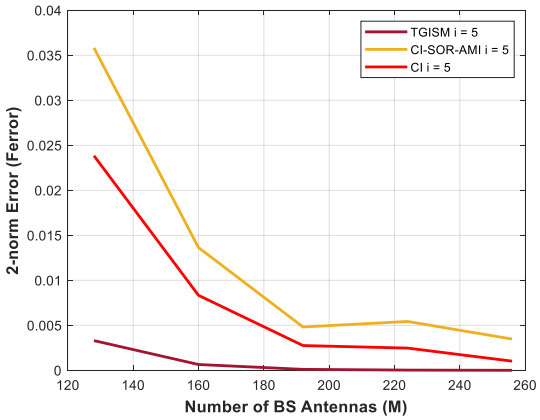

Fig. 4.10. The MSE comparison of approximate matrix inversion algorithms, correlated channel condition ($K = 8$, $i = 5$).

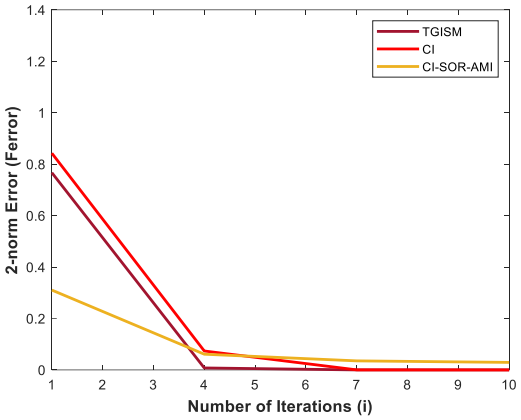

Fig. 4.11. The MSE comparison of approximate matrix inversion algorithms, correlated channel condition ($M = 256, K = 8$).

Fig. 4.12 compares the sum-rate performance of the ZF precoding with the proposed TGSIM algorithm and the ZF precoding with direct inverse matrix calculation. In this case, ZF precoding with direct inversion was the benchmark. It can be seen that in case of imperfect channel estimation, the sum-rate performance of the precoding algorithms decreases. Moreover, if the estimated channel is imperfect and the channels are correlated, including the antenna array manifolds, the sum-rate performance decreases significantly, and although the SNR increases, it becomes almost stationary. However, in each case, the sum-rate performance of the proposed algorithm was close to the optimum.

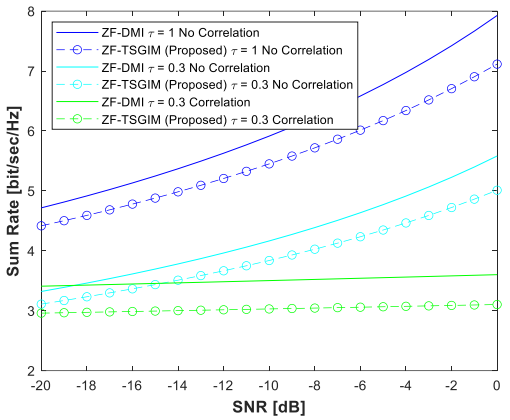

Fig. 4.12. Sum-rate vs SNR ($M = 256, K = 32,\ i = 1$).

4.5. Conclusions

The main focus of this study was to propose a matrix inverse approximation algorithm for precoding transmissions in 5G and 6G massive MIMO systems. The proposed algorithm outperformed the existing techniques in terms of BER, convergence speed, and Frobenius norm error when the number of BS antennas are increased. The algorithm is based on a three-step approximation method using Homeier's approach and an iterative generalized inverse matrix approximation algorithm employing KKT conditions.

To evaluate the performance of the proposed algorithm under realistic massive MIMO conditions, we propose a correlated channel model based on antenna array manifolds that includes mutual coupling, RF and radiating element impairments, and multipath channels with an angular spread. We then investigate the correlated channel effects on the ZF precoding algorithm. The proposed method required four iterations to converge to a direct inverse matrix with a Frobenius norm error magnitude of 10^{-4}. However, at least seven iterations are required for the CI algorithm to achieve the same error magnitude, and the CI-SOR-AMI algorithm cannot achieve the same performance even after ten iterations. The proposed TSGIM algorithm is suitable for approximating the inverse of non-symmetric matrices without any preconditions for convergence.

Finally, algorithms such as SOR and CI-SOR-AMI require matrix decomposition and the calculation of the optimum relaxation parameter, which increases the computation time. The compared algorithms, including SOR and CI-SOR-AMI, require pre-calculations to fulfill the pre-conditions to guarantee convergence to the exact matrix inverse. The proposed TSGIM algorithm has better BER performance and less computation time than the compared algorithms. Therefore, the proposed algorithm is feasible for use in 5G, 6G and future communications systems. Moreover, the proposed algorithm can be also used for applications which involves matrix inversion.

4.6. References Chapter 4

[1] J. Chung and M. Chung, “Computing optimal low-rank matrix approximations for image processing,” in 2013 Asilomar Conference on Signals, Systems and Computers, Pacific Grove, CA, USA: IEEE, Nov. 2013, pp. 670–674. doi: 10.1109/ACSSC.2013.6810366.

[2] V. H. Dang and T. D. Nguyen, “Construction of Pseudoinverse Matrix Over Finite Field and Its Applications,” Wireless Pers Commun, vol. 94, no. 3, pp. 455–466, Jun. 2017, doi: 10.1007/s11277-015-3095-6.

[3] C.-T. Nguyen and T. Yao-Wen, “Finite-Time Output Feedback Controller Based on Observer for the Time-Varying Delayed Systems: A Moore-Penrose Inverse Approach,” Mathematical Problems in Engineering, vol. 2017, 2017, doi: 10.1155/2017/2808094.

[4] A. Cordero, J. G. Maimó, J. R. Torregrosa, and M. P. Vassileva, “Improving Newton–Schulz Method for Approximating Matrix Generalized Inverse by Using Schemes with Memory,” Mathematics, vol. 11, no. 14, Art. no. 14, Jan. 2023, doi: 10.3390/math11143161.

[5] F. Toutounian and F. Soleymani, “An iterative method for computing the approximate inverse of a square matrix and the Moore–Penrose inverse of a non-square matrix,” Applied Mathematics and Computation, vol. 224, pp. 671–680, Nov. 2013, doi: 10.1016/j.amc.2013.08.086.

[6] S. M. Abbas and C.-Y. Tsui, “Approximate Matrix Inversion for Linear Pre-coders in Massive MIMO,” in VLSI-SoC: System-on-Chip in the Nanoscale Era – Design, Verification and Reliability, vol. 508, T. Hollstein, J. Raik, S. Kostin, A. Tšertov, I. O’Connor, and R. Reis, Eds., in IFIP Advances in Information and Communication Technology, vol. 508. , Cham: Springer International Publishing, 2017, pp. 192–212. doi: 10.1007/978-3-319-67104-8_10.

[7] W. Zhang, R. C. de Lamare, C. Pan, M. Chen, B. Wu, and X. Bao, “Correlation-driven optimized Taylor expansion precoding for massive MIMO systems with correlated channels,” in 2017 IEEE International Conference on Communications (ICC), Paris, France: IEEE, May 2017, pp. 1–6. doi: 10.1109/ICC.2017.7996527.

[8] X. Xue et al., “Improved Massive MIMO RZF Precoding Algorithm Based on Truncated Kapteyn Series Expansion,” Information, vol. 10, no. 4, p. 136, Apr. 2019, doi: 10.3390/info10040136.

[9] A. Mueller, A. Kammoun, E. Björnson, and M. Debbah, “Linear precoding based on polynomial expansion: reducing complexity in massive MIMO,” J Wireless Com Network, vol. 2016, no. 1, p. 63, Dec. 2016, doi: 10.1186/s13638-016-0546-z.

[10] H. Wu, B. Shen, S. Zhao, and P. Gong, “Low-Complexity Soft-Output Signal Detection Based on Improved Kaczmarz Iteration Algorithm for Uplink Massive MIMO System,” Sensors, vol. 20, no. 6, p. 1564, Mar. 2020, doi: 10.3390/s20061564.

[11] S. Hashima and O. Muta, “Fast matrix inversion methods based on Chebyshev and Newton iterations for zero forcing precoding in massive MIMO systems,” J Wireless Com Network, vol. 2020, no. 1, p. 34, Dec. 2020, doi: 10.1186/s13638-019-1631-x.

[12] C. Zhang, Z. Li, L. Shen, F. Yan, M. Wu, and X. Wang, “A Low-Complexity Massive MIMO Precoding Algorithm Based on Chebyshev Iteration,” IEEE Access, vol. 5, pp. 22545–22551, 2017, doi: 10.1109/ACCESS.2017.2760881.

[13] M. A. Albreem, M. Juntti, and S. Shahabuddin, “Massive MIMO Detection Techniques: A Survey,” IEEE Commun. Surv. Tutorials, vol. 21, no. 4, pp. 3109–3132, 2019, doi: 10.1109/COMST.2019.2935810.

[14] B. Yin, M. Wu, J. R. Cavallaro, and C. Studer, “Conjugate gradient-based soft-output detection and precoding in massive MIMO systems,” in 2014 IEEE Global Communications Conference, Austin, TX, USA: IEEE, Dec. 2014, pp. 3696–3701. doi: 10.1109/GLOCOM.2014.7037382.

[15] A. Abdaoui, M. Berbineau, and H. Snoussi, “GMRES Interference Canceler for doubly iterative MIMO system with a Large Number of Antennas,” in 2007 IEEE International Symposium on Signal Processing and Information Technology, Dec. 2007, pp. 449–453. doi: 10.1109/ISSPIT.2007.4458142.

[16] H. H. H. Homeier, “On Newton-type methods with cubic convergence,” Journal of Computational and Applied Mathematics, vol. 176, no. 2, pp. 425–432, Apr. 2005, doi: 10.1016/j.cam.2004.07.027.

[17] Y. Xia, T. Chen, and J. Shan, “A Novel Iterative Method for Computing Generalized Inverse,” Neural Computation, vol. 26, no. 2, pp. 449–465, Feb. 2014, doi: 10.1162/NECO_a_00549.

[18] J. Brinkhuis and V. M. Tikhomirov, Optimization: insights and applications. in Princeton series in applied mathematics. Princeton, N.J: Princeton University Press, 2005.

[19] K. Manjunatha Prasad and R. B. Bapat, “The generalized Moore-Penrose inverse,” Linear Algebra and its Applications, vol. 165, pp. 59–69, Mar. 1992, doi: 10.1016/0024-3795(92)90229-4.

[20] F. Rosario, F. A. Monteiro, and A. Rodrigues, “Fast Matrix Inversion Updates for Massive MIMO Detection and Precoding,” IEEE Signal Process. Lett., vol. 23, no. 1, pp. 75–79, Jan. 2016, doi: 10.1109/LSP.2015.2500682.

[21] K. Zheng, S. Ou, and X. Yin, “Massive MIMO Channel Models: A Survey,” International Journal of Antennas and Propagation, vol. 2014, pp. 1–10, 2014, doi: 10.1155/2014/848071.

[22] M. A. Salas-Natera, R. M. Rodriguez-Osorio, L. de Haro Ariet, and M. Sierra-Perez, “Novel Reception and Transmission Calibration Technique for Active Antenna Array Based on Phase Center Estimation,” IEEE Trans. Antennas Propagat., vol. 65, no. 10, pp. 5511–5522, Oct. 2017, doi: 10.1109/TAP.2017.2738067.

[23] E. Ali, M. Ismail, R. Nordin, and N. F. Abdulah, "Beamforming techniques for massive MIMO systems in 5G: overview, classification, and trends for future research," Frontiers Inf Technol Electronic Eng, vol. 18, no. 6, pp. 753–772, Jun. 2017, doi: 10.1631/FITEE.1601817.

[24] F. Rusek et al., "Scaling up MIMO: Opportunities and Challenges with Very Large Arrays," IEEE Signal Process. Mag., vol. 30, no. 1, pp. 40–60, Jan. 2013, doi: 10.1109/MSP.2011.2178495.

[25] J. G. Andrews et al., "What Will 5G Be?," IEEE J. Select. Areas Commun., vol. 32, no. 6, pp. 1065–1082, Jun. 2014, doi: 10.1109/JSAC.2014.2328098.

[26] I. Ahmed et al., "A Survey on Hybrid Beamforming Techniques in 5G: Architecture and System Model Perspectives," IEEE Commun. Surv. Tutorials, vol. 20, no. 4, pp. 3060–3097, 2018, doi: 10.1109/COMST.2018.2843719.

[27] V. L. Babu, L. Mathews, and S. S. Pillai, "Performance Analysis of Linear and Nonlinear Precoding in MIMO Systems," vol. 4, no. 6, p. 4, 2015.

[28] M. A. Salas-Natera, R. M. Rodriguez-Osorio, and L. de Haro, "Procedure for Measurement, Characterization, and Calibration of Active Antenna Arrays," IEEE Trans. Instrum. Meas., vol. 62, no. 2, pp. 377–391, Feb. 2013, doi: 10.1109/TIM.2012.2217662.

[29] M. Wu, B. Yin, K. Li, C. Dick, J. R. Cavallaro, and C. Studer, "Implicit vs. Explicit Approximate Matrix Inversion for Wideband Massive MU-MIMO Data Detection," J Sign Process Syst, vol. 90, no. 10, pp. 1311–1328, Oct. 2018, doi: 10.1007/s11265-017-1313-z.

[30] B. Kang, J.-H. Yoon, and J. Park, "Low complexity massive MIMO detection architecture based on Neumann method," in 2015 International SoC Design Conference (ISOCC), Nov. 2015, pp. 293–294. doi: 10.1109/ISOCC.2015.7401703.

[31] H. Prabhu, J. Rodrigues, O. Edfors, and F. Rusek, "Approximative matrix inverse computations for very-large MIMO and applications to linear pre-coding systems," in 2013 IEEE Wireless Communications and Networking Conference (WCNC), Shanghai, Shanghai, China: IEEE, Apr. 2013, pp. 2710–2715. doi: 10.1109/WCNC.2013.6554990.

[32] H. F. Walker, "Implementation of the GMRES Method Using Householder Transformations," SIAM J. Sci. and Stat. Comput., vol. 9, no. 1, pp. 152–163, Jan. 1988, doi: 10.1137/0909010.

[33] X. Gao, L. Dai, Y. Ma, and Z. Wang, "Low-complexity near-optimal signal detection for uplink large-scale MIMO systems," Electronics Letters, vol. 50, no. 18, pp. 1326–1328, 2014, doi: 10.1049/el.2014.0713.

[34] C. Xiao, X. Su, J. Zeng, L. Rong, X. Xu, and J. Wang, "Low-complexity soft-output detection for massive MIMO using SCBiCG and Lanczos methods," China Communications, vol. 12, no. Supplement, pp. 9–17, Dec. 2015, doi: 10.1109/CC.2015.7386166.

[35] X. Jing, A. Li, and H. Liu, “A low-complexity Lanczos-algorithm-based detector with soft-output for multiuser massive MIMO systems,” Digital Signal Processing, vol. 69, pp. 41–49, Oct. 2017, doi: 10.1016/j.dsp.2017.06.018.

[36] M. Wu, C. Dick, J. R. Cavallaro, and C. Studer, “High-Throughput Data Detection for Massive MU-MIMO-OFDM Using Coordinate Descent,” IEEE Trans. Circuits Syst. I, vol. 63, no. 12, pp. 2357–2367, Dec. 2016, doi: 10.1109/TCSI.2016.2611645.

[37] M. Wu, C. Dick, J. R. Cavallaro, and C. Studer, “FPGA design of a coordinate descent data detector for large-scale MU-MIMO,” in 2016 IEEE International Symposium on Circuits and Systems (ISCAS), Montréal, QC, Canada: IEEE, May 2016, pp. 1894–1897. doi: 10.1109/ISCAS.2016.7538942.

[38] A. E. Zorkun, M. A. Salas-Natera, and R. Martinez Rodriguez-Osorio, “Improved Iterative Inverse Matrix Approximation Algorithm for Zero Forcing Precoding in Large Antenna Arrays,” IEEE Access, vol. 10, pp. 100964–100975, 2022, doi: 10.1109/ACCESS.2022.3208155.

5. Chapter 5: Novel Antenna Array Calibration Proposals

5.1. Introduction

In the calibration procedure, signal samples are collected from each antenna element or subarrays and then these signal samples are used to determine the compensation weights [1]. The calibration process of phased antenna arrays, whether transmitting or receiving, are similar to each other except for minor differences [1], [2]. In receive mode, a test signal is injected as the input of each element, a special reference or self-correlation process with a beamformer is required to combine all inputs [3], [4]. On the contrary, in the transmit mode, each element must be excited by a source signal and a combined signal monitoring at the output is required [2], [5], therefore only RF chain information can be obtained or an external sensor is used to receive and monitor the signal from each element. The calibration methods can be divided into four subgroups: the near-field or far-field probing methods, the peripheral-fixed probe method, the mutual (MC) coupling methods and the built-in network methods [4], [6], [7].

The near-field or far-field probing methods employ a test probe moved across a phased antenna array to measure the relative phase and amplitude of each antenna element [8], [9], [10]. The peripheral fixed probe methods use one or more fixed probes around the periphery of the phased array to measure the coupling between antennas and compensate for excitation errors [11], [12]. Probing methods can be considered on-site calibration methods since the phased antenna array under test must be within the field of view of the test probe/s. In mutual coupling methods, coupling between all pairs of antenna elements is used to characterize the exact relative phase and amplitude errors of each antenna element [7], [13], [14]. Lastly, in built-in network calibration methods, couplers are connected to the terminals of each antenna element in the phased array to sample the reference signal from the radiating element. The received or transmitted signals measured at the connected end are then used to determine phase and amplitude mismatches of the antenna elements [4], [15], [16], [17], [18]. Depending on the application, calibration methods can be used in off-line, on-site, or online calibration systems by implementing application specific calibration algorithms and additional hardware [5], [14], [19], [20]. Moreover, as mentioned in Chapter Ⅱ, unequal co-polarized and cross-polarized wavefields due to the array impairments must be also taken into account.

Achieving accurate and reliable performance from the antenna arrays requires precise calibration of axial ratio. The axial ratio is a key parameter that characterizes the polarization purity of an antenna, and calibration is necessary to ensure optimal signal quality and minimize interference. In addition to that also provides an effective and

reliable communication network. Moreover, circularly polarized antenna arrays are extremely favorable since such antennas have low polarization loss and most importantly have less multi-path propagation. The errors in antenna array and mutual coupling also affect the axial ratio (AR) in the case of circularly polarized active antenna arrays. In order to compensate for the impacts of each individual element, such as the position, gain, and phase errors of the antenna and the coupling effect, antenna arrays must be polarized with the required attributes. This process is known as axial ratio calibration [21].

There are vast number of studies on antenna array calibration. The most desirable key points for the antenna array calibration can be listed as:

- Eliminate the time-consuming trial-and-error method with visual inspection
- Compensate mutual coupling effects
- Compensate gain/phase uncertainties and location errors
- Improve axial ratio
- Low number of auxiliary elements
- Low complexity calibration algorithms and as well as methods
- Compliance with all off-line, on-site, and online calibration schemes

In line with those requirements, in this chapter two novel calibration methods are proposed, namely, a mutual coupling-based uplink online self-calibration method and calibration and axial ratio improvement method base-on polarization agile system capability.

5.2. A Mutual Coupling-Based Uplink Online Self-Calibration Method for Antenna Arrays

A novel built-in self-calibration method for transmit mode large-scale phased antenna arrays based on mutual coupling measurements is proposed. The proposed calibration method capable of compensating gain/phase uncertainties, antenna element location errors and mutual coupling. The calibration procedure can be used in online calibration scheme as it will not cause any disruption to the system while it is operating. However, inter-element coupling measurements in the antenna array generally take a long time and may cause a delay in online calibration. These measurements are made automatically in advance and given as input to the system just once since the coupling between antennas does not depend on the pointing direction of the antenna array. In addition, accurate calibration can be made by measuring the couplings of the elements in the first and second-order neighbors of an antenna element in two directions which leads significant reduction in measurement time and cost. Therefore, the proposed calibration method takes into account the couplings of certain number of neighboring elements. In online procedure, the proposed calibration method combines the error feedback signal related to scan reflection coefficient (depends on the pointing direction) and the premeasured

couplings to construct the array manifold. An error matrix is then estimated from the array manifold. The direct inverse of the error matrix is used for compensation matrix of the antenna weights. Direct inverse matrix operations in hardware generally lead to inaccurate results because they involve division operations. Hence, a generalized inverse matrix approximation method is adopted, which reduces the matrix inverse operation to matrix sums and multiplications and also suitable in case of unequal couplings which leads unsymmetric array manifold matrix. The detailed explanation about the adopted generalized inverse matrix approximation method has been already given in Chapter Ⅳ. Simulation results with worst case errors and a simple experimental study are presented. The results show that with the proposed method, accurate calibration can be made with couplings only in the first and second order neighbors of an antenna element.

5.2.1. Evolution of Antenna Array Calibration

In Table 5-III a chronological order of some of the prominent antenna array calibration work done over the last decade. In this table, the methods used in relevant studies are briefly given. The errors that are calibrated for the antenna arrays, types of suitability for implementation of these calibration methods, the types of measurements required for calibration, and operating modes of the antenna arrays are given comparatively.

Table 5-III. Comparison of discussed calibration methods from literature.

Ref.	Method	Year	Calibration			Implementation				Measurement	Mode
			Amp.	Phase	MC.	Off-line	On-site	Online	Self-Cal.		
[22]	Orthogonal coded signals	2013	✓	✓	×	✓	✓	×	✓	Power	Tx
[23]	Element pattern reconstruction	2014	×	×	✓	✓	✓	✓	✓	Pattern	Rx
[24]	Iterative algorithm	2014	✓	✓	×	✓	✓	✓	✓	Amp., Phase	Rx
[25]	Phase center optimization	2015	×	✓	×	✓	✓	✓	×	Phase	Rx
[2]	Impulse response difference	2016	✓	✓	×	✓	✓	✓	✓	Amp., Phase	Tx
[20]	Solving linear equations	2017	×	×	✓	✓	✓	×	×	MC	Tx
[7]	Active element pattern	2017	✓	✓	✓	✓	✓	×	×	Pattern	Tx
[26]	Graph coloring	2018	✓	✓	×	✓	✓	✓	✓	MC	Rx/Tx
[27]	Code-Modulated Interferometry	2018	✓	✓	×	×	✓	×	✓	Power	Rx/Tx
[28]	Measured complex signals	2019	✓	✓	×	✓	✓	×	×	Amp., Phase	Tx
[15]	Measured complex signals	2019	✓	✓	×	×	✓	✓	✓	Power	Rx
[5]	MC measurement	2019	✓	✓	✓	✓	✓	✓	✓	MC	Rx/Tx
[14]	MC measurement	2020	✓	✓	✓	✓	✓	✓	✓	MC	Rx/Tx
[19]	Modified genetic algorithm	2020	✓	✓	×	✓	×	×	✓	Power	Tx
[17]	Coupler integrated calibration	2020	✓	✓	×	×	✓	×	✓	Power	Rx
[29]	Improved REV method	2021	✓	✓	✓	✓	×	×	×	Power	Rx
[30]	Simultaneous perturbation	2022	✓	✓	×	×	✓	✓	×	Power	Rx
[4]	Closed-loop testing	2022	✓	✓	✓	✓	×	×	✓	Amp., Phase, MC	Tx
[31]	Compressed sensing	2022	✓	✓	×	✓	✓	×	×	Power	Tx
[32]	Minimum vector-sum point	2023	✓	✓	×	✓	×	×	✓	Power	Tx
[33]	Code-division calibration	2023	✓	✓	×	×	✓	✓	×	Power	Rx
[10]	Gaussian process model	2023	✓	✓	✓	✓	✓	×	×	Amp., Phase, MC	Rx

5.2.2. Main Contributions

The main contributions of a mutual coupling-based uplink online self-calibration method for antenna arrays are summarized as follows:

- The uncertainties as a function of scan reflection coefficient [7] for transmitting phased array antennas is described.
- The proposed calibration method compensates for phase and amplitude changes caused by static and dynamic errors since automatic and continuous calibration is performed while the system is operating.
- The proposed calibration method requires no additional testing reference signal. In addition, it is suitable for off-line, on-site and on-line calibration.
- A generalized iterative inverse matrix approximation method [34] is adopted to improve the accuracy of estimation of the error compensation matrix in hardware.
- The isolation problem related to the non-directional couplers mentioned in [4], is tackled by employing RF circulators for each antenna branch.

5.2.3. Theoretical Formulation

The basic concepts on phased array antennas, the main assumptions used through the proposed calibration method and error models are briefly explained. In this paper, the calibration of the phased antenna array operating in transmission mode is discussed and the contribution of the thermal effect is ignored.

5.2.3.1. Active Antenna Array Pattern

In applications of narrowband antenna arrays, radiating antennas are assumed to operate only in fundamental mode and it is considered that each element in the antenna array has almost the same pattern [7]. The antenna array pattern can be characterized by multiplying the array factor (AF) and the antenna element pattern. The array factor is the characterization of the antenna array in terms of complex phase shifts and amplitudes. The complete ideal active array pattern of the entire transmitting antenna array in the pointing direction (θ_n, φ_n) which is defined in a $N_\theta \times N_\varphi$ angle grid, $E_a(\theta_n, \varphi_n) \epsilon\, \mathbb{C}^{N_\theta \times N_\varphi}$, with M antennas can be expressed as follows:

$$E_a(\theta_n, \varphi_n) = E_e(\theta_n, \varphi_n) \underbrace{\sum_{m=1}^{M} V_m e^{jk\hat{\mathbf{r}}_n \vec{\mathbf{r}}_m}}_{\hat{AF}} \tag{5-1}$$

where $E_e(\theta_n, \varphi_n)$ is the active element pattern defined in a $N_\theta \times N_\varphi$ angle grid, V_m is the excitation voltage of the m-th element being as $V_m = V_m{}^+ + V_m{}^-$, the phase of the m-th element is $\hat{\mathbf{r}}_n\vec{\mathbf{r}}_m = (x_m \sin\theta_n \cos\varphi_n + y_m \sin\theta_n \sin\varphi_n + z_m \cos\theta_n)$, $k = 2\pi/\lambda$ and λ is the wavelength of the operating frequency and interelement spacing between two adjacent antenna element is $\lambda/2$ in both axis.

For a planar array, the excitation voltage of the m-th element in the pointing direction (θ_0, φ_0) can be expressed as:

$$V_m{}^+ = V_o e^{-jk(x_m \sin\theta_0 \cos\varphi_0 + y_m \sin\theta_0 \sin\varphi_0)} \tag{5-2}$$

where $V_o = 1$ for the brevity. Thus, the scan reflection of the one of those surrounding to the m-th element when the all of the antenna elements are excited and properly phased to steer the array beam in the direction (θ_0, φ_0), can be expressed as:

$$\Gamma_m(\theta_0, \varphi_0) = \frac{V_m{}^-}{V_m{}^+} = e^{-jk\hat{\mathbf{r}}_0\vec{\mathbf{r}}_m} \cdot \left(\mathbf{a_0}^T \mathbf{s}_{(m)}\right) \tag{5-3}$$

where $\mathbf{a_0} = \left[e^{jk\hat{\mathbf{r}}_0\vec{\mathbf{r}}_1}, \dots, e^{jk\hat{\mathbf{r}}_0\vec{\mathbf{r}}_k}, \dots, e^{jk\hat{\mathbf{r}}_0\vec{\mathbf{r}}_K}\right]^T$ and $\mathbf{s}_{(m)}$ is a column of the scattering matrix of the planar antenna array up to K neighboring element for each antenna element being as $\mathbf{s}_{(m)} = [S_{m1}, \dots S_{mk}, \dots S_{mK}]^T$.

The complete general planar array including reflection coefficients with all elements excited can be written in more compact form as [7]:

$$\bar{E}_a(\theta, \varphi) = E_a(\theta, \varphi)\, \mathbf{a^H}(\mathbf{I} - \mathbf{\Gamma_0})\mathbf{v}^+ \tag{5-4}$$

where $\mathbf{v}^+$ is the vector of excitation voltages being as $\mathbf{v}^+ = \left[V_1{}^+, \dots V_m{}^+, \dots . V_M{}^+\right]^T$, $\mathbf{\Gamma_0}$ is a diagonal matrix of reflection coefficients and $\mathbf{I}_M$ is a $M \times M$ identity matrix.

As a next step, the active array pattern including modelling errors (reflection coefficients are also included) can be expressed as [35]:

$$\tilde{E}_a(\theta_0, \varphi_0) = \boldsymbol{w}^H \tilde{\boldsymbol{m}}(\theta_0, \varphi_0) E_a(\theta_0, \varphi_0) \tag{5-5}$$

where $\mathbf{w} \in \mathbb{C}^{M\times 1}$ is the beamforming vector whose m-th term represents the complex beamforming weights of the m-th antenna element and $\tilde{\boldsymbol{m}}(\theta_0, \varphi_0) \in \mathbb{C}^{M\times 1}$ is the array manifold including mutual coupling effects, gain/phase errors and location errors of the antenna elements. The array manifold $\tilde{\boldsymbol{m}}(\theta_0, \varphi_0)$ can be expressed as:

$$\tilde{\boldsymbol{m}}(\theta_0, \varphi_0) = \mathbf{M}_e(\theta_0, \varphi_0)\mathbf{G}_{RF}\left(\boldsymbol{g}(\theta_0, \varphi_0) \odot \mathbf{a}(\theta_0, \varphi_0)\right) \tag{5-6}$$

where $\mathbf{G}_{RF} \in \mathbb{C}^{M\times M}$ is the diagonal matrix, whose m-th diagonal element, $g_m^{RF} e^{-j\Psi_m^{RF}}$, represents the ideal gain/phase coefficient of the RF chain of the m-th element, $\boldsymbol{g}(\theta_0, \varphi_0) \in \mathbb{C}^{M\times 1}$ and $\mathbf{a}(\theta_0, \varphi_0) \in \mathbb{C}^{M\times 1}$ are the vectors, whose m-th elements, $g_m e^{-j\Psi_m}$ and

$e^{-j\delta_m}$ represent the ideal gain/phase coefficient and phase coefficients of the m-th element in the pointing direction (θ_0, φ_0), respectively, and $\mathbf{M}_e(\theta_0, \varphi_0) \in \mathbb{C}^{M\times M}$ is the error matrix expressed as:

$$\mathbf{M}_e(\theta_0, \varphi_0) = \mathbf{C}\left(\Delta\mathbf{G}_{RF}\Delta\mathbf{G}(\theta_0, \varphi_0)\Delta\mathbf{A}(\theta_0, \varphi_0)\right) \tag{5-7}$$

where $\mathbf{C} \in \mathbb{C}^{M\times M}$ is the mutual coupling matrix, $\Delta\mathbf{G}_{RF} \in \mathbb{C}^{M\times M}$ is a diagonal matrix, whose m-th diagonal element, $\Delta g_m^{RF} e^{j\Delta\Psi_m^{RF}}$ represents the gain/phase uncertainty coefficient of the RF chain of the m-th element, $\Delta\mathbf{G}(\theta_0, \varphi_0) \in \mathbb{C}^{M\times 1}$ and $\Delta\mathbf{A}(\theta_0, \varphi_0) \in \mathbb{C}^{M\times 1}$ are the diagonal matrices, whose m-th diagonal elements, $\Delta g_m e^{j\Delta\Psi_m}$ and $e^{j\Delta\delta_m}$ represent the gain/phase uncertainty and phase uncertainty due to the location errors coefficients of the m-th element in the pointing direction (θ_0, φ_0), respectively.

In large-scale phased antenna array, the mutual coupling matrix, $\mathbf{C}$, can be constructed by taking account the only K neighbor elements of the m-th element where $K \ll M$. Phase and amplitude coupling coefficients of matrix $\mathbf{C}$ can be model based on the scan reflection coefficient, $C_{m,m}$, [7] and the coupling coefficients, $C_{m,k}$. The mutual coupling coefficients can be expressed as:

$$C_{m,m} = \frac{V_m^-}{V_m^+} = e^{jk(\hat{\mathbf{r}}_0 - \hat{\mathbf{r}}_n)\vec{\mathbf{r}}_m}\left(S_{mm} + \sum_{k=1}^{K} S_{mk} e^{-jk\hat{\mathbf{r}}_n\vec{\mathbf{r}}_k}\right) \tag{5-8}$$

$$C_{m,k} = \frac{V_k^-}{V_m^+} = S_{mk} e^{jk\hat{\mathbf{r}}_n\vec{\mathbf{r}}_m} e^{-jk\hat{\mathbf{r}}_n\vec{\mathbf{r}}_k} \tag{5-9}$$

where $\hat{\mathbf{r}}_n$ is the broadside unit vector, $\hat{\mathbf{r}}_k$ is the position vector of the k-th neighbor of the m-th element, S_{mk} is the magnitude of the scattering (coupling) coefficients of the m-th element and its k-th neighbor.

In line with (5-5)-(5-9), an array manifold matrix, $\widetilde{\mathbf{M}}(\theta_0, \varphi_0)$, which is later on defined as measurement matrix, in the pointing direction can be defined as:

$$\widetilde{\mathbf{M}}(\theta_0, \varphi_0) = \mathbf{M}_e(\theta_0, \varphi_0)\mathbf{G}_{RF}\left(\mathbf{G}(\theta_0, \varphi_0)\mathbf{A}(\theta_0, \varphi_0)\right) \tag{5-10}$$

where $\mathbf{G}(\theta_0, \varphi_0) \in \mathbb{C}^{M\times M}$ and $\mathbf{A}(\theta_0, \varphi_0) \in \mathbb{C}^{M\times M}$ are the diagonal matrices, whose m-th diagonal elements, $g_m e^{j\Psi_m}$ and $e^{j\delta_m}$ represent ideal gain/phase coefficient and phase coefficients of the m-th element in the pointing direction (θ_0, φ_0), respectively.

5.2.3.2. Active Element Pattern

The characterization of a single active element pattern is useful the in characterization of an antenna array since, as stated in (5-1), the fully excited antenna array can be expressed in terms of the active element pattern and the array factor [35]. The active antenna element pattern of the m-th element of an antenna array can be expressed in terms of scan

reflection coefficient and scattering coefficients in the pointing direction (θ, φ)as:

$$E_m(\theta_0, \varphi_0) = E_e(\theta_0, \varphi_0) e^{jk(\hat{\mathbf{r}}_0 - \hat{\mathbf{r}}_n)\vec{\mathbf{r}}_m} \left(1 + \mathbf{s}_{(m)}\mathbf{d}_{(m)}\right) \tag{5-11}$$

where $E_m(\theta_0, \varphi_0)$ is the active element pattern of the m-th element defined a $N_\theta \times N_\varphi$ angle grid, $\mathbf{s}_{(m)} \in \mathbb{C}^{1\times K}$ is the vector of magnitude of the scattering coefficients of the m-th element being as $\boldsymbol{s}_{(m)} = [S_{m1}, \dots, S_{mk} \dots, S_{mK}]$ and $\mathbf{d}_{(m)} \in \mathbb{C}^{1\times K}$ is the phase differences vector due to the location of K neighboring elements of the m-th element being as $\mathbf{d}_{(m)} = \left[e^{-jk\hat{\mathbf{r}}_0(\vec{\mathbf{r}}_1 - \vec{\mathbf{r}}_m)}, \dots, e^{-jk\hat{\mathbf{r}}_0(\vec{\mathbf{r}}_k - \vec{\mathbf{r}}_m)}, \dots e^{-jk\hat{\mathbf{r}}_0(\vec{\mathbf{r}}_K - \vec{\mathbf{r}}_m)}\right]^T$.

In general, for large-scale antenna arrays, it is assumed that all the coupling coefficients are reciprocal as $S_{km} = S_{mk}$, however, this assumption may not always be valid as each element in the antenna array may have different excitation due to different error contributions. The gain/phase uncertainties that the active antenna element is exposed due to static and dynamic errors can be formulated in terms of mutual coupling. The radiated signal from the m-th antenna, which is imposed to gain/phase uncertainties, can be detected at a lower signal power level at neighboring antennas. Hence, by measuring the coupled signal from the neighboring antennas, gain and phase errors can be estimated.

The amplitude coefficients of the error matrix $\mathbf{M}_e(\theta_0, \varphi_0)$ are defined in terms of the element amplitude error (Δg_m), the amplitude error matrix of RF circuits (Δg_m^{RF}), and the mutual coupling. The amplitude error coefficients related with the m-th element and its k-th neighbor, $|g_{e(m,k)}|$, and due to the scan reflection, $|g_{e(m,m)}|$, can be expressed as [7]:

$$|g_{e(m,k)}| = |S_{mk}\Delta g_k^{RF}\Delta g_k| \tag{5-12}$$

$$|g_{e(m,m)}| = \left|S_{mm}\Delta g_m^{RF}\Delta g_m + \sum_{k=1}^{K} S_{mk}\Delta g_k^{RF}\Delta g_k\right| \tag{5-13}$$

The phase coefficients of the error matrix $\mathbf{M}_e(\theta_0, \varphi_0)$ are defined in terms of the phase uncertainty of the element due to the location error, phase uncertainty of the antenna element, phase uncertainty of RF circuit, and the mutual coupling. The amplitude error coefficients related with the m-th element and its k-th neighbor, $e^{j\Delta\Psi_{(m,k)}}$, and due to the scan reflection, $e^{j\Delta\Psi_{(m,m)}}$, can be expressed as [7]:

$$e^{j\Delta\Psi_{(m,k)}} = e^{j\Delta\delta_k} e^{j\Delta\Psi_k} e^{j\Delta\Psi_k^{RF}} e^{jk\hat{\mathbf{r}}_0(\vec{\mathbf{r}}_m - \vec{\mathbf{r}}_k)} \tag{5-14}$$

$$e^{j\Delta\Psi_{(m,m)}} = e^{j\Delta\delta_m} e^{j\Delta\Psi_m} e^{j\Delta\Psi_m^{RF}} \prod_{k=1}^{K} e^{j\Delta\Psi_{(m,k)}} \tag{5-15}$$

Then we can describe the entries of $\mathbf{M}_e(\theta, \varphi)$ as:

$$\mathbf{M}_e^{m,k} = \left|g_{e(m,k)}\right| e^{j\Delta\Psi_{(m,k)}} \tag{5-16}$$

$$\mathbf{M}_e^{m,m} = \left|g_{e(m,m)}\right| e^{j\Delta\Psi_{(m,m)}} \tag{5-17}$$

5.2.3.3. Error Matrix Estimation

The phased antenna array can be calibrated once the error matrix estimation performed. In order to estimate the error matrix $\mathbf{M}_e(\theta_0, \varphi_0)$ least-squares criteria can be used [7], [36]. The cost function of the minimization problem can be expressed as:

$$\min_{\mathbf{M}_e(\theta_0,\varphi_0)} \left\| \widetilde{\mathbf{M}}(\theta_0, \varphi_0) - \mathbf{G}_{RF}\left(\mathbf{G}(\theta_0, \varphi_0)\mathbf{A}(\theta_0, \varphi_0)\right) \mathbf{M}_e(\theta_0, \varphi_0) \right\|_F^2 \tag{5-18}$$

Since the matrices $\mathbf{G}_{RF}$, $\mathbf{G}(\theta_0, \varphi_0)$ and $\mathbf{A}(\theta_0, \varphi_0)$ are priorly known, the unknown coefficients of the error matrix, $\mathbf{M}_e(\theta_0, \varphi_0)$, can be estimated as follows:

$$\mathbf{M}_e(\theta_0, \varphi_0) = \left(\begin{pmatrix} \left(\mathbf{G}_{RF}\left(\mathbf{G}(\theta_0, \varphi_0)\mathbf{A}(\theta_0, \varphi_0)\right)\right)^T \\ \left(\mathbf{G}_{RF}\left(\mathbf{G}(\theta_0, \varphi_0)\mathbf{A}(\theta_0, \varphi_0)\right)\right) \end{pmatrix} \right)^{-1} \left(\mathbf{G}_{RF}\left(\mathbf{G}(\theta_0, \varphi_0)\mathbf{A}(\theta_0, \varphi_0)\right)\right)^T \widetilde{\mathbf{M}}(\theta_0, \varphi_0) \tag{5-19}$$

5.2.4. Detailed Explanation of The Proposed Calibration Method

In this section, the flow of the proposed calibration method, the proposed online calibration system, calibration procedure and the required measurements, the adopted inverse matrix approximation method and the complexity of the proposed calibration method in terms of computational complexity and number of measurements are explained in detail.

5.2.4.1. Flow of The Proposed Calibration Method

The main idea of the calibration process is to acquire the coupled signals from the K neighbors of each antenna element to estimate the error matrix $\mathbf{M}_e(\theta_0, \varphi_0)$The error matrix, then, can be used for compensating the gain/phase errors and the mutual coupling effects. The flow chart of the proposed procedure is given in Fig. 5.1.

The steps of the procedure are given as:

- The theoretical ideal array pattern is pre-calculated according to pattern multiplication rule as in (5-1). The ideal weights of each element are determined according to the ideal gain/phase coefficients of $g_{\mathrm{m}}^{\mathrm{RF}} e^{-\mathrm{j}\Psi_{\mathrm{m}}^{\mathrm{RF}}}$, $g_{\mathrm{m}} e^{-\mathrm{j}\Psi_{\mathrm{m}}}$ and $\mathrm{e}^{-\mathrm{j}\delta_{\mathrm{m}}}$. The pattern of single element is pre-measured and assumed to be identical for all elements. It should be noted the array geometry is known preliminary.
- The mutual coupling coefficients of each antenna element from its K neighbors are measured. The calibration procedure is online; therefore, the mutual couplings should be pre-measured and saved in a look-up table.

- The measurement signals are acquired from each antenna elements as $\widetilde{M}_{1,1}(\theta_0, \varphi_0), \ldots, \widetilde{M}_{M,M}(\theta_0, \varphi_0)$ in the pointing direction while the system is operating. It should be noted $\widetilde{M}_{m,m}(\theta_0, \varphi_0)$ is the scan reflection coefficient of the m-th element.
- Construct the array manifold matrix, $\widetilde{\mathbf{M}}(\theta_0, \varphi_0)$, in the pointing direction by using the pre-measured mutual coupling coefficients and the measured scan reflection coefficients.
- Estimate the error matrix, $\mathbf{M}_{\mathrm{e}}(\theta_0, \varphi_0)$, using least squares solutions in (18). The inverse matrix in (18) can be pre-calculated since the coefficients of $\mathbf{G}_{\mathrm{RF}}$, $\mathbf{G}(\theta_0, \varphi_0)$ and $\mathbf{A}(\theta_0, \varphi_0)$ are known.
- An inverse matrix approximation method is used for calculating the inverse of the error matrix, $\mathbf{M}_{\mathrm{e}}(\theta_0, \varphi_0)$ to obtain the compensation coefficients of the all elements.
- The compensated array pattern in the pointing direction, $\tilde{E}_{\mathrm{a}}^{\mathrm{c}}(\theta_0, \varphi_0)$, is calculated as:

$$\tilde{E}_{\mathrm{a}}^{\mathrm{c}}(\theta_0, \varphi_0) = \boldsymbol{w}^{\mathrm{H}}\left(\mathbf{M}_{\mathrm{e}}(\theta_0, \varphi_0)\right)^{-1}\tilde{\boldsymbol{m}}(\theta_0, \varphi_0) \tag{5-20}$$

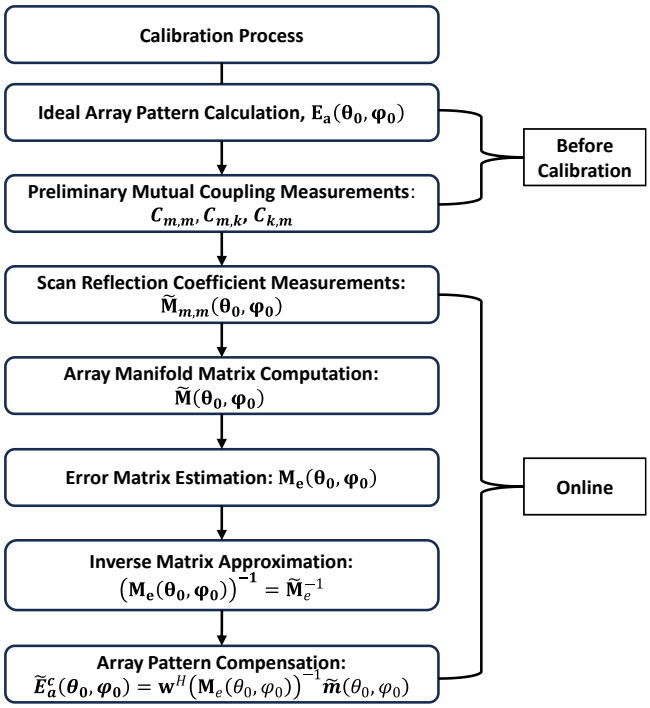

Fig. 5.1. The flow chart of the proposed mutual coupling-based calibration method.

5.2.4.2. Proposed Calibration System

The topology of the proposed transmit array calibration system is depicted in Fig. 5.2. The calibration system consists of four main parts: 1) a transmit antenna array composed of M antenna elements, each connected to a circulator (CR) along with active and/or passive RF front end components such as band-pass filters (BF) and power amplifiers (PA) or power driver amplifiers (PDA), 2) a switching network (SW) composed of RF switches, down-converters baluns, 3) a RF system-on-chip (RF-SoC) FPGA for signal generation, base-band signal processing, switch controlling.

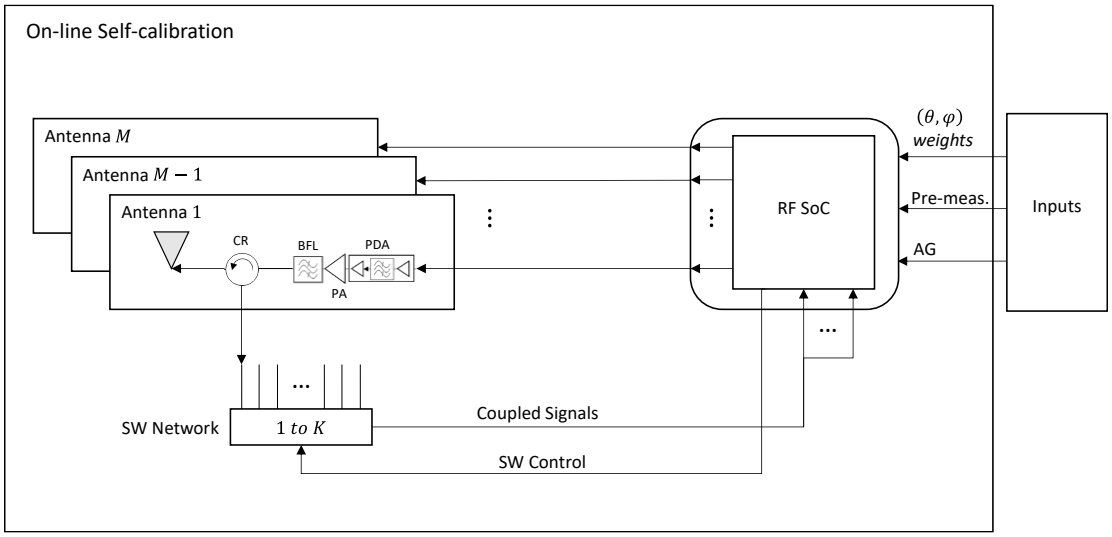

Fig. 5.2. The proposed online large-scale antenna array self-calibration system.

It should be noted that the proposed transmission array system calibration system has flexibility in RF component selection and circuitry. For example, if the frequency of the signal to be transmitted is lower than that of the DACs in the RF-SoC, there is no need to use up-converters in the RF beamformer chips or circuits. The same is valid for the switching network, since the received signals from the circulators will be at the same frequency as the transmitting signal, therefore, there is no need to use down-converters. Moreover, if precision is not required for phase shifts, pin diodes or varactor diodes can be used instead of phase shifter chips for low frequencies to reduce system cost. Finally, in some cases, phase shifts can be performed in the baseband signal processing and in this case, phase shifters may not be needed. However, in order to realize the proposed on-line self-calibration method, circulators, and an RF-SoC are required to receive the feedback signals from the antenna elements or antenna groups and process them in real-time to compensate for the described mutual coupling effects, gain/phase uncertainties, and location errors.

5.2.4.3. Calibration Procedure

The main idea of the calibration process with the transmit array calibration system defined above is to acquire signal samples from each antenna elements or each antenna sub-array with the aid of circulators to estimate the error matrix, $\mathbf{M}_e(\theta_0, \varphi_0)$, in the desired pointing direction with the signal processing in the RF-SoC, and then compensate the weight vector by taking the inverse of the error matrix.

Circulators provide high isolation at the cost of losing signal information of the RF chains connected to the antenna elements. However, measurements of the gain/phase uncertainties of the RF chains are not required since, as stated in (5-12) and (5-15), the gain/phase uncertainties of the m-th RF chain are included in total gain/phase deviation of the signal coupled to its k-th neighboring element and from the reflected signal from m-th element.

Assuming the single element pattern is known primarily, then, the $\mathbf{M}_e(\theta_0, \varphi_0)$, effects the AF and calibration is performed to improve the AF. The array manifold in the pointing direction (θ_0, φ_0) of the transmitting array including all the contributed errors only considering K neighboring element can be expressed as:

$$\widetilde{\mathbf{M}}(\theta_0, \varphi_0) = \begin{bmatrix} w_1 & 0 & \cdots & 0 \\ 0 & w_2 & \cdots & 0 \\ \vdots & \vdots & \ddots & \vdots \\ 0 & \cdots & 0 & w_M \end{bmatrix} \mathbf{M}_e(\theta_0, \varphi_0) \mathbf{G}_{RF}\big(\mathbf{G}(\theta_0, \varphi_0)\mathbf{A}(\theta_0, \varphi_0)\big) \tag{5-21}$$

$$\widetilde{\mathbf{M}}(\theta_0, \varphi_0) = \begin{bmatrix} \widetilde{M}_{1,1} \cdots & \widetilde{M}_{1,k} \cdots & \widetilde{M}_{1,K} \cdots & 0 \\ \vdots \cdots & \vdots \cdots & \vdots \cdots & 0 \\ 0 & \widetilde{M}_{m,k} \cdots & \widetilde{M}_{m,K} & \widetilde{M}_{M,M} \end{bmatrix} \tag{5-22}$$

Then, with a single measurement from all the active antennas while the system is operating, we can derive the following vector:

$$\begin{bmatrix} \widetilde{M}_{1,1}(\theta_0, \varphi_0) \\ \vdots \\ \widetilde{M}_{m,m}(\theta_0, \varphi_0) \\ \vdots \\ \widetilde{M}_{M,M}(\theta_0, \varphi_0) \end{bmatrix} = \begin{bmatrix} \mathbf{M}_e^{1,1} g_1^{RF} e^{-j\Psi_1^{RF}} g_1 e^{-j\Psi_1} e^{-j\delta_1} + \cdots + \mathbf{M}_e^{1,K} g_{1,K}^{RF} e^{-j\Psi_{1,K}^{RF}} g_{1,K} e^{-j\Psi_{1,K}} e^{-j\delta_{1,K}} \\ \vdots \\ \mathbf{M}_e^{m,m} g_m^{RF} e^{-j\Psi_m^{RF}} g_m e^{-j\Psi_m} e^{-j\delta_m} + \cdots + \mathbf{M}_e^{m,K} g_{m,K}^{RF} e^{-j\Psi_{m,K}^{RF}} g_{m,K} e^{-j\Psi_{m,K}} e^{-j\delta_{m,K}} \\ \vdots \\ \mathbf{M}_e^{M,M} g_M^{RF} e^{-j\Psi_M^{RF}} g_M e^{-j\Psi_M} e^{-j\delta_M} + \cdots + \mathbf{M}_e^{M,K} g_{M,K}^{RF} e^{-j\Psi_{M,K}^{RF}} g_{M,K} e^{-j\Psi_{M,K}} e^{-j\delta_{M,K}} \end{bmatrix} \tag{5-23}$$

Finally, the proposed calibration procedure is based on the construction of the error matrix through automated measurements. The integrated circulators in the proposed transmission array calibration system are shown as in Fig. 5.2 allows measurements of only $\widetilde{M}_{m,m}$ and $\widetilde{M}_{m,k}$ but higher isolation yields higher precision.

The measurement procedure consists of two parts: first, to perform the off-line measurements of $\widetilde{M}_{m,k}$ and $\widetilde{M}_{k,m}$ coefficients that are independent of the pointing direction that are registered for later look-up-table and, second, the on-line measurements of $\widetilde{M}_{m,m}$ coefficients that depend on the pointing direction.

The coefficients, $\widetilde{M}_{m,m}$, are measured while the system is operating on the contrary the coefficients, $\widetilde{M}_{m,k}$ and $\widetilde{M}_{k,m}$ are premeasured automatically Fig. 5.3 depicts the measurements of $\widetilde{M}_{m,m}$ and Fig. 5.4 depicts the measurements of $\widetilde{M}_{m,k}$ and $\widetilde{M}_{k,m}$ (in case of unequal coupling). In Fig. 5.3 and Fig. 5.4 y denotes the radiated signal and x denotes the transmitted signal. The calibration system takes premeasured $\widetilde{M}_{m,k}$ and $\widetilde{M}_{k,m}$, coefficients, the array geometry (AG), antenna weights and the pointing direction as input.

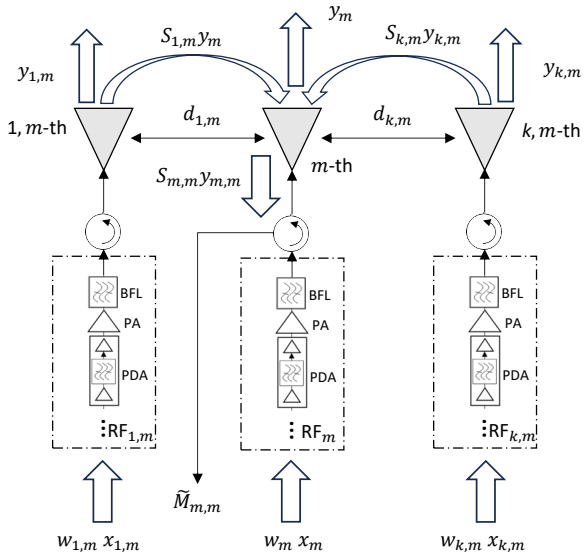

Fig. 5.3. The measurements of the $\widetilde{M}_{m,m}$ coefficients related to scan reflection.

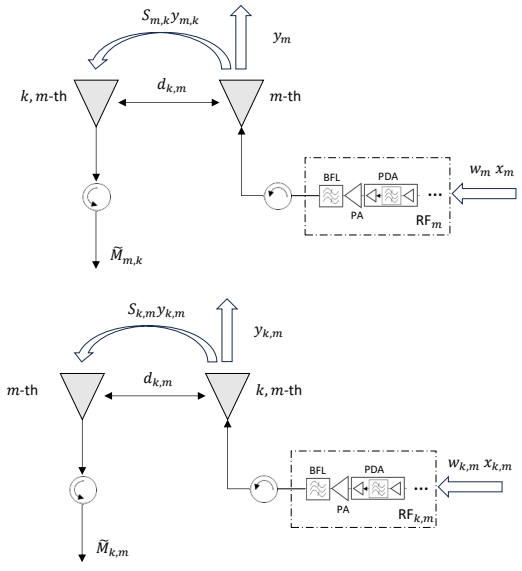

Fig. 5.4. The measurements of the $\widetilde{M}_{m,k}$ and $\widetilde{M}_{k,m}$ coefficients related to inter-element coupling.

5.2.4.4. Inverse Matrix Approximation

Direct inversion of matrices is unfavourable for hardware since direct inversion involves a division operator, which often leads to inaccurate results [34]. Therefore, many inverse matrix approximation methods have been proposed in the literature that degrades the inverse matrix operation to matrix multiplications and matrix sums. The most prominent inverse matrix approximation methods can be listed as Newton iteration method (NI), Chebyshev iteration method (CI) and successive over relaxation-based approximate matrix inversion method [37]. However, all of these methods require initial conditions and a Toeplitz or a symmetrical precondition matrix to guarantee the convergence [34].

In absence of reciprocity of mutual coupling between neighbouring antennas, ($C_{mk} \neq C_{km}$), the convergence of these inverse matrix approximation methods is not guaranteed. Therefore, we adopted the inverse matrix approximation method in [34], which is globally convergent without needing any initial Toeplitz or symmetric matrix and preconditions. Then the error compensation matrix in the desired pointing direction, $\widetilde{\mathbf{M}}_e^{-1} \epsilon\, \mathbb{C}^{M\times M}$, can be approximated as:

$$\widetilde{\mathbf{M}}_e^{-1}(i+1) = \widetilde{\mathbf{M}}_e^{-1}(i) + \mathbf{X}\left(\mathbf{M}_e^T - \mathbf{B}\widetilde{\mathbf{M}}_e^{-1}(i)\right) \tag{5-24}$$

where i is the iteration number, $\mathbf{X} = (\mathbf{I}_M + (\mathbf{M}_e^T\mathbf{M}_e)^2)^{-1}$, $\mathbf{B} = (\mathbf{M}_e^T\mathbf{M}_e)^2$. The detailed formulation for the adopted inverse matrix approximation can be found in [34].

5.2.4.5. Complexity of The Method

The computational complexity of the proposed method lies in inverse matrix approximation method. According to [34], computational complexity for an antenna array with the number of antennas, M, is $O(8M^3 + 2M^2 + M)$ in terms of number of complex multiplications. If only K neighboring elements taking into account the computational complexity can be greatly reduced because of the zero entries in the error matrix. However, this discussion is not the subject of this paper. On the other hand, $2M(M-1)$ measurements are needed to extract the coupling coefficients if all the array elements are taken into account and there is no reciprocity between the elements. However, only $K(K-1)$ measurements are needed if only K neighboring elements are taken into account and there is reciprocity between the elements, then the number of measurements decrease significantly since $K \ll M$.

5.2.5. Simulation Results

In this section the simulation results are given to validate the effectiveness of the proposed calibration method. The numerical examples are based on a planar uniform hexagonal array (UHA) formed by active antenna elements. Number of antenna elements are $M = 61$. Each antenna element has its own RF chain composed of active and passive RF components. Moreover, all elements follow the cosine squared antenna pattern. The inter element distances are $\lambda/2$ and $\sqrt{3}\,\lambda/4$ along x-axis and y-axis, respectively. The operating frequency is selected as 2.4 GHz.

Scattering parameters which represent the mutual coupling between antenna elements are calculated based on an assumption that 30 dB loss per wavelength, λ, on radiated signal power from one active antenna element. The corresponding coupled power is $\approx 3\%$ of the radiated signal power from one element to its neighboring element (-15 dB coupling). The scattering parameters are formed by multiplying magnitude coefficients, S_{mk}, and the phase coefficients, $e^{-j\vec{\mathbf{k}}_0(\hat{\mathbf{r}}_k-\hat{\mathbf{r}}_m)}$ (location errors are included).

In simulations it is assumed no reciprocity between the elements ($C_{mk} \neq C_{km}$). The gain/phase deviations and location errors are modelled according to uncertainty analysis in [38] and are given in Table 5-IV. Please noted that parameters are selected randomly with gamma distribution within the deviation bounds and the phase uncertainty, $\Delta\delta_m$, due to the location errors are related to shift in x-axis as $\Delta\hat{x}_m$ and shift in y-axis as $\Delta\hat{y}_m$.

Table 5-IV. Standard uncertainties.

Parameter	Deviation Bounds
$\Delta\hat{x}_m$[mm]	$\pm$9.8157
$\Delta\hat{y}_m$[mm]	$\pm$9.8157
$\Delta\Psi_m$[o]	$\pm$1.7619
Δg_m[dB]	$\pm$0.5763
$\Delta\Psi_m^{RF}$[o]	$\pm$1.7619
Δg_m^{RF}[dB]	$\pm$0.5763

Fig. 5.5 represents the UHA used in the simulations. In order to provide a better sight, the true locations and the erroneous locations of the antenna elements are given. In simulations, calibrations are performed according to the elements in the first-order neighbourhood of the antenna elements, in the second-order neighbourhood of the antenna elements and all other antenna elements in the array.

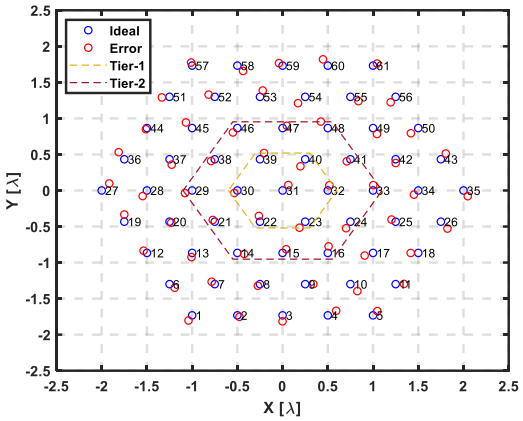

Fig. 5.5. General uniform hexagonal antenna array with the true and the erroneous locations of the antenna elements.

Fig. 5.6 represents the deviations due to the uncertainties in sensor location and gain/phase errors for the simulations for broadside. Similar errors are computed for the other twos cases with $(\theta_0, \varphi_0) = (45°, 0°)$ and $(\theta_0, \varphi_0) = (30°, 60°)$. It can be observed that the total phase errors vary up to 8 degrees and gain errors vary up to 4.5 dB. High deviations are taken in account to demonstrate the performance of the method in the worst case.

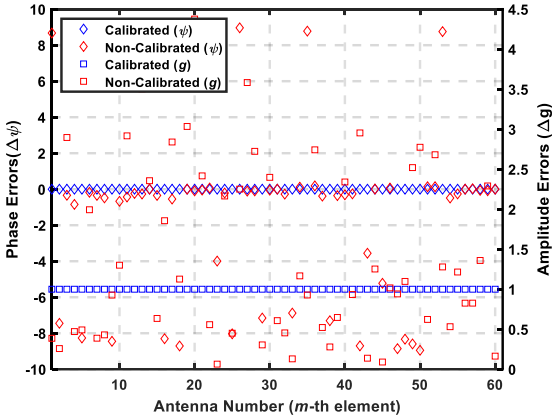

Fig. 5.6. Element wise gain and phase deviations for broadside.

Fig. 5.7 (a) shows the broadside $(\theta_0, \varphi_0) = (0°, 0°)$ pattern compensation. The comparison is performed taking into account calibration with the first-tier and the second-tier of antenna elements as well as full array elements using the inverse matrix approximation (IMA) method in [34]. Moreover, calibration using direct inversion (DI) for full array elements is also included. Furthermore, ideal and not calibrates patterns are given for comparison with calibrated results.

After calibration, the pointing direction of compensated results are correct. In simulations, the maximum phase and locations errors are not too large to produce a phase center plane deviation. Besides, null depths vary as a function of the number of tiers used for mutual

coupling effect meaning in a more accurate phase center location compensation. In broadside case, the high variations lead high side-lobe levels almost same level with pointing direction, also shallow nulls are occurred. In all compensation cases it results in significant improvements on reducing side-lobe levels and deeper nulls. As a remark, the deep nulls are important in interference mitigation. However, the results show that first-order tier compensation has the worst performance.

In Fig. 5.7 (b) same compensation performance can be observed for pointing direction in $(\theta_0, \varphi_0) = (45°, 0°)$. Comparisons show that the compensated patterns have at least 2.5 dB improvement in side-lobe level. Finally, Fig. 5.7 (c) represents the results for $(\theta_0, \varphi_0) = (30°, 60°)$ and it can be concluded that the compensation can be performed in two-dimensional plane. Finally, in all three cases the compensation is performed on the array factor and the antenna patterns are identical for all antenna elements.

As final remarks, 1) compensation performances of full-array inverse matrix approximation method and direct inversion are almost identical, 2) to reduce the side-lobe levels, the mutual coupling of more neighbouring antenna elements are needed to be taken into account, 3) compensation with only first-order or second-order tiers result in reduced precision in calibration, however, more practical for large-scale antenna arrays since only K measurements are needed instead of M measurements where $K \ll M$. It should be noted K or M measurements are needed if reciprocity is assumed between elements, otherwise, $2K$ or $2M$ measurements are needed.

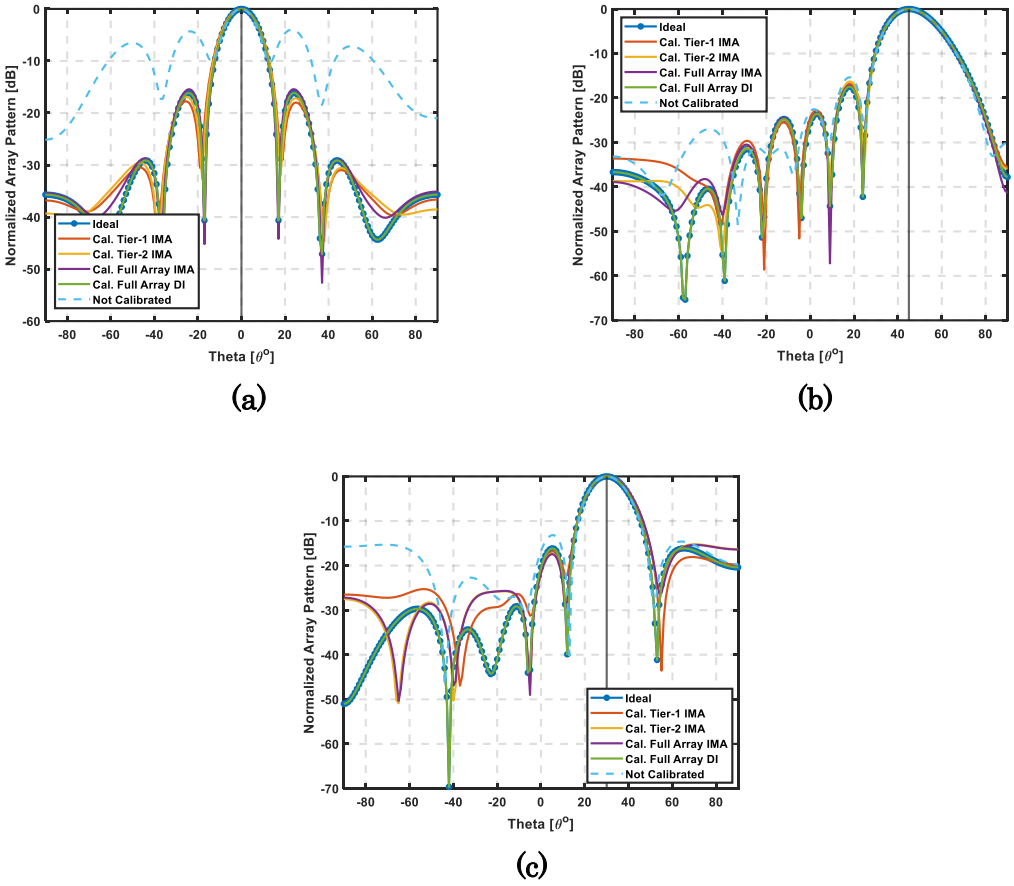

Fig. 5.7. Comparison of ideal array pattern, array pattern after calibration with tier-1 and tier-2 using IMA, array pattern after calibration with full array elements using IMA, array pattern after calibration with full array elements using DI, and not calibrated array pattern in pointing directions: (a) $\theta_0 = 0°$ and $\varphi_0 = 0°$, (b) $\theta_0 = 45°$ and $\varphi_0 = 0°$, (c) $\theta_0 = 30°$ and $\varphi_0 = 60°$.

5.2.6. Experimental Study

In this section we present an experimental study to validate our proposed calibration method. For reduction of complexity and general implementation without lack of validity we conducted a simple experimental study using a linear four-element dipole antenna array ($M = 4$). Fig. 5.9 and Fig. 5.10 show the experimental set-up and its main components. The components of the proposed experimental setup can be listed as follows:

- Antenna array in two pairs to produce differences in gain and phase, for a total of 4 dipole antennas,
- RF cables,
- An on-the-shelf circulator,
- A RFSoC 4x2 board, a high-performance computing system optimized for sampling and generating signals at up to 9.85GSPS. Based on AMD-Xilinx ZYNQ

Ultrascale+ Gen3 RFSoC device, the board offers four high-speed ADC ports (white blocks, tile 224 and 226), two high-speed DAC ports (white blocks, tile 228 and 230), 8GBytes of fast DDR4 memory, and a QSFP28 port for high-speed data offload. The RFSoC board is ideally suited to serve as a powerful and highly configurable software defined radio (SDR) system. The AMD-Xilinx ZYNQ UltraScale+ device includes a quad-core ARM Cortex-A53, a dual-core ARM Cortex R5F, monolithic direct RF-sampling ADCs and DACs, and several other high-performance cores to assist with acquiring and processing high speed data.

- The RFSoC board works with all AMD-Xilinx Vitis/Vivado tools and the PYNQ open-source framework.
- The RFSoC 4x2 board is centered around the ZYNQ XCZU48DR UltraScale+ RFSoC device from AMD-Xilinx, and the most critical features are implemented in the AMD-Xilinx device. The XCZUDR48 includes:

  Processing System:

- A 64-bit quad-core ARM Cortex-A53 and a 32-bit dual-core ARM Cortex-R5F
- An ARM Mali-400 based GPU and NEON advanced SIMD media processing engine Programmable Logic
- Large Programmable logic array with 930K logic cells and 4.2K DSP slices
- IEEE 802.3 compliant 100G Ethernet

  RF System:

- 8 14-bit RF ADCs with 5.0GSPS max sample rate
- 8 14-bit RF DACs with 9.85GSPS max sample rate
- 8 SD-FEC IP blocks

All elements works at the frequency used for the tests (2.4 GHz). It should be noted that the mutual coupling measurements were made using the FGPA board, but the calibration was done with post-processing using MATLAB on the raw data obtained.

Fig. 5.8 shows the components used in the test. In the Processing System (PS) an application has been implemented to obtain the data of the synchronized signals on the Jupyter notebooks, using the PYNQ framework on Linux. In the Programmable Logic (PL) two different chains have been implemented, one for signal transmission and the other for reception.

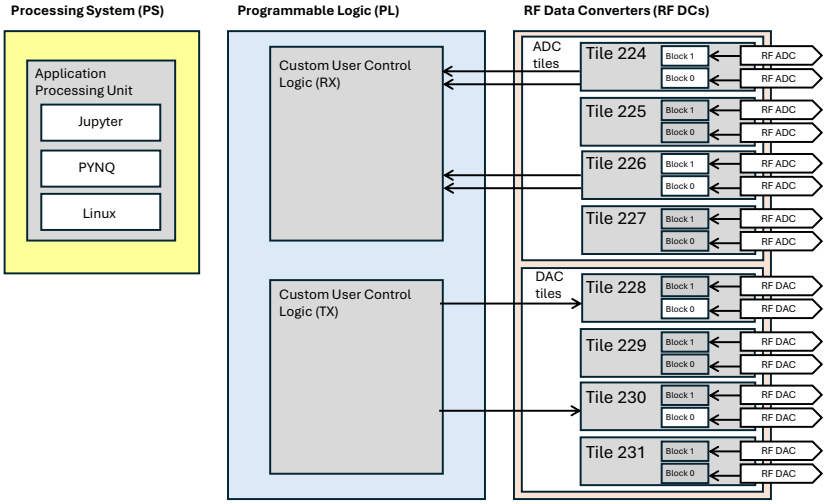

Fig. 5.8. Processing system description for the FPGA unit for the measurements.

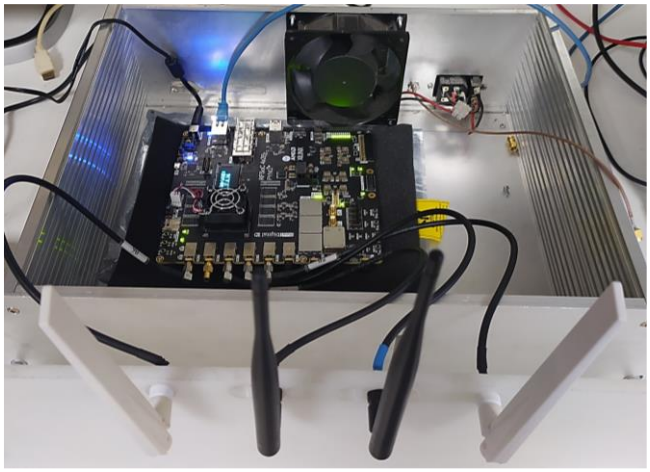

Fig. 5.9. Rack with RFSoC and experimental antenna elements for coupling coefficient measurements C_{mk} and C_{km}.

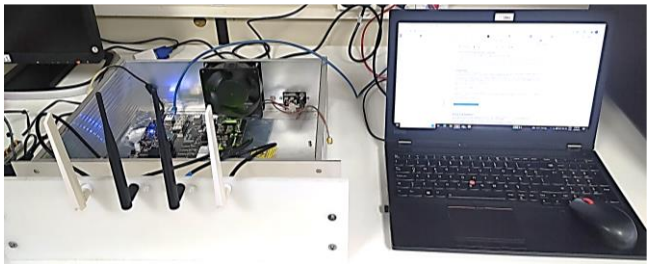

Fig. 5.10. Measurement setup including computer for measurement acquisition for coupling coefficient measurements C_{mk} and C_{km}.

Finally, the RF Data Converters used all the modules available on the board (4 ADCs and 2 DACs), marked in white in the Fig. 5.8, synchronized using the Multi Tile Synchronization algorithm.

In the proposed experimental system, the RF beamformer chip(s) or circuit(s) and switching network proposed in Figure 1 are excluded. Note that BF chips can be used for hybrid architecture implementation while circuits only include RF chains. Additionally, since the RF-SoC used has only 2 DACs, in the baseband, no phase shift is applied to the generated signal. Therefore, experimental work is carried out only on the broadside. The relationship between source direction and mutual coupling is described above in the scan factor of the mutual coupling model used. However, as per Fig. 5.7 the mutual coupling effects, gain/phase uncertainties, and location errors on the antenna array pattern at the broadside is the most significant case.

The details of the experimental procedure are given as below:

1) In the measurements, first premeasurements of the coupling coefficients are conducted. Each element in the antenna array is respectively in transmitter mode and connected to the DAC-A connector on the RF-SoC (which can also be connected to DAC-B). Then, the transmitter antenna is fed with a sinusoidal signal of 2.4 GHz frequency and 0 dBm power, respectively, and the couplings (C_{km}) between the antennas are measured. Then, 3 antennas are connected to the DAC-A port to operate in transmitter mode with an on-the-self power divider, and C_{mk} coefficients are measured one-by-one. In order to compensate for the losses in the power divider, the DAC-A port was fed with a sinusoidal signal at 2.4 GHz frequency and 7 dBm power. Since the phase shifts and losses are different in the cables to which the antennas are connected, non-reciprocity occurs as, $C_{mk} \neq C_{km}$. Additionally, there are slightly different phase shifts and losses between ports in the power divider.

2) In the second part, the measurements of the scan reflection coefficients, C_{mm}, are conducted. In this regard, all antennas are operated in transmitting mode. For this, the power divider is connected to the DAC-A port on the RF-SoC, and the DAC-A port is fed with a sinusoidal signal at 2.4 GHz frequency and 10 dBm power. Then, a circulator is connected sequentially between each antenna and the power divider outputs, and the feedback signals are measured one-by-one by connecting the third port of the circulator to the ADC-A port on the RF-SoC.

3) As a third step, two array manifold matrices including mutual coupling, gain/phase uncertainties and location errors, are created for comparison, one for calibration with the first-order tiers and one for calibration the full array elements. Since the relationship between mutual coupling and phase changes due to gain/phase uncertainties and position errors has been explained previously, the measured C_{mk}, C_{mk} and C_{mm} coefficients are the entries of the array manifold matrix $\tilde{\mathbf{M}}(\theta_0, \varphi_0)$. The two array matrices (pointing to broadside) are given respectively as:

$$\widetilde{\mathbf{M}}_1 = \begin{bmatrix} C_{11} & C_{12} & 0 & 0 \\ C_{21} & C_{22} & C_{23} & 0 \\ 0 & C_{32} & C_{33} & C_{34} \\ 0 & 0 & C_{43} & C_{44} \end{bmatrix} \tag{5-25}$$

$$\widetilde{\mathbf{M}}_2 = \begin{bmatrix} C_{11} & C_{12} & C_{13} & 0 \\ C_{21} & C_{22} & C_{23} & C_{24} \\ C_{31} & C_{32} & C_{33} & C_{34} \\ 0 & C_{42} & C_{43} & C_{44} \end{bmatrix} \tag{5-26}$$

$$\widetilde{\mathbf{M}}_F = \begin{bmatrix} C_{11} & C_{12} & C_{13} & C_{14} \\ C_{21} & C_{22} & C_{23} & C_{24} \\ C_{31} & C_{32} & C_{33} & C_{34} \\ C_{41} & C_{42} & C_{43} & C_{44} \end{bmatrix} \tag{5-27}$$

4) Once the first-order tier, $\widetilde{\mathbf{M}}_1$, the second-order tier $\widetilde{\mathbf{M}}_2$ and full array, $\widetilde{\mathbf{M}}_F$, manifolds are created, then, the coefficients of the error matrices are estimated according to (5-15)-(5-16).

5) In the last step, the inverse matrix approximation method is applied to compensate the error matrices.

Fig. 5.11 represents the 4-element uniform linear array consisting of dipole antenna elements which are used in the experimental study. In order to provide a better sight, the true locations and the coarse erroneous locations of the antenna elements are given. The separation between antenna elements is half wavelength for 2.4 GHz. The coarse erroneous locations of the antenna elements are extracted by using the equations (5-12)-(5-15) once we measure all the phase uncertainties of cables, antenna elements, circulators and so on in the experimental setup. It should be noted this step does not effect nor is related with the calibration procedure, however, Fig. 5.11 is given to show that after measuring the phase errors of the elements in the system, the coarse location of the antenna elements can be estimated if required.

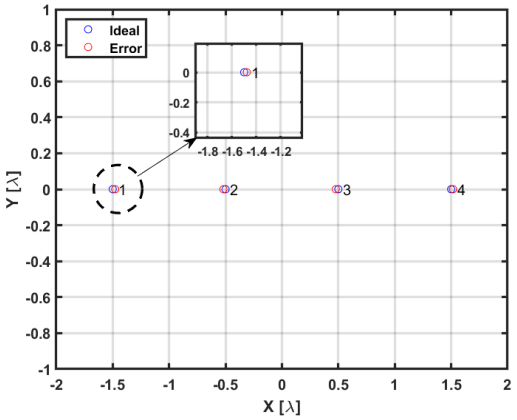

Fig. 5.11. General uniform 4-element linear antenna array with the true and the erroneous locations of the antenna elements.

Fig. 5.12 represents the deviations in amplitude and phase of each element due to the uncertainties in antenna location and gain/phase errors from the measurement results for broadside. In addition, element wise calibrated gain/phase values for broadside using IMA Tier-2 are given in Fig. 5.12. It can be observed that the total phase errors vary up to 1.1 degrees and gain errors vary up to 0.25 dB. In the measurements it can be seen that the amplitude and phase variations are much lower than simulations.

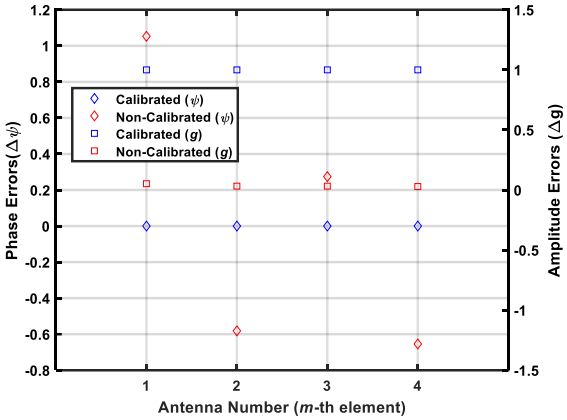

Fig. 5.12. Element wise gain/phase deviations and calibrated gain/phase values for broadside using IMA Tier-2.

Fig. 5.13 shows the broadside $\widetilde{\mathbf{M}}(\theta_0, \varphi_0) = (0°, 0°)$ pattern compensation. The comparison between calibration with the first-tier and the second-tier of antenna elements as well as full array elements using the inverse matrix approximation (IMA) method in [34], calibration using direct inversion (DI) for full array elements, and ideal and not calibrated patterns is given just like in the simulation results. It can be seen that, in practice, the elements in the system have different amplitude and phase deviations resulting in unequal mutual couplings. In addition, since 2.4 GHz is the Wi-Fi frequency, other radiating components in the environment also interacts with the experimental setup in either constructive or destructive way. Moreover, even the amplitude and phase deviations are lower than those in simulations the unequal patterns of the individual antennas cause phase center plane shift, thus, shift in the pointing direction of uncalibrated array can be observed in Fig. 5.13. However, since the calibration is done on array factor, with calibrating each element according to estimated errors, the pointing direction can be also corrected.

The calibration results in Fig. 5.13 for the broadside demonstrates that the compensation of amplitudes and phases, as well as, phase center plane shift are correct. It can be seen that null depths vary as a function of the number of tiers used for mutual coupling effect meaning in a more accurate phase center location compensation as demonstrated in simulation results. In Fig. 5.13, it can be seen that with the proposed method at least 3 dB reduction in the left-side side-lobe level and also the side-lobe levels are equalized.

Moreover, the shallow nulls are improved and most important of all the shift in pointing direction is compensated.

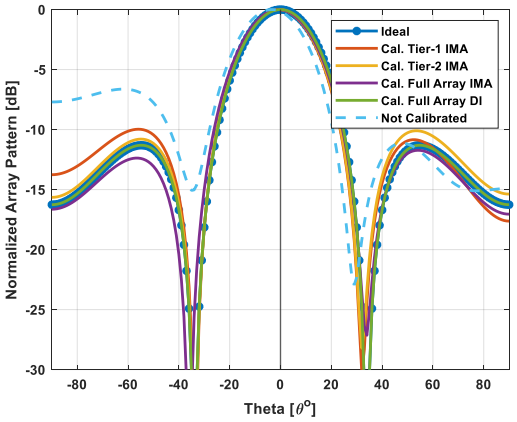

Fig. 5.13. Comparison of ideal array pattern, array pattern after calibration with tier-1 and tier-2 using IMA, array pattern after calibration with full array elements using IMA, array pattern after calibration with full array elements using DI, and not calibrated array pattern in pointing direction: $\theta_0 = 0°$.

5.3. Calibration and Axial Ratio Improvement Method Based on Polarization Agile System Capability

A calibration and AR improvement method based on polarization agile antenna systems is proposed. It is demonstrated that by optimizing the AR based on the element feeding network including amplitude and phase control capability mutual coupling, gain/phase and location errors can be compensated. In case of full digital beamforming, the use of attenuators and phase shifter is not needed so better noise figure and reduction of complexity in distributed elements and analog beamforming network is achieved. The cost in full digital architecture will remain in ADC and DAC components.

The goal of this work is to present a novel calibration solution based on a signal model that includes the effect of mutual coupling and the location, gain/phase errors of the antenna, and to compensate their effects on the radiation pattern based on the capability for AR optimization of agile polarization antenna such as the antenna under test (AUT) used here. The signal model takes into account the characteristics of the updated AUT presented in [39]. One of the characteristics of this antenna is the capacity of controlling the polarization at each radiating element through the control of devices such as signal attenuators and Low Noise Amplifiers (LNA).

The active or phased antenna array systems must comply the following properties: 1. The active antenna array or phased array may consist of sub-arrays of several radiating elements each with its amplifiers and phases shifters, 2. The active antenna array or phased array may have both transmitting and receiving modes with transmitting modules

and those can be included in the analysis of the mutual coupling and errors, 3. The radiation patterns of elements of the antenna array may differ with a non-uniform distribution, 4. Different field modes can be analysed if those are excited with different ports as equivalent narrowband radiating element or by implementing active loads in order to shift the frequency of resonance, and 5. The scan reflection coefficient based on the active element pattern used for the evaluation of the mutual coupling includes the weights to steer the antenna array beam.

The mutual coupling effect on the axial ratio is described as well as how general errors are also compensated. For the demonstration of the method results of simulations with worst case errors and experimental examples are presented.

5.3.1. Main Contributions

The main contributions of a calibration and axial ratio improvement method based on polarization agile system capability are summarized as follows:

- The equations of circular polarized antenna array is derived under antenna array impairments and errors.
- The proposed method is capable of compensating location, gain/phase errors and mutual coupling effects automatically.
- The proposed method suitable for off-line and on-site calibration processes.
- The proposed method compensates all errors and as well as mutual coupling effects by optimizing the axial ratio by only correcting the amplitudes of both cross-polarized and co-polarized components.

5.3.2. Theoretical Formulation

Modelling of the coupling, gain/phase deviations, and location errors to be used in the analysis in conjunction with the active element pattern and the antenna array are explained.

5.3.2.1. Element Pattern and Polarization

Fig. 5.14 presents a general definition of a planar array and the 3D problem of miss-pointing due to errors. The coordinates system is defined with z-axis pointing to the broadside direction of the planar antenna array. Furthermore, the circular polarized field as a function of the two electric field components is represented. The depicted phase difference between the orthogonal components is 90 degrees obtaining a right hand circular polarized electric field (dotted blue line) from each single radiating element.

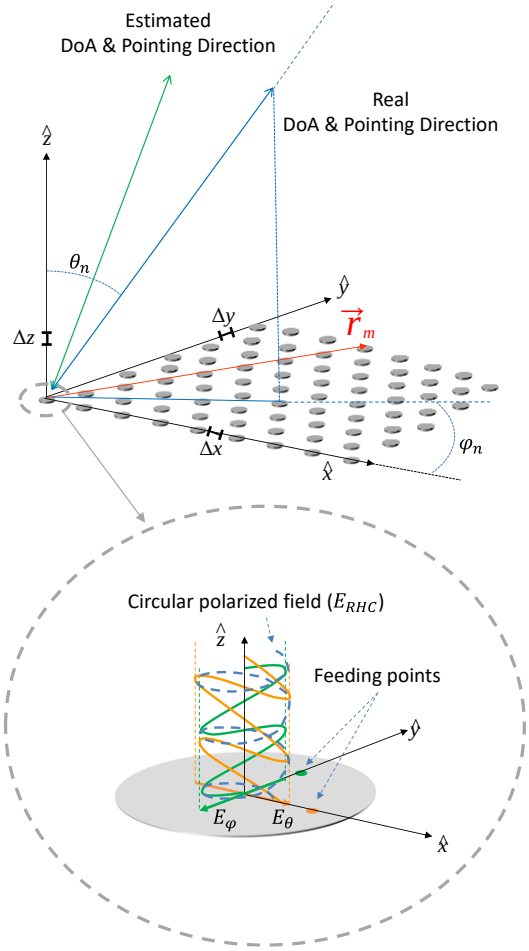

Fig. 5.14. General definition of planar array geometry and circular polarization components.

The antenna element pattern of the right-hand circular polarization and left-hand circular polarization in the direction (θ_n, φ_n) which is defined in a $N_\theta \times N_\varphi$ angle grid, in spherical coordinates can be expressed as:

$$E_{RHC}(\theta_n, \varphi_n) = \frac{1}{\sqrt{2}}\left[E_\theta(\theta_n, \varphi_n) + jE_\varphi(\theta_n, \varphi_n)\right] \tag{5-28}$$

$$E_{LHC}(\theta_n, \varphi_n) = \frac{1}{\sqrt{2}}\left[E_\theta(\theta_n, \varphi_n) - jE_\varphi(\theta_n, \varphi_n)\right] \tag{5-29}$$

The polarized isolated element patterns along θ-axis and φ-axis of the m-th element in an antenna array with M elements can be expressed as:

$$E_\theta^m(\theta_n, \varphi_n) = E_\theta(\theta_n, \varphi_n)V_m^+ P_{x,m} e^{-jk\hat{\mathbf{r}}_n\vec{\mathbf{r}}_m} \tag{5-30}$$

$$E_\varphi^m(\theta_n, \varphi_n) = E_\varphi(\theta_n, \varphi_n)V_m^+ P_{y,m} e^{-jk\hat{\mathbf{r}}_n\vec{\mathbf{r}}_m} \tag{5-31}$$

where , V_m is the excitation voltage of the m-th element being as $V_m = {V_m}^+ + {V_m}^-$, the phase of the m-th element is $\hat{\mathbf{r}}_n\vec{\mathbf{r}}_m = (x_m \sin\theta_n \cos\varphi_n + u_m \sin\theta_n \sin\varphi_n + z_m \cos\theta_n)$, $k = 2\pi/\lambda$ and

λ is the wavelength of the operating frequency, $P_{x,m}$ and $P_{y,m}$ are the complex valued polarization coefficients of the m-th element denoting the polarization direction along x-axis and y-axis, respectively and interelement spacing between two adjacent antenna element is $\lambda/2$ in both axis. The coefficients $P_{x,m}$ and $P_{y,m}$ can be calculated as [40]:

$$P_{x,m} = [-sin\,\varphi_n \quad cos\,\varphi_n\,cos\,\theta_n]\begin{bmatrix}\cos\gamma_m \\ \sin\gamma_m e^{j\eta_m}\end{bmatrix} \tag{5-32}$$

$$P_{y,m} = [cos\,\varphi_n \quad sin\,\varphi_n\,cos\,\theta_n]\begin{bmatrix}\cos\gamma_m \\ \sin\gamma_m e^{j\eta_m}\end{bmatrix} \tag{5-33}$$

where $\gamma_m \epsilon [0, \pi/2]$ and $\eta_m \epsilon [-\pi, \pi]$ are the polarization auxiliary angle and polarization phase difference, respectively, to denote the polarization state of the signal m-th element. However, we consider only right-hand or left-hand circular polarizations in this study, thus, $\gamma_m = \pi/4$ and $\eta_m = \pm\pi/2$.

Applying pattern multiplication, the radiated electric field patterns of the complete array E_θ^a and E_φ^a can be written as:

$$E_\theta^a(\theta_n, \varphi_n) = E_\theta(\theta_n, \varphi_n)\big((\boldsymbol{v}^+)^T(\boldsymbol{p}_x \odot \boldsymbol{a})\big) \tag{5-34}$$

$$E_\varphi^a(\theta_n, \varphi_n) = E_\varphi(\theta_n, \varphi_n)\Big((\boldsymbol{v}^+)^T\big(\boldsymbol{p}_y \odot \boldsymbol{a}\big)\Big) \tag{5-35}$$

where $\odot$ is the Hadamard product, $\boldsymbol{v}^+ \epsilon \mathbb{C}^{M\times 1}$ is the excitation coefficient vector being as $\boldsymbol{v}^+ = [V_1^+ \ldots V_m^+, \ldots V_M^+]$, $\boldsymbol{p}_x \epsilon \mathbb{C}^{M\times 1}$ and $\boldsymbol{p}_y \epsilon \mathbb{C}^{M\times 1}$ are the polarization coefficient vectors being as $\boldsymbol{p}_x = \big[P_{x,1}, \ldots P_{x,m}, \ldots P_{x,M}\big]$ and $\boldsymbol{p}_y = \big[P_{y,1}, \ldots P_{y,m}, \ldots P_{y,M}\big]$, $\boldsymbol{a} \epsilon \mathbb{C}^{M\times 1}$ is the ideal steering vector being as $\boldsymbol{a} = \big[e^{-jk\hat{\mathbf{r}}_n\vec{\mathbf{r}}_1}, \ldots e^{-jk\hat{\mathbf{r}}_n\vec{\mathbf{r}}_m}, \ldots e^{-jk\hat{\mathbf{r}}_n\vec{\mathbf{r}}_M}\big]$.

5.3.2.2. Error Models

Once the expressions of polarized active antenna array are explained it is possible to introduce the mutual coupling, gain/phase deviations, and location errors to the pattern models. Error modelling consists of two subheadings: inter-element errors and intra-element errors. In inter-element errors we consider the errors between the antenna array elements, on the contrary, in intra-element errors we take into account the errors between two feeding points on the same antenna element. The mutual coupling formulation is based on the active element model in [41] resulting the mutual coupling matrix, $\mathbf{C} \epsilon\, \mathbb{C}^{M\times M}$.

The array manifold matrix, $\widetilde{\mathbf{M}}(\theta_n, \varphi_n) \epsilon\, \mathbb{C}^{M\times M}$, including inter-element errors and mutual coupling between array elements can be expressed as [41]:

$$\widetilde{\mathbf{M}}(\theta_n, \varphi_n) = \mathbf{C}\big(\Delta\mathbf{G}_{RF}\Delta\mathbf{G}(\theta_n, \varphi_n)\Delta\mathbf{A}(\theta_n, \varphi_n)\big)\big(\mathbf{G}_{RF}\mathbf{G}(\theta_n, \varphi_n)\mathbf{A}(\theta_n, \varphi_n)\big) \tag{5-36}$$

where $\Delta\mathbf{G}_{RF} \epsilon\, \mathbb{C}^{M\times M}$ is a diagonal matrix, whose m-th diagonal element, $\Delta g_m^{RF} e^{j\Delta\Psi_m^{RF}}$ represents the gain/phase uncertainty coefficient of the RF chain of the m-th element,

$\Delta\mathbf{G}(\theta_n,\varphi_n)\in\mathbb{C}^{M\times M}$ and $\Delta\mathbf{A}(\theta_n,\varphi_n)\in\mathbb{C}^{M\times M}$ are the diagonal matrices, whose m-th diagonal elements, $\Delta g_m e^{j\Delta\Psi_m}$ and $e^{j\Delta\delta_m}$ represent the gain/phase uncertainty and phase uncertainty due to the location errors coefficients of the m-th element and $\mathbf{G}(\theta_n,\varphi_n)\in\mathbb{C}^{M\times M}$ and $\mathbf{A}(\theta_n,\varphi_n)\in\mathbb{C}^{M\times M}$ are the diagonal matrices, whose m-th diagonal elements, $g_m e^{j\Psi_m}$ and $e^{j\delta_m}$ represent ideal gain/phase coefficient and phase coefficients of the m-th element for (θ_n,φ_n), respectively. The mutual coupling coefficients of matrix $\mathbf{C}$ can be expressed as:

$$C_{m,m}=\frac{V_m^-}{V_m^+}=e^{jk(\hat{\mathbf{r}}_0-\hat{\mathbf{r}}_n)\vec{\mathbf{r}}_m}\left(S_{mm}+\sum_{k=1}^{K}S_{mk}e^{-jk\hat{\mathbf{r}}_n\vec{\mathbf{r}}_k}\right) \tag{5-37}$$

$$C_{m,k}=\frac{V_k^-}{V_m^+}=S_{mk}e^{jk\hat{\mathbf{r}}_n\vec{\mathbf{r}}_m}e^{-jk\hat{\mathbf{r}}_n\vec{\mathbf{r}}_k} \tag{5-38}$$

where $\vec{\mathbf{r}}_k$ is the position vector of the k-th neighbor of the m-th element, S_{mk} is the magnitude of the scattering (coupling) coefficients of the m-th element and its k-th neighbor. Since the coupling depends on the distance between two antenna elements, the location errors of the antenna elements directly affect the coupling as phase and amplitude deviations, therefore, no particular notation is given for location errors in (5-37) and (5-38).

The antenna element is fed by two orthogonal ports in order to provide circular polarization. In this sense, the intra-element errors are the mutual coupling between two feeding ports and the location errors of the ports which effect the polarization phase difference, η, and the RF circuit phase and gain deviations of each port. We define the polarization phase difference of the m-th element, η_m, between ports a and b as:

$$\eta_m=\Theta_{a,m}-\Theta_{b,m}=90^o \qquad (RHCP) \tag{5-39}$$

$$\eta_m=\Theta_{a,m}-\Theta_{b,m}=-90^o \qquad (LHCP) \tag{5-40}$$

where $\Theta_{a,m}$ and $\Theta_{b,m}$ are the ideal phases of the ports a and b of the m-th element, respectively. The location errors of feeding ports add additional polarization phases of η_m, are $\Delta\eta_{a,m}$ and $\Delta\eta_{b,m}$. Besides, the RF circuits connected to each port contributes phase errors. Considering, right-hand circular polarization, including phase errors then the polarization phase difference, η_m, takes the form as:

$$\hat{\eta}_m=\left(\Theta_{a,m}+\Delta\eta_{a,m}+\Delta\Psi_{a,m}^{RF}\right)-\left(\Theta_{b,m}+\Delta\eta_{b,m}+\Delta\Psi_{b,m}^{RF}\right) \tag{5-41}$$

where $\Delta\Psi_{a,m}^{RF}$ and $\Delta\Psi_{b,m}^{RF}$ are the phase deviations of the RF circuits. Then, the mutual coupling matrix of the ports of the m-th element can be expressed as:

$$\tilde{\mathbf{C}}_m = \begin{bmatrix} S_{aa}^m & S_{ba}^m e^{j\hat{\eta}_m} \\ S_{ab}^m e^{-j\hat{\eta}_m} & S_{bb}^m \end{bmatrix} \tag{5-42}$$

where S_{aa}, S_{ab}, S_{ba} and S_{bb} are the scattering coefficients of the ports of the m-th element. According to [42], we assume port a effects the $E_\theta(\theta_n, \varphi_n)$ field and port b effects the $E_\varphi(\theta_n, \varphi_n)$ Then, based on the aforementioned statements, we can derive the array manifold matrices $\mathbf{M}_\theta(\theta_n, \varphi_n) \in \mathbb{C}^{M\times M}$ and $\mathbf{M}_\varphi(\theta_n, \varphi_n) \in \mathbb{C}^{M\times M}$ in the pointing direction, (θ_n, φ_n), as follows:

$$\mathbf{M}_\theta(\theta_n, \varphi_n) = (\mathbf{I}_{M\times M} + \boldsymbol{s}_{ba}\boldsymbol{d}_{ba})\widehat{\mathbf{G}}_{\mathrm{RF,a}}\left(\Delta\mathbf{G}(\theta_n, \varphi_n)\widehat{\mathbf{P}}_x\Delta\mathbf{A}(\theta_n, \varphi_n)\right)\widetilde{\mathbf{M}}(\theta_n, \varphi_n) \tag{5-43}$$

$$\mathbf{M}_\varphi(\theta_n, \varphi_n) = (\mathbf{I}_{M\times M} + \boldsymbol{s}_{ab}\boldsymbol{d}_{ab})\widehat{\mathbf{G}}_{\mathrm{RF,b}}\left(\Delta\mathbf{G}(\theta_n, \varphi_n)\widehat{\mathbf{P}}_y\Delta\mathbf{A}(\theta_n, \varphi_n)\right)\widetilde{\mathbf{M}}(\theta_n, \varphi_n) \tag{5-44}$$

where $\boldsymbol{s}_{ba} \in \mathbb{C}^{M\times 1}$ and $\boldsymbol{s}_{ab} \in \mathbb{C}^{M\times 1}$ are the intra-element scattering coefficient vectors of M element being as $\boldsymbol{s}_{ba} = \left[S_{ba}^1, \dots S_{ba}^m, \dots S_{ba}^M\right]$ and $\boldsymbol{s}_{ab} = \left[S_{ab}^1, \dots S_{ab}^m, \dots S_{ab}^M\right]$, respectively, $\boldsymbol{d}_{ba} \in \mathbb{C}^{M\times 1}$ and $\boldsymbol{d}_{ab} \in \mathbb{C}^{M\times 1}$ are the intra-element phase difference vectors of M element being as $\boldsymbol{d}_{ba} = \left[e^{j\hat{\eta}_1}, \dots e^{j\hat{\eta}_m}, \dots e^{j\hat{\eta}_M}\right]^T$ and $\boldsymbol{d}_{ab} = \left[e^{-j\hat{\eta}_1}, \dots e^{-j\hat{\eta}_m}, \dots e^{-j\hat{\eta}_m}\right]^T$,respectively, $\widehat{\mathbf{G}}_{\mathrm{RF,a}} \in \mathbb{C}^{M\times M}$ and $\widehat{\mathbf{G}}_{\mathrm{RF,b}} \in \mathbb{C}^{M\times M}$ are the diagonal matrices, whose complex valued elements represent the phases and gains of the RF circuits including gain/phase deviations of the ports a and b, respectively, $\widehat{\mathbf{P}}_x \in \mathbb{C}^{M\times M}$ and $\widehat{\mathbf{P}}_y \in \mathbb{C}^{M\times M}$ are the diagonal matrices whose diagonal elements represent faulty polarization coefficients and can be obtained by substituting η_m by $\tilde{\eta}_m$ in (5-39) and (5-40).

Finally, we can reformulate expressions in (5-28) and (5-29) including the coupling, gain/phase deviations, and location errors as:

$$E_{RHC}(\theta, \varphi) = \frac{1}{\sqrt{2}}\left[\mathbf{M}_\theta(\theta_n, \varphi_n) + j\mathbf{M}_\varphi(\theta_n, \varphi_n)\right] \tag{5-45}$$

$$E_{LHC}(\theta, \varphi) = \frac{1}{\sqrt{2}}\left[\widehat{\mathbf{M}}_\theta(\theta_n, \varphi_n) - j\widehat{\mathbf{M}}_\varphi(\theta_n, \varphi_n)\right] \tag{5-46}$$

5.3.2.3. Error Matrix Estimation

The array manifolds $\mathbf{M}_\theta(\theta_n, \varphi_n)$ and $\mathbf{M}_\varphi(\theta_n, \varphi_n)$ contain the gain/phase uncertainties due to RF components, location errors, element mismatches and mutual coupling effects, and also contain the ideal array parameters, thus, these matrices are known as measurement matrices. Therefore, for calibration error coefficients have to be estimated from the array manifolds. The error matrices for both field components can be estimated by adopting the least squares criteria and can be expressed as:

$$\min_{\mathbf{M}_\theta^e} \left\| \mathbf{M}_\theta(\theta_n,\varphi_n) - \mathbf{G}_{\mathrm{RF,a}}\big(\mathbf{G}(\theta_n,\varphi_n)\mathbf{P}_x\mathbf{A}(\theta_n,\varphi_n)\big) \mathbf{G}_{RF}\mathbf{G}(\theta_n,\varphi_n)\mathbf{A}(\theta_n,\varphi_n)\mathbf{M}_\theta^e \right\|_F^2 \tag{5-47}$$

$$\min_{\mathbf{M}_\varphi^e} \left\| \mathbf{M}_\varphi(\theta_n,\varphi_n) - \mathbf{G}_{\mathrm{RF,b}}\left(\mathbf{G}(\theta_n,\varphi_n)\mathbf{P}_y\mathbf{A}(\theta_n,\varphi_n)\right) \mathbf{G}_{RF}\mathbf{G}(\theta_n,\varphi_n)\mathbf{A}(\theta_n,\varphi_n)\mathbf{M}_\varphi^e \right\|_F^2 \tag{5-48}$$

Since the matrices and vectors $\mathbf{G}_{RF,a}$, $\mathbf{G}_{RF,b}$, $\mathbf{P}_x$, $\mathbf{P}_y$, $\mathbf{G}_{RF}$, $\mathbf{G}(\theta_n,\varphi_n)$ and $\mathbf{A}(\theta_n,\varphi_n)$ are primarily known, the unknown coefficients of the error matrices can be estimated as follows:

$$\mathbf{M}_\theta^e = \left(\left(\acute{\mathbf{M}}_\theta\right)^T\acute{\mathbf{M}}_\theta\right)^{-1}\left(\acute{\mathbf{M}}_\theta\mathbf{M}_\theta(\theta_n,\varphi_n)\right)^T \tag{5-49}$$

$$\mathbf{M}_\varphi^e = \left(\left(\acute{\mathbf{M}}_\varphi\right)^T\acute{\mathbf{M}}_\varphi\right)^{-1}\left(\acute{\mathbf{M}}_\varphi\mathbf{M}_\varphi(\theta_n,\varphi_n)\right)^T \tag{5-50}$$

where $\acute{\mathbf{M}}_\theta$ and $\acute{\mathbf{M}}_\varphi$ can be denoted as:

$$\acute{\mathbf{M}}_\theta = \mathbf{G}_{\mathrm{RF,a}}\big(\mathbf{G}(\theta_n,\varphi_n)\mathbf{P}_x\mathbf{A}(\theta_n,\varphi_n)\big)\mathbf{G}_{RF}\mathbf{G}(\theta_n,\varphi_n)\mathbf{A}(\theta_n,\varphi_n) \tag{5-51}$$

$$\acute{\mathbf{M}}_\varphi = \mathbf{G}_{\mathrm{RF,b}}\left(\mathbf{G}(\theta_n,\varphi_n)\mathbf{P}_y\mathbf{A}(\theta_n,\varphi_n)\right)\mathbf{G}_{RF}\mathbf{G}(\theta_n,\varphi_n)\mathbf{A}(\theta_n,\varphi_n) \tag{5-52}$$

The gain/phase compensation of the complete phased antenna array, then, can be performed. By simply taking the inverses of the $\mathbf{M}_\theta^e$ and $\mathbf{M}_\varphi^e$, then, multiplying with $\mathbf{M}_\theta(\theta_n,\varphi_n)$ and $\mathbf{M}_\varphi(\theta_n,\varphi_n)$, respectively, the both field component are compensated.

However, the direct inversion of matrices often leads to inaccurate results in hardware because of the division operator, therefore, invers matrix approximations are widely used in order to degrade the inverse matrix operation into matrix sums and matrix multiplications [43]. In general, the inverse matrix approximation methods require initial conditions and a Toeplitz or a symmetrical precondition matrix to guarantee the convergence [43].

In case of non-reciprocity of mutual coupling between neighboring antennas, as well as, non-reciprocity in intra-element coupling, the convergence of the standard methods, such as Newton iteration method and Chebyshev iteration method, is not guaranteed. Therefore, in this study we adopted the inverse matrix approximation method in [43]. The adopted method is globally convergent and initial Toeplitz or symmetric matrix is not required without depending on any preconditions.

The inverse approximations of the error matrices in the desired pointing direction can be estimated as:

$$\left(\mathbf{M}_{\theta}^{e}(i+1)\right)^{-1} = \left(\mathbf{M}_{\theta}^{e}(i)\right)^{-1} + \mathbf{X}_{\theta}\left(\left(\mathbf{M}_{\theta}^{e}(i)\right)^{T}\mathbf{B}_{\theta}\left(\mathbf{M}_{\theta}^{e}(i)\right)^{-1}\right) \tag{5-53}$$

$$\left(\mathbf{M}_{\varphi}^{e}(i+1)\right)^{-1} = \left(\mathbf{M}_{\varphi}^{e}(i)\right)^{-1} + \mathbf{X}_{\varphi}\left(\left(\mathbf{M}_{\varphi}^{e}(i)\right)^{T}\mathbf{B}_{\theta}\left(\mathbf{M}_{\varphi}^{e}(i)\right)^{-1}\right) \tag{5-54}$$

where i is the iteration number, $\mathbf{X}_{\theta} \in \mathbb{C}^{M\times M}$ and $\mathbf{X}_{\varphi} \in \mathbb{C}^{M\times M}$ are the initial matrices, $\mathbf{B}_{\theta} = \left(\mathbf{M}_{\theta}^{e}(i)\right)^{T}\mathbf{M}_{\theta}^{e}(i)$ and $\mathbf{B}_{\varphi} = \left(\mathbf{M}_{\varphi}^{e}(i)\right)^{T}\mathbf{M}_{\varphi}^{e}(i)$. The detailed formulation for the adopted inverse matrix approximation can be found in [43].

Then, the compensated fields, $E_{RHC}(\theta,\varphi)$ and $E_{LHC}(\theta,\varphi)$ can be reformulated as:

$$E_{RHC}(\theta,\varphi) = \frac{1}{\sqrt{2}}\left[(\mathbf{M}_{\theta}^{e})^{-1}\mathbf{M}_{\theta}(\theta_n,\varphi_n) + j\left(\mathbf{M}_{\varphi}^{e}\right)^{-1}\mathbf{M}_{\varphi}(\theta_n,\varphi_n)\right] \tag{5-55}$$

$$E_{LHC}(\theta,\varphi) = \frac{1}{\sqrt{2}}\left[(\mathbf{M}_{\theta}^{e})^{-1}\mathbf{M}_{\theta}(\theta_n,\varphi_n) - j\left(\mathbf{M}_{\varphi}^{e}\right)^{-1}\mathbf{M}_{\varphi}(\theta_n,\varphi_n)\right] \tag{5-56}$$

5.3.2.4. Axial Ratio Optimization

Concerning the expressions for right-hand and left-hand circular polarization fields including array manifolds, axial ratio can be optimized considering its definition as $AR = |E_{RHC}| + |E_{LHC}|/|E_{RHC}| - |E_{LHC}|$. Then we can reformulate AR as:

$$AR = \frac{\left(|\mathbf{M}_{\theta} + j\mathbf{M}_{\varphi}| + |\mathbf{M}_{\theta} - j\mathbf{M}_{\varphi}|\right)}{\left(|\mathbf{M}_{\theta} + j\mathbf{M}_{\varphi}| - |\mathbf{M}_{\theta} - j\mathbf{M}_{\varphi}|\right)} \tag{5-57}$$

where $\widetilde{\mathbf{M}}_{\theta} = (\mathbf{M}_{\theta}^{e})^{-1}\mathbf{M}_{\theta}(\theta_n,\varphi_n)$ and $\widetilde{\mathbf{M}}_{\varphi} = \left(\mathbf{M}_{\varphi}^{e}\right)^{-1}\mathbf{M}_{\varphi}(\theta_n,\varphi_n)$.

By definition the AR depends on right-hand and left-hand circular polarization field components. Since the right-hand and left-hand circular polarization components are compensated by the measured coupled signals the compensation of $E_{RHC}(\theta_n,\varphi_n)$ and $E_{LHC}(\theta_n,\varphi_n)$ directly effects the AR, thus, the improvement and optimization of AR is performed.

5.3.3. Calibration Procedure

The main idea of the calibration process is to acquire the coupled intra-element and inter-element signals from each antenna element to estimate the error matrices $\mathbf{M}_{\theta}^{e}$ and $\mathbf{M}_{\varphi}^{e}$. The error matrices, then, can be used for compensating the right-hand side and left-hand side pattern components, thus, the axial ratio of the array is improved. The flow chart of the proposed procedure is given in Fig. 5.15.

The steps of the procedure are given as:

- In the first step theoretical formulations are derived and uncertainty analysis are performed.
- The proper calibration technique is defined in accordance with the system requirements and capabilities.
- The intra-element and inter-element couplings of each antenna in an array are measured since these measurements contain the error and ideal array coefficients.
- Then, the estimation of error matrices, $\mathbf{M}_{\theta}^{e}$ and $\mathbf{M}_{\varphi}^{e}$, are performed to acquire the error coefficients.
- The calibration is simply done by multiplying the inverses of the error signals by the measurement matrices. In that part inverse matrix approximation method is applied.
- Lastly, put the calibrated field matrices $\widetilde{\mathbf{M}}_{\theta}$ and $\widetilde{\mathbf{M}}_{\varphi}$ in the AR formulation, thus, AR improvement is done.

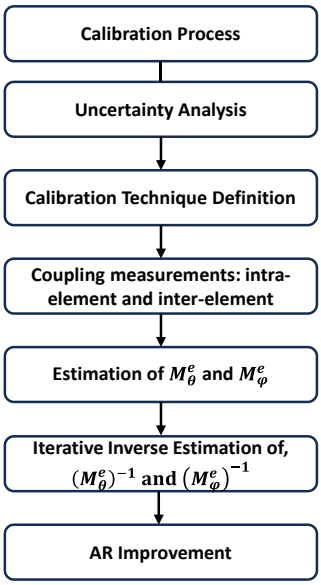

Fig. 5.15. Procedure for the calibration and improvement of the AR for circular polarized active antenna arrays.

5.3.4. Simulation Results

In this section, the simulation results are given to validate the effectiveness of the proposed calibration method. The numerical examples are based on a planar uniform triangular array (URA) formed by $M = 45$ active antenna elements. The inter element distances are $\lambda/2$ and $\sqrt{3}\lambda/4$ along x-axis and y-axis, respectively. The operating frequency for the array is 2.1 GHz. Each antenna element has its own RF chain composed of active and passive RF components (see Figure 5). Moreover, S-parameters between antenna elements are calculated based on an assumption that 30 dB loss per wavelength, λ, on radiated signal power from one active antenna element. Therefore, about 3% of the

radiated signal power from one element is coupled to its adjacent element (−15 dB coupling). It should be noted the mutual coupling is formed by multiplying S-parameters by phase difference coefficient, $e^{-jk(\hat{\mathbf{r}}_m-\hat{\mathbf{r}}_k)\vec{\mathbf{r}}_n}$ (location errors are included). The mutual coupling between self-element ports from the performed measurements is $S_{ab}^m = S_{ba}^m = -4.7$ dB and $\hat{\eta}_m = -121$ degrees. The gain/phase deviations and location errors are modeled according to uncertainty analysis in [44] and are given in Table 5-V. Standard uncertainties. It should be noted that parameters are selected randomly with gamma distribution within the deviation bounds.

Table 5-V. Standard uncertainties.

Parameter	Deviation Bounds	Parameter	Deviation Bounds
$\Delta\hat{x}_m$[mm]	±9.8157	$\hat{G}_{\mathrm{RF,b}}^m$[dB]	±0.6739
$\Delta\hat{y}_m$[mm]	±9.8157	$\Delta\Psi_{b,m}$[o]	±4.8753
Ψ_m[o]	±1.7619	ΔS_{ab}^m[dB]	±0.3388
g_m[dB]	±0.5763	ΔS_{ba}^m[dB]	±0.3388
$\hat{G}_{\mathrm{RF,a}}^m$[dB]	±0.6739	$\hat{\eta}_m$[o]	±7.6894

Fig. 5.16 presents the deviation due to the uncertainties used in sensor location and amplitude/phased errors used for the simulations for broadside. Similar errors are computed for the other twos cases with $(\theta_0, \varphi_0) = (20°, 0°)$ and $(\theta_0, \varphi_0) = (45°, 35°)$. This is noticed that phase errors vary up to 8 degrees in total and amplitude does up to 3.5 gain in total. Those high maximum deviation are taken in account to demonstrate the performance of the method in the worst case. Finally, it is important to mention that location errors include a bias that makes the elements to aim into an oblique plane.

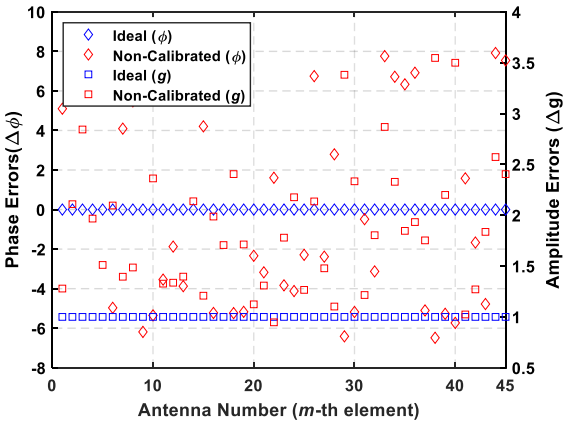

Fig. 5.16. Element wise phase and gain deviation for broadside.

Fig. 5.17 (a) shows the patterns after compensation applying first-order and second-order tiers mutual coupling of elements as well as complete array mutual coupling for $(\theta_0, \varphi_0) = (0°, 0°)$. Furthermore, ideal and non-compensated patterns are shown to be compared with compensated results. The pointing direction of compensated results is accurate. Besides, nulls depth varies as a function of the number of tiers used for mutual coupling effect. The

last affects the capability of mitigate undesired signals in interference presence scenarios. Finally, the bias observed in the simulated errors deviates the pointing direction as well as it is observed the coma effect because of the phase distribution that contains the new phase centers compensating the sensor location, gain/phase and mutual coupling errors. Fig. 5.17 (b) and (c) show the 3D antenna array pattern before and after calibration, respectively.

The large amplitude variation included in simulations produce unsymmetric side-lobes as well as modification on the direction of nulls is observed in Fig. 5.17 (a) in dotted turquoise color curve. Furthermore, the bias that put the elements aiming into an oblique plane makes the array pointing not to broadside and the compensation results shows small comma effect in side-lobes. The last produces higher side-lobe level at left of the pattern.

Fig. 5.18 (a) presents same compensation performance but for $(\theta_0, \varphi_0) = (20°, 0°)$ where the compensated patterns show correction in pointing direction as well as 2.5 dB improvement in side-lobe level. Fig. 5.18 (b) and (c) show the 3D antenna array pattern before and after calibration, respectively. Finally, Fig. 5.19 (a) presents the results for $(\theta_0, \varphi_0) = (45°, 35°)$. This is important to highlight that in the three cases the array factor presents the correct compensation in pointing direction and side-lobe level. Furthermore, it is demonstrated that for improving the side-lobe level mutual coupling from more elements are required to be taken into account in the solution of the problem. Therefore, full array compensation results in lower sidelobe levels, and the compensated array pattern is the same as the ideal case. Fig. 5.19 (b) and (c) show the 3D antenna array pattern before and after calibration, respectively.

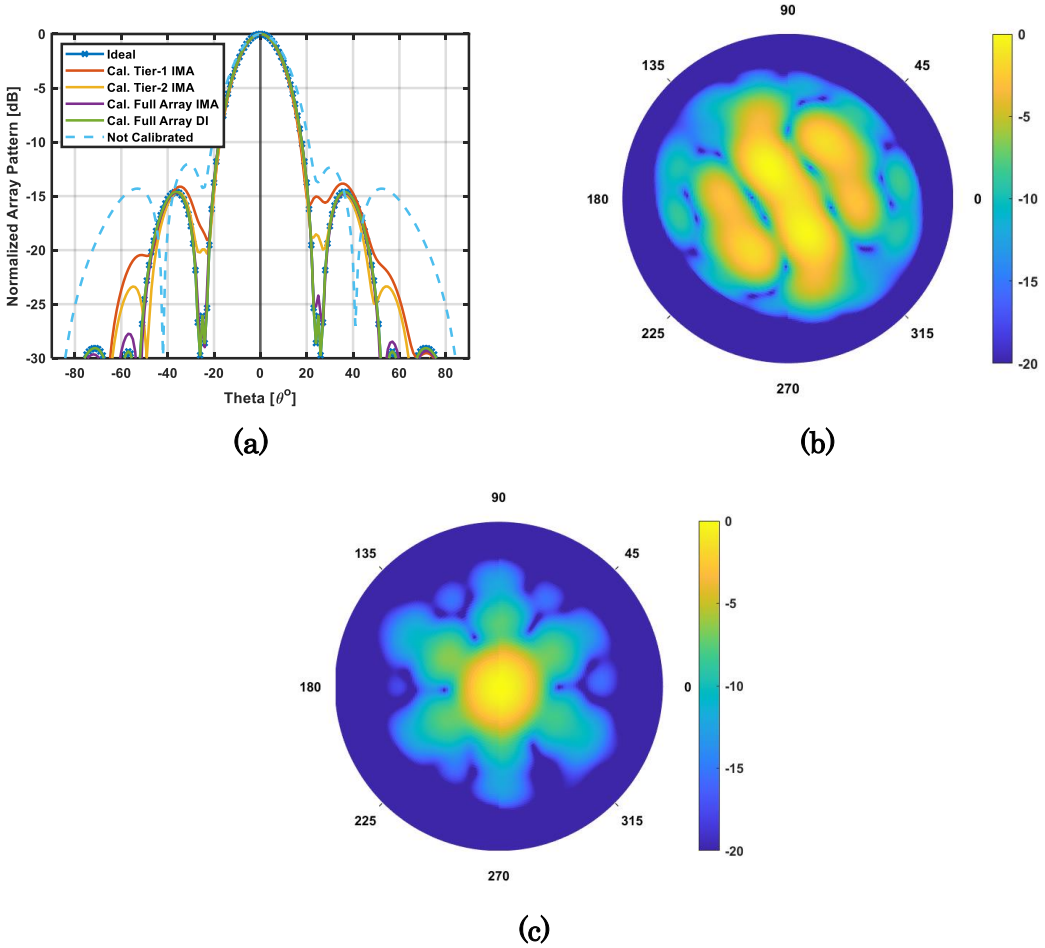

Fig. 5.17. Pattern comparison of array, ideal, compensated with tier-1, tier-2, complete array elements and at: $\theta_o = 0°$ and $\varphi_o = 0°$.

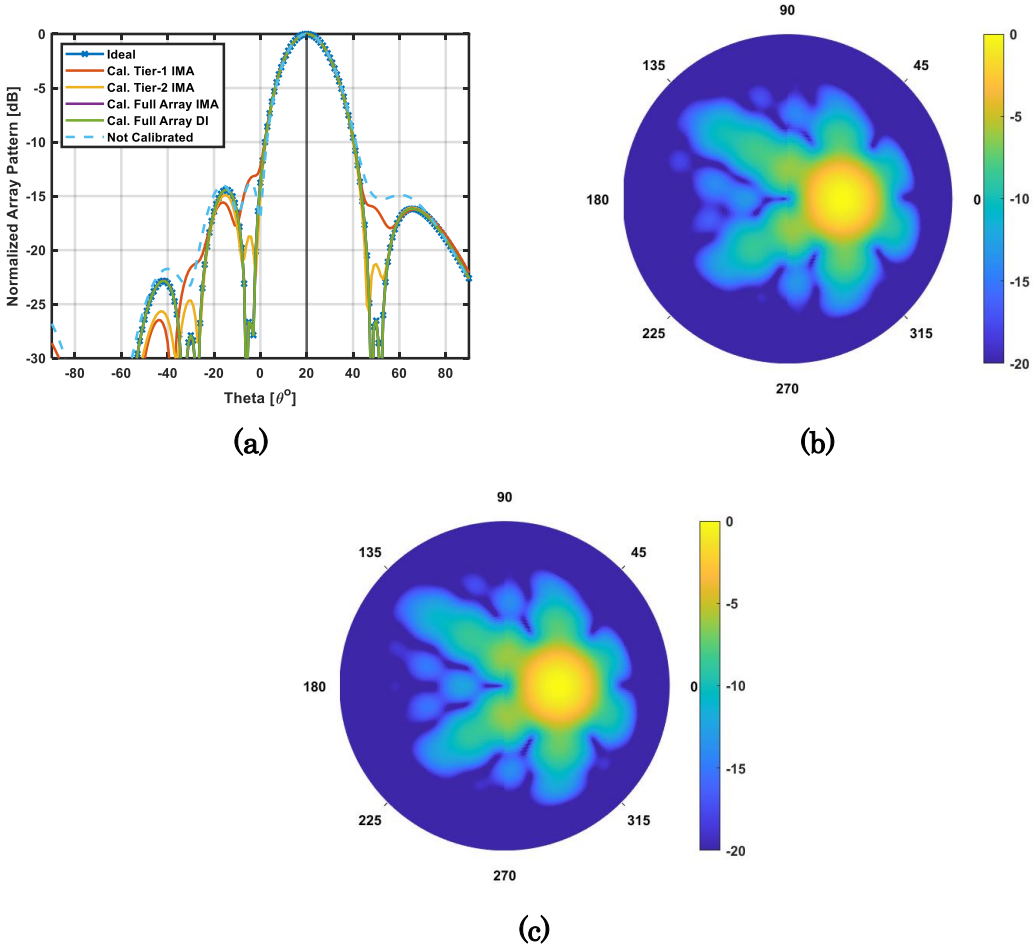

Fig. 5.18. Pattern comparison of array, ideal, compensated with tier-1, tier-2, complete array elements and at: $\theta_o = 20°$ and $\varphi_o = 0°$.

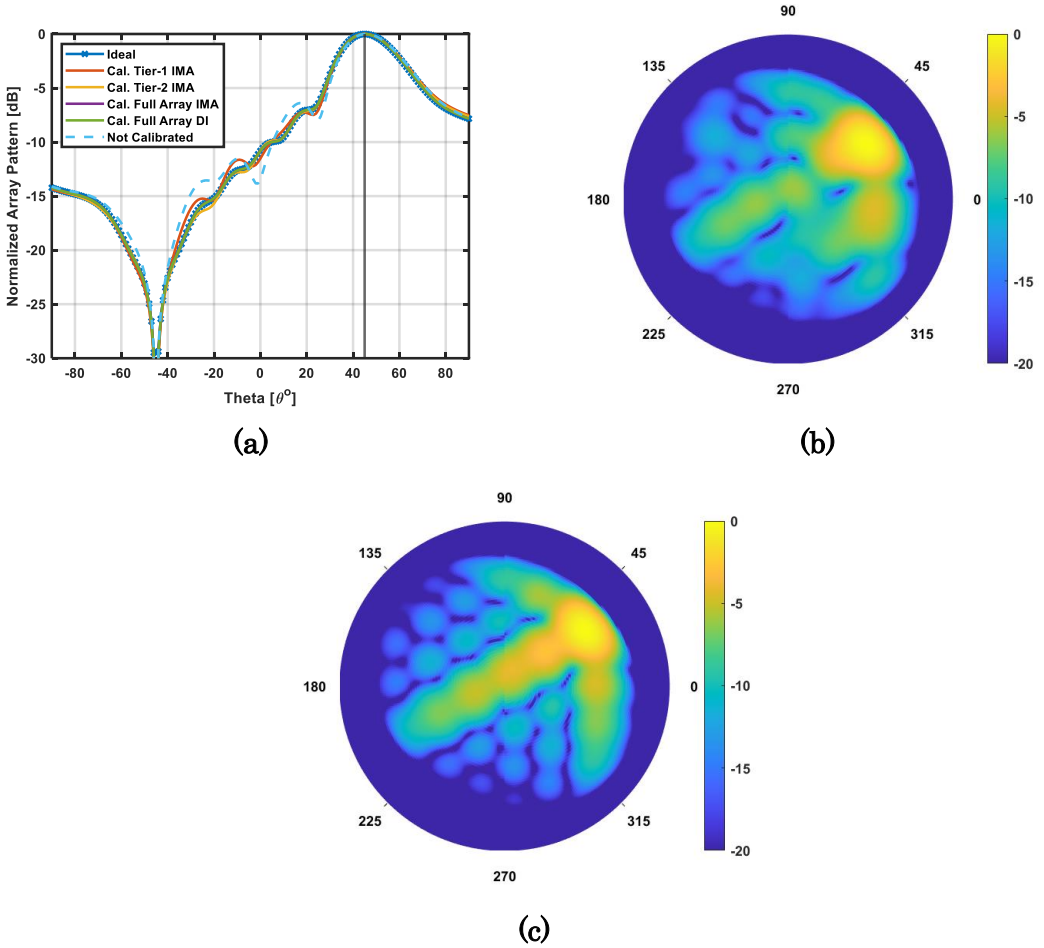

Fig. 5.19. Pattern comparison of array, ideal, compensated with tier-1, tier-2, complete array elements and at: $\theta_o = 45°$ and $\varphi_o = 35°$.

Fig. 5.20 presents the uncompensated and compensated CP and XP patterns of 45 element uniform triangular active antenna array. Fig. 5.20 (a), (b) and (c) show the results of this example for $\theta_o = 0°$, $\theta_o = 20°$ and $\theta_o = 30°$. The $\varphi_o = 0°$ for all of the cases. In those results, a reduction of the XP component higher than 1 dB, 3.2 dB and 4.7 dB at the direction of its main beam is obtained. Moreover, there are significant sidelobe level suppression in both CP and XP. Besides, in Fig. 5.20 it can be observed the reduction of the XP level in the direction of the main beam, while improved variation of AR of 0,02 dB, 0,89 dB and 2,49 dB for $\theta_o = 0°$, $\theta_o = 20°$ and$\theta_o = 30°$. respectively. This is a significant compensation in terms of typical AR requirements. For large number of antenna elements more significant will be the compensation for the CP and XP patterns.

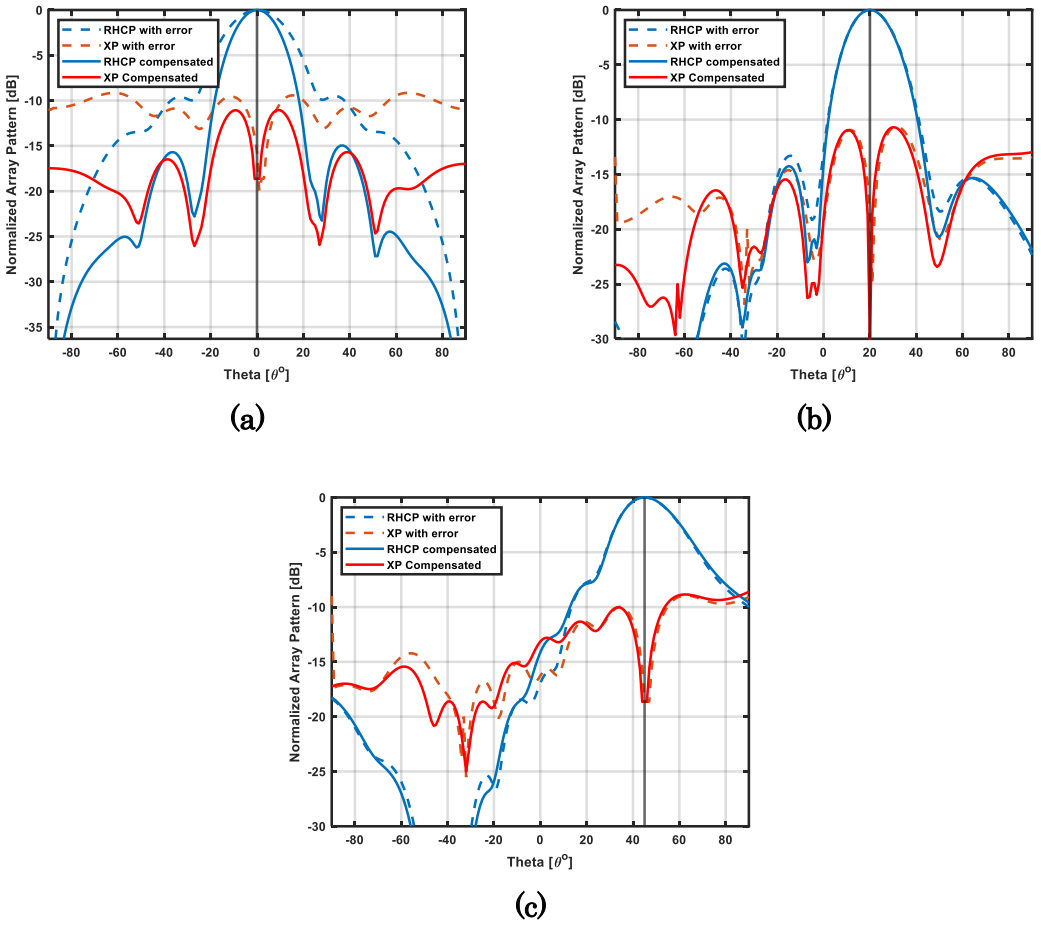

Fig. 5.20. Co-polar and cross-polar pattern of a planar uniform triangular array (UTA) formed by $M = 45$ active antenna element for (a) $\theta_o = 0°$ and $\varphi_o = 0°$, (b) $\theta_o = 20°$ and $\varphi_o = 0°$, (c) $\theta_o = 45°$ and $\varphi_o = 35°$.

5.3.5. Experimental Study

In this section the experimental example is presented. In previous work it was developed the automated system for measurement and characterization [45] of the AUT and its calibration with different techniques as those proposed in [41], [46], [47]. The system was initially designed to operate at 1.7 GHz. For the actual work, the AUT proposed for tracking LEO satellites has been modified and new design proposed. This evolution [39] consisted on moving the operating frequency up to S-band covering both, the transmission band (2.025 – 2.12 GHz) and the reception band (2.2 – 2.3 GHz). Furthermore, the radiating elements of the new AUT are capable to provide dual circular polarization working simultaneously in transmission and reception (Fig. 5.21).

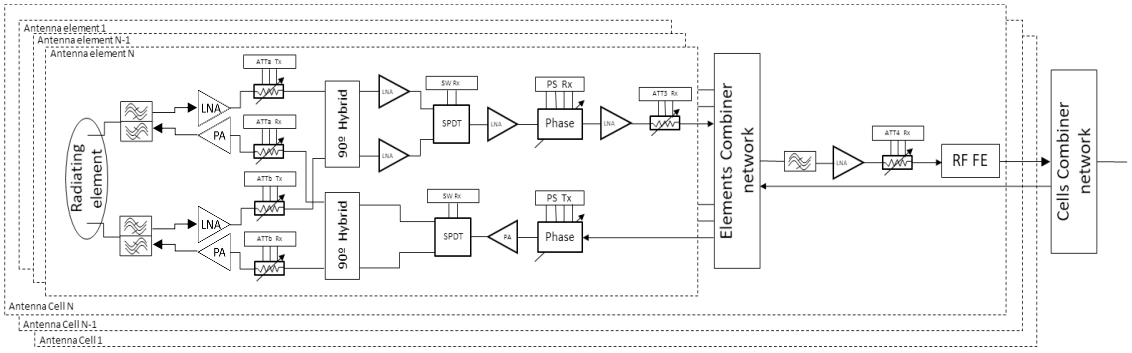

Fig. 5.21. Antenna array architecture used in the experimental example.

Fig. 5.22 presents the 45 elements array of the AUT and the 15 and 5 elements subarrays subject of its evaluation in the experimental example including deviation for simulation in red color.

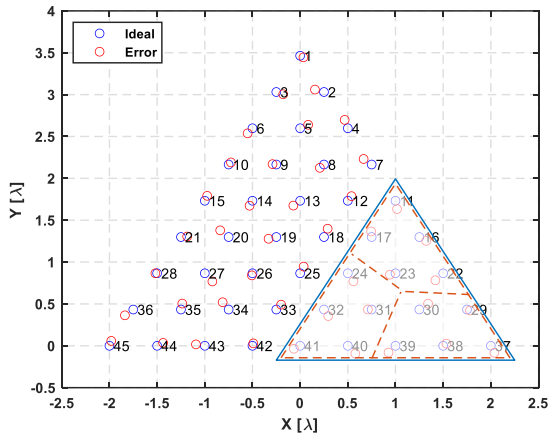

Fig. 5.22. General 45 elements planar antenna array sketch with 15 and 5 elements subarrays definition.

The parameters S_{mk} and S_{ab}^{m} are known values that have been obtained in the measurement campaign of the AUT as described for active antenna arrays in [45]. The parameter S_{ab}^{m} represents the existing relation between the two ports of a single radiating element of the antenna whereas the parameter S_{mk} is a vector that contains the relations of each radiant element of the antenna with their neighbors. The parameter S_{mk} depends on the position of the radiant element.

The coupling values are presented in Table 5-VI, Table 5-VII and Table 5-VIII. Table 5-VI presents the S21 parameters between the radiating element 45th and its first-tier neighbors. Table 5-VII presents the S21 parameters between the radiating element 30th and its first-tier neighbors. Finally, Table 5-VIII presents the S21 parameters between the radiating element 42nd and its first-tier neighbors.

The amplitude and the phase of these parameters represent the S_{mk} and D_{mk} terms. These measured parameters are used for all the elements with the same position and its same neighbor situation within the AUT. The parameters S_{ab}^{m} and $e^{j\hat{\eta}_m}$ represent the relation in

amplitude and phase between two ports of the same radiating element. The typical values of the S_{ab}^{m} and $e^{j\hat{\eta}_m}$ parameters for all de radiating elements of this AUT are of -4.7 dB and -121 degrees, respectively.

Table 5-VI. S21 parameter measured of the radiating element 45 with respect to elements 43 and 44.

Neighbor element	Amplitude [dB]	Phase [º]
45 - 43	-24,51	119,30
45 – 44	-25,15	128,66

Table 5-VII. S21 parameter measured of the radiating element 30 with respect to elements 43, 41, 29 and 28.

Neighbor element	Amplitude [dB]	Phase [º]
30 - 43	-37,26	39,16
30 - 41	-25,13	168,67
30 – 29	-24,22	145,84
30 - 28	-24,65	-129,90

Table 5-VIII. S21 parameter measured of the radiating element 42 with respect to elements 25, 29, 41, 40, 39 and 37.

Neighbor element	Amplitude [dB]	Phase [º]
42 - 25	-24,11	176,85
42 - 29	-38,12	41,28
42 - 41	-24,96	-40,88
42 - 40	-27,26	-31,01
42 - 39	-24,37	143,55
42 - 37	-24,29	137,38

In order to evaluate the proposed calibration method two cases of compensation of errors and mutual couplings effect are presented. These two cases consist of two different pointing directions, for Theta 0 and 45 degrees. For this, it is considered the ideal radiation pattern as well as the effect of errors and mutual coupling using the antenna pattern measured in the anechoic chamber.

A. Compensation of the radiation pattern in the case study for $\theta_o = 0°$ and $\varphi_o = 0°$.

Fig. 5.23 (a) and (b) presents the results of the ideal radiation pattern computed as reference from the isolated radiating element measured in anechoic chamber. This pattern is computer to contrast the radiation pattern that includes errors and mutual coupling effect as well as to the compensated patterns. Fig. 5.23 (a) presents the radiation pattern of the complete sub-array of 15 elements presented in Fig. 5.22 for $\theta_o = 0°$ and $\varphi_o = 0°$ based on the isolated pattern, whereas (b) presents the cuts of the radiation pattern.

The gain of the AUT in this case is 21.62 dBi, the beamwidth is 16.7 degrees whereas the side lobe level is -6.81 dB. Those results will be contrasted with those obtained with the radiation pattern measured (active element patterns measured that includes errors as it is detailed explained in [45]) and the pattern obtained after the compensation.

Fig. 5.23 (c) and (d) show the radiation pattern with errors to be compared with the ideal radiation pattern and the compensated radiation pattern in Fig. 5.23 (e) and (f). Fig. 5.23 (c) presents the radiation pattern of the complete sub-array of 15 elements for $\theta_o = 0°$ and $\varphi_o = 0°$ with errors, Fig. 5.23 (d) presents the cuts of its radiation pattern. In this case, the gain is 20.58 dBi, the beamwidth is 18.81 degrees, and the side lobe level is -6.78 dBi. As it can be observed, the gain is reduced 0.96 dB and the beamwidth increased 2.1 degrees with respect to the reference patterns.

Fig. 5.23 (e) and (f) present the results after applying the compensation of the radiation pattern. Thus, Fig. 5.23 (e) presents the complete radiation pattern compensated of the sub-array of 15 elements for $\theta_o = 0°$ and $\varphi_o = 0°$, whereas Fig. 5.23 (f) presents the cuts of the compensated radiation pattern. In this case, the gain is 21.12 dBi which is 0.54 dB higher with respect to the radiation pattern with errors. The beamwidth is 17.83 degrees being reduced 1 degree with respect to the case with errors as expected. Finally, the side lobe level is -6.8 dB being also enhanced with respect to the uncompensated case. Fig. 5.23 (c) and (e) it is observed that the reduction of the beamwidth after compensation means to increase the low level of the pattern.

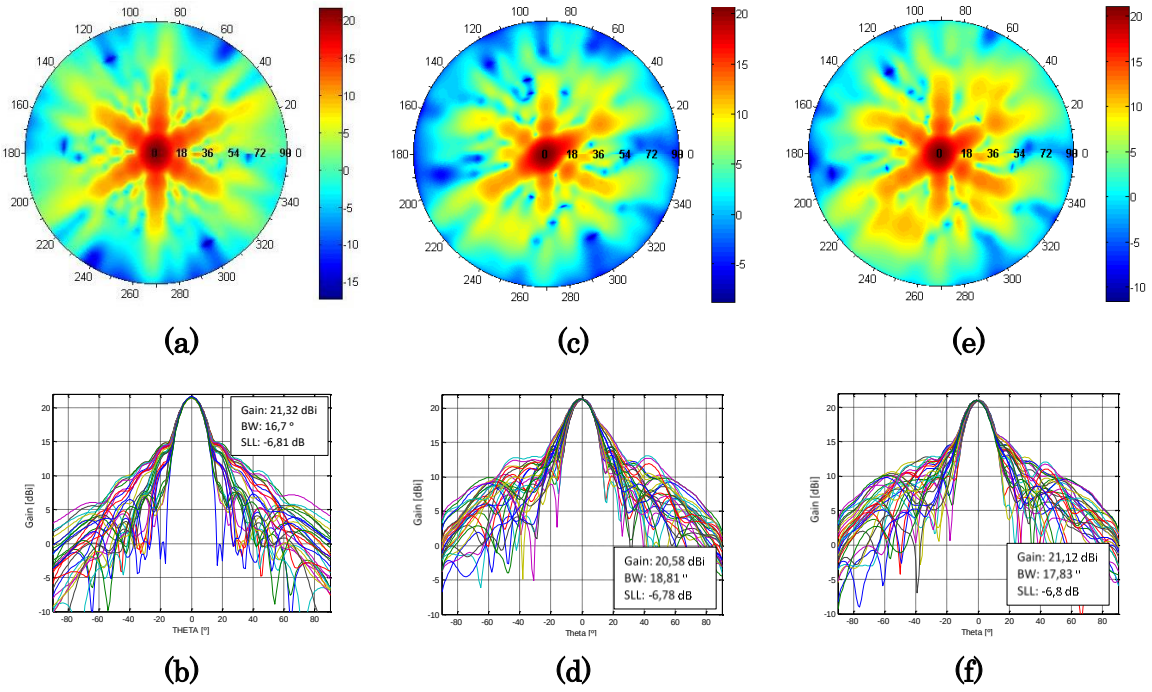

Fig. 5.23. (a) and (b): Pattern of the AUT based on the measured isolated element for $\theta_o = 0°$ and $\varphi_o = 0°$, (c) and (d): Pattern of the AUT before compensation for $\theta_o = 0°$ and $\varphi_o = 0°$, and (e) and (f): Pattern of the AUT after compensation for $\theta_o = 0°$ and $\varphi_o = 0°$.

B. Compensation of the radiation pattern in the case study for $\theta_o = 45°$ and $\varphi_o = 35°$.

The second study case is for $\theta_o = 45°$ and $\varphi_o = 35°$. The ideal radiation pattern based on the isolated radiating element pattern measured is presented as the reference in the Fig. 5.24 (a) and (b). Fig. 5.24 (a) presents the complete radiation pattern of the sub-array of 15 elements for $\theta_o = 45°$ and $\varphi_o = 35°$, whereas Fig. 5.24 (b) presents the cuts of the radiation pattern.

Fig. 5.24 (c) and (d) present the radiation pattern with errors of the case study. Fig. 5.24 (c) presents the complete radiation pattern, whereas (d) presents the cuts of the radiation pattern. In this case, the gain is 19.27 dBi which is 0.76 dB lower with respect to the reference pattern. The beamwidth is 22.09 degrees, which is 1.92 degrees larger than the reference pattern. The side lobe level is -6.12 dB, therefore 1.32 dB lower. Besides, the shape of the main lobe is now elliptical instead of circular due to errors and mainly to mutual coupling.

Fig. 5.24 (e) and (f) present the compensated radiation pattern of the case study, whereas (f) presents the cuts of the radiation pattern. In this case, the gain is 19.48 dBi being 0.21 dB higher than the gain of the uncompensated patterns. The beamwidth is 21.36 degrees which is 0.64 degrees less than with errors. The side lobe level is -5.89 dB which is about 1 dB less than the obtained in the reference patterns. Besides, as observed in the previous case study, in Fig. 5.24 (c) it is noticed that the main beam has an elliptic shape instead of circular due to errors and mutual coupling effect is then corrected in Fig. 5.24 (e).

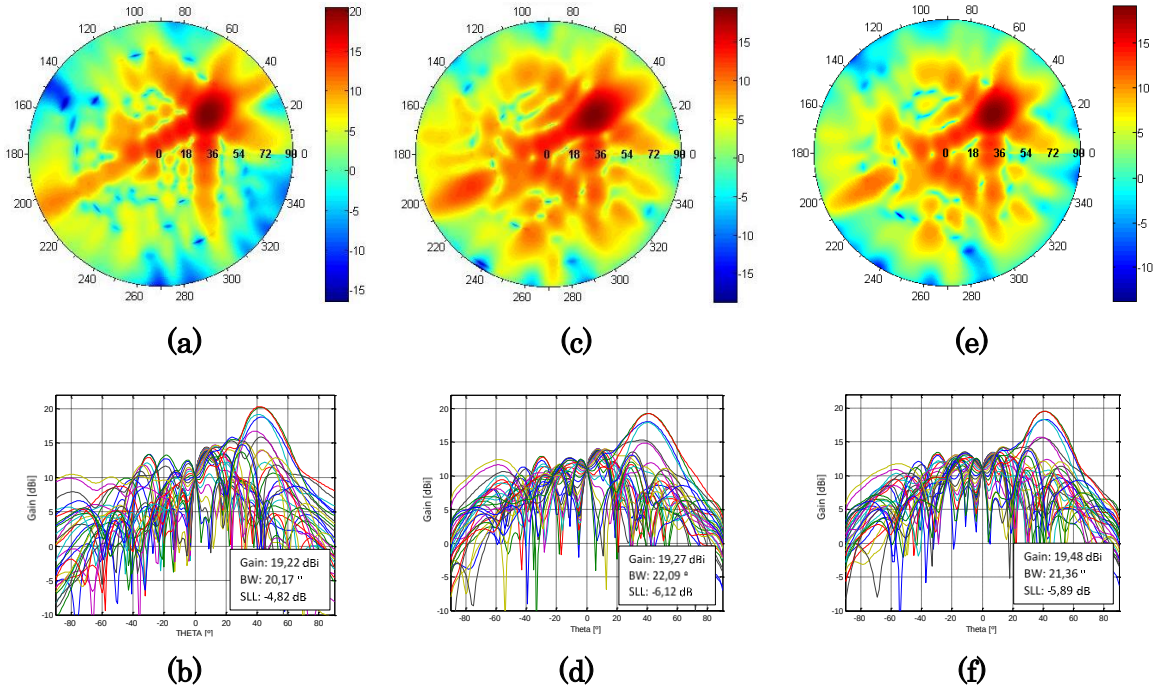

Fig. 5.24. (a) and (b): Pattern of the AUT based on the measured isolated element for $\theta_o = 45°$ and $\varphi_o = 35°$, (c) and (d): Pattern of the AUT before compensation for $\theta_o = 45°$ and $\varphi_o = 35°$, and (e) and (f): Pattern of the AUT after compensation for $\theta_o = 45°$ and $\varphi_o = 35°$.

Table 5-IX and Table 5-X present a comparison of the results obtained in the two-case study. For this, the obtained gain, beamwidth and side lobe level are presented. It is observed that for a pointing direction of theta 45°, the errors and mutual coupling effect contribute to a gain reduction of 1.31 dB in addition to the reduction of 1,59 dB with respect to the broadside pattern gain. This total gain loss higher than 2.9 dB with respect to the gain at broadside direction is too large for the use of a planar antenna in satellite communication system. Thus, calibration systems and its control software are key sub-systems of active antenna array in active antenna arrays system application.

In order to present the significant improvement of the proposed method in the reduction of the XP component (interferer component) we explored the improvement obtained while a reduction of the number of elements of the sub-array under test is done. In this sense, we obtained that a sub-array of 9 elements is a simple and appropriate size for the AUT in order to observe a significant reduction higher than 1 dB, 5 dB and 10 dB of the XP component in the main beam direction as well as the compensation of the CP pattern component, not only in the main beam but also in SLL that impacts in the reduction of the antenna temperature in reception.

Table 5-IX. Pattern parameters comparison for case study of $\theta_o = 0°$ and $\varphi_o = 0°$.

Parameter	Ideal	Uncompensated	Compensated
Gain [dBi]	21,62	20,58	21,12
Beamwidth [º]	16,70	18,81	17,83
Side lobe level [dB]	-6,81	-6,78	-6,80

Table 5-X. Pattern parameters comparison for case study of $\theta_o = 45°$ and $\varphi_o = 35°$.

Parameter	Ideal	Uncompensated	Compensated
Gain [dBi]	20,03	19,27	19,48
Beamwidth [º]	20,17	22,09	21,36
Side lobe level [dB]	-4,82	-6,12	-5,89

Fig. 5.25 presents the uncompensated and compensated CP and XP patterns of one sub-array of the AUT with only 9 active elements. Fig. 5.25 (a), (b) and (c) show the results of this example for $\vartheta_o = 0°$, $\vartheta_o = 20°$ and $\vartheta_o = 30°$. In those results, a reduction of the XP component higher than 1 dB, 5 dB and 10 dB at the direction of its main beam is obtained. Finally, the main beam direction of those cases is also compensated.

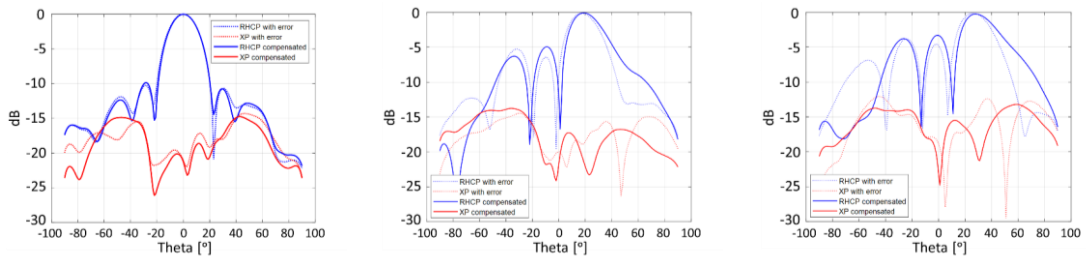

(a) (b) (c)

Fig. 5.25. Co-polar and Cross-polar pattern of a 9 elements sub-arrays of the AUT for (a) $\vartheta_o = 0°$, (b) $\vartheta_o = 20°$ and (c) $\vartheta_o = 0°$.

Nowadays, polarization-agile antenna systems are a promising antenna system concept that needs appropriate calibration methods like the proposed in this work to optimize the antenna performance guarantying optimum AR at the time the antenna is changing the pointing direction.

Table 5-XI presents the parameters comparison for the example of the AUT with 9 active elements for $\vartheta_o = 0°$, $\vartheta_o = 20°$ and $\vartheta_o = 30°$. This table presents the improvements in the CP and XP patterns in terms of the main beam pointing, XPD (XP discrimination) and AR improvements. Besides, in Fig. 8 it can be observed the reduction of the XP level in the direction of the main beam (highlighted with green line), while Table 7 presents the Improved variation of AR of 0,02 dB, 0,89 dB and 2,49 dB for $\vartheta_o = 0°$, $\vartheta_o = 20°$ and $\vartheta_o = 30°$, respectively. This is a significant compensation in terms of typical AR requirements.

For large number of antenna elements more significant will be the compensation for the CP and XP patterns.

Furthermore, the elliptic main beam cross-section of the pattern of a rectangular planar antenna array system is an important issue in SATCOM systems due to the skew angle limitation in onboard satellite communications terminals. If the major axis of the elliptic section of the main beam is too large, for lower skew angles the interference contribution to other adjacent satellite systems will be prohibitive. In this sense, circular polarized antenna systems for SATCOM such as those working at X and K/Ka bands will need to optimize not only the AR at the time the pointing direction is changed but also the correction of the antenna main beam shape is important.

Table 5-XI. Compensated pattern parameters comparison for case study of $\theta_o = 0°, 20°$ and $30°$, and $\varphi_o = 0°$.

Parameter	$(\theta_o, \varphi_o) = (0°, 0°)$	$(\theta_o, \varphi_o) = (20°, 0°)$	$(\theta_o, \varphi_o) = (30°, 0°)$
ΔPointing [º]	0°	~0.5°	~2°
ΔXP [dB]	-0,10	-4,50	-8,50
XPD uncalibrated [dB]	21,90	18,05	13,00
XPD calibrated [dB]	22,00	22,55	21,50
AR uncalibrated [dB]	1,40	2,19	3,96
AR calibrated [dB]	1,38	1,30	1,47
Improved ΔAR [dB]	0,02	0,89	2,49

5.4. Conclusions

A mutual coupling-based self-calibration method which is suitable for off-line, on-site and online calibration schemes was proposed. Numerical simulations are provided to evaluate the calibration performance of the method and a four-element simple experimental system is set-up to verify the effectiveness of the proposed method. The calibration method capable of compensating mutual coupling effect, and gain and phase errors, as well as, phase center plane shift. The method is based on the estimation of the phase center and suitable for any array topology. The compensation weights were derived from the phase center obtained with least-squares solutions, and the expansion of the active element pattern for active antenna arrays. However, the compensation matrix was derived with an inverse matrix approximation method.

The theory for the analytical validation of the proposed method has been addressed, and the effect of gain/phase uncertainties, location errors and mutual coupling on phase center has been demonstrated. The effectiveness of the proposed method is validated by simulation results under worst conditions. The simulation results show that the compensated patterns have at least 2.5 dB improvement in side-lobe levels and have deeper nulls.

Furthermore, a four-element simple experimental system is set-up to verify the effectiveness of the proposed method in practice. An RF-SoC FPGA was used to measure the coupling between antenna elements and the measured raw data was post-processed. It has been seen that unequal mutual couplings and antenna patterns lead in unequal side-lobe levels and phase center plane shift in practice. The experimental study shows that the proposed method at least 3 dB improvement in side-lobe levels and have deeper nulls, as well as, has the capability of compensating phase center plane shift.

A novel calibration method for circularly polarized active antenna array based on AR optimization for improvement of antenna array performance compensating errors and mutual coupling effect was proposed. Furthermore, the coupling parameters were measured as well as gain, phase and manufacturing errors data were used in the model presented for the analysis of the proposed method.

It is demonstrated that the proposed method compensates errors and mutual coupling effect. The compensation capability was explored and discussed based on the AUT simulated pattern for worst case errors and measured patterns within the two-case study for different pointing directions. From the experimental example, the compensation of the AUT radiation pattern was confirmed as well in terms of the enhancement of the gain, beamwidth, side lobe level and axial ratio.

Furthermore, this is observed significant improvement in the compensated CP and XC patterns. This compensation improved the axial ratio in 2.5 dB for Theta equal to 30 degrees as well as an improvement on XPD of 8.5 dB is observed in the patterns presented.

In addition, the theory for the analytical validation of the proposed solutions has been addressed, and the proposed method for calibration has been validated in terms of the compensation capability.

5.5. References Chapter 5

[1] G. He, X. Gao, and R. Zhang, “Impact Analysis and Calibration Methods of Excitation Errors for Phased Array Antennas,” IEEE Access, vol. 9, pp. 59010–59026, 2021, doi: 10.1109/ACCESS.2021.3073222.

[2] K. Kim, H. Yang, J. Jang, T. Sun, S. Choi, and J. Jung, “Online Calibration for LTE-Based Antenna Array System,” International Journal of Antennas and Propagation, vol. 2016, pp. 1–10, Jan. 2016, doi: 10.1155/2016/2645870.

[3] D. H. Rogstad, “The SUMPLE Algorithm for Aligning Arrays of Receiving Radio Antennas: Coherence Achieved with Less Hardware and Lower Combining Loss”.

[4] B. M. Fabiani et al., “Closed-loop controlled microwave beamformer,” International Journal of RF and Microwave Computer-Aided Engineering, vol. 32, no. 3, p. e23020, 2022, doi: 10.1002/mmce.23020.

[5] A. Nafe, K. Kibaroglu, M. Sayginer, and G. M. Rebeiz, “An In-Situ Self-Test and Self-Calibration Technique Utilizing Antenna Mutual Coupling for 5G Multi-Beam TRX Phased Arrays,” in 2019 IEEE MTT-S International Microwave Symposium (IMS), Jun. 2019, pp. 1229–1232. doi: 10.1109/MWSYM.2019.8701072.

[6] I. Seker, Calibration methods for phased array radars, vol. 8714. 2013. doi: 10.1117/12.2015694.

[7] M. A. Salas-Natera, R. M. Rodriguez-Osorio, L. de Haro Ariet, and M. Sierra-Perez, “Novel Reception and Transmission Calibration Technique for Active Antenna Array Based on Phase Center Estimation,” IEEE Trans. Antennas Propagat., vol. 65, no. 10, pp. 5511–5522, Oct. 2017, doi: 10.1109/TAP.2017.2738067.

[8] Y. Ji, J. Ø. Nielsen, and W. Fan, “A Simultaneous Wideband Calibration for Digital Beamforming Arrays at Short Distances [Measurements Corner],” IEEE Antennas and Propagation Magazine, vol. 63, no. 3, pp. 102–111, Jun. 2021, doi: 10.1109/MAP.2021.3069244.

[9] R. Long, J. Ouyang, F. Yang, W. Han, and L. Zhou, “Fast Amplitude-Only Measurement Method for Phased Array Calibration,” IEEE Transactions on Antennas and Propagation, vol. 65, no. 4, pp. 1815–1822, Apr. 2017, doi: 10.1109/TAP.2016.2629467.

[10] S. S. Tambovskiy, G. Fodor, and H. M. Tullberg, “Antenna Array Calibration Via Gaussian Process Models.” arXiv, Jan. 31, 2023. Accessed: Jul. 22, 2023. [Online]. Available: http://arxiv.org/abs/2301.06582

[11] A. Stark, B. Rohrdantz, U. Johannsen, and A. F. Jacob, “In-situ probes for patch antenna array calibration,” Int. J. Microw. Wireless Technol., vol. 3, no. 3, pp. 273–280, Jun. 2011, doi: 10.1017/S1759078711000316.

[12] C. Fulton et al., “Cylindrical polarimetric phased array radar: Beamforming and calibration for weather applications,” IEEE Trans. Geosci. Remote Sensing, vol. 55, no. 5, pp. 2827–2841, May 2017, doi: 10.1109/TGRS.2017.2655023.

[13] J. Lujan, C. J. Fulton, M. Yeary, E. A. Langley, S. McCormick, and A. Hedden, "Phased array radar initial alignment algorithm using mutual coupling: an iterative approach," vol. 11408, p. 1140811, Apr. 2020, doi: 10.1117/12.2562963.

[14] R. M. Lebron, P.-S. Tsai, J. M. Emmett, C. Fulton, and J. L. Salazar-Cerreno, "Validation and Testing of Initial and In-Situ Mutual Coupling-Based Calibration of a Dual-Polarized Active Phased Array Antenna," IEEE Access, vol. 8, pp. 78315–78329, 2020, doi: 10.1109/ACCESS.2020.2983523.

[15] D.-C. Kim, S.-J. Park, T.-W. Kim, L. Minz, and S.-O. Park, "Fully Digital Beamforming Receiver With a Real-Time Calibration for 5G Mobile Communication," IEEE Trans. Antennas Propagat., vol. 67, no. 6, pp. 3809–3819, Jun. 2019, doi: 10.1109/TAP.2019.2902712.

[16] O. Inac, D. Shin, and G. M. Rebeiz, "A Phased Array RFIC With Built-In Self-Test Capabilities," IEEE Trans. Microwave Theory Techn., vol. 60, no. 1, pp. 139–148, Jan. 2012, doi: 10.1109/TMTT.2011.2170704.

[17] S.-C. Chae, H.-W. Jo, J.-I. Oh, G. Kim, and J.-W. Yu, "Coupler Integrated Microstrip Patch Linear Phased Array for Self-Calibration," IEEE Antennas and Wireless Propagation Letters, vol. 19, no. 9, pp. 1615–1619, Sep. 2020, doi: 10.1109/LAWP.2020.3011862.

[18] A. Dreher, N. Niklasch, F. Klefenz, and A. Schroth, "Antenna and receiver system with digital beamforming for satellite navigation and communications," IEEE Trans. Microwave Theory Techn., vol. 51, no. 7, pp. 1815–1821, Jul. 2003, doi: 10.1109/TMTT.2003.814309.

[19] C.-N. Hu, P. Lo, C.-P. Ho, and D.-C. Chang, "Automatic Calibration Using a Modified Genetic Algorithm for Millimeter-Wave Antenna Modules in MIMO Systems," International Journal of Antennas and Propagation, vol. 2020, p. e4286026, Jun. 2020, doi: 10.1155/2020/4286026.

[20] R. Long, J. Ouyang, F. Yang, W. Han, and L. Zhou, "Multi-Element Phased Array Calibration Method by Solving Linear Equations," IEEE Trans. Antennas Propagat., vol. 65, no. 6, pp. 2931–2939, Jun. 2017, doi: 10.1109/TAP.2017.2694767.

[21] M. A. Salas-Natera, R. Martínez Rodríguez-Osorio, L. de Haro y Ariet, and M. Sierra Pérez, "Circularly Polarized Active Antenna Array System Calibration for Improved Axial Ratio Systems," in 2019 13th European Conference on Antennas and Propagation (EuCAP), Mar. 2019, pp. 1–5. Accessed: Dec. 01, 2023. [Online]. Available: https://ieeexplore.ieee.org/abstract/document/8740023/authors#authors

[22] Y. Dong, S. Dong, Y. Wang, and L. Gong, "Calibration method of retrodirective antenna array for microwave power transmission," in 2013 IEEE Wireless Power Transfer (WPT), Perugia, Italy: IEEE, May 2013, pp. 41–43. doi: 10.1109/WPT.2013.6556876.

[23] Qiulin Huang, Hongxing Zhou, Jianhui Bao, and Xiaowei Shi, "Mutual Coupling Calibration for Microstrip Antenna Arrays via Element Pattern Reconstruction

Method," Antennas Wirel. Propag. Lett., vol. 13, pp. 51–54, 2014, doi: 10.1109/LAWP.2013.2296073.

[24] S. Daneshmand, N. Sokhandan, M. Zaeri-Amirani, and G. Lachapelle, "Precise Calibration of a GNSS Antenna Array for Adaptive Beamforming Applications," Sensors, vol. 14, no. 6, Art. no. 6, Jun. 2014, doi: 10.3390/s140609669.

[25] K. Hu, X. Zhang, J. Shi, and S. Wei, "A novel antenna phase center estimation method for synthetic aperture radar," in 2015 IEEE Radar Conference (RadarCon), May 2015, pp. 1340–1344. doi: 10.1109/RADAR.2015.7131203.

[26] L. Yang, R. Dang, M. Li, K. Zhao, C. Song, and Z. Xu, "A Fast Calibration Method for Phased Arrays by Using the Graph Coloring Theory," Sensors (Basel), vol. 18, no. 12, p. 4315, Dec. 2018, doi: 10.3390/s18124315.

[27] K. Greene, V. Chauhan, and B. Floyd, "Built-In Test of Phased Arrays Using Code-Modulated Interferometry," IEEE Trans. Microwave Theory Techn., vol. 66, no. 5, pp. 2463–2479, May 2018, doi: 10.1109/TMTT.2017.2784373.

[28] F. Zhang, W. Fan, Z. Wang, Y. Zhang, and G. F. Pedersen, "Improved Over-the-Air Phased Array Calibration Based on Measured Complex Array Signals," Antennas Wirel. Propag. Lett., vol. 18, no. 6, pp. 1174–1178, Jun. 2019, doi: 10.1109/LAWP.2019.2911725.

[29] H.-J. Yoon and B.-W. Min, "Improved Rotating-Element Electric-Field Vector Method for Fast Far-Field Phased Array Calibration," IEEE Trans. Antennas Propagat., vol. 69, no. 11, pp. 8021–8026, Nov. 2021, doi: 10.1109/TAP.2021.3083796.

[30] H. Xing et al., "Antenna array calibration methods based on simultaneous perturbation," IET Microwaves Antenna & Prop, vol. 16, no. 14, pp. 898–909, Nov. 2022, doi: 10.1049/mia2.12304.

[31] A. O. Fadamiro and F. Lin, "A compressed sensing approach for antenna array calibration," TELKOMNIKA, vol. 20, no. 4, p. 892, Aug. 2022, doi: 10.12928/telkomnika.v20i4.23767.

[32] S. Kim, H.-J. Dong, J.-W. Yu, and H. L. Lee, "Phased array calibration system with high accuracy and low complexity," Alexandria Engineering Journal, vol. 69, pp. 759–770, Apr. 2023, doi: 10.1016/j.aej.2023.02.026.

[33] Y. Lin, C. Hu, Z. Shi, B. Liang, and J. Li, "Low-Complexity Online Calibration for Large-Scale Multi-Beam Antennas," Electronics, vol. 12, no. 7, p. 1690, Apr. 2023, doi: 10.3390/electronics12071690.

[34] A. E. Zorkun, M. A. Salas-Natera, and R. Martínez Rodriguez-Osorio, "Improved Iterative Inverse Matrix Approximation Algorithm for Zero Forcing Precoding in Large Antenna Arrays," IEEE Access, vol. 10, pp. 100964–100975, 2022, doi: 10.1109/ACCESS.2022.3208155.

[35] M. A. Salas-Natera, R. M. Rodriguez-Osorio, and L. de Haro, "Procedure for Measurement, Characterization, and Calibration of Active Antenna Arrays," IEEE

Trans. Instrum. Meas., vol. 62, no. 2, pp. 377–391, Feb. 2013, doi: 10.1109/TIM.2012.2217662.

[36] M. Mowlér, B. Lindmark, E. G. Larsson, and B. Ottersten, "Joint Estimation of Mutual Coupling, Element Factor, and Phase Center in Antenna Arrays," J Wireless Com Network, vol. 2007, no. 1, Art. no. 1, Dec. 2007, doi: 10.1155/2007/30684.

[37] F. Rosario, F. A. Monteiro, and A. Rodrigues, "Fast Matrix Inversion Updates for Massive MIMO Detection and Precoding," IEEE Signal Process. Lett., vol. 23, no. 1, pp. 75–79, Jan. 2016, doi: 10.1109/LSP.2015.2500682.

[38] M. A. Salas-Natera and Rodrez-Osorio, "Analytical Evaluation of Uncertainty on Active Antenna Arrays," IEEE Trans. Aerosp. Electron. Syst., vol. 48, no. 3, pp. 1903–1913, Jul. 2012, doi: 10.1109/TAES.2012.6237569.

[39] Á. N. S. de Toca, J. M. Inclán-Alonso, J. G.-G. Trujillo, J. M. F. González, and M. S. Pérez, "GEODA-SARAS: Multi-phased array planar antenna for satellite communications," in 2013 7th European Conference on Antennas and Propagation (EuCAP), Apr. 2013, pp. 252–253. Accessed: Dec. 12, 2023. [Online]. Available: https://ieeexplore.ieee.org/abstract/document/6546257

[40] N. Wu, Z. Qu, W. Si, and S. Jiao, "DOA and Polarization Estimation Using an Electromagnetic Vector Sensor Uniform Circular Array Based on the ESPRIT Algorithm," Sensors, vol. 16, no. 12, Art. no. 12, Dec. 2016, doi: 10.3390/s16122109.

[41] M. A. Salas-Natera, R. M. Rodríguez-Osorio, L. de Haro Ariet, and M. Sierra-Pérez, "Novel Reception and Transmission Calibration Technique for Active Antenna Array Based on Phase Center Estimation," IEEE Transactions on Antennas and Propagation, vol. 65, no. 10, pp. 5511–5522, Oct. 2017, doi: 10.1109/TAP.2017.2738067.

[42] S. Gao, A. Sambell, and S. S. Zhong, "Polarization-agile antennas," IEEE Antennas Propag. Mag., vol. 48, no. 3, pp. 28–37, Jun. 2006, doi: 10.1109/MAP.2006.1703396.

[43] A. E. Zorkun, M. A. Salas-Natera, and R. Martinez Rodriguez-Osorio, "Improved Iterative Inverse Matrix Approximation Algorithm for Zero Forcing Precoding in Large Antenna Arrays," IEEE Access, vol. 10, pp. 100964–100975, 2022, doi: 10.1109/ACCESS.2022.3208155.

[44] M. A. Salas-Natera and Rodrez-Osorio, "Analytical Evaluation of Uncertainty on Active Antenna Arrays," IEEE Trans. Aerosp. Electron. Syst., vol. 48, no. 3, pp. 1903–1913, Jul. 2012, doi: 10.1109/TAES.2012.6237569.

[45] M. A. Salas-Natera, R. M. Rodriguez-Osorio, and L. de Haro, "Procedure for Measurement, Characterization, and Calibration of Active Antenna Arrays," IEEE Trans. Instrum. Meas., vol. 62, no. 2, pp. 377–391, Feb. 2013, doi: 10.1109/TIM.2012.2217662.

[46] M. A. Salas Natera, R. Martinez Rodriguez-Osorio, L. de Haro Ariet, and M. Sierra Perez, "Calibration Proposal for New Antenna Array Architectures and Technologies

for Space Communications," IEEE Antennas and Wireless Propagation Letters, vol. 11, pp. 1129–1132, 2012, doi: 10.1109/LAWP.2012.2215952.

[47] M. A. Salas Natera, "Contribution to the uncertainty analysis and calibration of active antenna arrays," http://purl.org/dc/dcmitype/Text, Universidad Politécnica de Madrid, 2011. Accessed: Dec. 12, 2023. [Online]. Available: https://dialnet.unirioja.es/servlet/tesis?codigo=185421

6. Chapter VI: Direction of Arrival and Channel Estimation Proposals in RIS-Aided MIMO Systems

6.1. Introduction

Millimeter wave (mm-Wave) massive MIMO systems are considered to play the major role not only in fifth-generation (5G) mobile communications technology but also in beyond-5G (B5G) technology, sixth generation (6G) technology that will be used mainly for autonomous driving and industry 4.0, and will be used in the internet of things (IoT), respectively [1], [2], [3], [4]. One of the main advantages of using massive MIMO systems at ultrahigh frequencies is to compensate for the high free path losses at millimeter wavelengths by using a large number of antenna elements [3], [5]. The densely numbered antenna structure of massive MIMO systems increases the transmission rate, spectral efficiency and power spectral efficiency [6], [7], [8], moreover, communication strictly relies on the line-of-sight path (LoS) in mm-wave bands [9]. In the dense communications scenario, the link between communication ends is most likely blocked. However, in highly dense environments the LoS channel between the transmitter and receiver is likely to be blocked [10], moreover, signal reflections, refractions, diffractions and scatterers highly effect the positioning signal [1]. In order to mitigate the effects of factors hindering the data transfer and provide a virtual LoS channel where it is required, a new concept known as reconfigurable intelligent surface (RIS) has been proposed [11], [12].

Reconfigurable intelligent surfaces are the candidates to form a virtual LoS path to provide coverage between the blocked ends while improving the communication quality of wireless systems [13]. A RIS essentially consists of passive reflecting elements with the ability to change the electromagnetic (EM) characteristics of the reflection of the incident radio frequency (RF) signals by altering the phases of each element in the array [14]. Therefore, RISs are cost-effective and energy-efficient auxiliary elements for massive MIMO systems [14]. Although, RISs are additional auxiliary elements for massive MIMO systems which enhance the overall communication quality, DoA and channel estimation becomes more challenging task in RIS-aided massive MIMO systems than the conventional MIMO systems since the total number of antennas is larger and there are multiple different channels (direct, cascaded, multiple cascaded, etc.).

In massive MIMO systems, the three-dimensional (3D) beamforming is considered to enable the link reliability enhancement [15]. The accurate estimation of the direction-of-arrival (DoA) is the preliminary stage of 3D beamforming [16], target localization [17] and channel estimation [18] in RIS-aided mm-Wave massive MIMO systems, as in many communication

applications. The subspace DoA estimation algorithms, such as, multiple signal classification (MUSIC) [19], estimation of signal parameters via rotational invariance technique (ESPIRIT) [20], weighted subspace fitting (WSF) [21] and maximum likelihood (ML) [22], are widely used in RIS-aided communication systems. The performance of subspace DoA algorithms depends on the correlation, which requires the signal information from each antenna in an array. However, the implementation of such algorithms becomes impractical in massive MIMO systems since the power consumption of the radio frequency chain (RF) connected to each antenna in the access receiver will be high. Additionally, these algorithms include eigen value decomposition (EVD) or matrix inversion operations with high computational complexity. The high computation leads latency and disruptions in high-speed data flow, especially if targets are dynamic. Considering that current 5G networks consume 3 times more power [23] and require ~15 times less latency [24] than previous fourth generation (4G) networks, energy-efficient receiver architectures and low-complexity DoA algorithms for low latency are needed to be developed.

In practical communication systems mixed far-field and near-field signals exist resulting in hybrid-field communication scenario [25], [26]. The hybrid-field estimation is more complex than the conventional channel estimation problem. Hence, there is not much work on hybrid-field channel estimation. In [27], hybrid-field channel estimation for extremely large-scale massive MIMO system. The structural characteristic of far-field path components in the angle domain and the sparsity of near-field path components in polar domain were exploited for channel estimation employing a combination of support detection and orthogonal matching pursuit algorithms. Moreover, in [28], a fixed point network-based channel estimator was proposed for hybrid-field Terahertz XL-MIMO systems. On the other hand, among the limited number of studies on RIS-aided massive MIMO channel estimation, in [29], a hybrid-field vehicle-to-vehicle (V2V) channel model for RIS-aided systems has been proposed and in [25] an U-shaped network based on the dedicated multilayer perceptron (MLP) based hybrid-field channel estimation method has been proposed. However, those approaches to hybrid-field channel estimation problem in RIS-aided mm-Wave massive MIMO systems are lack of DoD and DoA resolution which effects the channel estimation. Therefore, a more effective channel estimation methods are in need.

Based on the open issues mentioned for RIS-assisted mm-wave massive MIMO systems, this chapter proposes an energy-efficient fast DoA estimation and tracking algorithm and an efficient hybrid-field channel estimation method for such systems. The estimation of direction of arrivals (DoAs), direction of departures (DoDs) and range arrivals, range of departures depend on the higher order statics of the received signal at receiver.

6.2. Energy Efficient Low-Complexity RIS-Aided 3-D DoA Estimation and Target Tracking Algorithm via Matrix Completion

In order to reduce the total power consumption in the receiver and at same time increase the DoA estimation and tracking capability in RIS-aided mm-Wave massive MIMO systems, a novel algorithm is developed. Based on the works in [30], [31], the reduced RF chain by antenna switching in the receiver architecture is adopted, thus, the total power consumption is reduced pro rata the percentage of the switched off antennas. However, random antenna nulling leads significant signal information loss which causes the performance loss in DoA estimation. The missing signal data from selected subset of elements in receiver array is recovered by using the truncated nuclear norm regularization alternating direction of multipliers (TNNR-ADMM) matrix completion algorithm. Then the recovered data matrix is used for DoA estimation and tracking. An adaptive RLS-based DoA estimation and increased tracking capability by exploiting computational effectiveness of adaptive moment estimation method to update the forgetting factor by using the first gradient of the error signal is proposed. The proposed algorithm does not involve the heavy matrix computation such as eigen value decomposition or inverse matrix operation which are essential in subspace DoA estimation algorithms. The proposed algorithm is evaluated under single-propagation and multi-propagation path conditions, and the performance of the proposed algorithm is compared with state-of-the-art algorithms under various performance metrics. Based on the analysis and simulation results, after applying matrix completion, the proposed DoA tracking algorithm outperforms the state-of-the-art algorithms.

6.2.1. Main Contributions

The main contributions of the proposed energy efficient low-complexity RIS-aided 3-D DoA estimation and tracking algorithm via matrix completion are listed below:

- The proposed DoA estimation and tracking algorithm does not involve any correlation matrix and eigen value decomposition or inverse matrix operation in contrast to the approaches in [19], [20], [22], [32].
- The proposed algorithm does not require all elements in the antenna array for processing.
- The number of RF chains is reduced by antenna switching in the receiver. Hence, the total power consumption in the systems is reduced.
- Reducing RF chains and random nulling of antennas cause signal information loss which yields performance degradation in DoA estimation and tracking. The missing received signal information is recovered by using TNNR-ADMM matrix completion algorithm.

- A novel reduced computational complexity adaptive forgetting factor (AF-RLS), as explained in Chapter 3 is used for fast DoA estimation and increased tracking capability.

6.2.2. System Model and Theoretical Formulation

An uplink narrow-band RIS-aided mm-Wave massive MIMO system for indoor or outdoor target tracking, as illustrated in Fig. 6.1, is considered for this study. The system consists of one AP with M_{AP} antennas and M_{RF} ($M_{RF} \ll M_{AP}$) RF chains communicate with one dynamic user (UE) with a single antenna via RIS with M_{RIS} antennas. The AP and RIS are equipped with uniform planar arrays (UPA). The AP receives N snapshots for the processing in each epoch t. We define epoch as signal samples received within a certain time frame. In every t-th epoch, UE is blocked and, paths UE to RIS satisfy the far-field condition while and RIS is placed in the near-field region of the AP. The power density of the signal reaching RIS and AP is considered to be the same due to the far-field assumption as referred in [32]. Moreover, the near-field range dependent phase components are ignored since power density is assumed same at RIS and AP. Therefore, in this study, the steering vector is given according to the far-field assumption. The radiated signal waveform is narrowband, therefore, we assume that multi-path propagations (scatters) between RIS and AP can be ignored [19], [32]. However, there are L propagation paths (one UE and its scatterers) at each t-th epoch. The proposed approach can be easily extended to multi-user case by adapting a matched filter at the receiver if the signals of the sources are known or a blind source separation method if the number of users is known or estimated.

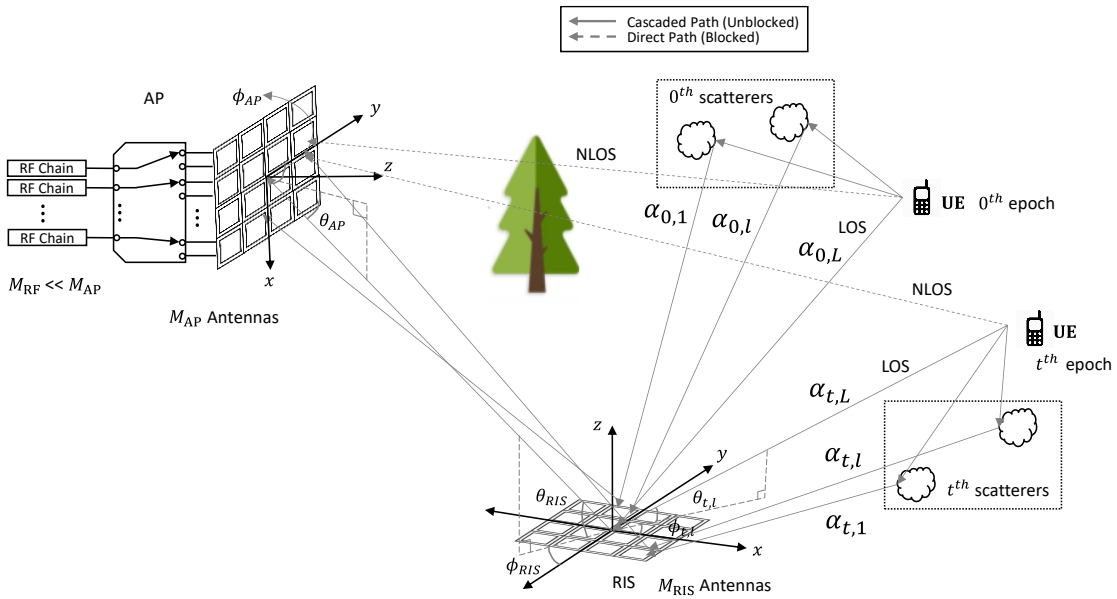

Fig. 6.1. RIS-aided 3-D DoA estimation and target tracking system.

The incident signals from L paths in t-th epoch, received by the m_{RIS}-th element of the RIS, $x_{m_{RIS}}(n)$, in snapshot n can be expressed as:

$$x_{t,m_{RIS}}(n) = \sum_{l=1}^{L} \alpha_{t,l} s_t(n) e^{-j\frac{2\pi}{\lambda}\hat{\mathbf{r}}_{t,l}\vec{\mathbf{r}}_{m_{RIS}}} \tag{6-1}$$

where $\alpha_{t,l}$ is the complex amplitude of the l-th path in t-th epoch, $s_t(n)$ is the radiated signal from UE, λ is the wavelength, $\hat{\mathbf{r}}_{t,l}$ is being the unitary vector associated with the far-field signal and its mutli-paths as $\hat{\mathbf{r}}_{t,l} = \left[\sin\theta_{t,l}\cos\phi_{t,l},\ \sin\theta_{t,l}\sin\phi_{t,l},\ \cos\theta_{t,l}\right]^T$, $\theta_{t,l}$ and $\phi_{t,l}$ are the elevation and azimuth DoAs from the of the k-th path in t-th epoch and $\vec{\mathbf{r}}_{m_{RIS}}$ is being the location of the m_{RIS}-th element as $\vec{\mathbf{r}}_{m_{RIS}} = \left[x_{m_{RIS}}, y_{m_{RIS}}, z_{m_{RIS}}\right]$ (inter-element spacing is set to $\lambda/2$).

The reflected signal by the m_{RIS}-th element of RIS in t-th epoch, $\psi_{t,n}(n)$, then can be expressed as:

$$\psi_{t,m_{RIS}}(n) = e^{-j\omega_{t,m_{RIS}}} x_{t,m_{RIS}}(n) \tag{6-2}$$

where $e^{-j\omega_{t,m_{RIS}}}$ denotes the reflection phase at the m_{RIS}-th element of RIS in t-th epoch. Then, the observed signal at the m_{AP}-th element of AP in t-th epoch, $y_{t,m_{AP}}(n)$ is given by:

$$y_{t,m_{AP}}(n) = \sum_{m_{AP}=1}^{M_{AP}} \psi_{t,m_{RIS}}(n)\, e^{j\frac{2\pi}{\lambda}\hat{\mathbf{r}}_{RIS,t}\vec{\mathbf{r}}_{m_{RIS}}} e^{-j\frac{2\pi}{\lambda}\hat{\mathbf{r}}_{AP,t}\vec{\mathbf{r}}_{m_{AP}}} + z_{t,m_{AP}}(n) \tag{6-3}$$

where $\hat{\mathbf{r}}_{RIS,t}$ and $\hat{\mathbf{r}}_{AP,t}$ are the direction-of-departure (DoD) unitary vector of RIS and DoA unitary vector of AP in t-th epoch, respectively and $z_{t,m_{AP}}(n)$ denotes the additive white Gaussian noise received by the m-th element of AP. The related elevation and azimuth angles of the wave vectors are, $\theta_{RIS,t}$, $\phi_{RIS,t}$, $\theta_{AP,t}$ and $\phi_{AP,t}$. We sort each value $y_{t,m_{AP}}(l)$ into matrix-wise form in each t-th epoch, then the compact form of resulting matrix $\mathbf{Y}_t \in \mathbb{C}^{M_{AP}\times N}$ of the M_{AP} receiving antennas can be expressed as:

$$\mathbf{Y}_t = \begin{bmatrix} y_1(1) & \cdots & y_1(n) \\ \vdots & \ddots & \vdots \\ y_{M_{AP}}(1) & \cdots & y_M(N) \end{bmatrix} = \sum_{l=1}^{L} \left(\mathbf{q}^T \mathbf{b}\boldsymbol{\Gamma}\mathbf{a}_l^T\right)\mathbf{s} + \mathbf{Z} \tag{6-4}$$

where $\mathbf{q} = e^{-j\hat{\mathbf{r}}_{AP,t}\vec{\mathbf{R}}_{AP}} \in \mathbb{C}^{M_{AP}\times 1}$ is the steering vector of DoA in each epoch t to AP and $\vec{\mathbf{R}}_{AP} \in \mathbb{R}^{3\times M_{AP}}$ location matrix of antenna elements in AP, $\mathbf{b} = e^{j\hat{\mathbf{r}}_{RIS,t}\vec{\mathbf{R}}_{RIS}} \in \mathbb{C}^{M_{RIS}\times 1}$ is the steering vector of DoD from RIS in each epoch t and $\vec{\mathbf{R}}_{RIS} \in \mathbb{R}^{3\times M_{RIS}}$ location matrix of antenna elements in RIS, $\boldsymbol{\Gamma} = diag\left(e^{j\omega_1}, e^{j\omega_{m_{RIS}}}, \ldots, e^{j\omega_{M_{RIS}}}\right) \in \mathbb{C}^{M_{RIS}\times M_{RIS}}$ is the diagonal phase shift matrix of RIS in each t-th epoch, $\mathbf{a}_l = e^{-j\hat{\mathbf{r}}_{t,l}\vec{\mathbf{R}}_{RIS}} \in \mathbb{C}^{M_{RIS}\times 1}$ is the steering vector of DoA from the k-th path to the RIS in each epoch t, $\mathbf{s} = [s_l(1), \ldots, s_l(N)] \in \mathbb{C}^{1\times N}$ is the transmitted signal vector from UE, $\mathbf{Z} = [\mathbf{z}_{1:M_{AP}}(1), \ldots, \mathbf{z}_{1:M_{AP}}(N)] \in \mathbb{C}^{M_{AP}\times N}$ is the noise matrix in AP.

6.2.3. Proposed Algorithm

In this section, the problems arising from antenna switching, the flow of the proposed algorithm and the convergence analysis of the proposed adaptive forgetting factor are given. The flow chart of the proposed algorithm is shown Fig. 6.2.

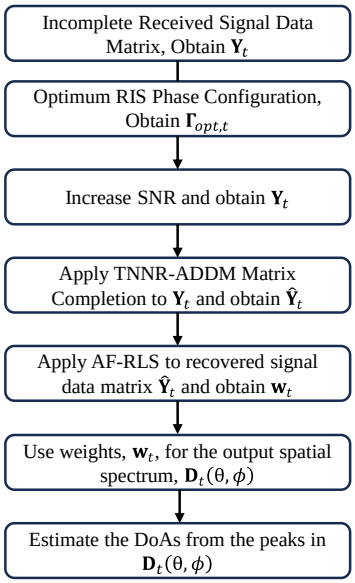

Fig. 6.2. Flow chart of the proposed 3-D DoA estimation and tracking algorithm.

The steps for the proposed algorithm:

1) The optimum phase shift configuration of the RIS elements is found by maximizing the received signal-to-noise ratio (SNR). Thus, the overall DoA estimation and tracking performance increases.

2) The TNNR-ADMM matrix completion algorithm is applied in order to recover the missing entries in the received signal data matrix caused by the switching antenna array structure.

3) The recovered signal data matrix is then used for DoA estimation and tracking. An adaptive approach is adopted for DoA estimation and tracking. The RLS algorithm is adopted since it has proven superior convergence and convergence rate compared to existing adaptive algorithms in the literature [33]. Furthermore, it is also proven the high-resolution matching with the requirements of the multi-path propagation channel. In addition, ADAM-based adaptive forgetting factor is implemented to increase the convergence rate of the RLS algorithm. Thus, this novel RLS implementation solve the DoA.

6.2.3.1. Problem Statement

The performance of subspace DoA estimation methods and also adaptive beamforming algorithms rely on fully-digital receiver structure meaning each antenna element requires an RF chain accompanying with individual analog-to-digital converters (ADCs). The acquired signals from ADCs are used for the construct signal data matrix. Along with the RF chains, the large number of ADCs yields high power consumption, especially, in massive MIMO systems. In order to reduce the power consumption at the receiver part, switched antenna structures are widely used [18], [23], [30]. However, switched antenna structures yield two major issues to overcome.

Firstly, because of the switched-off antennas the receiver cannot acquire data from all of the antenna elements, therefore, in received signal data matrix there are missing entries. These missing entries are usually replaced by nulls (zeros) [30], [31], thus, simply, the periodic phase relation between consecutive antennas is lost. Additionally, switched antenna structures cannot be considered as sparse antenna arrays since different antenna subsets are switched on in each sample, so there is no relation between consecutive signal samples (snapshots). Therefore, the missing data yields significant performance loss in DoA estimation either the adopted methods are blind or not. For this reason, the signal data matrix must be recovered and matrix completion is a necessary step before DoA estimation. Fig. 6.3 simply illustrates the relation between the incomplete signal data matrix, $\mathbf{Y}_t$, and the recovered signal data matrix $\widehat{\mathbf{Y}}_t$.

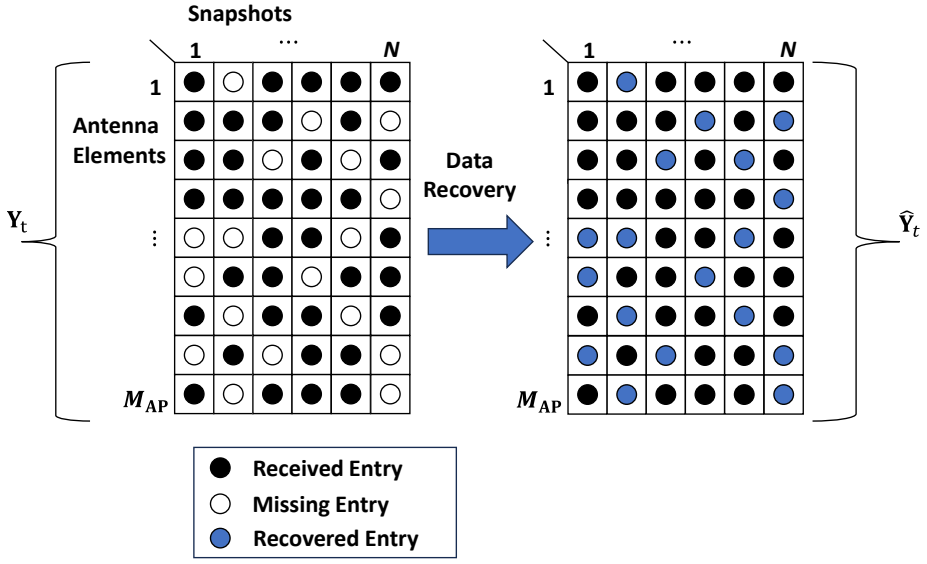

Fig. 6.3. Illustration of the incomplete noisy signal data matrix, $\mathbf{Y}_t$, and the recovered signal data matrix, $\widehat{\mathbf{Y}}_t$.

The second major problem arising from the antenna switching structure is the possibility of low-rank in the signal data matrix. In cases where the number of sources is less than the number of antennas, low-rank does not occur when the number of samples (snapshots)

exceeds the number of antennas. However, since we have random antenna switching structure and assuming there is no change in signal power and waveform, there will be concurrent columns in the signal data matrix causing linearly dependent columns which might cause low-rank problem. In order to guarantee the rank, low-rank completion is necessary. Fig. 6.4 simply shows the low-rank situation in the signal data matrix. It should be noted the numbers are not related to the antenna phases, but are given only to indicate linearly dependent columns.

$$\mathbf{Y}_t \begin{bmatrix} 1\,1\,1 & 1\,1\,1 & 1\,1\,1 \\ 2\,2\,2 & 3\,3\,3 & 3\,3\,3 \\ 3\,3\,3 & 4\,4\,4 & 4\,4\,4 \\ 4\,4\,4 & \cdots\cdots\; 5\,5\,5 & \cdots\cdots\; 5\,5\,5 \\ 0\,0\,0 & 0\,0\,0 & 0\,0\,0 \\ 1\,1\,1 & 1\,1\,1 & 1\,1\,1 \\ 0\,0\,0 & 4\,6\,8 & 2\,3\,2 \\ 0\,0\,0 & 3\,0\,0 & 1\,0\,1 \end{bmatrix}$$

Fig. 6.4. Low-rank case in signal data matrix, $\mathbf{Y}_t$.

In line with these problems, the main goal is to estimate the rank-M_{AP} noiseless recovered signal data matrix, $\widehat{\mathbf{Y}}_t$, from the observed incomplete signal data matrix, $\mathbf{Y}_t$, either $\mathbf{Y}_t$ is low-rank matrix or not. In this manner, matrix completion methods can be used to recover the incomplete data, provide the full-rank if necessary and at the same time mitigate the received noise.

As a final remark, even though the switched antenna structure reduces the overall power consumption it increases the computational complexity since matrix completion methods require matrix-matrix multiplication and most of the time, singular value decomposition. However, main reason for the increase in computational complexity is the term $0(\max(M_{AP}, N).\min(M_{AP}, N)^2)$ resulting from singular value decomposition. The TNNR-ADMM algorithm adopts the unitary matrices resulting from the singular value decomposition to perform matrix completion. The dimensions of the unitary matrices do not change during the operation and depend on the number of antennas, M_{AP}, as well as the number of snapshots, N.

Therefore, it should be noted that the computational complexity does not depend on the percentage of the switched-off. The percentage of the switched-off antennas only affects the DoA estimation accuracy since as the number of missing entries increases, it becomes harder to estimate recovered signal matrix, $\mathbf{Y}_t$, from the lower number of singular values.

6.2.3.2. Optimal RIS Phase Configuration

Higher signal-to-noise ratio (SNR) in AP increases the overall DoA estimation and tracking. The optimal phase shift configuration of RIS provides higher SNR. We assume that the DoAs to RIS remain constant during per epoch. Therefore, optimizing the phase shift matrix, $\mathbf{\Gamma}$, for per epoch is sufficient rather than optimizing for each snapshot.

At t-th epoch, the optimal phase shifts can be found by maximizing the received SNR [9]. Then, the optimal phase shift matrix can be expressed as:

$$\mathbf{\Gamma}_{opt,t} = arg\,max \left| \frac{\sum_{l=1}^{L} \left(\mathbf{q}^T \mathbf{b} \mathbf{\Gamma} \mathbf{a}_l^T\right) \mathbf{s}}{\sigma^2} \right|^2 \tag{6-5}$$

where σ is the variance of the noise, $\mathbf{Z}$.

Then the m_{RIS}-th element of the diagonal optimal phase configuration matrix of RIS (in t-th epoch) can be given as:

$$\omega_{t,m_{RIS}} = \sum_{l=1}^{L} \frac{2\pi}{\lambda} \left[x_{m_{RIS}} d_x \grave{u} + y_{m_{RIS}} d_y \grave{v} + z_{m_{RIS}} d_z \grave{w} \right] \tag{6-6}$$

where d_x, d_y and d_z are the element spacing (both equals to 0.5) of RIS elements along x-axes, y-axes and z-axes respectively, and $\grave{u}$, $\grave{v}$ and $\grave{w}$ can be expressed as:

$$\begin{aligned} \grave{u} &= \left(\sin\theta_{t,l} \cos\phi_{t,l} - \sin\theta_{RIS,t} \cos\phi_{RIS,t}\right) \\ \grave{v} &= \left(\sin\theta_{t,l} \sin\phi_{t,l} - \sin\theta_{RIS,t} \sin\phi_{RIS,t}\right) \\ \grave{w} &= \left(\cos\theta_{t,l} - \cos\theta_{RIS,t}\right) \end{aligned} \tag{6-7}$$

6.2.3.3. Data Recovery by Matrix Completion

Matrix completion methods are widely used to recover the incomplete signal data matrix when the insufficient number of signal samples received or the number of users exceeds the number of elements in receiving antenna array [30], [31]. The incomplete matrix $\mathbf{Y}_t$ can be expressed as:

$$P_{\Omega}[\mathbf{Y}_t(m_{AP}, n)] = \begin{cases} \mathbf{Y}_t(m_{AP}, n), & (m_{AP}, n) \epsilon\, \Omega \\ 0 & otherwise \end{cases} \tag{6-8}$$

where $P_{\Omega}[\mathbf{Y}_t]$ is the observation operator and Ω is the subset of known entries of matrix $\mathbf{Y}_t(m_{AP}, n)$.

The objective is to estimate a matrix $\widehat{\mathbf{Y}}_t$ with rank $r < min\{M_{AP}, N\}$ from the low-rank matrix $\mathbf{Y}_t$ with a rank $r = min\{M_{AP}, N\}$. The matrix completion problem is formulated as:

$$\min_{\widehat{\mathbf{Y}}_t} \quad \text{rank}\left(\widehat{\mathbf{Y}}_t\right) \tag{6-9}$$

$$\text{s.t } P_{\Omega}(\widehat{\boldsymbol{Y}}_{\boldsymbol{t}}) = P_{\Omega}[\boldsymbol{Y}_{\boldsymbol{t}}]$$

where $\text{rank}(\widehat{\mathbf{Y}}_t)$ denotes the rank of the matrix $\widehat{\mathbf{Y}}_t$. The rank minimization problem in (6-9) is a non-convex problem and an NP-hard problem. Unfortunately, the existing algorithms are not sufficient to solve the rank minimization problem directly [34], [35]. It has been proved that the nuclear norm minimization, which is the sum of singular values of a matrix, is the tightest convex lower bound of the rank function [34], [35].

On the other hand, the rank minimization problem can be relaxed and converted into convex semi-definite problem, then, the convex problem can be solved by one of the off-the-shelf solvers such as SDPT3, SeDuMi or CVX. However, these solvers are not efficient for larges sized problems and, in our case, massive MIMO structure can contain hundreds of antennas. Therefore, one of the proposed algorithms to solve non-convex rank minimization problem in [36] is favorable. In this study, we adopted the prominent TNNR-ADMM [37]. There are two reasons; 1) we know the number of receiving antennas M_{AP} required for minimum rank, 2) $\widehat{\mathbf{Y}}_t: P_{\Omega}(\widehat{\mathbf{Y}}_t) = P_{\Omega}[\,\mathbf{Y}_t(m_{AP}, n)]$ can be easily solved by various gradient-based algorithms.

In order to solve non-convex rank minimization problem iteratively by TNNR-ADMM, we first replace the rank operator by the nuclear norm operator and rewrite (6-9) as follows:

$$\begin{aligned} &\min_{\widehat{\mathbf{Y}}_t} \ \left\|\widehat{\mathbf{Y}}_{\boldsymbol{t}}\right\|_* \\ &\text{s.t } P_{\Omega}(\widehat{\mathbf{Y}}_{\boldsymbol{t}}) = P_{\Omega}[\mathbf{Y}_{\boldsymbol{t}}] \end{aligned} \tag{6-10}$$

where $\|.\|_*$ is the nuclear norm operator. The rank of the matrix is not affected by the largest r nonzero singular values, thus, the nuclear norm focuses on minimizing the sum of the smallest $min\{M_{AP}, N\} - r$ singular values and this operation is known as truncated nuclear norm. The $\left\|\widehat{\mathbf{Y}}_t\right\|_*$ is non-convex, therefore, (6-10) cannot be solved directly. The following theorem and proof are given as in [34]. Without loss of generality $\widehat{\mathbf{Y}}_t = \mathbf{W}$ for the proof.

Theorem 1. For any given matrix $\mathbf{W} \in \mathbb{C}^{M_{AP} \times N}$, any matrices $\mathbf{U}_r \in \mathbb{C}^{r \times M_{AP}}$, $\mathbf{V}_r \in \mathbb{C}^{r \times N}$ that $\mathbf{U}_r\mathbf{U}_r^T = \mathbf{I}_{r\times r}$, $\mathbf{V}_r\mathbf{V}_r^T = \mathbf{I}_{r\times r}$. For any non-negative integer r $(r <= min\{M_{AP}, N\})$, the following expression holds:

$$\text{Tr}(\mathbf{U}_r\mathbf{W}\mathbf{V}_r^T) \leq \sum_{i=1}^{r} \sigma_i(\mathbf{W}) \tag{6-11}$$

where σ_i is the i-th eigen value of the matrix $\widehat{\mathbf{Y}}_t$.

Proof. The Von Neumann's trace inequality proves the above theorem as

$$\text{Tr}(\mathbf{U}_r\mathbf{W}\mathbf{V}_r^T) = \text{Tr}(\mathbf{W}\mathbf{V}_r^T\mathbf{U}_r) \leq \sum_{i=1}^{min\{M,L\}} \sigma_i(\mathbf{W})\sigma_i(\mathbf{V}_r^T\mathbf{U}_r) \tag{6-12}$$

where $\sigma_1(\mathbf{W}) \geq \cdots \geq \sigma_{min\{M,L\}}(\mathbf{W}) \geq 0$. The $rank(\mathbf{U}_r) = rank(\mathbf{V}_r) = r$, and $rank(\mathbf{V}_r^T\mathbf{U}_r) = s \leq r$. According these criteria, for $i = 1,2,\dots,s$, $\sigma_i(\mathbf{V}_r^T\mathbf{U}_r) = 1$ and the rest of the eigen values are zero. Thus, the following expression holds:

$$\sum_{i=1}^{min\{M_{AP},N\}} \sigma_i(\mathbf{W})\sigma_i(\mathbf{V}_r^T\mathbf{U}_r) = \sum_{i=1}^{s} \sigma_i(\mathbf{W}) \tag{6-13}$$

Combining (6-12) and (6-13) results in the following inequality:

$$\mathrm{Tr}(\mathbf{U}_r\mathbf{W}\mathbf{V}_r^T) \leq \sum_{i=1}^{s} \sigma_i(\mathbf{W}) \leq \sum_{i=1}^{r} \sigma_i(\mathbf{W}) \tag{6-14}$$

In line with (6-11)-(6-14), when we apply singular value decomposition on $\mathbf{W}$, the same inequalities hold without loss of generality. Starting with singular value decomposition of $\mathbf{W}$ we get:

$$\begin{gathered} svd(\mathbf{W}) = \mathbf{U}\sum\mathbf{V}^T \\ \mathbf{U} = \left(\mathbf{u}_1, \dots, \mathbf{u}_{M_{AP}}\right), \mathbf{V} = (\mathbf{v}_1, \dots, \mathbf{v}_N) \\ \mathbf{U}_r = (\mathbf{u}_1, \dots, \mathbf{u}_r)^T, \mathbf{V}_r = (\mathbf{v}_1, \dots, \mathbf{v}_r)^T \end{gathered} \tag{6-15}$$

where $\mathbf{U}\epsilon\mathbb{C}^{M_{AP}\times M_{AP}}$ and $\mathbf{V}\epsilon\mathbb{C}^{N\times N}$ are the unitary matrices, whose columns are the singular vectors and $\sum\epsilon\mathbb{C}^{M_{AP}\times N}$ is a rectangular diagonal matrix, whose diagonal entries are the singular values of $\mathbf{W}$.

Then, from (6-15) the below equality can be written:

$$\max_{\mathbf{U}_r\mathbf{U}_r^T=\mathbf{I},\mathbf{V}_r\mathbf{V}_r^T=\mathbf{I}} \mathrm{Tr}(\mathbf{U}_r\mathbf{W}\mathbf{V}_r^T) = \sum_{i=1}^{r} \sigma_i(\mathbf{W}) \tag{6-16}$$

As the final step, when we apply truncation to the nuclear norm operator, we get following expression:

$$\left\|\widehat{\mathbf{Y}}_t\right\|_* - \max_{\mathbf{U}_r\mathbf{U}_r^T=\mathbf{I},\mathbf{V}_r\mathbf{V}_r^T=\mathbf{I}} \mathrm{Tr}(\mathbf{U}_r\mathbf{W}\mathbf{V}_r^T) = \sum_{i=1}^{min\{M_{AP},N\}} \sigma_i(\mathbf{W}) - \sum_{i=1}^{r} \sigma_i(\mathbf{W}) \tag{6-17}$$

From (6-17), we can derive the final form of the (6-10) as:

$$\begin{gathered} \min_{\widehat{\mathbf{Y}}_t} \left\|\widehat{\mathbf{Y}}_t\right\|_* - \max_{\mathbf{U}_r\mathbf{U}_r^T=\mathbf{I},\mathbf{V}_r\mathbf{V}_r^T=\mathbf{I}} \mathrm{Tr}(\mathbf{U}_r\mathbf{W}\mathbf{V}_r^T) \\ \text{s.t } P_{\boldsymbol{\Omega}}\left(\widehat{\mathbf{Y}}_t\right) = P_{\boldsymbol{\Omega}}[\mathbf{Y}_t] \end{gathered} \tag{6-18}$$

Then, (6-18) can be efficiently solved by iterative steps as below:

$$\min_{\widehat{\mathbf{Y}}_t\mathbf{W}} \left\|\widehat{\mathbf{Y}}_t\right\|_* - \mathrm{Tr}\left(\mathbf{U}_{r,i}\mathbf{W}\mathbf{V}_{r,i}^T\right) \tag{6-19}$$

$$\text{s.t } \widehat{\mathbf{Y}}_t = \mathbf{W},\ P_{\boldsymbol{\Omega}}\left(\widehat{\mathbf{Y}}_t\right) = P_{\boldsymbol{\Omega}}[\mathbf{Y}_t]$$

where i is the iteration number, $\mathbf{U}_{r,i} \in \mathbb{C}^{r\times M_{AP}}$, $\mathbf{V}_{r,i} \in \mathbb{C}^{r\times N}$ and $\mathbf{W} \in \mathbb{C}^{M_{AP}\times N}$ are the auxiliary matrices where r is the desired rank of the incomplete matrix $\mathbf{Y}_t$. Then, (6-19) can be solved by ADMM algorithm.

The augmented Lagrange function of (6-19) is written as:

$$L\left(\widehat{\mathbf{Y}}_t, \mathbf{T}, \mathbf{W}, \mu\right) = \left\|\widehat{\mathbf{Y}}_t\right\|_* - \mathrm{Tr}\left(\mathbf{U}_{r,i}\mathbf{W}\mathbf{V}_{r,i}^T\right) + \frac{\mu}{2}\left\|\widehat{\mathbf{Y}}_t - \mathbf{W}\right\|_F^2 + \mathrm{Tr}\left(\mathbf{T}^T\left(\widehat{\mathbf{Y}}_t - \mathbf{W}\right)\right) \tag{6-20}$$

where $\mu > 0$ is the penalty parameter.

Then, the steps required to solve (6-20) by ADMM are as follows:

$$\widehat{\mathbf{Y}}_{t(i+1)} = \arg\min_{\widehat{\mathbf{Y}}_{t(i)}} \left\|\widehat{\mathbf{Y}}_{t(i)}\right\|_* + \frac{\mu}{2}\left\|\widehat{\mathbf{Y}}_{t(i)} - (\mathbf{W}_i - \mu^{-1}\mathbf{T}_i)\right\|_F^2 \tag{6-21}$$

Alternatively, the closed form solution of the (6-21) can be expressed as:

$$\widehat{\mathbf{Y}}_{t(i+1)} = \mathcal{D}_{\mu^{-1}}(\mathbf{W}_i - \mu^{-1}\mathbf{T}_i) \tag{6-22}$$

where $\mathcal{D}_{\mu^{-1}}(.)$ is the singular value shrinkage operator.

In the second step, we update the $\mathbf{W}_i$ as follows:

$$\mathbf{W}_{i+1} = \underset{P_{\boldsymbol{\Omega}}(\widehat{\mathbf{Y}}_{t(i)}) = P_{\boldsymbol{\Omega}}[\mathbf{Y}_{t(i)}]}{\arg\min} \frac{\mu}{2}\left\|\mathbf{W}_i - \mu^{-1}\left(\widehat{\mathbf{Y}}_{t(i+1)} + \mathbf{U}_{r,i}^T\mathbf{V}_{r,i} + \mathbf{T}_i\right)\right\|_F^2 \tag{6-23}$$

The closed form of (6-23) can be expressed as:

$$\mathbf{W}_{i+1} = \widehat{\mathbf{Y}}_{t(i+1)} + \mu^{-1}\left(\mathbf{U}_{r,i}^T\mathbf{V}_{r,i} + \mathbf{T}_i\right) \tag{6-24}$$

The final step is to update $\mathbf{T}_i$ as follows:

$$\mathbf{T}_{i+1} = \mathbf{T}_i + \mu^{-1}\left(\widehat{\mathbf{Y}}_{t(i+1)} - \mathbf{W}_{i+1}\right) \tag{6-25}$$

The low-rank matrix completion algorithm, TNNR-ADMM, is summarized in **Algorithm 1**.

Algorithm 1 TNNR-ADMM Algorithm

Inputs: $\mathbf{Y}_t, \varepsilon, r, \mu, i$
Initialize: $\widehat{\mathbf{Y}}_{t(1)} = P_{\Omega}[\mathbf{Y}_t], \mathbf{W}_1 = \widehat{\mathbf{Y}}_{t(1)}, \mathbf{T}_1 = \widehat{\mathbf{Y}}_{t(1)}$
Repeat
    $[\mathbf{U}, \sum, \mathbf{V}] = svd(\widehat{\mathbf{Y}}_{t(i)})$
    $\mathbf{U}_{r,i} = [\mathbf{u}_1, \dots, \mathbf{u}_r]^T, \mathbf{V}_{r,i} = [\mathbf{v}_1, \dots, \mathbf{v}_r]^T$
    $\widehat{\mathbf{Y}}_{t(i+1)} = \mathcal{D}_{\mu^{-1}}(\mathbf{W}_i - \mu^{-1}\mathbf{T}_i)$
    $\mathbf{W}_{i+1} = \widehat{\mathbf{Y}}_{t(i+1)} + \mu^{-1}\left(\mathbf{U}_{r,i}^T \mathbf{V}_{r,i} + \mathbf{T}_i\right)$
    $\mathbf{T}_{i+1} = \mathbf{T}_i + \mu^{-1}\left(\widehat{\mathbf{Y}}_{t(i+1)} - \mathbf{W}_{i+1}\right)$
until $\left\|\widehat{\mathbf{Y}}_{t(i+1)} - \widehat{\mathbf{Y}}_{t(i)}\right\|_F \leq \varepsilon$
Output: $\widehat{\mathbf{Y}}_t$,

where ε is the tolerance or stopping criteria, r is the desired rank ($r = M_{AP}$) of the incomplete matrix $\mathbf{Y}_t$ and $svd(.)$ is the singular value decomposition operator.

6.2.3.4. AF-RLS Based DoA Estimation Algorithm

We improve the tracking capability of the RLS algorithm by proposing low complexity and robust adaptive moment estimation method (ADAM) based adaptive forgetting factor. The forgetting factor controls the overall performance of the RLS algorithm. The forgetting factor is a parameter that reduce the effects of the past error samples in a system. In RLS forgetting factor, ρ, can take values as $0 < \rho \leq 1$. There is a trade-off between low mis-adjustment and stability and fast convergence and tracking depending on the value of forgetting factor [33], [38].

The lower the forgetting factor, the faster the convergence rate, however, the convergence rate is low for a fixed and high-value (closer to 1) of forgetting factor, hence, it causes tracking performance degradation. The adaptive forgetting factor can take values between 0 and 1 in each iteration, depending on the error gradient. Thus, for lower ρ values, faster tracking is achieved due to the higher convergence rate. Therefore, an adaptive mechanism can be implemented for the forgetting factor by exploiting the direction of the error gradient. In each iteration the error gradient can be calculated and according to its direction the value of ρ can be increased or decreased with a certain amount in its bounds. In this study, ADAM method is proposed to determine the increase or decrease in ρ value.

The RLS algorithm updates the weight vectors by taking into account the sum of the past least square errors. The RLS algorithm has high convergence rate since past samples effects are stored and the forgetting factor regulates the stored samples [33]. The RLS algorithm with using the output of **Algorithm 1** is given in the equations below [31], [39]:

$$\mathbf{P}(0) = \Delta^{-1}\begin{bmatrix}1 & \cdots & 0\\ 0 & \ddots & 0\\ 0 & 0 & 1\end{bmatrix}_{(M_{AP}-1)\times(M_{AP}-1)}, \mathbf{w}(0) = 0 \tag{6-26}$$

$$e(n) = y(1,n) - \mathbf{w}^H(n-1)\hat{\mathbf{y}}(n) \tag{6-27}$$

$$\mathbf{r}(n) = \frac{\rho^{-1}\mathbf{P}(n-1)\hat{\mathbf{y}}(n)}{1+\rho^{-1}\hat{\mathbf{y}}^H(n)\mathbf{P}(n-1)\hat{\mathbf{y}}(n)} \tag{6-28}$$

$$\mathbf{w}(n) = \mathbf{w}(n-1) + \mathbf{r}(n)e^*(n) \tag{6-29}$$

$$\mathbf{P}(n) = \rho^{-1}\big(\mathbf{P}(n-1) - \mathbf{r}(n)\hat{\mathbf{y}}^H(n)\mathbf{P}(n-1)\big) \tag{6-30}$$

where $\mathbf{P}\epsilon\,\mathbb{C}^{(M_{AP}-1)\times(M_{AP}-1)}$ is the correlation matrix, Δ is the regularization factor, $\mathbf{w}\epsilon\,\mathbb{C}^{(M_{AP}-1)\times 1}$ is the weight coefficient vector, r is the Kalman gain, e is the error, $y(1,n)$ is the signal of reference antenna element (first element) in the i-th snapshot, $\hat{\mathbf{y}}\epsilon\,\mathbb{C}^{(M_{AP}-1)\times 1}$ is the recovered signal vector.

In each iteration, running averages of both gradient and the second moment of the gradient according to the cost function $J(n) = \sum_{n=0}^{N}\rho^{N-n}|e(n)|^2$ are computed. Then, the forgetting factor is updated. Thus, the proposed adaptive forgetting factor $\rho(n)$ can be expressed as following equations [40]:

$$\rho(n) = \rho(n-1) - \left[\mathrm{Re}\left\{\eta\frac{c(n)}{\sqrt{h(n)}+\xi}\right\}\right]_{\rho_{min}}^{\rho_{max}} \tag{6-31}$$

$$c(n) = \beta_1 c(n) + (1-\beta_1)\nabla_\rho(n) \tag{6-32}$$

$$h(n) = \beta_2 h(n) + (1-\beta_2)\nabla_\rho(n)^2 \tag{6-33}$$

where Re{.} is the real part selection operator, η is the step size, ξ is a small scalar value to prevent division by 0, $c(n)$ is the first moment (mean) update step, $h(n)$ is the second gradient (uncentered variance) update step where hyper-parameters β_1, $\beta_2 \in [0,1)$ control the exponential decay rates of the moving averages and $\nabla_\rho(n)$ is the gradient of the forgetting factor. It should be noted the ADAM update is not applied per epoch. By taking the partial derivative of the $J(n)$ with respect to ρ, the gradient of the forgetting factor, $\nabla_\rho(n)$, can be expressed as [39], [41]:

$$\nabla_\rho(n) = \frac{dJ(n)}{d\rho} = -\frac{1}{2}\mathrm{E}[\boldsymbol{\psi}^H(n-1)\hat{\mathbf{y}}(n)e^*(n) + \hat{\mathbf{y}}^H(n)\boldsymbol{\psi}(n-1)e(n)] \tag{6-34}$$

where $\boldsymbol{\psi}(n) = \frac{d\mathbf{w}(n)}{d\rho}$ and can be expressed as:

$$\boldsymbol{\psi}(n) = \big[\mathbf{I}_{M_{AP}} - \mathbf{r}(n)\hat{\mathbf{y}}^H(n)\big]\boldsymbol{\psi}(n-1) + \mathbf{S}(n)\,\hat{\mathbf{y}}(n)e^*(n) \tag{6-35}$$

where $\mathbf{S}(n) = \frac{d\mathbf{P}(n)}{d\rho}$ and can be expressed as:

$$\mathbf{S}(n) = \rho(n-1)^{-1}\left[\mathbf{I}_{M_{AP}} - \mathbf{r}(n)\hat{\mathbf{y}}^H(n)\right]\mathbf{S}(n-1) + \left[\mathbf{I}_{M_{AP}} - \mathbf{r}(n)\hat{\mathbf{y}}^H(n)\right] + \rho(n-1)^{-1}\mathbf{r}(n)\mathbf{r}^H(n) - \rho(n-1)^{-1}\mathbf{P}(n) \tag{6-36}$$

The proposed AF-RLS DoA estimation algorithm is summarized in **Algorithm 2**.

Algorithm 2 AF-RLS Algorithm

Inputs: $\mathbf{y}(1,n)$, $\widehat{\mathbf{Y}}_t$

Initialize: $\mathbf{w}(0) = \mathbf{0}$, $\mathbf{P}(0) = \Delta^{-1}\mathbf{I}_M$, $\Delta = 0.08$, $\rho(0) = 0.975$, $c(0) = 0$, $h(0) = 0$, $\beta_1 = 0.9$, $\beta_2 = 0.999$, $\xi = 10^{-6}$, $\eta = 0.001$

Repeat

$e(n) = y(1,n) - \mathbf{w}^H(n-1)\hat{\mathbf{y}}(n)$

$\mathbf{r}(n) = \dfrac{\rho^{-1}\mathbf{P}(n-1)\hat{\mathbf{y}}(n)}{1 + \rho^{-1}\hat{\mathbf{y}}^H(n)\mathbf{P}(n-1)\hat{\mathbf{y}}(n)}$

$\mathbf{w}(n) = \mathbf{w}(n-1) + \mathbf{r}(n)e^*(n)$

$\mathbf{P}(n) = \rho^{-1}\left(\mathbf{P}(n-1) - \mathbf{r}(n)\hat{\mathbf{y}}^H(n)\mathbf{P}(n-1)\right)$

$\boldsymbol{\psi}(n) = \left[\mathbf{I}_{M_{AP}} - \mathbf{r}(n)\hat{\mathbf{y}}^H(n)\right]\boldsymbol{\psi}(n-1) + \mathbf{S}(n)\,\hat{\mathbf{y}}(n)e^*(n)$

$\mathbf{S}(n) = \rho(n-1)^{-1}\left[\mathbf{I}_{M_{AP}} - \mathbf{r}(n)\hat{\mathbf{y}}^H(n)\right]\mathbf{S}(n-1) + \left[\mathbf{I}_{M_{AP}} - \hat{\mathbf{y}}(n)\mathbf{r}^H(n)\right] + \rho(n-1)^{-1}\mathbf{r}(n)\mathbf{r}^H(n) - \rho(n-1)^{-1}\mathbf{P}(n)$

$\nabla_\rho(n) = -\dfrac{1}{2}\mathrm{E}[\boldsymbol{\psi}^H(n-1)\hat{\mathbf{y}}(n)e^*(n) + \hat{\mathbf{y}}^H(n)\boldsymbol{\psi}(n-1)e(n)]$

$c(n) = \beta_1 c(n-1) + (1-\beta_1)\nabla_\rho(n)$

$h(n) = \beta_2 h(n-1) + (1-\beta_2)\nabla_\rho(n)^2$

$\rho(n) = \rho(n-1) - \left[\mathrm{Re}\left\{\eta\dfrac{c(n)}{\sqrt{h(n)} + \xi}\right\}\right]_{\rho_{min}}^{\rho_{max}}$

$n = n + 1$

Until $n = N$

Output: $\mathbf{w}_t = \mathbf{w}(N)$

Initial values selection descriptions for the **Algorithm 2**:

1) The value of the regularization parameter, Δ, is selected small for high SNR and large for low SNR [31] and it regulates the noise variations. The optimum regularization factor has no closed-form solution [33], and since the SNR is high ($\mathrm{SNR} \geq 0$), the regulation factor is selected based on the best simulation results, starting from small values.

2) The values of update states are initialized as $c(0) = 0$ and $\mathrm{h}(0) = 0$, to force moment estimates to zero during the initialization.

3) The decay rate for the gradient, β_1, is typically selected as 0.9 to give high weighting to recent gradients. On the other hand, decay rate for the squared gradient, β_2, is typically selected as 0.999 to stabilize the estimate of variance by keeping the gradients for long-term [40], [42].

4) The value of the step size, η, is selected to low-step changes in the forgetting factor update step, in its specified boundaries. ($\rho_{max} = 0.999, \rho_{min} = 0.96$).

5) The initial value of the forgetting factor is selected randomly and closer to the lower limit to provide fast convergence rate and high mis-adjustment during the initial update steps.

Once the weights of the antenna array are calculated, the output spatial spectrum in t-th epoch can be written as:

$$\mathbf{D}_t(\theta, \phi) = \frac{1}{|\widehat{\mathbf{w}}_t^H \mathbf{a}(\theta, \phi)|} \tag{6-37}$$

where $\widehat{\mathbf{w}}_t = [1; -\boldsymbol{w}_t] \epsilon\, \mathbb{C}^{M_{AP} \times 1}$, $\mathbf{a}(\theta, \phi) \epsilon\, \mathbb{C}^{M \times \Theta}$ is the steering vector and Θ is the total number of elevation and azimuth pairs, (θ, ϕ), to be scanned in output spatial spectrum.

It should be noted that, in this study, we assume that the scatters are uncorrelated. In realistic multipath scenarios the conventional DoA estimation techniques may not work efficiently, however, sparse reconstruction techniques overcome this problem by formulating an over-complete array output dictionary under the constraint of sparsity and the spatial information of the incident sources can be recovered by this way [43]. The problem in (6-10) can be extended to matrix completion sparse recovery problem and can be solved by semidefinite programming [44] following ADMM, then, the $\widehat{\mathbf{w}}_t$ can be estimated with the proposed method.

6.2.3.5. Convergence Analysis

The DoA estimation and tracking are performed based on adaptive filtering, therefore, the proposed DoA estimation and tracking algorithm is convergent, and its convergence properties can be investigated similarly to adaptive filters.

In dynamic scenarios, the optimum solutions are in a time-varying form and the minimum point of the error curve is not fixed, thus, tracking is required. In time-varying scenarios the optimum weight coefficients can be expressed as [45]:

$$\mathbf{w}_0(n) = \mathbf{w}_0(n-1) + \mathbf{q}_p(n) \tag{6-38}$$

where $\mathbf{q}_p(n) \epsilon\, \mathbb{C}^{(M_{AP}-1) \times 1}$ denotes a random perturbation which is an independently generated sequence with zero mean and positive definite autocorrelation matrix as $\mathbf{R} = E\left[\mathbf{q}_p(n)\mathbf{q}_p^H(n)\right]$ and $\mathbf{w}_0(n) \epsilon\, \mathbb{C}^{(M_{AP}-1) \times 1}$ is the optimum weight vector and can be calculated by the Wiener optimal solution as:

$$\mathbf{w}_0 = \mathbf{R}^{-1}\mathbf{p} + \mathbf{q}_p(n) = E\left[\left(\hat{\mathbf{y}}(n)\hat{\mathbf{y}}^H(n)\right)^{-1}\right] E[\hat{\mathbf{y}}(n) y^*(1, n)] + \mathbf{q}_p(n) \tag{6-39}$$

and,

$$y(1,n) = \mathbf{w}_0^H(n-1)\hat{\mathbf{y}}(n) + z_{t,1}(n) \tag{6-40}$$

where $z_{t,1}(n)$ is the received noise from the reference antenna with zero mean and variance as, σ_0^2, where $\sigma_0^2 = 1 - \mathbf{w}_0^H(n)\mathbf{s} - \mathbf{s}^H\mathbf{w}_0(n) + \mathbf{w}_0^H(n)\hat{\mathbf{y}}(n)\hat{\mathbf{y}}^H(n)\mathbf{w}_0(n)$.

The above definitions are typical for tracking analyses of adaptive filters [45], [46]. In order to continue the analysis, first, the weight error vector is defined as follows:

$$\boldsymbol{\epsilon}(n) = \mathbf{w}(n) - \mathbf{w}_0(n) = \mathbf{w}(n-1) - \mathbf{w}_0(n-1) - \mathbf{q}_p(n) + \mathbf{R}^{-1}\hat{\mathbf{y}}(n) \tag{6-41}$$

Then, when we put σ_0^2 in (43) we have,

$$\boldsymbol{\epsilon}(n) = \left(\mathbf{I}_{M_{AP}} - \mathbf{R}^{-1}\hat{\mathbf{y}}(n)\hat{\mathbf{y}}^H(n)\right)\boldsymbol{\epsilon}(n-1) + \mathbf{R}^{-1}\hat{\mathbf{y}}(n)\mathbf{z}_{t,1}^*(n) - \mathbf{q}_p(n) \tag{6-42}$$

The weight error vector is used in determining the mean square error (MSE). The mean square error for in time-varying environment can be expressed as:

$$\zeta(n) = E\left[\left|y(1,n) - \mathbf{w}_0^H(n-1)\hat{\mathbf{y}}(n)\right|^2\right] \tag{6-43}$$

By expanding and simplifying (42), we get

$$\zeta(n) = \mathbf{w}_0^H(n-1)\mathbf{R}\mathbf{w}(n-1) + \mathrm{tr}\big(\mathbf{R}\mathbf{K}(n)\big) + 1 - \mathbf{w}_0^H(n-1)\mathbf{s} - \mathbf{s}^H\mathbf{w}_0(n-1) \tag{6-44}$$

where $\mathbf{K}(n) = E[\boldsymbol{\epsilon}(n)\boldsymbol{\epsilon}^H(n)]$.

The MSE value of the tracking can be calculated by taking the limit of $\zeta(n)$ where $N \to \infty$. The MSE can be computed as [45]:

$$\zeta(\infty) \approx \zeta_{min} + \frac{(1 - E[\rho(\infty)])}{(1 + E[\rho(\infty)])}\sigma_0^2 M_{AP} + \frac{\mathrm{tr}\big(\mathbf{R}E\big[\mathbf{q}_p(n)\mathbf{q}_p^H(n)\big]\big)}{(1 - E^2[\rho(\infty)])} \tag{6-45}$$

It should be noted that in order to compute (6-45) quantities $E[\rho(\infty)]$ and $E\big[\mathbf{q}_p(n)\mathbf{q}_p^H(n)\big]$ have to be calculated.

The MSE is critical to analyze the adaptive filters, as well as, its derivation adaptive DoA estimation and tracking algorithms which indicates how far the estimate is from the correct value and is a convergence indicator. The convergence itself relies on the eigen values of correlation matrix. Thus, the critical parameter in RLS algorithm is $\mathbf{P}(n)$ where when we choose $\rho < 1$ the algorithm is convergent since all the eigen values are in unit circle. For any bounded input the algorithm converges regardless of the eigen values [45] as long as $0 < \rho \leq 1$. Therefore, any adaptive forgetting factor method will only affect the convergence rate.

The gradient based variable or adaptive forgetting factor methods are prominently used for improving the convergence rate of RLS algorithm, thus, tracking performance [39], [47], [48]. In order to obtain the gradient differentiation is applied to both sides of (6-44) with respect to forgetting factor, ρ, as:

$$\frac{d\zeta(n)}{d\rho} = \frac{dA}{d\rho} + \frac{dB}{d\rho} + \frac{d\sigma_0^2}{d\rho} \tag{6-46}$$

where $A = \mathbf{w}_0^H(n-1)\mathbf{R}\mathbf{w}(n-1)$ and $B = \mathrm{tr}\big(\mathbf{R}\mathbf{K}(n)\big)$. Then, the gradient based controlling scheme for the RLS algorithm can be expressed as:

$$\rho(n) = \left[\rho(n-1) - \frac{d\zeta(n)}{d\rho}\right]_{p_{min}}^{p_{max}} \tag{6-47}$$

where $\frac{d\zeta(n)}{d\rho} = \nabla_\rho(n)$.

In the literature, there are many existing methods to update forgetting factor according to its gradient's direction, however, in this study the low-complexity ADAM method is adopted as mentioned before.

6.2.4. Simulation Results

In this section, we evaluate the performance of the proposed algorithm by numerical simulations and compares its performance with MUSIC [19], NLMS [49], VSS-NLMS [49] and RLS [31] algorithms in terms of spatial spectrum, root mean square error (RMSE), mean square error (MSE), and computational complexity. The scatters may interfere with received signals resulting degradation in DoA estimation accuracy. It is worth paying attention to show the effect of scatter on the accuracy of DoA estimation. Thus, simulations were conducted for single-path propagation and multi-path propagation case. For each n-th snapshot, 25 % of antennas are switched-off randomly, then, matrix completion is applied. The optimal weight vector for MSE is calculated according to Wiener formula [31]. Initial values and parameters are same as in **Algorithm 2** for the proposed algorithm. The parameters of the compared algorithms are used as suggested by the corresponding publications. The results are evaluated by an average of 250 Monte Carlo trails.

Fig. 6.5, the comparison of computational complexities in terms of complex multiplications per iteration for all algorithms but MUSIC are given according to the , where $\mathcal{N}$ denotes the computational complexity of TNNR-ADMM (denoted in **Algorithm** 1) and equals to $\mathrm{O}(\max(M_{AP}, N).\min(M_{AP}, N)^2 + M_{AP}^3 + M_{AP}^2 + 2M_{AP}N)$, where O(.) is the big-O notation denoting the complexity of the algorithms. Since DoA estimation and tracking are performed after the TNNR-ADMM step, $\mathcal{N}$ is mentioned in all DoA algorithms.

Table 6-I. Computational complexity comparisons of the algorithms: MUSIC, NLMS, VSS-NLMS, RLS and AF-RLS.

Algorithm	Complex Multiplications	Example[1]
MUSIC	$O(\mathcal{N} + M_{AP}^3 + M_{AP}^3 N^3 (M_{AP}^3 - 1) + M_{AP}^3 N^2)$	$\cong 444\text{E}10$
NLMS	$O(\mathcal{N} + 3(M_{AP} - 1))$	429
VSS-NLMS	$O(\mathcal{N} + 5(M_{AP} - 1))$	715
RLS	$O(\mathcal{N} + 4(M_{AP} - 1)^2 + 4(M_{AP} - 1))$	$\cong 82\text{E}3$
AF-RLS	$O(\mathcal{N} + 9(M_{AP} - 1)^2 + 6(M_{AP} - 1))$	$\cong 184\text{E}3$

[1]Number of complex multiplications are given when $M_{AP} = 144$ and $N = 600$. The computational complexity of $\mathcal{N}$ is excluded.

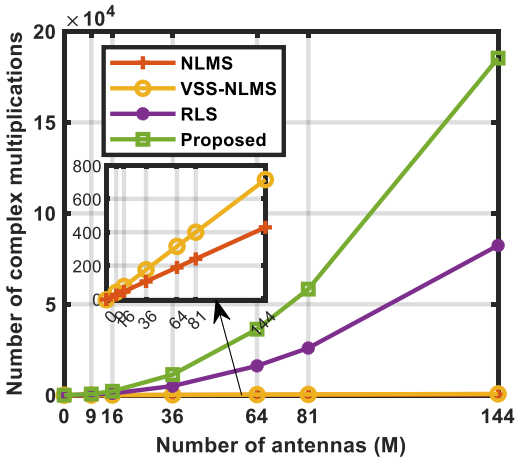

Fig. 6.5. Computational complexity comparison of algorithms in terms of number of complex multiplications.

6.2.4.1. Single-Path Propagation

In the single-path propagation case, the tracking average error (TAE) [32] is defined in addition to other performance metrics.

$$\text{TAE}_{t,1} \triangleq \left(\left|\hat{\theta}_{t,1} - \theta_{t,1}\right| + \left|\hat{\phi}_{t,1} - \phi_{t,1}\right|\right)/2 \tag{6-48}$$

where $\hat{\theta}_{t,1}$ and $\hat{\phi}_{t,1}$ are the estimated theta and phi angles, respectively, at the t-th epoch for single source.

The simulation parameters for single-path propagation case are given in Table 6-II.

Table 6-II. Simulation parameters for the single-path propagation case.

Parameters	Values
N, L, T	(600,1,6)
Initial angles, $(\theta_{0,1}, \varphi_{0,1})$	$(45^o, 45^o)$
Displacement, $(\Delta\theta, \Delta\varphi)$	$(1^o, 1^o)$
Tolerance, ε	10^{-3}
Iteration, i	20
M_{AP}, M_{RIS}	(144,144)
SNR	10 dB

Fig. 6.6 (a) and (b) demonstrate the spatial spectrum of MUSIC, NLMS, VSS-NLMS, RLS and proposed algorithm under 10 dB SNR. The tracking capabilities of the algorithms are compared. Along with the proposed algorithm, RLS algorithm has estimated the final theta and phi angles efficiently. The DoA estimation performances of RLS and the proposed algorithm are better than the other algorithms. However, the proposed algorithm has almost 3 dB more spectral gain than the RLS algorithm. We can conclude that the proposed algorithm and RLS algorithm track the target precisely. In (c), it can be seen that the proposed algorithm has at least 10 dB better MSE than the compared algorithms. In (d) TAE shows the average error between true angles and the estimated angles of target in each epoch during the observation. It is seen that the proposed algorithm has the lowest average error. As a final remark, adaptive forgetting factor has increased the tracking capability of the RLS algorithm. The more detailed analysis is given in multi-path propagation case.

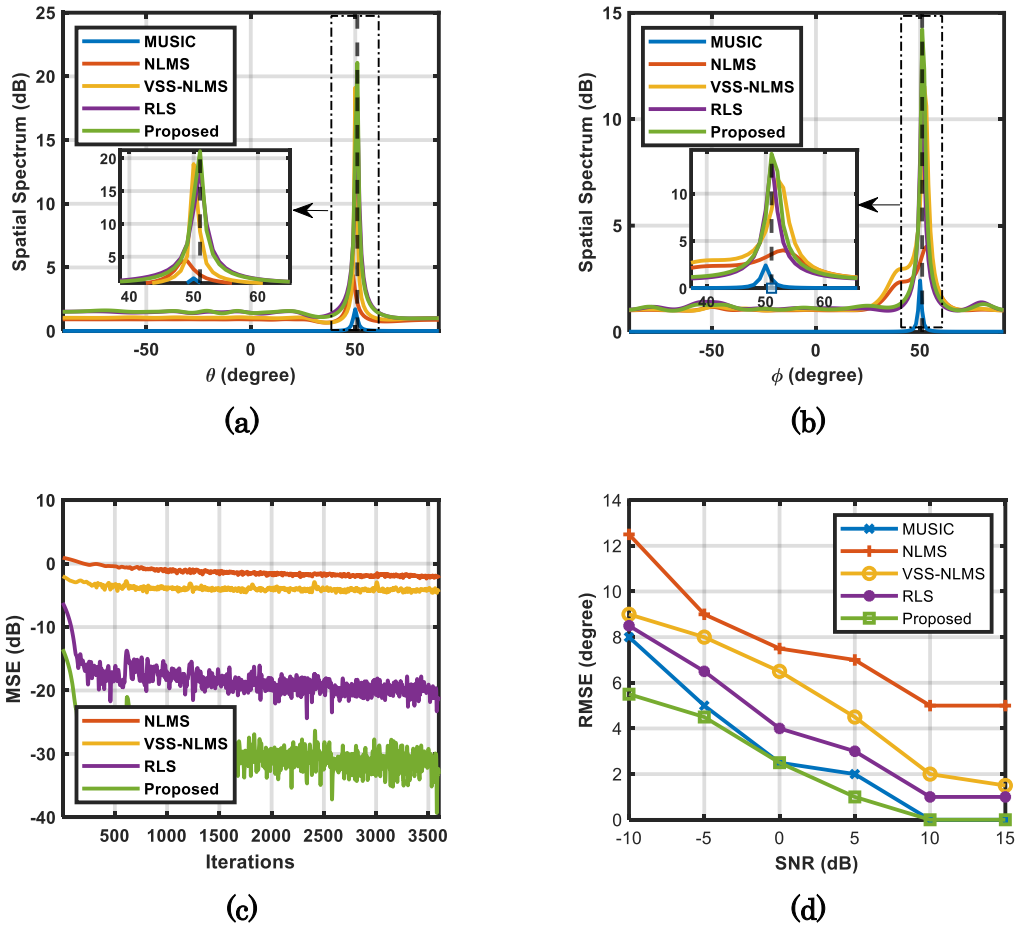

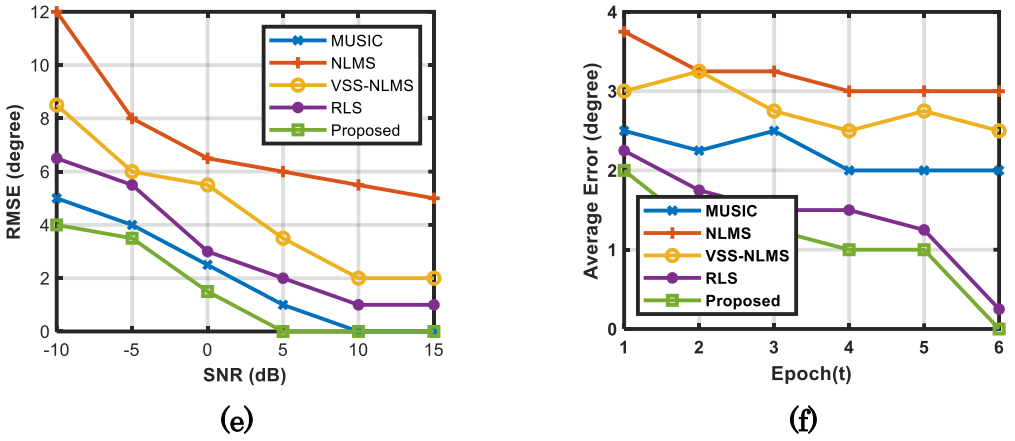

Fig. 6.6. Comparative representations of MUSIC, NLMS, VSS-NLMS, RLS and the proposed algorithm, (a) final theta spectrum, $\theta_{6,1} = 51^o$, (b) final phi spectrum, $\phi_{6,1} = 51^o$, (c) mean square errors at 10 dB SNR, (d) estimation RMSE of final theta angle under varying SNR, (e) estimation RMSEs of final phi angle under varying SNR, (f) performance of target tracking at 10 dB SNR, tracking average error.

6.2.4.2. Multi-Path Propagation

In the multi-path propagation case, the total error (TE) is defined in addition to other performance metrics. Besides, to evaluate the maximum percentage of the switched-off elements in the antenna array for accurate DoA estimation, RMSE with respect to percentage of signal information loss is analyzed.

$$TE_t \triangleq \sum_{l=1}^{L} \left(\left| \hat{\theta}_{t,l} - \theta_{t,l} \right| + \left| \hat{\phi}_{t,l} - \phi_{t,l} \right| \right) \tag{6-49}$$

where $\hat{\theta}_{t,l}$ and $\hat{\phi}_{t,l}$ are the estimated theta and phi angles, respectively, at the t-th epoch for l-th propagation path.

The simulation parameters for multi-path propagation case are given in Table 6-III.

Table 6-III. Simulation parameters for the multi-path propagation case.

Parameters	Values
N, L, T	(600,5,6)
Tolerance, ε	10^{-3}
Iteration, i	20
M_{AP}, M_{RIS}	(144,144)

For the multi-path propagation case, we assume user has constant speed with 1^o per epoch only in elevation along $T = 6$ epochs. There are $L = 5$ propagation paths and $\theta_{t,l}$ follows a uniform distribution $\mathcal{U}(0, \pi/3)$, $\alpha_{t,l}$ follows a normal distribution $\mathcal{CN}(0,1)$, however, $\phi_{t,l} = \pi/4$. In each iteration, n, 25 % of antennas are switched-off randomly, then, matrix completion is applied. The SNR for strongest path is 10 dB. Fig. 6.7 (a) shows the

comparative spatial spectrum in elevation of algorithms at the end of the final epoch. According to the results, only the proposed algorithm and MUSIC accurately estimate the final DoA. In contrast, VSS-NLMS and RLS deviates from the final DoA by $\approx 2^o$ and $\approx 1^o$, respectively. Even 1^o degree deviation is critical since the user can be lost as the aperture of RIS or AP as the number of epochs increases. On the other hand, NLMS has 5^o deviation and we can conclude it fails to track the user. By the proposed algorithm, the spectral gain of the user and its two significant scatterers are estimated as ≈ 18.7 dB, ≈ 4.82 dB and ≈ 4.05 dB, respectively. It should be noted, since the powers of the other scatters are located at the two extremes of the distribution ($\geq |3\sigma|$) their contributions are negligible. Besides, proposed algorithm has 6 dB more sensitivity in the power spectrum than RLS. As a final remark, the proposed algorithm has better DoA estimation and tracking capabilities than the compared algorithms. The RLS tracking performance is degraded by the presence of scatters. The MUSIC algorithm performs better in multi-path propagation case since user displacement is only in elevation angle. Compared to MUSIC algorithm the proposed algorithm has better DoA estimation performance and has 2.41e7 times less computational complexity.

Fig. 6.7 (b) and (c) shows that final theta and phi RMSE estimations. The proposed algorithm is superior than the compared algorithms. In (d), the comparative MSE values of the proposed algorithm and RLS algorithm are given. The results show that the proposed algorithm has faster convergence rate due to the adaptive forgetting factor and has almost 10 dB better accuracy than the RLS algorithm. In (e) the TE between true angles and the estimated angles of the user and its scatters in each epoch are given. It can be seen that as the tracking time increases TE of the algorithms but the proposed algorithm and MUSIC increases. The proposed algorithm has $> 3^o$ better TE performance than RLS. In (f), final theta RMSE estimations demonstrates that as the percentage of switched-off antennas increases DoA estimation accuracy decreases and 25 % switch-off can be considered as a limit for 10 dB SNR.

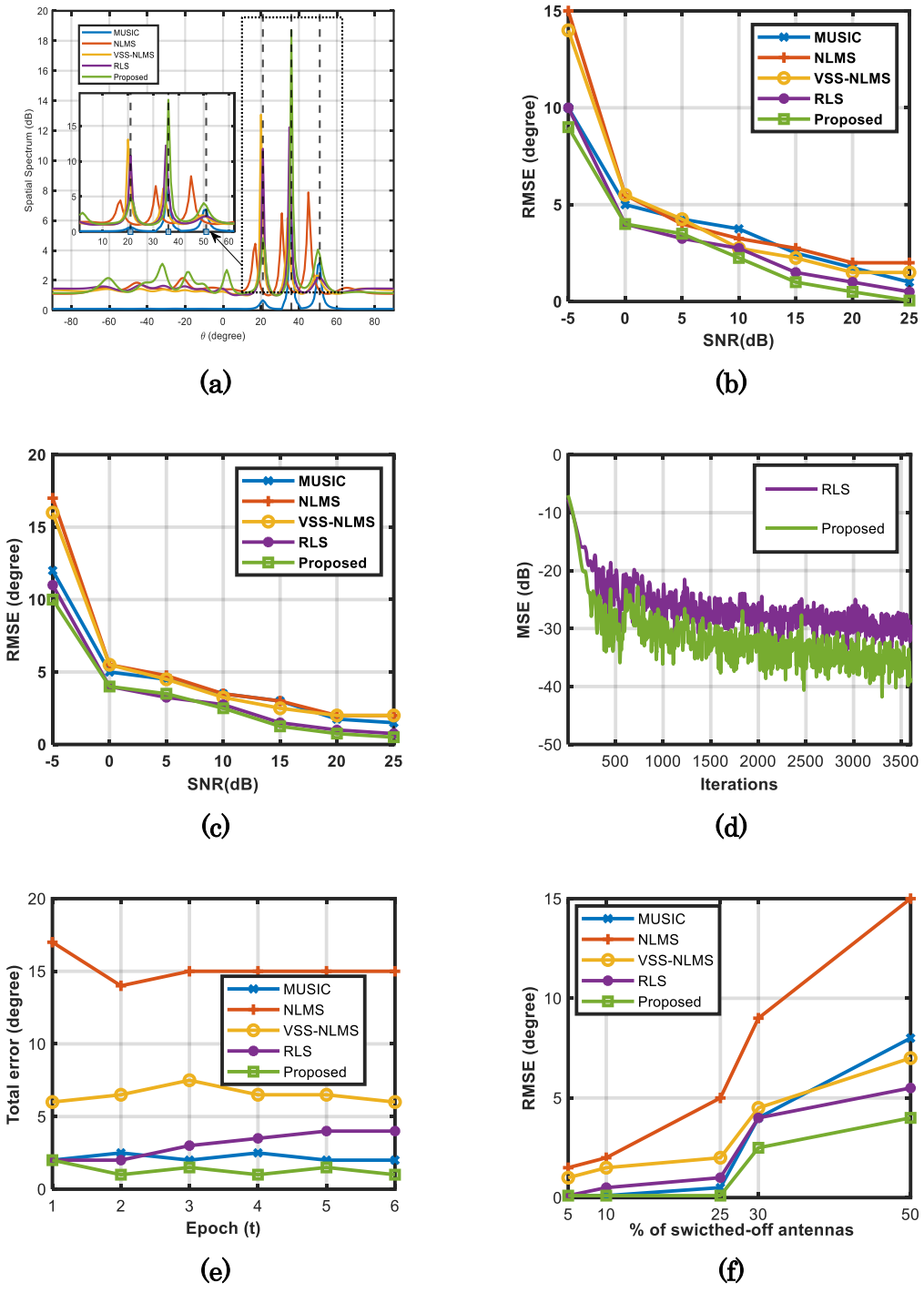

Fig. 6.7. Comparisons of MUSIC, NLMS, VSS-NLMS, RLS and the proposed algorithm, (a) the spatial spectrum of the final DoAs of the user and its scatters: $\theta_{T,2} = 21^o$, $\theta_{T,3} = 36^o$ and $\theta_{T,4} = 51^o$, (b) and (c) RMSE of final elevation and azimuth angles of the user under varying SNR, (d) MSE at 10 dB SNR, (e) TE in each epoch at 10 dB SNR, (f) signal loss under varying (%) of switched-off antennas.

Fig. 6.8 shows the resolution probabilities of MUSIC, RLS and the proposed algorithms against varying SNR with two signals with final DoAs, $\theta_{T,1} = 36^o$ and $\theta_{T,2} = 41^o$ under %25 random switched-off antennas condition, angle separation between two finals DoAs from $\theta_{T,1} = 36^o$ and $\theta_{T,2} = 36^o + \Delta\theta$, $\Delta\theta$ changes from 2^o to 8^o and signal loss under varying (%) of switched-off antennas with final DoAs, $\theta_{T,1} = 36^o$ and $\theta_{T,2} = 41^o$. The resolution probability analyses demonstrate the capability of all algorithms to resolve the DoAs of closely separated signal sources. The resolution probability is an important factor since the estimated DoAs might be used for subsequent processing schemes such as localization and channel estimation where the closely spaced multi-path signals effect the system performance significantly. In general, the angular spread between the main signal and its scatters are relative closely spaced as $\approx 5^o$ [8] which indicates the importance of resolution probability. The resolution possibilities of the NLMS and VSS-NLMS algorithms are excluded because Fig. 6.8 shows that their multipath DoA estimates and tracking performances are insufficient and are no longer necessary for further analysis. It can be seen that the resolution probability of the proposed method is higher than the MUSIC and RLS algorithms.

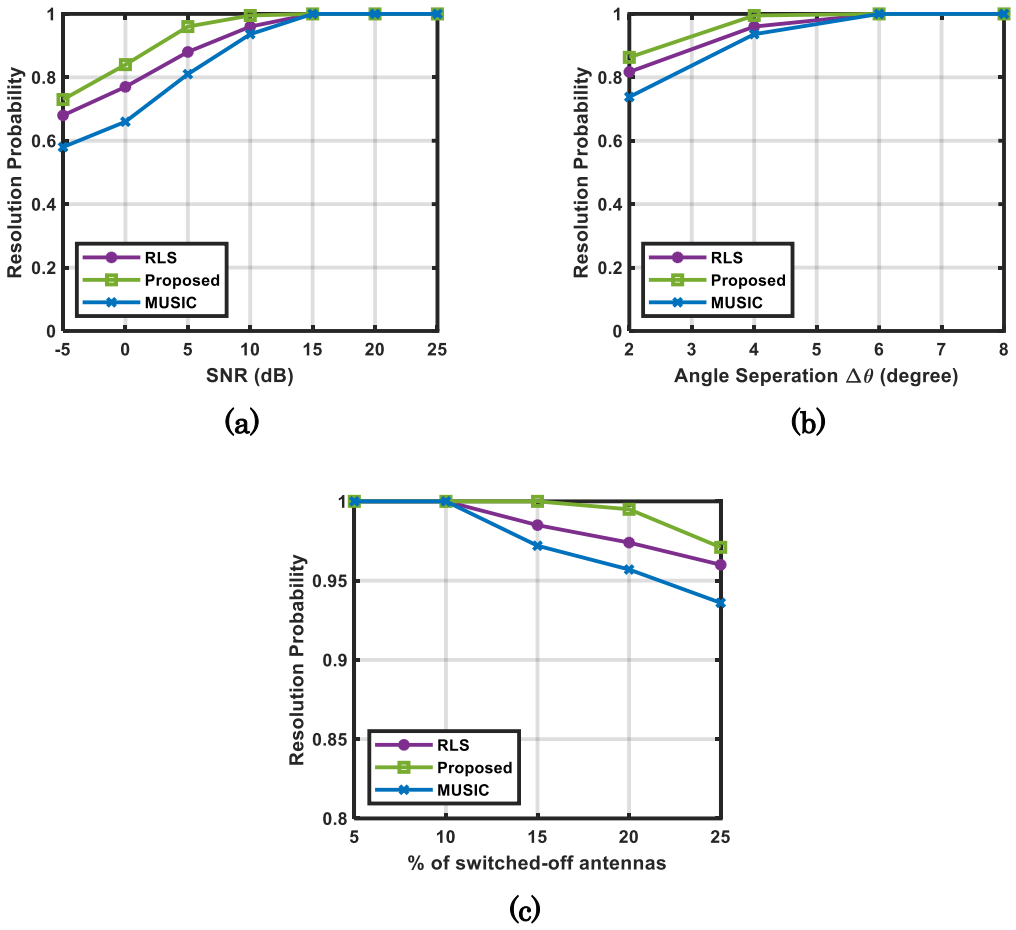

Fig. 6.8. Resolution probabilities of MUSIC, RLS and the proposed algorithm for $L = 3600$, (a) varying SNR with two signals with final DoAs, $\theta_{T,1} = 36^o$ and $\theta_{T,2} = 41^o$ under %25 random switched-off antennas condition, (b) angle separation between two finals DoAs from $\theta_{T,1} = 36^o$ and $\theta_{T,2} = 36^o + \Delta\theta$, $\Delta\theta$ changes from 2^o to 8^o, (c) varying (%) of switched-off antennas with final DoAs, $\theta_{T,1} = 36^o$ and $\theta_{T,2} = 41^o$.

6.3. Hybrid-Field Channel Estimation for RIS-Aided Millimeter-Wave Massive MIMO Systems

An efficient hybrid-field channel estimation method for RIS-aided mm-Wave massive MIMO systems is presented. The estimation of direction of arrivals (DoAs), direction of departures (DoDs) and range arrivals, range of departures depend on the higher order statics of the received signal at receiver. A fourth-order cumulant matrix is constructed to eliminate near-field phase components on ensuing scatters of the transmitted and reflected signals. The atomic norm minimization (ANM) reconstruction is applied on the resultant cumulant matrix, then to extract the information of DoAs and DoDs rank minimization problem is used. However, due to the rank operator this problem is non-convex. The non-convex minimization problem is transformed into a convex minimization problem by using nuclear

trace/norm relaxation. A 2-D multiple classification (MUSIC) spectrum is formed to extract the DoAs and DoDs. Then, the similar procedure is followed for range estimations and a 2-D MUSIC range spectrum is adopted to match the range values to the corresponding DoAs and DoDs [50], [51]. The performance of the proposed method is evaluated and compared with state-of-the art channel estimators. The numerical results denotes that the channel estimation performance of the proposed method outperforms the state-of-the-art channel estimation methods.

6.3.1. Main Contributions

The main contributions of the proposed hybrid-field channel estimation for RIS-aided mm-Wave massive MIMO systems are listed below:

- New channel formulation is presented for RIS-aided massive MIMO systems.
- The higher statistics of the received signal is used for eliminate the near-field phase components. Hence, a special fourth-order cumulant matrix is constructed.
- The ANM reconstruction, which allows continuous angle domain, is used to recover the fourth-order cumulant matrix. Thus, higher resolution on the estimation of the DoDs and DoAs of the scatters is achieved.
- This is first study on hybrid-field channel estimation for RIS-aided mm-Wave massive MIMO systems using the higher statistics of the received signal.

6.3.2. System Model and Theoretical Formulation

We consider a general (indoor or outdoor) uplink narrow-band RIS-aided mm-Wave massive MIMO system, as presented in Fig. 6.9. The system consists of one receiver (BS) with $M_{BS} = 2m_{BS} + 1$ antennas communicate with one user equipment (UE) with $M_{UE} = 2m_{UE} + 1$ antennas via a RIS with $M_{RIS} = 2m_{RIS} + 1$ antennas. The RIS is deployed at an arbitrary location relative to the BS. The BS, RIS and UE are equipped with uniform linear arrays (ULA). Therefore, only the azimuth (φ) angles are considered in this study. However, the system can be extended to a multi-user case and uniform planar arrays for all components (BS, RIS, UE) at the cost of increased computational complexity. The direct LOS channel between UE and BS is blocked and the communication relies on the cascaded channel (UE-RIS-BS). We assume that there are L_1 mixed far-field and near-field scatters in the vicinity of UE and RIS, and L_2 mixed far-field and near-field scatters in the vicinity of RIS and BS. The UE sends pilot signals and with applying a matching filter at the BS the pilot signals can be distinguished.

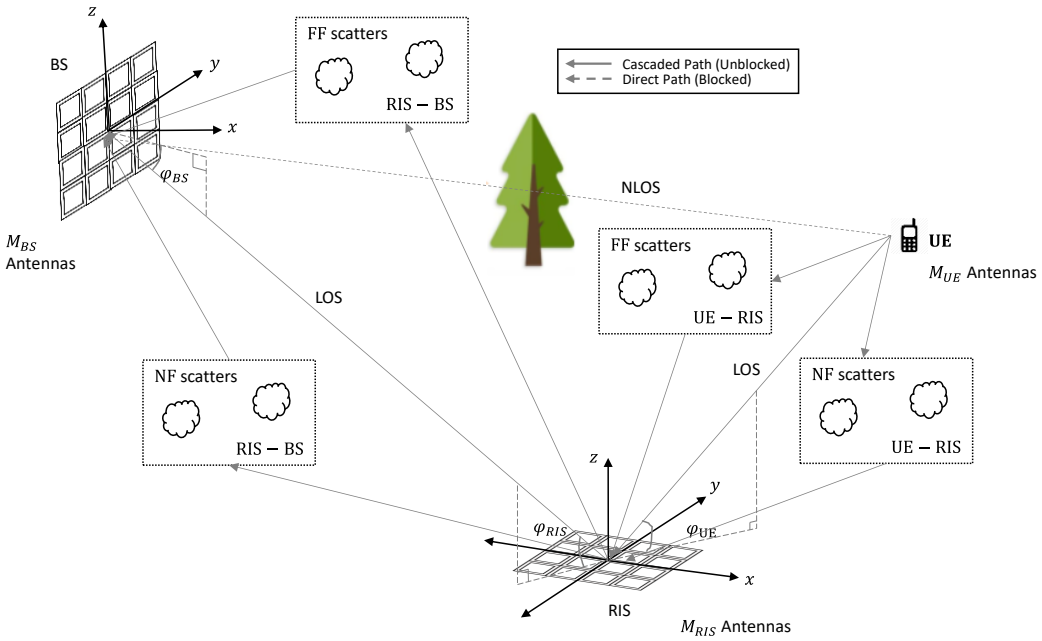

Fig. 6.9. The uplink narrow-band RIS-aided mm-Wave massive MIMO system with mixed far-field and near-field scatters.

In line with these assumptions and definitions, channel and signal models are given in the next stage.

We consider the Saleh-Valenzuela channel model [52] which is very prominent in mm-Wave communication system, to model cascaded channel between UE and BS. The cascaded channel consists of two components, the channel between UE and RIS, $\mathbf{H}_1$, and the channel between RIS and BS, $\mathbf{H}_2$. The cascaded channel components can be modelled as:

$$\mathbf{H}_1 = \sum_{l_1=1}^{L_1} \alpha_{l_1} \boldsymbol{a}\left(\varphi_{l_1}^{RIS}\right)\boldsymbol{a}\left(\varphi_{l_1}^{UE}\right)^T \tag{6-50}$$

$$\mathbf{H}_2 = \sum_{l_2=1}^{L_2} \alpha_{l_2} \boldsymbol{a}\left(\varphi_{l_2}^{BS}\right)\boldsymbol{a}\left(\varphi_{l_2}^{RIS}\right)^T \tag{6-51}$$

where $\boldsymbol{a}(.)$ denotes the steering vector and for a general angle, φ, it can be expressed as:

$$\boldsymbol{a}(\varphi, r) = \left[e^{-m\omega(\varphi)-m^2\gamma(\varphi,r)}, \ldots, 1, \ldots, e^{m\omega(\varphi)+m^2\gamma(\varphi,r)}\right]^T \tag{6-52}$$

where m is the element index in the antenna array with $2m+1$ antennas, ω and γ are the far-field, and near-field phase components of the m-th element, and the value 1 is the phase of the middle element where $m = 0$. The far-field and near-field phase components for an ULA can be written as [53]:

$$\omega(\varphi) = -\frac{2\pi d}{\lambda}\sin\varphi, \quad \gamma(\varphi, r) = \frac{\pi d^2}{\lambda r}\cos^2\varphi \tag{6-53}$$

where d is the inter-element spacing, r is the range and λ is the wavelength of the operating frequency.

The effective cascaded uplink channel, $\mathbf{H}\epsilon\mathbb{C}^{M_{BS}\times M_{UE}}$, can be expressed as:

$$\mathbf{H} = \mathbf{H}_1\boldsymbol{\Theta}\mathbf{H}_2 \tag{6-54}$$

where $\boldsymbol{\Theta}\epsilon\mathbb{C}^{M_{RIS}\times M_{RIS}}$ is a diagonal matrix, whose complex elements denotes the gain and phase coefficients of the RIS elements as $g_{m_{RIS}}e^{j\Phi_{m_{RIS}}}$.

Then, the received uplink pilot signal at the BS,$\bar{\boldsymbol{y}}\ \epsilon\mathbb{C}^{M_{BS}\times 1}$, is given by:

$$\bar{\boldsymbol{y}} = \mathbf{H}\boldsymbol{s} + \mathbf{n} \tag{6-55}$$

where $\boldsymbol{s}\epsilon\mathbb{C}^{M_{UE}\times 1}$ is the pilot signal and $\mathbf{n}\epsilon\mathbb{C}^{M_{BS}\times 1}$ is the zero mean and unit variance additive Gaussian noise. At BS we apply matching filter to vector $\bar{\boldsymbol{y}}$ and the filtered received vector, $\boldsymbol{y}\boldsymbol{\epsilon}\mathbb{C}^{M_{BS}\times 1}$, can be expressed as:

$$\boldsymbol{y} = \bar{\boldsymbol{y}}\boldsymbol{s}^T = \mathbf{H}\boldsymbol{s}\boldsymbol{s}^T + \mathbf{n}\boldsymbol{s}^T \tag{6-56}$$

where $|\boldsymbol{s}\boldsymbol{s}^T| = 1$.

Finally, we can derive and rewrite the effective cascaded channel as:

$$\mathbf{H} = \sum_{l_2=1}^{L_2}\sum_{l_1=1}^{L_1}\alpha_{l_2}\alpha_{l_1}\boldsymbol{a}\left(\varphi_{l_2}^{BS}\right)\boldsymbol{a}\left(\varphi_{l_2}^{RIS}\right)^T\boldsymbol{\Theta}\,\boldsymbol{a}\left(\varphi_{l_1}^{RIS}\right)\boldsymbol{a}\left(\varphi_{l_1}^{UE}\right)^T \tag{6-57}$$

From (6-57), we can define the cascaded channel gain, $\eta_{p,k}$, as:

$$\eta_{l_1,l_2} = \alpha_{l_1}\alpha_{l_2}\boldsymbol{a}\left(\varphi_{l_2}^{RIS}\right)^T\boldsymbol{\Theta}\boldsymbol{a}\left(\varphi_{l_1}^{RIS}\right) \tag{6-58}$$

Then, the cascaded channel is reduced the form of [19]:

$$\mathbf{H} = \sum_{l_2=1}^{L_2}\sum_{l_1=1}^{L_1}\eta_{l_1,l_2}\,\boldsymbol{a}\left(\varphi_{l_2}^{BS}\right)\boldsymbol{a}\left(\varphi_{l_1}^{UE}\right)^T \tag{6-59}$$

Similar to [19], we can omit the effects of DoD, $\varphi_{l_2}^{RIS}$, and DoA, $\varphi_{l_1}^{RIS}$, components of RIS since the phase optimization of the RIS elements depends on the $\varphi_{l_1}^{UE}$ and $\varphi_{l_2}^{BS}$. The main focus of this study is mixed-field channel estimation in RIS-aided MIMO systems; hence, no additional optimum RIS phase configuration is proposed. However, we assume that the optimum phase configuration of RIS elements are estimated by least-squares solution as

referred in [19]. It should also be noted that RIS phase optimization is done by considering both ω and γ for the steering vectors in the channel model.

Once we model the cascaded channel, the element-wise signal model for the system can be formulated.

The received signal, at time τ, with N signal samples corresponding the path between the m_{RIS}-th element of the RIS and the m_{UE}-th element of the UE, $x_{m_{RIS},m_{UE}}$, is can be expressed as:

$$x_{m_{RIS},m_{UE}}(n) = \sum_{l_1=1}^{L_1} \alpha_{l_1} e^{j\Psi^{RIS}_{m_{RIS},l_1}} e^{-j\Psi^{UE}_{m_{UE},l_1}} s(n) \tag{6-60}$$

where $s(n)$ is the transmitted pilot signal from the UE, α_{l_1} is the path loss of the propagation path corresponding to UE and its scatters, $\Psi^{RIS}_{m_{RIS},l_1}$ and $\Psi^{UE}_{m_{UE},l_1}$ are the mixed-field signal phase coefficients of direction-of-arrivals (DoA) and direction-of-departures (DoD), respectively. The phase coefficients can be expressed as:

$$\begin{aligned} \Psi^{RIS}_{m_{RIS},l_1} &= m_{RIS}\omega\left(\varphi^{RIS}_{l_1}\right) + (m_{RIS})^2\gamma\left(\varphi^{RIS}_{l_1}\right) \\ \Psi^{UE}_{m_{UE},l_1} &= m_{UE}\omega\left(\varphi^{UE}_{l_1}\right) + (m_{UE})^2\gamma\left(\varphi^{UE}_{l_1}\right) \end{aligned} \tag{6-61}$$

Then, the received signal, at time τ, with N signal samples corresponding the path between the m_{BS}-th element of the BS and the m_{RIS}-th element of the RIS, $y_{m_{BS},m_{RIS}}$, can be expressed as:

$$\begin{aligned} y_{m_{BS},m_{RIS}}(n) = \sum_{l_2=1}^{L_2}\sum_{l_1=1}^{L_1} \left(\alpha_{l_2} e^{j\Psi^{BS}_{m_{BS},l_2}} e^{j\Psi^{RIS}_{m_{RIS},l_2}}\right)\left(g_{m_{RIS}}(n) e^{j\Phi_{m_{RIS}}(n)}\right) x_{m_{RIS},l_1}(n) \\ + z_{m_{BS},m_{RIS}}(n) \end{aligned} \tag{6-62}$$

where α_{l_2} is the path loss of the propagation paths (scatters) between RIS and BS, $g_{m_{RIS}}(n)$ and $e^{j\Phi_{m_{RIS}}(n)}$ denote the reflection gain and phase at the m_{RIS}-th element of the RIS, respectively, $z_{m_{BS}}(n)$ is the complex Gaussian noise, $\Psi^{BS}_{m_{BS},l_2}$ and $\Psi^{RIS}_{m_{RIS},l_2}$ are the mixed-field signal phase coefficients of direction-of-arrivals (DoA) and direction-of-departures (DoD), respectively. The phase coefficients can be expressed as:

$$\begin{aligned} \Psi^{BS}_{m_{BS},l_2} &= m_{BS}\omega\left(\varphi^{BS}_{l_2}\right) + (m_{BS})^2\gamma\left(\varphi^{BS}_{l_2}\right) \\ \Psi^{RIS}_{m_{RIS},l_2} &= m_{RIS}\omega\left(\varphi^{RIS}_{l_2}\right) + (m_{RIS})^2\gamma\left(\varphi^{RIS}_{l_2}\right) \end{aligned} \tag{6-63}$$

Finally, we can rewrite (6-42) by using (6-33) and (6-39). Then, $y_{m_{BS},m_{RIS}}$ takes the form of:

$$y_{m_{BS},m_{RIS}}(n) = \sum_{l_2=1}^{L_2}\sum_{l_1=1}^{L_1} \eta_{l_1,l_2} e^{jm_{BS}\omega\left(\varphi_{l_2}^{BS}\right)+(m_{BS})^2\gamma\left(\varphi_{l_2}^{BS}\right)} \cdot e^{-jm_{UE}\omega\left(\varphi_{l_1}^{UE}\right)+(m_{UE})^2\gamma\left(\varphi_{l_1}^{UE}\right)} s(n) + z_{m_{BS},m_{RIS}}(n) \tag{6-64}$$

6.3.3. Proposed Method

In this section, we explain the adopted method to estimate DoDs and DoAs, ranges and cascaded channel. The first step of the proposed method is forming a special fourth-order cumulant matrix. Before going into more detailed explanation, some assumptions for the proposed method need to be stated [50], [53], [54], [55]:

1) The inter-element spacings d should be equal to $\lambda/4$ for BS and UE antenna arrays. Since RIS elements only contribute as gain and phase coefficients as, η_{l_1,l_2}, inter-element spacing for RIS can be $d = \lambda/2$.
2) The path gains or losses, α_{l_1} and α_{l_2}, later degraded to η_{l_1,l_2}, are mutually independent and identically distributed (i.i.d).
3) The additive noise is uncorrelated to the signals and is zero-mean (defined before) white Gaussian process with $E\{z_{m_{BS},m_{RIS}}(n) z^*_{m_{BS},m_{RIS}}(n)\} = \sigma_z^2$.
4) The number of propagation paths (scatters) is less than the number of UE antennas as $L_1 + L_2 < \min(L_1, L_2)$ (we assume $M_{BS} \gg M_{UE}$).
5) The condition $|\boldsymbol{s}\boldsymbol{s}^{\boldsymbol{T}}| = 1$ should be satisfied.

6.3.3.1. Fourth-Order Cumulant Matrix

The proposed method relies on the higher order statistics of the received signal. The fourth-order joint cumulant of the received signals can be expressed as [53], [56], [57]:

$$\begin{aligned} C\left(y_{a,e}(n), y^*_{b,f}(n), y_{c,g}(n), y^*_{d,h}(n)\right) = {} & E\{y_{a,e}(n) y^*_{b,f}(n) y_{c,g}(n) y^*_{d,h}(n)\} \\ & - E\{y_{a,e}(n) y^*_{b,f}(n)\} E\{y_{c,g}(n) y^*_{d,h}(n)\} \\ & - E\{y_{a,e}(n) y^*_{d,h}(n)\} E\{y_{c,g}(n) y^*_{b,f}(n)\} \\ & - E\{y_{a,e}(n) y_{c,g}(n)\} E\{y^*_{d,h}(n) y^*_{b,f}(n)\} \end{aligned} \tag{6-65}$$

where the complex fourth-order cumulant coefficients can be extended as:

$$C\left(y_{a,e}(n), y^*_{b,f}(n), y_{c,g}(n), y^*_{d,h}(n)\right) = \sum_{l_2=1}^{L_2}\sum_{l_1=1}^{L_1} \eta_{l_1,l_2} \cdot e^{j\left[(a-b+c-d)\omega\left(\varphi_{l_2}^{BS}\right)+(a^2-b^2+c^2-d^2)\gamma\left(\varphi_{l_2}^{BS}\right)\right]} \tag{6-66}$$

$$. e^{-j\left[(e-f+g-h)\omega\left(\varphi_{l_1}^{UE}\right)+(e^2-f^2+g^2-h^2)\gamma\left(\varphi_{l_1}^{UE}\right)\right]} + c_z$$

where $c_{l_1,l_2} = C\left(\eta_{l_1,l_2}, \eta_{l_1,l_2}^*, \eta_{l_1,l_2}, \eta_{l_1,l_2}^*\right)$ is the fourth-order cumulant fourth-order cumulant of the cascaded channel gain and $c_z = C\left(z_{a,e}(n), z_{b,f}^*(n), z_{c,g}(n), z_{d,h}^*(n)\right)$ is the fourth-order joint cumulant of the received noises.

In order to retain the angles and eliminate the range parameters we construct a special spatial cross-cumulant matrix, $\mathbf{C}\epsilon\mathbb{C}^{M_{BS}\times M_{UE}}$, whose (m_{BS}, m_{UE})-th entries are given as:

$$\begin{aligned} &C_{m_{BS},m_{UE}}\left(y_{m_{BS}^1,m_{UE}^1}(n), y_{-m_{BS}^1,-m_{UE}^1}^*(n), y_{m_{BS}^2,m_{UE}^2}(n), y_{-m_{BS}^2,-m_{UE}^2}^*(n)\right) \\ &\qquad = \sum_{l_2=1}^{L_2}\sum_{l_1=1}^{L_1} c_{l_1,l_2}\, e^{j2(m_{BS}^1-m_{BS}^2)\omega\left(\varphi_{l_2}^{BS}\right)} e^{-j2(m_{UE}^1-m_{UE}^2)\omega\left(\varphi_{l_1}^{UE}\right)} + c_z^{m,l} \end{aligned} \tag{6-67}$$

where m_{BS}^1, m_{BS}^2 are the BS antenna indices and $m_{UE}^1, m_{UE}^2$are the UE antenna indices and the cumulant of the received signal is $c_z^{m_{BS},m_{UE}} = C\left(z_{m_{BS}^1,m_{UE}^1}(n), z_{-m_{BS}^1,-m_{UE}^1}^*(n), z_{m_{BS}^2,m_{UE}^2}(n), z_{-m_{BS}^2,-m_{UE}^2}^*(n)\right)$.

Then, the compact form of the cumulant matrix $\mathbf{C}\epsilon\mathbb{C}^{M_{BS}\times M_{UE}}$ can be expressed as:

$$\mathbf{C} = \mathbf{B}_1(\boldsymbol{\varphi}^{BS}, \boldsymbol{\varphi}^{UE})\mathbf{C}_\eta \mathbf{B}_1(\boldsymbol{\varphi}^{BS}, \boldsymbol{\varphi}^{UE})^H \tag{6-68}$$

where $\mathbf{C}_\eta\epsilon\mathbb{C}^{L_1L_2\times L_1L_2}$ is a diagonal matrix, whose complex elements represent the cascaded channel gains being as $diag(c_{1,1}, \dots, c_{l_1,l_2}, \dots c_{L_1,L_2})$ and $\mathbf{B}_1(\boldsymbol{\varphi}^{BS}, \boldsymbol{\varphi}^{UE})\epsilon\mathbb{C}^{M_{BS}M_{UE}\times L_1L_2}$ is the steering matrix and can be expressed as:

$$\mathbf{B}_1(\boldsymbol{\varphi}^{BS}, \boldsymbol{\varphi}^{UE}) = \mathbf{A}_1\left(\boldsymbol{\omega}(\boldsymbol{\varphi}^{UE})\right)^* \odot \mathbf{A}_2\left(\boldsymbol{\omega}(\boldsymbol{\varphi}^{BS})\right) \tag{6-69}$$

where $\mathbf{A_1}$ and $\mathbf{A_2}$ are steering matrices whose p-th column k-th column can be expressed as:

$$\boldsymbol{a}_{l_2}\left(\varphi_{l_2}^{BS}\right) = \left[e^{-m_{BS}\omega\left(\varphi_{l_2}^{BS}\right)}, \dots, 1, \dots, e^{m_{BS}\omega\left(\varphi_{l_2}^{BS}\right)}\right]^T \tag{6-70}$$

$$\boldsymbol{a}_{l_1}\left(\varphi_{l_1}^{UE}\right) = \left[e^{-m_{UE}\omega\left(\varphi_{l_1}^{UE}\right)}, \dots, 1, \dots, e^{m_{UE}\omega\left(\varphi_{l_1}^{UE}\right)}\right]^T \tag{6-71}$$

and

$$\mathbf{b}_1\left(\varphi_{l_2}^{BS}, \varphi_{l_1}^{UE}\right) = \boldsymbol{a}_{l_1}\left(\varphi_{l_1}^{UE}\right)^* \otimes \boldsymbol{a}_{l_2}\left(\varphi_{l_2}^{BS}\right) \tag{6-72}$$

From (6-50) and (6-51), we can conclude that the fourth-order cumulant matrix, $\mathbf{C}$, only contains the far-field components $\boldsymbol{\varphi}^{BS}$ and $\boldsymbol{\varphi}^{UE}$ of the received signal, $\boldsymbol{y}$. Subsequently, the DoD and DoA parameters can be estimated by adopting a sparse reconstruction method.

6.3.3.2. DoD and DoA Estimation

The atomic norm minimization (ANM) sparse reconstruction method is adopted in this study to obtain the DoD an DoA parameters. The special fourth-order cumulant matrix $\mathbf{C}$ can be considered as the covariance matrix of the cascaded channel. Thus, an atomic set can be defined over the $\mathbf{C}$ as:

$$\mathcal{A} \triangleq \left\{\overline{\mathbf{B}}\left(\varphi_{l_2}^{BS}, \varphi_{l_1}^{UE}\right) = \left(\boldsymbol{a}_{l_1}\left(\varphi_{l_1}^{UE}\right)^* \otimes \boldsymbol{a}_{l_2}\left(\varphi_{l_2}^{BS}\right)\right)\left(\boldsymbol{a}_{l_1}\left(\varphi_{l_1}^{UE}\right)^* \otimes \boldsymbol{a}_{l_2}\left(\varphi_{l_2}^{BS}\right)\right)^H, \quad \varphi_{l_2}^{BS}, \varphi_{l_1}^{UE} \epsilon (-90^o, 90^o]\right\} \tag{6-73}$$

Then the angle recovery can be performed by using atomic l_0 norm. The atomic l_0 norm of $\mathbf{C}$ is defined as the smallest number of atoms in $\mathcal{A}$ and can be expressed as:

$$\|\mathbf{C}\|_{\mathcal{A},0} = \inf\left\{PK: \mathbf{C} = \sum_{l_2=1}^{L_2}\sum_{l_1=1}^{L_1} c_{l_1,l_2}\overline{\mathbf{B}}\left(\varphi_{l_2}^{BS}, \varphi_{l_1}^{UE}\right), \overline{\mathbf{B}}\left(\varphi_{l_2}^{BS}, \varphi_{l_1}^{UE}\right)\epsilon\mathcal{A}, c_{l_1,l_2} > 0\right\} \tag{6-74}$$

The atomic l_0 norm should be transformed into a rank minimization problem to extract the DoDs and DoAs. The rank minimization problem can be expressed as:

$$\begin{aligned} &\min_{\mathbf{Z},\mathbf{u},\hat{\mathbf{C}}} \operatorname{rank}[\mathbf{W}] \\ \text{s.t } &\mathbf{W} = \begin{bmatrix} \mathbf{Z} & \hat{\mathbf{C}}^H \\ \hat{\mathbf{C}} & \mathbf{T}(\mathbf{u}) \end{bmatrix} \geq 0, \\ &\left\|\hat{\mathbf{C}} - \mathbf{C}\right\|_F \leq \varepsilon \end{aligned} \tag{6-75}$$

where Z is an auxiliary matrix, $\hat{\mathbf{C}}$ is introduced as the exact cumulant matrix since we only observe the certain number of samples the additive noise cannot be completely eliminated even though, high-order signal statistics are used, and $\mathbf{u}$ is the reconstructed weight vector whose entries contain the DoDs and DoAs information, which defines the positive Hermitian Toeplitz matrix, $\mathbf{T}(\mathbf{u})$, as $\mathbf{T}(\mathbf{u}) = \mathbf{u}\mathbf{u}^H$, and ε is the error term (tolerance).

The rank minimization is a non-convex problem; therefore, it should be converted to a convex optimization problem, in order to be solved by the off-the-shelf solvers such as SDPT3, SeDuMi or CVX (interior-point algorithms). The convex relaxation can be applied by using trace/nuclear norm operator, thus the problem in (6-55) can take the form of:

$$\begin{aligned} &\min_{\mathbf{Z},\mathbf{u},\hat{\mathbf{C}}} \operatorname{tr}[\mathbf{Z} + \mathbf{T}(\mathbf{u})] + \zeta\left\|\hat{\mathbf{C}} - \mathbf{C}\right\|_F^2 \\ \text{s.t } &\mathbf{W} = \begin{bmatrix} \mathbf{Z} & \hat{\mathbf{C}}^H \\ \hat{\mathbf{C}} & \mathbf{T}(\mathbf{u}) \end{bmatrix} \geq 0, \mathbf{W} \geq 0 \end{aligned} \tag{6-76}$$

where tr[.] is the trace operator.

The convex optimization problem in (27) can be solved by using one of the off-the-shelf solvers which are robust solvers for semi-definite medium-sized optimization problems, however, not efficient for solving large-sized problems [58]. Therefore, we adopted alternating direction method of multipliers (ADMM) method to solve (27). The ADMM decreases the dimension of the problem, is fast, and has superior convergence.

In order to apply iteration step, first, the augmented Lagrangian function is constructed as:

$$\mathcal{L}(\mathbf{u},\mathbf{Z},\hat{\mathbf{C}},\mathbf{W},\mathbf{P}) = \mathrm{tr}[\mathbf{Z}+\mathbf{T}(\mathbf{u})] + \beta\left\|\hat{\mathbf{C}}-\mathbf{C}\right\|_F^2 + \langle \mathbf{P}, \mathbf{W} - \begin{bmatrix}\mathbf{Z} & \hat{\mathbf{C}}^H \\ \hat{\mathbf{C}} & \mathbf{T}(\mathbf{u})\end{bmatrix}\rangle + \frac{\rho}{2}\left\|\mathbf{W} - \begin{bmatrix}\mathbf{Z} & \hat{\mathbf{C}}^H \\ \hat{\mathbf{C}} & \mathbf{T}(\mathbf{u})\end{bmatrix}\right\|_F^2 \tag{6-77}$$

where $\zeta > 0$ and $\rho > 0$ denote the penalty and Langrange coefficients, respectively.

The updating steps of the ADMM of (28) for iterations $i = 1,2,\dots,I$, can be expressed as:

$$\left(\mathbf{u}^{i+1},\mathbf{Z}^{i+1},\hat{\mathbf{C}}^{i+1}\right) = \underset{\mathbf{Z},\mathbf{u},\hat{\mathbf{C}}}{\mathrm{argmin}}\,\mathcal{L}\left(\mathbf{u},\mathbf{Z},\hat{\mathbf{C}},\mathbf{P}^i,\mathbf{W}^i\right) \tag{6-78}$$

$$\mathbf{W}^{i+1} = \underset{\mathbf{W}}{\mathrm{argmin}}\,\mathcal{L}\left(\mathbf{u}^{i+1},\mathbf{Z}^{i+1},\hat{\mathbf{C}}^{i+1},\mathbf{P}^i,\mathbf{Z}\right) \tag{6-79}$$

$$\mathbf{P}^{i+1} = \mathbf{P}^i + \rho\left(\mathbf{W}^{i+1} - \begin{bmatrix}\mathbf{Z}^{i+1} & \left(\hat{\mathbf{C}}^{i+1}\right)^H \\ \hat{\mathbf{C}}^{i+1} & \mathbf{T}\left(\mathbf{u}^{i+1}\right)\end{bmatrix}\right) \tag{6-80}$$

The partitions can be given as:

$$\mathbf{W}^i = \begin{bmatrix}\mathbf{W}_0^i & \left(\mathbf{W}_1^i\right)^H \\ \mathbf{W}_1^i & \mathbf{W}_2^i\end{bmatrix} \tag{6-81}$$

$$\mathbf{P}^i = \begin{bmatrix}\mathbf{P}_0^i & \left(\mathbf{P}_1^i\right)^H \\ \mathbf{P}_1^i & \mathbf{P}_2^i\end{bmatrix} \tag{6-82}$$

and the updates of $\mathbf{u},\mathbf{Z}$, and $\hat{\mathbf{C}}$ can be calculated in closed-forms as:

$$\mathbf{Z}^{i+1} = \mathbf{W}_0^i - \frac{2}{\rho}\left(\mathbf{P}_0^i - \mathbf{I}_{ML}\right) \tag{6-83}$$

$$\hat{\mathbf{C}}^{i+1} = \frac{1}{\beta+\rho}\left(\beta\hat{\mathbf{C}} + \mathbf{P}_1^i + \rho\mathbf{W}_1^i\right) \tag{6-84}$$

$$\mathbf{u}^{i+1} = \mathbf{D}\left(\mathbf{T}^*\left(\mathbf{W}_2^i + \frac{\mathbf{P}_2^i}{\rho}\right) - \frac{ML\boldsymbol{e}_1}{\rho}\right) \tag{6-85}$$

where $\mathbf{D} = diag\left(\frac{1}{ML},\frac{1}{2(ML-1)},\dots,\frac{1}{2}\right)$, $\boldsymbol{e}_1 = [1,0,\dots,0]^T$, and $\mathbf{T}^*(.)$ Denotes the adjoint operator of $\mathbf{T}(.)$. Finally, the $\mathbf{W}$ update step can be expressed as:

$$\mathbf{W}^{i+1} = \underset{\mathbf{W}}{\operatorname{argmin}} \left\| \mathbf{W} - \begin{bmatrix} \mathbf{Z}^{i+1} & \left(\hat{\mathbf{C}}^{i+1}\right)^H \\ \hat{\mathbf{C}}^{i+1} & \mathbf{T}\left(\mathbf{u}^{i+1}\right) \end{bmatrix} + \frac{\mathbf{P}^i}{\rho} \right\|_F^2 \tag{6-86}$$

Once the optimal estimate $\mathbf{T}(\mathbf{u})$ is obtained, the DoDs and DoAs information of the propagation paths can be extracted by applying 2-D MUSIC on $\mathbf{T}(\mathbf{u})$.

6.3.3.3. Range Estimation

The range parameters $r_{l_2}^{BS}$ and $r_{l_1}^{UE}$ can be estimated after DoDs and DoAs are extracted. In order to estimate the range parameters a new fourth-order cumulant matrix $\mathbf{C}_r$ can be formed as [51]:

$$\begin{aligned} C_{m_{BS},m_{UE}}\left(y_{m_{BS}^1,m_{UE}^1}(n), y_{0,0}^*(n), y_{m_{BS}^2,m_{UE}^2}(n), y_{-m_{BS}^2,-m_{UE}^2}^*(n)\right) &= \sum_{l_2=1}^{L_2}\sum_{l_1=1}^{L_1} c_{l_1,l_2} \\ e^{-j\left(2m_{BS}^1\omega\left(\varphi_{l_2}^{BS}\right)-2m_{UE}^1\omega\left(\varphi_{l_1}^{UE}\right)\right)} & \\ .\, e^{j\left(m_{BS}^2\omega\left(\varphi_{l_2}^{BS}\right)+\left(m_{BS}^2\right)^2\gamma\left(\varphi_{l_2}^{BS},r_{l_2}^{BS}\right)-m_{UE}^2\omega\left(\varphi_{l_1}^{UE}\right)+\left(m_{UE}^2\right)^2\gamma\left(\varphi_{l_2}^{UE},r_{l_2}^{UE}\right)\right)} &+ c_z^{m_{BS},m_{UE}} \end{aligned} \tag{6-87}$$

This time $\mathbf{C}_r$ takes the form of:

$$\mathbf{C}_r = \mathbf{B}_1(\boldsymbol{\varphi}^{BS}, \boldsymbol{\varphi}^{UE}, \boldsymbol{r})\mathbf{C}_\eta \mathbf{B}_1(\boldsymbol{\varphi}^{BS}, \boldsymbol{\varphi}^{UE})^H \tag{6-88}$$

After inserting the DoDs and DoAs, the range information can be found by applying eigenvalue decomposition. Then, the range estimation of $L_1 + L_2 = J$ scatters can be performed by adopting a MUSIC pseudo-spectrum search as [50]:

$$\left\{r_j^{BS}, r_j^{UE}\right\} = \underset{r_j^{BS}, r_j^{UE}}{\operatorname{argmax}} \frac{1}{\boldsymbol{a}\left(\hat{\theta}_j, r_j\right)\mathbf{U}_{\mathrm{n}}^H\mathbf{U}_{\mathrm{n}}\boldsymbol{a}\left(\hat{\theta}_j, r_j\right)^H} \tag{6-89}$$

where $\mathbf{U}_{\mathrm{n}}$ is the noise subspace matrix and $\hat{\theta}_j$ is the element of the set $\hat{\boldsymbol{\theta}}$ which contains all the estimated DoDs and DoAs of the J scatters. This method is a joint estimation, thus, no additional pairing algorithm between the angles and the ranges is needed. Further, the estimated range parameters can be used to classify the scatters as far-field or near-field source according to the Fresnel region. However, since we perform channel estimation, the source classification is not needed. Once the DoDs, DoAs and ranges are estimated they are used for channel estimation.

6.3.3.4. Gain Coefficient Estimation

After DoDs, DoAs and range parameters are estimated, the last step for the channel estimation is to extract the gain coefficients. The separate estimations of the α_{l_1} and α_{l_2} are almost impossible, however, the joint gain parameter η_{l_1,l_2} can be extracted and it is sufficient for the channel estimation. The element wise signal model in (6-42) can be formulated in the matrix form at time τ as:

$$\mathbf{Y}(n) = \mathbf{A}(\boldsymbol{\varphi}^{BS}, \mathbf{r}^{BS})\mathbf{H}_{\eta}(n)\mathbf{A}(\boldsymbol{\varphi}^{UE}, \mathbf{r}^{UE})^{T}\mathbf{S}(n) + \mathbf{Z}(n) \tag{6-90}$$

where $\mathbf{Y}(n)\epsilon\mathbb{C}^{M_{BS}\times M_{UE}}$ is the received signal matrix, $\mathbf{A}(\boldsymbol{\varphi}^{BS}, \mathbf{r}^{BS})\epsilon\mathbb{C}^{M_{BS}\times L_2}$ is the steering matrix whose l_2-th column represents the steering vector of the l_2-th scatter, $\mathbf{A}(\boldsymbol{\varphi}^{UE}, \mathbf{r}^{UE})\epsilon\mathbb{C}^{M_{UE}\times L_1}$ is the steering matrix whose l_1-th column represents the steering vector of the l_1-th scatter where steering vectors can be computed with (3), $\mathbf{S}(n)\epsilon\mathbb{C}^{M_{UE}\times M_{UE}}$ is a diagonal matrix as $\mathbf{S}(n) = \mathbf{s}\mathbf{I}_{M_{UE}}$, $\mathbf{Z}(n)\epsilon\mathbb{C}^{M_{BS}\times M_{UE}}$ is the noise matrix, $\mathbf{H}_{\eta}(n)\epsilon\mathbb{C}^{L_1L_2\times L_1L_2}$ is a diagonal matrix as:

$$\mathbf{H}_{\eta}(n) = \begin{bmatrix} \eta_1 & 0 & 0 & 0 \\ 0 & \eta_g & 0 & 0 \\ \vdots & \vdots & \ddots & \vdots \\ 0 & 0 & 0 & \eta_G \end{bmatrix} \tag{6-91}$$

where η_g can be expressed as:

$$\eta_g = \prod_{l_1=1}^{L_1} \alpha_{l_1}\,\alpha_{l_2}\boldsymbol{a}\left(\varphi_{l_2}^{RIS}\right)^{T}\boldsymbol{\Theta}\boldsymbol{a}\left(\varphi_{l_1}^{RIS}\right) \tag{6-92}$$

The $\mathbf{Y}(n)$is vectorized as the first step of estimation $\mathbf{H}_{\eta}(\tau)$ as:

$$\hat{\boldsymbol{y}}(n) = \underbrace{\mathbf{A}(\boldsymbol{\varphi}^{UE}, \mathbf{r}^{UE})^{*} \odot \mathbf{A}(\boldsymbol{\varphi}^{BS}, \mathbf{r}^{BS})}_{\mathbf{Q}}\,\mathrm{vec}\{\mathbf{H}_{\eta}(n)\} + \hat{\boldsymbol{z}}(n) \tag{6-93}$$

Then, the gain coefficients can be estimated by using least-squares (LS) as [19], [50]:

$$\hat{\mathbf{H}}_{\eta}(n) = (\mathbf{Q}^{H}\mathbf{Q})^{-1}\mathbf{Q}^{H}\hat{\boldsymbol{y}}(n) \tag{6-94}$$

Finally, the estimated channel can be obtained as:

$$\hat{\mathbf{H}}(n) = \hat{\mathbf{A}}(\boldsymbol{\theta}^{BS}, \mathbf{r}^{BS})\hat{\mathbf{H}}_{\eta}(n)\hat{\mathbf{A}}(\boldsymbol{\varphi}^{UE}, \mathbf{r}^{UE})^{H} \tag{6-95}$$

6.3.4. Simulation Results

This section shows the simulations results to evaluate and compare the performance of the proposed channel estimation method. In the first step, DoD, DoA and range estimation performances of the proposed method is evaluated and compared with two of the prominent

state-of-the art methods which are known as 2D spatial smoothing multiple signal classification (SS-MUSIC) [59] and ADMM based 2D least absolute shrinkage selection operator (LASSO) [60]. The Cramer-Rao bound (CRB) is selected for the benchmark for DoD, DoA and range estimation. The CRB calculation is given in [61]. The root mean square error (RMSE) is selected for DoD, DoA and range estimations as the performance metric at $\mathrm{MC} = 250$ Monte Carlo trails and $S = 200$ snapshots. The RMSE can be defined as:

$$RMSE_{\varphi^{BS}} = \frac{1}{L_2}\sum_{l_2=1}^{L_2}\sqrt{\frac{1}{\mathrm{MC}}\sum_{j=1}^{\mathrm{MC}}\left[\left(\tilde{\varphi}_{l_2,j}^{BS} - \varphi_{l_2}^{BS}\right)^2\right]} \tag{6-96}$$

$$RMSE_{\varphi^{UE}} = \frac{1}{L_1}\sum_{l_1=1}^{L_1}\sqrt{\frac{1}{\mathrm{MC}}\sum_{j=1}^{\mathrm{MC}}\left[\left(\tilde{\varphi}_{l_1,j}^{UE} - \varphi_{l_1}^{UE}\right)^2\right]} \tag{6-97}$$

where $\tilde{\varphi}_{l_2,j}^{BS}$ and $\tilde{\varphi}_{l_1,j}^{UE}$ are the estimated DoAs and DoDs in each trail. The RMSE of the range estimations are calculated similar to (6-75) and (6-76).

The related parameters for the RMSE simulations are given in Table 6-IV.

Table 6-IV. Simulation parameters.

Parameter	Value
L_2, L_1	$5, 3$
d_x^{BS}, d_x^{UE}	$\lambda/4\,, \lambda/4$
M_{BS}, M_{UE}	$17, 5$
DoAs	$[12.15^o, 23.27^o, 27.97^o, 32.56^o, 37.34^o]$
DoDs	$[-5.56^o, 7.73^o, 15.78^o]$
r_{BS}	$[3\lambda, 6\lambda, 23\lambda, 52\lambda, 78\lambda]$
r_{UE}	$[2\lambda, 3.5\lambda, 34\lambda]$
$\alpha_{l_1}, \alpha_{l_2}$	$\mathcal{CN}(0,1)$

The uniform searching grids of the DoA and DoD estimations for SS-MUSIC and ADMM-based LASSO are assumed as $[10^o : 0.01^o : 40^o]$ and $[-10^o : 0.01^o : 20^o]$, respectively, and for range estimation $[1\lambda : 0.5\lambda : 80\lambda]$.

Before the RMSE performance comparisons, we evaluate the DoA and DoD estimation accuracy of the proposed method with respect to the estimated ranges. Fig. 6.10 (a) and (b) show scatter diagrams to illustrate the localization of the scatters between the RIS-BS channel and between the UE-RIS channel. It can be seen that all the 5 scatters between RIS-BS and all the 3 scatters between UE-RIS are accurately located. The localization performance of the proposed method is evaluated under 10 dB SNR with $\mathrm{MC} = 250$ Monte Carlo trails as well. Estimating DoD, DoA and range components is known as localization and additional estimation on path gains would give the channel estimation.

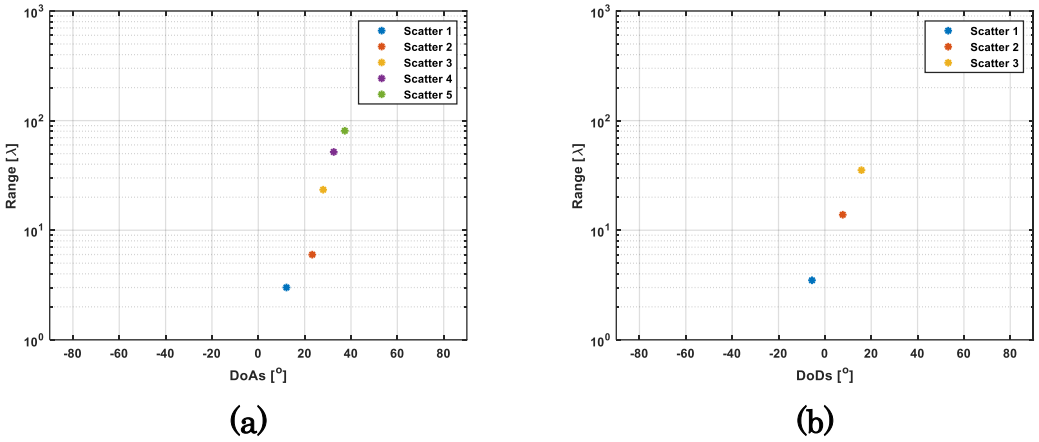

Fig. 6.10. Scatter plots for localization of the scatters: (a) between the RIS-BS channel (DoAs), (b) between the UE-RIS channel (DoDs).

Fig. 6.11 (a) and (b) shows the RMSE performances of the proposed method, ADMM-based LASSO and SS-MUSIC. It can be seen that the proposed method has the best performance and its DoA RMSE is close to CRB when the SNR is higher than 0 dB and gets better as the SNR increases. However, DoA RMSE performances of ADMM-based LASSO and SS-MUSIC are also at acceptable. It should be noted that the number of snapshots is selected more than the product of the numbers of the BS and UE antennas ($N > M_{BS}M_{UE} = 85$) in order for SS-MUSIC to provide better performance and regularization coefficient for ADMM-based LASSO, which arranges the trade-off between sparsity and accuracy, is selected optimum as in [60] for the same manner. On the other hand, the DoD RMSE performances of the ADMM-based LASSO and SS-MUSIC degrade since the number of antennas at the UE side is lower. We can conclude that even though, we provide advantage to both ADMM-based LASSO and SS-MUSIC, in overall, the proposed method has better DoD, DoA and range estimation accuracy.

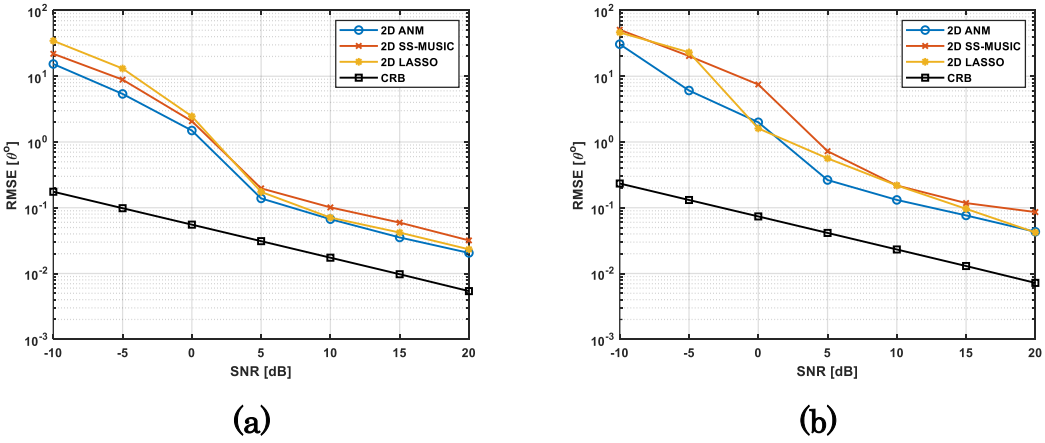

Fig. 6.11. The RMSE comparison with respect to SNR of the 2D ANM, 2D SS-MUSIC and 2D LASSO: (a) DoAs, (b) DoDs.

The error performance of the proposed channel estimation method is evaluated and compared with the state-of-the art channel estimators by the normalized mean square error (NMSE) as a performance metric. The NMSE can we defined as:

$$\text{NMSE} \triangleq \text{E}\left(\frac{\left\|\mathbf{H}-\widehat{\mathbf{H}}\right\|_F^2}{\left\|\widehat{\mathbf{H}}\right\|_F^2}\right) \tag{6-98}$$

The simulation parameters for the channel estimation are same as in Table 6-IV. However, the angles φ^{BS}, φ^{UE} and ranges r^{BS}, r^{UE} follow the uniform distribution as $\varphi^{BS}\epsilon\mathcal{U}(-\pi/6,\pi/6)$ $\varphi^{UE}\epsilon\mathcal{U}(-\pi/4,\pi/4)$, $\text{r}^{BS}\epsilon\mathcal{U}(0,20\lambda)$ and $\text{r}^{UE}\epsilon\mathcal{U}(0,20\lambda)$. The scanning resolutions for the angle grids and range grids are 0.1^o and $\lambda/10$, respectively.

Fig. 6.12 shows the NMSE comparison for the proposed method and the state-of-the art channel estimator of the least-squares estimator (LS) [50], orthogonal matching pursuit (OMP) [62] estimator and the oracle [63] estimator. It should be noted that the oracle channel estimator only estimates the diagonal channel gain matrix $\mathbf{H}_\eta$ where the all the angles and ranges are assumed to be exactly known, therefore, it can be considered as a benchmark. From the figure, it can be seen that the proposed method has the best performance gain over the LS, the far-field model based OMP and the near-field model based OMP estimators. The proposed method has only ≈ 5 dB difference between the benchmark. Since the range parameters, thus the near-field phase components, are included in the steering vectors in the near-field model based OMP estimator, its performance is close to the proposed method. The far-field model based OMP has the worst performance since it does not take into account the near-field phase components, therefore, significant performance degradation is observed.

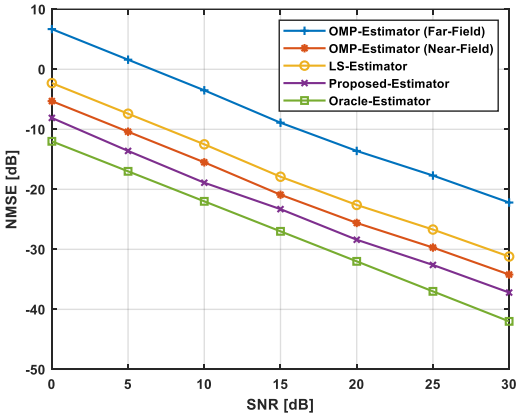

Fig. 6.12. The NMSE comparison of LS, far-field OMP, near-field-OMP, LS, oracle and the proposed channel estimators.

6.4. Conclusions

An algorithm to the challenging problems of high energy consumption and fast DoA tracking in RIS-aided systems was proposed. The proposed algorithm has been tested on a RIS-aided massive MIMO system, which includes large number of antenna elements. The low power consumption was achieved by reducing the number of RF chains and including a switched antenna array in the access point. However, this leads incomplete signal data matrix. The matrix completion problem was solved by TNNR-ADMM algorithm. On the other hand, the required fast computation time cannot be achieved by subspace DoA algorithms which involve heavy matrix computations such as matrix inversion or EVD. We proposed low-complexity ADAM based novel adaptive forgetting factor RLS algorithm AF-RLS for fast and accurate DoA tracking. The proposed algorithm evaluated and compared with the state-of-the art algorithms under single-path propagation and multi-path propagation conditions. As a final remark for multi-path propagation, employing only 70-75 % of the active elements in AP is sufficient for DoA estimation and tracking. The AF-RLS obtaining more accurate estimation than RLS by $> 2^o$ in elevation and $> 1^o$ in azimuth. The proposed AF-RLS has $\cong 2.41e7$ times less computational complexity than subspace algorithm MUSIC but $\cong 2.24$ times more than RLS algorithm, however, achieves at least 5 dB more spectral gain than the revised state-of-the DoA algorithms.

On the other hand, an efficient channel estimation method for the RIS-aided mm-Wave massive MIMO systems was proposed. It has been showed that the proposed method had performed accurate channel estimation and superior performance then the state-of-the art channel estimators. The proposed method accurately locates the scatters and simulation results validate that the channel estimation performance proposed method is comparable with the oracle channel estimator, which is considered as benchmark since the angles and ranges are known beforehand. The proposed method only has ≈ 5 dB lower NMSE value than the benchmark and achieves at least ≈ 4 dB better NMSE than near-field model based OMP, which has the closest performance among the revised state-of-the art channel estimator. To sum-up the proposed method is promising for channel estimation problems in RIS-aided system and one of the few studies in the literature on hybrid-field channel estimation.

As a future outline, it is planned to adopt the proposed AF-RLS DoA estimation algorithm in the hybrid-channel estimation for the RIS-aided mm-Wave massive MIMO systems instead of using MUSIC algorithm and extend the 2-D channel estimation to 3-D.

6.5. References Chapter 6

[1] R. Chen, M. Liu, Y. Hui, N. Cheng, and J. Li, "Reconfigurable Intelligent Surfaces for 6G IoT Wireless Positioning: A Contemporary Survey," IEEE Internet of Things Journal, vol. 9, no. 23, pp. 23570–23582, Dec. 2022, doi: 10.1109/JIOT.2022.3203890.

[2] J. He, F. Jiang, K. Keykhosravi, J. Kokkoniemi, H. Wymeersch, and M. Juntti, Beyond 5G RIS mmWave Systems: Where Communication and Localization Meet. 2021.

[3] J. He, H. Wymeersch, and M. Juntti, "Channel Estimation for RIS-Aided mmWave MIMO Systems via Atomic Norm Minimization," IEEE Trans. Wireless Commun., vol. 20, no. 9, pp. 5786–5797, Sep. 2021, doi: 10.1109/TWC.2021.3070064.

[4] S. Dang, O. Amin, B. Shihada, and M.-S. Alouini, "What should 6G be?," Nat Electron, vol. 3, no. 1, pp. 20–29, Jan. 2020, doi: 10.1038/s41928-019-0355-6.

[5] R. Wang, H. Ren, C. Pan, J. Fang, M. Dong, and O. A. Dobre, "Channel Estimation for RIS-aided mmWave Massive MIMO System Using Few-bit ADCs." arXiv, Jan. 26, 2023. Accessed: Apr. 28, 2023. [Online]. Available: http://arxiv.org/abs/2301.11066

[6] E. Ali, M. Ismail, R. Nordin, and N. F. Abdulah, "Beamforming techniques for massive MIMO systems in 5G: overview, classification, and trends for future research," Frontiers Inf Technol Electronic Eng, vol. 18, no. 6, pp. 753–772, Jun. 2017, doi: 10.1631/FITEE.1601817.

[7] F. Rusek et al., "Scaling up MIMO: Opportunities and Challenges with Very Large Arrays," IEEE Signal Process. Mag., vol. 30, no. 1, pp. 40–60, Jan. 2013, doi: 10.1109/MSP.2011.2178495.

[8] A. E. Zorkun, M. A. Salas-Natera, and R. Martinez Rodriguez-Osorio, "Improved Iterative Inverse Matrix Approximation Algorithm for Zero Forcing Precoding in Large Antenna Arrays," IEEE Access, vol. 10, pp. 100964–100975, 2022, doi: 10.1109/ACCESS.2022.3208155.

[9] P. Zhang, J. Zhang, H. Xiao, H. Du, D. Niyato, and B. Ai, "RIS-Aided 6G Communication System With Accurate Traceable User Mobility," IEEE Trans. Veh. Technol., vol. 72, no. 2, pp. 2718–2722, Feb. 2023, doi: 10.1109/TVT.2022.3214818.

[10] M. Xu, S. Zhang, C. Zhong, J. Ma, and O. A. Dobre, "Ordinary Differential Equation-Based CNN for Channel Extrapolation Over RIS-Assisted Communication," IEEE Commun. Lett., vol. 25, no. 6, pp. 1921–1925, Jun. 2021, doi: 10.1109/LCOMM.2021.3064596.

[11] M. Jian et al., "Reconfigurable intelligent surfaces for wireless communications: Overview of hardware designs, channel models, and estimation techniques," Intell. and Converged Netw., vol. 3, no. 1, pp. 1–32, Mar. 2022, doi: 10.23919/ICN.2022.0005.

[12] Y. Liu et al., "Reconfigurable Intelligent Surfaces: Principles and Opportunities," IEEE Communications Surveys Tutorials, vol. 23, no. 3, pp. 1546–1577, 2021, doi: 10.1109/COMST.2021.3077737.

[13] Z.-Q. He and X. Yuan, "Cascaded Channel Estimation for Large Intelligent Metasurface Assisted Massive MIMO," IEEE Wireless Communications Letters, vol. 9, no. 2, pp. 210–214, Feb. 2020, doi: 10.1109/LWC.2019.2948632.

[14] M. Dajer et al., "Reconfigurable intelligent surface: Design the channel – A new opportunity for future wireless networks," Digital Communications and Networks, Nov. 2021, doi: 10.1016/j.dcan.2021.11.002.

[15] T. Wang, B. Ai, R. He, and Z. Zhong, "Two-Dimension Direction-of-Arrival Estimation for Massive MIMO Systems," IEEE Access, vol. 3, pp. 2122–2128, 2015, doi: 10.1109/ACCESS.2015.2496944.

[16] H. Halbauer, S. Saur, J. Koppenborg, and C. Hoek, "3D beamforming: Performance improvement for cellular networks," Bell Labs Tech. J., vol. 18, no. 2, pp. 37–56, Sep. 2013, doi: 10.1002/bltj.21604.

[17] A. Fascista, A. Coluccia, H. Wymeersch, and G. Seco-Granados, "RIS-Aided Joint Localization and Synchronization with a Single-Antenna Mmwave Receiver," in ICASSP 2021 - 2021 IEEE International Conference on Acoustics, Speech and Signal Processing (ICASSP), Toronto, ON, Canada: IEEE, Jun. 2021, pp. 4455–4459. doi: 10.1109/ICASSP39728.2021.9413515.

[18] N. Ruan, H. Wang, F. Wen, and J. Shi, "DOA Estimation in B5G/6G: Trends and Challenges," Sensors, vol. 22, no. 14, p. 5125, Jul. 2022, doi: 10.3390/s22145125.

[19] L. Yashvanth and C. R. Murthy, "Cascaded Channel Estimation for Distributed IRS Aided mmWave Massive MIMO Systems," in GLOBECOM 2022 - 2022 IEEE Global Communications Conference, Rio de Janeiro, Brazil: IEEE, Dec. 2022, pp. 717–723. doi: 10.1109/GLOBECOM48099.2022.10001263.

[20] Y. Lin, S. Jin, M. Matthaiou, and X. You, "Channel Estimation and User Localization for IRS-Assisted MIMO-OFDM Systems," IEEE Trans. Wireless Commun., vol. 21, no. 4, pp. 2320–2335, Apr. 2022, doi: 10.1109/TWC.2021.3111176.

[21] H. Krim and M. Viberg, "Two decades of array signal processing research: the parametric approach," IEEE Signal Processing Magazine, vol. 13, no. 4, pp. 67–94, Jul. 1996, doi: 10.1109/79.526899.

[22] W. Zhang, Z. Wang, and W. P. Tay, "Approximate Maximum-Likelihood RIS-Aided Positioning," IEEE Trans. Wireless Commun., pp. 1–1, 2023, doi: 10.1109/TWC.2023.3266457.

[23] S. Buzzi, C.-L. I, T. E. Klein, H. V. Poor, C. Yang, and A. Zappone, "A Survey of Energy-Efficient Techniques for 5G Networks and Challenges Ahead," IEEE J. Select. Areas Commun., vol. 34, no. 4, pp. 697–709, Apr. 2016, doi: 10.1109/JSAC.2016.2550338.

[24] J. G. Andrews et al., "What Will 5G Be?," IEEE J. Select. Areas Commun., vol. 32, no. 6, pp. 1065–1082, Jun. 2014, doi: 10.1109/JSAC.2014.2328098.

[25] J. Xiao, J. Wang, Z. Chen, and G. Huang, "U-MLP-Based Hybrid-Field Channel Estimation for XL-RIS Assisted Millimeter-Wave MIMO Systems," IEEE Wireless

Commun. Lett., vol. 12, no. 6, pp. 1042–1046, Jun. 2023, doi: 10.1109/LWC.2023.3259465.

[26] M. Cui, Z. Wu, Y. Lu, X. Wei, and L. Dai, "Near-Field MIMO Communications for 6G: Fundamentals, Challenges, Potentials, and Future Directions," IEEE Commun. Mag., vol. 61, no. 1, pp. 40–46, Jan. 2023, doi: 10.1109/MCOM.004.2200136.

[27] Z. Hu, C. Chen, Y. Jin, L. Zhou, and Q. Wei, "Hybrid-Field Channel Estimation for Extremely Large-Scale Massive MIMO System," IEEE Commun. Lett., vol. 27, no. 1, pp. 303–307, Jan. 2023, doi: 10.1109/LCOMM.2022.3219937.

[28] W. Yu, Y. Shen, H. He, X. Yu, J. Zhang, and K. B. Letaief, "Hybrid Far- and Near-Field Channel Estimation for THz Ultra-Massive MIMO via Fixed Point Networks," in GLOBECOM 2022 - 2022 IEEE Global Communications Conference, Rio de Janeiro, Brazil: IEEE, Dec. 2022, pp. 5384–5389. doi: 10.1109/GLOBECOM48099.2022.10001564.

[29] H. Jiang, B. Xiong, H. Zhang, and E. Basar, "Hybrid Far- and Near-field Modeling for Reconfigurable Intelligent Surface Assisted V2V Channels: A Sub-Array Partition Based Approach," IEEE Trans. Wireless Commun., pp. 1–1, 2023, doi: 10.1109/TWC.2023.3262063.

[30] V. Garg, P. Giménez-Febrer, A. Pagès-Zamora, and I. Santamaria, "DOA estimation via shift-invariant matrix completion," Signal Processing, vol. 183, p. 107993, Jun. 2021, doi: 10.1016/j.sigpro.2021.107993.

[31] B. Jalal, O. Elnahas, and Z. Quan, "Efficient DOA Estimation Under Partially Impaired Antenna Array Elements," IEEE Trans. Veh. Technol., vol. 71, no. 7, pp. 7991–7996, Jul. 2022, doi: 10.1109/TVT.2022.3169404.

[32] H. Chen, Y. Bai, Q. Wang, H. Chen, L. Tang, and P. Han, "DOA Estimation Assisted by Reconfigurable Intelligent Surfaces," IEEE Sensors J., vol. 23, no. 12, pp. 13433–13442, Jun. 2023, doi: 10.1109/JSEN.2023.3273862.

[33] A. E. Zorkun, M. A. Salas-Natera, and R. M. Rodríguez-Osorio, "An Improved Hybrid Beamforming Algorithm for Fast Target Tracking in Satellite and V2X Communication," Remote Sensing, vol. 16, no. 1, Art. no. 1, Jan. 2024, doi: 10.3390/rs16010013.

[34] Debing Zhang, Yao Hu, Jieping Ye, Xuelong Li, and Xiaofei He, "Matrix completion by Truncated Nuclear Norm Regularization," in 2012 IEEE Conference on Computer Vision and Pattern Recognition, Providence, RI: IEEE, Jun. 2012, pp. 2192–2199. doi: 10.1109/CVPR.2012.6247927.

[35] B. Recht, M. Fazel, and P. A. Parrilo, "Guaranteed Minimum-Rank Solutions of Linear Matrix Equations via Nuclear Norm Minimization," SIAM Review, vol. 52, no. 3, pp. 471–501, 2010.

[36] L. T. Nguyen, J. Kim, and B. Shim, "Low-Rank Matrix Completion: A Contemporary Survey," IEEE Access, vol. 7, pp. 94215–94237, 2019, doi: 10.1109/ACCESS.2019.2928130.

[37] Y. Hu, D. Zhang, J. Ye, X. Li, and X. He, "Fast and Accurate Matrix Completion via Truncated Nuclear Norm Regularization," IEEE Transactions on Pattern Analysis and Machine Intelligence, vol. 35, no. 9, pp. 2117–2130, Sep. 2013, doi: 10.1109/TPAMI.2012.271.

[38] S. Ciochina, C. Paleologu, J. Benesty, and A. A. Enescu, "On the influence of the forgetting factor of the RLS adaptive filter in system identification," in 2009 International Symposium on Signals, Circuits and Systems, Iasi, Romania: IEEE, Jul. 2009, pp. 1–4. doi: 10.1109/ISSCS.2009.5206117.

[39] S. Lee, J. Lim, and K.-M. Sung, "A low-complexity AFF-RLS algorithm using a normalization technique," IEICE Electron. Express, vol. 6, no. 24, pp. 1774–1780, 2009, doi: 10.1587/elex.6.1774.

[40] Z. Fei, Z. Wu, Y. Xiao, J. Ma, and W. He, "A new short-arc fitting method with high precision using Adam optimization algorithm," Optik, vol. 212, p. 164788, Jun. 2020, doi: 10.1016/j.ijleo.2020.164788.

[41] S. Song, J.-S. Lim, S. Baek, and K.-M. Sung, "Gauss Newton variable forgetting factor recursive least squares for time varying parameter tracking," Electronics Letters, vol. 36, no. 11, pp. 1–2, 2000.

[42] D. P. Kingma and J. Ba, "Adam: A Method for Stochastic Optimization." arXiv, Jan. 29, 2017. Accessed: Apr. 23, 2024. [Online]. Available: http://arxiv.org/abs/1412.6980

[43] J. Yang, Y. Yang, J. Lu, and L. Yang, "Iterative methods for DOA estimation of correlated sources in spatially colored noise fields," Signal Processing, vol. 185, p. 108100, Aug. 2021, doi: 10.1016/j.sigpro.2021.108100.

[44] M. Fukuda, M. Kojima, K. Murota, and K. Nakata, "Exploiting Sparsity in Semidefinite Programming via Matrix Completion I: General Framework," SIAM Journal on Optimization, vol. 11, Feb. 1970, doi: 10.1137/S1052623400366218.

[45] S. S. Haykin, Adaptive filter theory, 4th ed. Upper Saddle River, N.J: Prentice Hall, 2002.

[46] A. H. Sayed, Adaptive filters. Hoboken, N.J: Wiley-Interscience : IEEE Press, 2008.

[47] Shu-Hung Leung and C. F. So, "Gradient-based variable forgetting factor RLS algorithm in time-varying environments," IEEE Trans. Signal Process., vol. 53, no. 8, pp. 3141–3150, Aug. 2005, doi: 10.1109/TSP.2005.851110.

[48] Y. Cai and R. C. De Lamare, "Low-complexity variable forgetting factor mechanism for RLS algorithms in interference mitigation applications," in 2012 International Symposium on Wireless Communication Systems (ISWCS), Paris, France: IEEE, Aug. 2012, pp. 471–475. doi: 10.1109/ISWCS.2012.6328412.

[49] H.-C. Huang and J. Lee, "A New Variable Step-Size NLMS Algorithm and Its Performance Analysis," IEEE Transactions on Signal Processing, vol. 60, no. 4, pp. 2055–2060, Apr. 2012, doi: 10.1109/TSP.2011.2181505.

[50] K. Seo, G.-T. Gil, G. Kwon, S. Hong, and H. Park, "Cumulant Matrix-based Channel Estimation for Near-Field Massive MIMO Systems," in 2021 International

Conference on Information and Communication Technology Convergence (ICTC), Jeju Island, Korea, Republic of: IEEE, Oct. 2021, pp. 1603–1608. doi: 10.1109/ICTC52510.2021.9620981.

[51] B. Wang, J. Liu, and X. Sun, "Mixed Sources Localization Based on Sparse Signal Reconstruction," IEEE Signal Process. Lett., vol. 19, no. 8, pp. 487–490, Aug. 2012, doi: 10.1109/LSP.2012.2204248.

[52] I. A. Hemadeh, K. Satyanarayana, M. El-Hajjar, and L. Hanzo, "Millimeter-Wave Communications: Physical Channel Models, Design Considerations, Antenna Constructions, and Link-Budget," IEEE Commun. Surv. Tutorials, vol. 20, no. 2, pp. 870–913, 2018, doi: 10.1109/COMST.2017.2783541.

[53] J. Liang, D. Liu, X. Zeng, W. Wang, J. Zhang, and H. Chen, "JOINT AZIMUTH-ELEVATION/(-RANGE) ESTIMATION OF MIXED NEAR-FIELD AND FAR-FIELD SOURCES USING TWO-STAGE SEPARATED STEERING VECTOR-BASED ALGORITHM," PIER, vol. 113, pp. 17–46, 2011, doi: 10.2528/PIER10110104.

[54] Q. Liu, W. Chen, and L. Jin, "Passive Localization for Mixed Near-Field and Far-Field Sources Based on Cumulant Sparse Representation," IJSIP, vol. 10, no. 5, pp. 67–78, May 2017, doi: 10.14257/ijsip.2017.10.5.06.

[55] B. Wang, Y. Zhao, and J. Liu, "Mixed-Order MUSIC Algorithm for Localization of Far-Field and Near-Field Sources," IEEE Signal Process. Lett., vol. 20, no. 4, pp. 311–314, Apr. 2013, doi: 10.1109/LSP.2013.2245503.

[56] A. M. Molaei, P. Del Hougne, V. Fusco, and O. Yurduseven, "Efficient Joint Estimation of DOA, Range and Reflectivity in Near-Field by Using Mixed-Order Statistics and a Symmetric MIMO Array," IEEE Trans. Veh. Technol., vol. 71, no. 3, pp. 2824–2842, Mar. 2022, doi: 10.1109/TVT.2021.3138251.

[57] J. He, L. Li, T. Shu, and T.-K. Truong, "Mixed Near-Field and Far-Field Source Localization Based on Exact Spatial Propagation Geometry," IEEE Trans. Veh. Technol., vol. 70, no. 4, pp. 3540–3551, Apr. 2021, doi: 10.1109/TVT.2021.3065954.

[58] Q. Wang, Z. Zhao, and Z. Chen, "Fast compressive sensing DOA estimation Via ADMM solver," in 2017 IEEE International Conference on Information and Automation (ICIA), Macau SAR, China: IEEE, Jul. 2017, pp. 53–57. doi: 10.1109/ICInfA.2017.8078882.

[59] Y. Wang, W. Cui, B. Yang, B. Ba, and F. Mei, "Symmetric thinned coprime array with reduced mutual coupling for mixed near-field and far-field sources localization," IET Radar, Sonar & Navigation, vol. 16, no. 8, pp. 1292–1303, 2022, doi: 10.1049/rsn2.12261.

[60] F. Afkhaminia and M. Azghani, "2D off-grid DOA estimation using joint sparsity," IET Radar, Sonar & Navigation, vol. 13, no. 9, pp. 1580–1587, 2019, doi: 10.1049/iet-rsn.2018.5442.

[61] P. Stoica and R. L. Moses, Spectral analysis of signals. Upper Saddle River, N.J: Pearson/Prentice Hall, 2005.

[62] J. Wu, Y. Li, and L. Xin, “Joint Channel Estimation for RIS-Assisted Wireless Communication System,” in 2022 IEEE Wireless Communications and Networking Conference (WCNC), Apr. 2022, pp. 1087–1092. doi: 10.1109/WCNC51071.2022.9771916.

[63] Y. C. Eldar and G. Kutyniok, Eds., Compressed sensing: theory and applications. Cambridge ; New York: Cambridge University Press, 2012.

7. Chapter 7: Conclusion and Future Work

7.1. Conclusion

Smart antennas, massive MIMO and RIS-aided communication systems provide effective solutions for both current, SATCOM, and next generation, 5G, B5G and 6G, wireless applications. We considered phased array antenna and RIS which are the fundamentals in modern wireless communication systems, as a whole. Therefore, in this thesis, different problems on the signal processing side related to phased antenna arrays and RISs were addressed, and various signal processing solutions to these problems has been presented.

1. In Chapter 3, explanation of the developed user-friendly adaptive beamforming algorithm tool was given. The trade-offs of the adaptive beamforming algorithms in order to determine pros and cons time reference, spatial reference and blind adaptive algorithms were determined. The developed tool provided the preliminary analysis which are the bases of rest of the other chapter. We have learnt, compared and determine the paths to improve the quality of the other methods. In line with the outcomes of the analyses an improved hybrid beamforming algorithm was developed. The proposed hybrid beamforming algorithm has superb convergence rate, tracking capability, output SNR level, and improved steady-state noise than its counterparts.
2. In Chapter 4, the proposed improved inverse matrix approximation algorithm was presented. This algorithm can be used in any array processing where the direct inversion of the matrix is needed, such as, inverse of correlation matrix in Wiener optimum, least-squares solutions to extract the coupling coefficients or estimation of gain coefficients in MIMO and RIS-aided MIMO channel estimation. The most of the inverse matrix approximation methods require pre-conditions, such as, Toeplitz or symmetric initial matrix, optimum initialization parameters and some pre-processing on received data to meet with the pre-conditions. The proposed inverse matrix approximation method does not require any pre-condition nor pre-processing to converge to a solution. The proposed algorithm was tested in zero forcing precoding in massive MIMO systems. The proposed algorithm outperformed the existing algorithms in terms of BER, convergence speed, and Frobenius norm error when the number of receiver antennas are increased.
3. In Chapter 5, two different automated calibration method were proposed. It is desirable to eliminate the time-consuming laboratory inspection on antenna array calibration procedure, thus, self-calibration methods have been derived. In fact, self-calibration methods are desired to be performed while the system is under operation. Therefore, a novel online self-calibration method based on mutual coupling for transmit antenna arrays was proposed. The proposed method has significant reduction

in both number of measurements and computational complexity. The proposed method is suitable for off-line, on-site and online calibration schemes. Numerical simulations are provided to evaluate the calibration performance of the method and a four-element simple experimental system is set-up to verify the effectiveness of the proposed method.

On the other hand, another novel calibration method for circularly polarized active antenna array based on axial ratio optimization for improvement of antenna array performance compensating errors and mutual coupling effect was proposed. The coupling parameters were measured, in addition, data of gain/phase uncertainties and location errors due to the manufacturing errors were used in the model presented for the analysis of the proposed method. It is demonstrated that the proposed method compensates errors and mutual coupling effect being suitable for the circularly polarized phased array antennas.

4. In Chapter 6, two major contributions for RIS-aided mm-Wave massive MIMO systems were presented. Firstly, an energy efficient low-complexity DoA estimation algorithm was proposed. The proposed algorithm is capable of detecting 3-D DoA estimation and tracking. It does not require all of the antenna elements in the antenna array to perform DoA estimation, but, the required signal samples can be collected by random switching in the receiver. Hence, the total power consumption in the system is reduced at the cost of low-rank signal data matrix. The low-rank matrix completion was performed using the TNNR-ADMM algorithm. Then the completed signal data was used for DoA estimation and tracking. For fast target tracking the algorithms needs adaptive parameters in order to achieve faster convergence rates. Therefore, a novel adaptive forgetting factor based on ADAM updating RLS algorithm was proposed for DoA estimation and fast tracking.

   On the other hand, an accurate channel estimation method for the RIS-aided mm-Wave massive MIMO systems was proposed. The proposed method is one of the few studies in the literature for hybrid near-field and far-field channel estimation for the RIS-aided MIMO systems. New channel formulation was derived and the higher statistics of the receive signal was used to eliminate the near-field phase components on the mixed field signal model. The ANM continuous angle domain sparse reconstruction method was used to increase the DoD and DoA estimation resolution. The proposed method accurately locates the scatters as well as estimate the gain coefficients for channel estimation. It has been showed that the proposed method had performed accurate channel estimation and superior performance then the state-of-the art channel estimators.

7.2. Future Work

Thanks to the contributions made to this thesis, it became clear that time was short for all lines of research opened. Therefore, the following paragraphs describe some research studies that complement the work presented in this thesis. Each paragraph gives extended future works for the related chapter.

- Following the proposed improved hybrid beamforming in the Chapter 3, the work can be extended to large phased array antennas for tracking low-earth-orbit (LEO) constellation. The geometric formulations of the LEO tracking systems can be extended for novel and more comprehensive communication scenarios. The novel Tx/Rx technologies and architectures can be investigated and the proposed algorithm can be implemented on those platforms as well as can be tested and analyzed. To be more precise the pros and cons of the analog, digital and hybrid architectures can be evaluated under extended formulated scenarios and certain trade-offs can be analysed such as field of view (FoV), power consumption and cost in LEO systems. Among the many scenarios and use cases smart beamforming for direct LEO satellite access of future internet-of-things (IoT) can be selected as one of the hot topics.
- Even though, the work in Chapter 4, the inverse matrix approximation algorithms for phased antenna array applications are a comprehensive work it could be improved in terms of computational complexity. The proposed algorithm includes the practical conditions in phased antenna arrays such as, mutual coupling effects, gain/phase uncertainties and location errors, and has superb convergence rate and BER performance over its counterparts. Moreover, the proposed algorithm converges globally, means it convergence does not depend on any initial condition or pre-computation. However, the proposed algorithm is based on matrix-matrix multiplications and sums which yields higher computational complexity and requires more memory storage in hardware. The algorithm can be reduced in matrix-vector or vector-vector multiplications and sums. Thus, the order of the computational complexity might be reduced as $N^3 \rightarrow N^2$.
- The proposals in Chapter 5 present valuable works on antenna array calibration. The self-calibration and the axial ratio improvement methods rely on mutual coupling which allows the system to identify the imperfections of each element by using the coupled signals. Such methods are useful since they do not require auxiliary antennas or hardware, as well as they reduce the time and cost. However, mutual coupling information can only be acquired by a large number of measurements, thus, it is important to get the coupling information of each antenna couple with a minimum number of measurements. Therefore, one of the blind separation algorithms, such as, independent component analysis (ICA),

ensuing a compressed sensing algorithm which allows single snapshot signal processing might be used to extract all the coupling coefficients with only one measurement.

- The RIS-aided communication systems are nowadays a hot topic and will be for a long time, perhaps have more open issues than the previously mentioned topics. Even though, Chapter 6 presents two related major works on two crucial open issues, there is a long way to go in this area. One of the promising future works on RIS-aided communication systems might be implementing the low-complexity DoA estimation algorithm which is presented in Chapter 6 into hybrid-field channel estimation problem. In addition, the practical conditions in phased antenna arrays such as, mutual coupling effects, gain/phase uncertainties and location errors were not included in the studies of Chapter VI. Hence, the effects of those impairments in antenna arrays on DoA and channel estimations must be evaluated and proper low-complexity yet efficient compensation techniques must be developed. On the other hand, in the dense communication environments it is expected to be tens maybe hundreds of distributed RIS components which brings huge computational burden to processing unit, thus, practical yet efficient optimum RIS selection and RIS-user matching algorithms could be developed. Moreover, the optimum emplacement of the RISs in the communication environment can be formulated as one of the new scenarios and the necessary can be derived for this scenario.

7.3. Publications

The list of publications that make up this doctoral thesis is given in this section.

7.3.1. Journals

1. **A. E. Zorkun**, M. A. Salas-Natera, and R. Martinez Rodriguez-Osorio, "Improved Iterative Inverse Matrix Approximation Algorithm for Zero Forcing Precoding in Large Antenna Arrays," IEEE Access, vol. 10, pp. 100964–100975, 2022, doi: 10.1109/ACCESS.2022.3208155.
2. **A. E. Zorkun**, M. A. Salas-Natera, and R. M. Rodríguez-Osorio, "An Improved Hybrid Beamforming Algorithm for Fast Target Tracking in Satellite and V2X Communication," Remote Sensing, vol. 16, no. 1, Art. no. 1, Jan. 2024, doi: 10.3390/rs16010013.
3. **A. E. Zorkun**, M. A. Salas-Natera, and R. M. Rodríguez-Osorio, "Efficient RIS-Aided 3-D DOA Estimation and Target Tracking Algorithm via Matrix Completion," IEEE Open Journal of Vehicular Technology, (submitted, second round review).

4. **A. E. Zorkun**, M. A. Salas-Natera, and R. M. Rodríguez-Osorio, “Hybrid-Field Channel Estimation for RIS-Aided Millimeter-Wave Massive MIMO Systems,” IEEE Open Journal of Antennas and Propagation, (submitted, first round review).
5. **A. E. Zorkun**, M. A. Salas-Natera, and R. M. Rodríguez-Osorio, “A Mutual Coupling-based Uplink Online Self-Calibration method for Antenna Arrays,” IEEE Open Journal of Antennas and Propagation, (2024). (Accepted)
6. M. A. Salas-Natera, **A. E. Zorkun**, and R. M. Rodríguez-Osorio, “Calibration and Axial Ratio Improvement method based on Polarization Agile System Capability,” IEEE Open Journal of Antennas and Propagation, (submitted, first round review).
7. M. A. Salas-Natera, **A. E. Zorkun**, and R. M. Rodríguez-Osorio, “Computer-Aided Experimental Studies for Adaptive Beamforming Algorithms and Array Processing in Engineering Education,” Computer Applications in Engineering Education (2024): e22741

7.3.2. Conferences

1. **A. E. Zorkun**, M. A. Salas-Natera, and R. M. Rodríguez-Osorio, " Hybrid CMA-RLS based Adaptive Beamforming Algorithm for Fast Target Tracking," in XXXVII Simposio Nacional de la Unión Científica Internacional de Radio. URSI 2022. Malaga, Spain. 5-7 September 2022.
2. **A. E. Zorkun**, M. A. Salas-Natera, and R. M. Rodríguez-Osorio, " Improved Hybrid Beamforming Algorithm for Fast Target Tracking in NTN-LEO and V2X Scenarios," in The 17th European Conference on Antennas and Propagation. Florence, Italy. 26-31 March 2023.

Aral Ertuğ Zorkun
Ph. D. in Technologies and Systems of Communication
Madrid, 2024